



**University of
Nottingham**

UK | CHINA | MALAYSIA

Piecewise Linear Dynamical Systems: From Nodes to Networks

Mustafa Şaylı

Thesis submitted to the University of Nottingham
for the degree of Doctor of Philosophy

June 2021

To my wife.

Abstract

Piecewise linear (PWL) modelling has many useful applications in the applied sciences. Although the number of techniques for analysing nonsmooth systems has grown in recent years, this has typically focused on low dimensional systems and relatively little attention has been paid to networks. We aim to redress this balance with a focus on synchronous oscillatory network states. For networks with smooth nodal components, weak coupling theory, phase-amplitude reductions, and the master stability function are standard methodologies to assess the stability of the synchronous state. However, when network elements have some degree of nonsmoothness, these tools cannot be directly used and a more careful treatment is required. The work in this thesis addresses this challenge and shows how the use of *saltation operators* allows for an appropriate treatment of networks of PWL oscillators. This is used to augment all the aforementioned methods. The power of this formalism is illustrated by application to network problems ranging from mechanics to neuroscience.

Acknowledgements

First of all, I would like to thank my supervisor Prof. Stephen Coombes, who has been a constant source of motivation and inspiration from the first day of my PhD studies till the end. I will be forever grateful for his support and mentorship. I also thank my co-supervisors Dr. Rüdiger Thul and Dr. Rachel Nicks for their guidance and advices. Secondly, I thank my wife, who has supported me at every step of this journey, and my daughter, who always brings great happiness to my life. Last but not least, I would like to thank my colleagues and friends for their helps and companionship. I also acknowledge the University of Nottingham and TUBITAK for financial support.

List of Publications

1. Publications associated with the thesis content:

- M. Şayli, Y. M. Lai, R. Thul, and S. Coombes. Synchrony in networks of franklin bells. *IMA Journal of Applied Mathematics*, 84(5):1001–1021, 2019.
- S. Coombes, Y. M. Lai, M. Şayli, and R. Thul. Networks of piecewise linear neural mass models. *European Journal of Applied Mathematics*, 29(5):869–890, 2018.
- S. Coombes, Y. M. Lai, M. Şayli, R. Thul, R. Nicks, and M. A. Porter. Oscillatory networks: insights from piecewise linear modelling. *SIAM Review*, (In preparation).

2. Other publications:

- M. Şayli and E. Yilmaz. Anti-periodic solutions for state-dependent impulsive recurrent neural networks with time-varying and continuously distributed delays. *Annals of Operations Research*, 258:159–185, 2017.
- M. Şayli and E. Yilmaz. Chaotifying delayed recurrent neural networks via impulsive effects. *Chaos*, 26:023114, 2016.
- M. Şayli and E. Yilmaz. State-dependent impulsive Cohen–Grossberg neural networks with time-varying delays. *Neurocomputing*, 171:1375–1386, 2016.
- M. Şayli and E. Yilmaz. Periodic solution for state-dependent impulsive shunting inhibitory CNNs with time-varying delays. *Neural Networks*, 68: 1–11, 2015.
- M. Şayli and E. Yilmaz. Global robust asymptotic stability of variable-time impulsive BAM neural networks. *Neural Networks*, 60:67–73, 2014.
- M. Şayli and E. Yilmaz. State-Dependent Impulsive Neural Networks. *International Conference on Dynamics Games and Science, Springer Chapter*, 389–413, 2014.

Glossary

Below is a list of abbreviations used in this thesis are given:

- ODEs - Ordinary differential equations,
- MSF - Master stability function,
- PRC - Phase response curve,
- iPRC - Infinitesimal phase response curve,
- IRC - Isostable response curve,
- iIRC - Infinitesimal isostable response curve,
- PWS - Piecewise smooth,
- PWL - Piecewise linear,
- ML - Morris-Lecar,
- PML - Piecewise linear Morris-Lecar,
- HH - Hodgkin-Huxley,
- SNIC - Saddle-node of invariant circle,
- FHN - FitzHugh-Nagumo,
- WC - Wilson-Cowan,
- LEs - Lyapunov exponents.

Contents

Abstract	i
Acknowledgements	ii
List of Publications	iii
Glossary	iv
1 Introduction	2
1.1 Motivation	2
1.2 Overview of the thesis	3
2 Background	7
2.1 Introduction	7
2.2 Isochrons and phase reduction	8
2.3 Isostables and phase-amplitude reduction	11
2.3.1 Phase and isostable reduction with second-order accuracy	17
2.3.2 An alternative strategy for calculation of second-order terms	21
2.4 Networks of oscillators	23
2.4.1 Weakly coupled phase oscillators	25
2.4.2 Phase locked states and stability	28
2.4.3 Synchrony	29
2.4.4 Coupled phase-amplitude oscillators	31
2.4.5 Master stability function technique	34
2.4.6 An illustrative example: a network of Stuart-Landau os- cillators	38
3 Nonsmooth oscillators with piecewise dynamics	44

3.1	Introduction	44
3.2	Nonsmooth dynamical systems and a classification	46
3.3	Planar piecewise linear models	50
3.4	Single neuron behaviour and the FitzHugh-Nagumo model . . .	55
3.4.1	The McKean model	57
3.4.2	The absolute model	61
3.4.3	A model with a homoclinic loop	62
3.4.4	Piecewise Linear Morris–Lecar model	66
3.5	Discussion	70
4	Stability and response of periodic orbits in PWL systems	73
4.1	Introduction	73
4.2	Stability: Adaptation of Floquet theory	76
4.3	Phase response curves for piecewise linear systems	81
4.4	Isostable response curves for piecewise linear systems	91
4.5	Second-order terms in response functions for piecewise linear systems	95
4.5.1	Computing $\mathcal{B}(t)$ for piecewise linear systems	99
4.5.2	Computing $\mathcal{C}(t)$ for piecewise linear systems	103
4.6	Synchronization of coupled oscillators with piecewise linear dy- namics	107
4.6.1	Networks of two phase-amplitude units	108
4.6.2	Master stability function approach	113
4.7	Applications and comparisons	116
4.7.1	Networks of the McKean and absolute models	116
4.7.2	Networks of piecewise linear Morris-Lecar model	116
4.7.3	Networks of the homoclinic (loop) model	117
4.8	Discussion	121
5	Networks of Franklin bells	127
5.1	Introduction	127

5.2	Model description and periodic orbits	130
5.2.1	Construction and stability of periodic solution	132
5.3	A piecewise linear smoothing technique	136
5.4	A Franklin bell network	139
5.4.1	Master stability function for a nonsmooth Franklin bell network	140
5.4.2	Master stability function for a smoothed Franklin bell network	143
5.5	Examples	145
5.6	Discussion	148
6	Piecewise linear neural mass models	153
6.1	Introduction	153
6.2	The Wilson-Cowan model	157
6.3	A piecewise linear reduction	158
6.4	A piecewise linear Wilson-Cowan network	162
6.4.1	Example: a ring network	167
6.5	The Heaviside world	170
6.5.1	Periodic orbits and their stability	173
6.5.2	An unstable periodic sliding orbit	176
6.6	A network of Heaviside Wilson-Cowan nodes	177
6.7	Discussion	183
7	The two process model for sleep-wake regulation	186
7.1	Introduction	186
7.2	Model description and periodicity	189
7.3	Construction and stability of periodic orbits	193
7.3.1	Stability I: Saltation approach	194
7.3.2	Implicit relation of the event times	197
7.3.3	Stability II: Using the implicit relation of the event times	198
7.3.4	Lyapunov exponents	200

7.3.5	Superstable solutions	204
7.4	Bifurcation of periodic solutions	204
7.4.1	Arnol'd tongues	205
7.4.2	Borders created by saddle-node bifurcations	205
7.4.3	Borders created by grazing bifurcations	207
7.4.4	Type I grazing bifurcation	209
7.4.5	Type II grazing bifurcation	210
7.4.6	Extended bifurcation set	211
7.5	The two process model and co-sleeping	217
7.6	Discussion	220
8	Summary and future perspectives	222
	Bibliography	227
	Appendices	252
A	Saltation matrix and the Floquet exponent formula	252
B	The absolute model: Period is independent of \bar{w}	256
C	Coupling functions	258

Chapter 1

Introduction

1.1 Motivation

Oscillations (e.g. limit cycle, periodic, quasi-periodic or chaotic) are one of the main forms of motion in nature and have fascinating properties. They can occur over a multitude of scales ranging from arbitrary openings of ion channels in cell membranes to the periodic motion of planets. In most cases, oscillatory systems are not isolated and may have rich connections and quite complicated interactions with other oscillatory units and evolve within a network setting. Understanding collective behaviours of such systems including synchronisation, clustering, and desynchronisation is an important research topic and has a strong history. In these systems the emergent network activity depends on both the connectivity structure and the dynamics of the network nodal components.

Synchronisation, first observed by Christian Huygens in 1665 [141], is an interesting emergent behaviour of coupled dynamical systems and ubiquitous in a wide range of research fields including engineering, biology, chemistry, and social sciences [19, 240]. The word *synchronous* is often used in both everyday and scientific language, and originated from the Greek word $\sigma\acute{\upsilon}\nu\chi\rho\acute{o}\nu\omicron\varsigma$, where prefix $\sigma\acute{\upsilon}\nu$ (*syn*) means the “same”, “together”, or “common” and $\chi\rho\acute{o}\nu\omicron\varsigma$ (*chronos*) means “time”. A direct translation of synchronous can be read as “happening at the same time” or “sharing the common clock” [240]. Here we

use the related term *synchronisation* to refer to the adjustment of rhythms of oscillatory units due to their interactions, and the term *synchronised* to emphasise all oscillating objects in a network doing the same thing at the same time. An extensive overview of synchronisation phenomena is given in [28, 240] where plenty of examples from the applied sciences are also presented.

In the mathematical modelling of many important real world problems (in various disciplines) the inclusion of nonsmooth phenomena plays a significant role to capture complex characteristics of dynamical evolution [35, 81]. Although there is a vast literature to explore synchronisation mechanisms of coupled systems, only a very limited amount is devoted to investigate the synchronisation of nonsmooth dynamical systems. Three of the major practical tools available from the smooth nonlinear dynamical system theory to determine stability of the synchronous state are weak coupling theory [96, 137, 270], phase-amplitude network formalism [92, 326], and the master stability function (MSF) methodology [230]. However, key components in each method need to be modified in the case where nodal components have some degree of nonsmoothness. This thesis addresses the extension and application of the theory for smooth dynamical systems to nonsmooth ones at both node and network levels by analysing some biological and mechanical oscillatory piecewise linear models. Our main motivation is to build a bridge between PWL systems and synchronisation theory thereby contributing to the mathematical theory of nonsmooth networks.

1.2 Overview of the thesis

The outline of this thesis is as follows.

Chapter 2

In this chapter we briefly summarise some of the main techniques that have been developed for smooth dynamical systems and that we will adapt and apply to nonsmooth models in the later chapters. We begin by reviewing the

notion of isochrons and phase reduction theory for weakly driven limit cycle attractors. We then recapitulate the concept of isostables and phase-amplitude reduction that is useful for investigating the behaviour of oscillatory networks beyond the weak coupling regime. We further present the second-order accurate phase-amplitude reduction framework by including higher order correction terms to the phase and amplitude coordinate equations. Subsequently, we restate the theory of weakly coupled oscillators and show how to perform linear stability analysis of the phase locked states with a particular focus on synchrony. Afterwards we outline a phase-amplitude network formalism that enables us to measure the effect of coupling strength on the bifurcations of network states. Finally, we recap the MSF methodology to assess the stability of a synchronous state and illustrate this technique by studying a network of linearly coupled Stuart-Landau oscillators.

Chapter 3

We start by introducing nonsmooth dynamical systems, some relevant terminology and a natural classification of them depending on their degree of nonsmoothness. Then we address a class of PWL systems with two linear zones and describe how to build periodic orbits systematically. Afterwards we present the PWL models (mainly drawn from neuroscience) that we study throughout Chapter 4. Finally we briefly discuss the practicalities and the utility of PWL modelling.

Chapter 4

We begin with modifying Floquet theory where the notion of saltation operators is used to determine the stability of periodic orbits for planar PWL systems. Then we derive the jump conditions relevant to the second-order accurate phase and amplitude equations. Subsequently, we present the explicit construction process for these terms and compare against direct numerical computations. Next we show how to determine the stability of a synchronous network state by using weak coupling theory, a phase-amplitude network framework, and the MSF in the case where nodes have PWL dynam-

ics. Moreover, we test the stability of the synchronous state and assess the accuracy of the predicted results from each method against direct numerical simulations. Finally, we give a discussion to highlight the power of PWL modelling for avoiding the limitation of phase and phase-amplitude reductions. We also debate which method best reflects the effect of variation in coupling strength on the bifurcations of network states for the models considered. The combination of PWL modelling and nonsmooth MSF analysis is recognised as an approach that does not require approximation and is the main tool used in Chapters 5 and 6.

Chapter 5

We first introduce the single electro-mechanical Franklin bell model and show how to build periodic orbits. We then use saltation operators to compute the nontrivial Floquet exponent to assess stability and analyse bifurcations. Afterwards we present a smoothing technique and show (numerically) that it recovers results obtained using saltation operators. Following this we utilise the MSF technique to determine the stability of synchronous network states, for both smooth and nonsmooth networks. We also present numerical examples to illustrate the theory. Finally, we discuss natural extensions and possible applications of the results for networks of Franklin bells in energy harvesting systems.

Chapter 6

First we introduce the model for an isolated Wilson-Cowan (WC) node with a continuous PWL firing rate function. Then we construct periodic solutions, derive an explicit formula to determine stability of these orbits and perform a bifurcation analysis. Afterwards we study a network of PWL Wilson-Cowan nodes, with nodal components arranged along a ring with distance-dependent interactions. Next we test the stability of the synchronous state by implementing the MSF methodology and study network bifurcations. Following this, we replace the continuous PWL firing rate function by a Heaviside function. Once again we build periodic orbits and formulate saltation matrices to determine

the stability of periodic orbits. We also observe that the model supports unstable sliding periodic orbits, and perform a bifurcation analysis. We highlight that the stability of the synchronous state is much harder to determine than for the continuous case. We show that stability is strongly influenced by the temporal order in which network components cross switching manifolds, and that this in turn is determined by the choice of initial perturbation. Finally, we discuss the new results about synchrony in networks of neural mass models, as well as natural extensions.

Chapter 7

Here we consider the challenge of modelling sleep in a PWL context. We start by introducing the PWL two process model, defining periodic orbits and presenting relevant one dimensional maps. We then show how to construct periodic orbits and determine their stability by utilising both nonsmooth Floquet theory and a linear stability analysis of the maps of switching event times around such orbits. Following this we derive a formula to compute Lyapunov exponents (LEs), indicating the location of different solution patterns in parameter space. We build Arnol'd tongue boundaries by investigating both saddle-node bifurcation of periodic orbits and grazing bifurcations. Next, we outline how social factors effects human sleep dynamics with a particular focus on partners sharing the same bed and develop a phenomenological PWL network model of this process. Finally, we summarise the work in this chapter and emphasise new directions.

Chapter 8

We conclude the thesis by reviewing the key results of the previous chapters, and highlight potential future research areas.

Chapter 2

Background

2.1 Introduction

In this chapter, some terminology, relevant concepts, and results from the existing literature are introduced to help understanding, self-containedness, and presentation of the thesis. The exposition is of the introductory level, and we sign-post the interested reader to the literature in favour of a less exhaustive and overly long presentation. Here we essentially review techniques for smooth dynamical systems that we will extend and apply in later chapters.

The organisation of the chapter is as follows. Section 2.2 introduces a dynamical system described by a system of nonlinear ordinary differential equations (ODEs) with a periodic solution, the notion of isochrons for limit cycle attractors and phase reduction, as well as related terminology. Section 2.3 introduces the concept of isostable coordinates and a phase-amplitude reduction to explore the behaviour of oscillatory systems beyond the weak perturbation paradigm. Moreover a higher order accurate phase-amplitude framework is presented together with a computationally efficient strategy to calculate necessary terms in the reduction process. Section 2.4 introduces a dynamical system representation of networks of limit cycle oscillators, and then focuses on an investigation of collective network behaviours. The theory of weakly coupled oscillators for providing a phase description of the underlying networks

dynamics is reviewed. Phase locked states and their linear stability analysis are examined with a particular focus on synchrony. To uncover the effect of coupling strength on the bifurcations of network states we further consider phase-amplitude coordinates. Additionally, the master stability function formalism for studying network synchrony in systems with identical oscillators and diffusive coupling is reviewed. To illustrate this technique numerically, a network of linearly coupled Stuart-Landau oscillators is considered.

This chapter is mainly based on the studies [15, 92, 96, 137, 230, 270, 325, 326, 328]. Particularly, interested readers are referred to: [15] for isochron and phase description; [325, 328] for isostable coordinates and a phase-amplitude reduction; [96, 137, 270] for the theory of weakly coupled oscillators; [92, 326] for coupled phase-amplitude oscillators, and finally [230] for the master stability function formalism.

2.2 Isochrons and phase reduction

Let us consider a differential equation of the form

$$\frac{dx}{dt} = f(x) + g(t), \quad x \in \mathbb{R}^n, \quad (2.1)$$

that has a stable hyperbolic periodic orbit, i.e. a limit cycle $x^\gamma(t)$, with period T for $g(t) = 0$ such that $x^\gamma(t + T) = x^\gamma(t)$. Here, $f(x)$ represents an unperturbed dynamics and $g(t)$ is a small external perturbation. We denote the point set of the limit cycle in phase space by $\gamma = \{x^\gamma(t) \in \mathbb{R}^n, t \in \mathbb{R}\}$. We assign a phase coordinate $\theta(x)$ to each point $x \in \gamma$ such that $\theta(x) : \mathbb{R}^n \rightarrow [0, 2\pi)$ for which $d\theta(x(t))/dt = \omega$ and $\theta(x(t)) = \theta(x(t + T))$ where the zero phase $\theta(x_0) = 0$ is assigned for an arbitrary point $x_0 \in \gamma$. Here we choose $\omega = 2\pi/T$, however the choice of ω is a personal preference and there are other common choices such as $\omega = 1$, so that $\theta \in [0, T)$ or $\omega = 1/T$, so that $\theta \in [0, 1)$. On the limit cycle, the use of phase coordinate reduces the nonlinear dynamics on

\mathbb{R}^n to a uniformly rotating dynamics on \mathbb{S}^1 with a constant velocity.

Let us denote the flow of the unperturbed system by $\varphi(t, \bar{x}_0)$ where \bar{x}_0 is the initial value when $t = 0$. Then, the basin of attraction of the limit cycle is defined as

$$\mathcal{B}_\gamma = \{x \in \mathbb{R}^n \mid \varphi(t, x) \rightarrow \gamma \text{ as } t \rightarrow \infty\}, \quad (2.2)$$

that is, the set of all initial conditions tends to γ as time goes to infinity. It is possible to extend the notion of phase to the entire basin of attraction \mathcal{B}_γ . We can assign a unique *asymptotic phase* $\theta(x_*) \in [0, 2\pi)$ to each point x_* in \mathcal{B}_γ by the condition

$$\lim_{t \rightarrow \infty} \left| \varphi(t, x_*) - \varphi\left(t + \frac{T}{2\pi} \theta(x_*), x_0\right) \right| = 0, \quad (2.3)$$

where x_0 is initial reference point on γ with zero phase. Thus two points, on and off the cycle in \mathcal{B}_γ , have the same asymptotic phase if the distance between unperturbed trajectories of the system (2.1) starting from these points vanishes as $t \rightarrow \infty$. The locus of all points $x \in \mathcal{B}_\gamma$ that share the same asymptotic phase values is called an *isochron*. Formally, the isochron associated with a given phase $\theta(\tilde{x}_0)$, $\tilde{x}_0 \in \gamma$ can be defined as the set

$$\Gamma_{\theta(\tilde{x}_0)} = \{x \in \mathcal{B}_\gamma \mid \theta(x) = \theta(\tilde{x}_0)\}, \quad (2.4)$$

where $\theta(x)$ is the asymptotic phase function. Thus, isochrons extend the phase dynamics $d\theta(x(t))/dt = \omega$ over the basin of attraction. The set of isochrons, for all $\theta \in [0, 2\pi)$, can also be considered as a foliation of \mathcal{B}_γ by $n - 1$ dimensional leaves. Although isochrons specify the full dynamics of a system with a stable limit cycle, in general, their analytical calculation is often not possible. An exception to this is plane-polar models where the radial component decouples from the angular one [15]. Therefore, numerical methods are often used for computing the isochron fibration of the basin \mathcal{B}_γ . For further mathematical properties and different methodologies that can be used during the computa-

tion of isochrons we refer the reader to [129, 131, 196, 221, 239, 299, 332].

We have defined the phase and corresponding phase equation in some neighbourhood U of the limit cycle by considering only the unperturbed system. However, oscillators are usually exposed to external force or are mutually interacting in a network setting [213]. For weak perturbations, although state points leave the limit cycle γ , they still stay within U . With this in mind, we consider the weakly perturbed system (2.1) in isochronal coordinates. This can be written as

$$\frac{d\theta}{dt} = \frac{\partial\theta}{\partial x} \cdot \frac{dx}{dt} = \frac{\partial\theta}{\partial x} \cdot (f(x) + g(t)) = \omega + \frac{\partial\theta}{\partial x} \cdot g(t). \quad (2.5)$$

We derive an equation for the phase dynamics by evaluating the right hand side of (2.5) on the limit cycle $x^\gamma(t)$, to a first approximation, as

$$\frac{d\theta}{dt} = \omega + \mathcal{Z}(\theta) \cdot g(t), \quad \mathcal{Z}(\theta) = \left. \frac{\partial\theta}{\partial x} \right|_{x^\gamma(\theta)} \equiv \nabla_{x^\gamma} \theta. \quad (2.6)$$

Here we call $\mathcal{Z}(\theta) \in \mathbb{R}^n$ the (*infinitesimal*) *phase response curve (iPRC)* and it is equal to the gradient of $\theta(x)$ evaluated on the limit cycle. The phase response curve (PRC) quantifies the change in phase for weak external perturbations acting along the limit cycle. To see this note that a perturbation δx in state x^γ , induces a corresponding change in phase given by:

$$\Delta\theta = \theta(x^\gamma + \delta x) - \theta(x^\gamma) \simeq \nabla_{x^\gamma} \theta \cdot \delta x.$$

A standard technique for calculation of the iPRC is to solve the adjoint equation [95, 96, 137]

$$\frac{d\nabla_{x^\gamma(t)} \theta}{dt} = -Df(x^\gamma(t))^\top \nabla_{x^\gamma(t)} \theta, \quad (2.7)$$

where $Df(x^\gamma(t))^\top$ is transpose of the Jacobian of f evaluated along the limit cycle $x^\gamma(t)$. Here, equation (2.7) is solved subject to the normalisation condition $\nabla_{x^\gamma(0)} \theta \cdot f(x^\gamma(0)) = \omega$, and T -periodicity of the solution $\nabla_{x^\gamma(t)} \theta$ must be

enforced. These two conditions give the required n initial conditions to solve for the iPRC uniquely. In general, solutions of equation (2.7) are obtained numerically, say, by implementing *the adjoint* routine in XPPAUT [91] or using the Matlab software package MatCont [125]. A detailed review of phase reduction techniques, both analytical and numerical, for limit cycle oscillators can be found in [239, 288].

2.3 Isostables and phase-amplitude reduction

Although the proposed phase reduction (2.6) is a widely used technique for studying weakly perturbed oscillators, it is valid only in a small neighbourhood of the limit cycle. In general, phase only reduction strategies are suitable for anticipating and examining the dynamics of coupled oscillators when individual limit cycles are strongly stable and robust to external perturbations. When the magnitude of external perturbation increases and states are driven away from the limit cycle, then the applicability of standard phase reduction techniques reduces and often gives incorrect predictions about actual dynamical behaviour. This is especially true if a nontrivial Floquet multiplier [157] of the limit cycle is close to unity so that the decay rate of transversal perturbations to the periodic orbit is slow. In many applications [289, 327], the presence and necessity of large amplitude perturbations requires the explicit consideration of the dynamical behaviour in transversal directions to the limit cycle $x^\gamma(t)$.

In order to overcome this limitation, Suvak and Demir [297] and Takeshita and Feres [299] proposed some methods to compute a local but quadratic approximations of the isochrons for different models. Nevertheless, in realistic settings, perturbations do not need to be small or they can act during a transient state, where perturbed solutions have not fully relaxed back to the limit cycle. Hence, to compute phase change accurately away from the cycle (in a transient state) or in response to strong driving effects, it is necessary to

consider an extra variable, the amplitude variable, which traces the transversal distance to the limit cycle. By utilising this new variable, Guillemin and Huguet [131] have proposed a computational and geometric approach to build a more accurate reduced system by introducing the concepts of Phase Response Functions (PRF), to measure phase changes, and the Amplitude Response Functions (ARF) to measure changes in amplitude. Letson and Rubin [181] and Wedgwood *et al.* [319] utilised a moving orthonormal coordinate framework along the limit cycle to define phase amplitude coordinates, and they applied this to the FitzHugh-Nagumo (FHN) model [101, 212] and Morris-Lecar (ML) model [209], respectively. We also note that, other dynamical modelling of phase-amplitude interactions (from a more numerical point of view) have been proposed in [98, 139].

Analogous to the isochrons, Wilson and Moehlis [328] and Shirasaka *et al.* [275, 277] have introduced the notion of *isostables* where isostable level sets identify the initial points around the limit cycle such that solutions starting from these points have the same relaxation property, namely their decay rate toward the limit cycle is the same. Wilson and Ermentrout [325] increased the accuracy of this phase-amplitude framework by introducing second-order correction terms. Moreover, Kotani *et al.* [164] studied this phase-amplitude reduction theory for limit cycle oscillators described by delay differential equations.

Here we will revisit the phase-amplitude reduction method proposed by Wilson and Moehlis [328], and Wilson and Ermentrout [325]. The main motivation to choose this recent reduction framework is that it simplifies and is computationally efficient when applied to the models that we work within later chapters. This is an n -dimensional reduction (n is dimension of system (2.1)) and uses the notion of both isochrons and isostables. Isostables are introduced as coordinates which represent a measure of distance in directions transverse to the limit cycle. In this n -dimensional reduction, the first dimension characterises the phase of the oscillator along the limit cycle and the remaining

$n - 1$ dimensions give a sense of transversal decay to the limit cycle along the $n - 1$ isostable directions. The standard phase reduction (2.6) is augmented to a phase-amplitude reduction by using these isostable coordinates as follows. Here we follow the presentation of Wilson and Moehlis [328] to introduce this theory.

Choose a point x_0 on the limit cycle $x^\gamma(t)$ and denote the corresponding isochron by Γ_0 where $\Gamma_0 = \{x \in \mathcal{B}_\gamma \mid \theta(x) = 0\}$. By considering Γ_0 to be a Poincaré surface define the Poincaré map P for the system (2.1) when $g(t) = 0$ as

$$P : \Gamma_0 \rightarrow \Gamma_0; \quad x \rightarrow P(x) = \varphi(T, x). \quad (2.8)$$

Recall that φ denotes the unperturbed flow of the system (2.1) and T is the period of the limit cycle $x^\gamma(t)$. This map satisfies $P(x_0) = x_0$ and therefore in a small neighbourhood x_0 one can approximate P from the equation (2.8) as

$$P(x) = x_0 + DP(x - x_0) + \mathcal{O}(\|x - x_0\|^2), \quad (2.9)$$

where DP is the Jacobian of P evaluated at x_0 . Assume that DP is diagonalisable with a matrix $V \in \mathbb{R}^{n \times n}$ whose columns form a basis of unit length eigenvectors $\{v_k \mid k = 1, \dots, n\}$ associated with the eigenvalues $\{\lambda_k \mid k = 1, \dots, n\}$ of DP . Note that the latter are often referred to as the Floquet multipliers of the periodic orbit. There is at least one eigenvalue equal to one (corresponding to perturbations along the periodic orbit), say by convention $\lambda_n = 1$. Then for every eigenvector v_k associated with the nontrivial Floquet multiplier λ_k , $k < n$, isostable coordinates for a limit cycle are introduced in [325, 328] as

$$\psi_k(x) = \lim_{l \rightarrow \infty} \underbrace{[e_k^\top V^{-1}(\varphi(t_\Gamma^l, x) - x_0)]}_{\tau_k(x, t)} \underbrace{\exp(-\log(\lambda_k)t_\Gamma^l/T)}_{\rho_k(x, t)}, \quad (2.10)$$

where $k = 1, \dots, n - 1$. Here t_Γ^l denotes the l th return time to Γ_0 under the flow φ , and e_k is the unit vector in the k th direction. In this definition, the flow sequence $\{\varphi(t_\Gamma^l, x)\}_{l \in \mathbb{Z}^+}$ approaches x_0 in such a way that for large enough l ,

its convergence can be well approximated by

$$\varphi(t_\Gamma^l, x) - x_0 = \sum_{i=1}^N \lambda_i s_i(x) v_i, \quad (2.11)$$

where s_i are coordinates of initial perturbation in the basis of eigenvectors of DP . Note that this approximation is only valid in close vicinity to the limit cycle. This is the case as $l \rightarrow \infty$ so that the dynamics is well approximated by a linearisation about the point x_0 . The term $e_k^\top V^{-1}$ in the definition (2.10) is used to choose the appropriate component of the equation (2.11) in the v_k direction and the resultant term $\tau_k(x, t)$ shrinks at a rate λ_k . From the above definition of a Poincaré map, the flow crosses the Poincaré section every T time units [213, 325, 326]. Therefore, the term $\rho_k(x, t)$ grows at a rate $1/\lambda_k$. The resultant multiplication $\tau_k(x, t)\rho_k(x, t)$ approaches a constant value as l tends to infinity, giving the isostable coordinate $\psi_k(x)$. By implementing the definition (2.10), isostable coordinates are defined for all x in the basin of attraction of the limit cycle, not just on the Poincaré section. Similar to the above asymptotic phase definition, ψ_k is an asymptotic isostable coordinate which is defined according to the infinite time approach to the limit cycle. Intuitively, each ψ_k coordinate can be considered as a signed distance from the limit cycle in a direction specified by v_k , and see [171, 321] for more details.

Although the definition of isostable coordinates seems complex, as demonstrated in [207, 325, 328], one can obtain the dynamics of the isostables ψ_k and its gradient $\nabla_{x^\gamma(t)} \psi_k$ as

$$\frac{d\psi_k}{dt} = \kappa_k \psi_k, \quad (2.12)$$

$$\frac{d\nabla_{x^\gamma} \psi_k}{dt} = \left(\kappa_k I - Df(x^\gamma(t))^\top \right) \nabla_{x^\gamma} \psi_k, \quad (2.13)$$

where $\kappa_k = \log(\lambda_k)/T$ is the k th Floquet exponent, I is the $\mathbb{R}^{n \times n}$ identity matrix and Df is the Jacobian of f . Isostable coordinates decay exponentially in the absence of external perturbations. The term $\nabla_{x^\gamma} \psi_k \equiv \mathcal{I}_k(\theta)$ is

referred as the *(infinitesimal) isostable response curve* (iIRC). Uniqueness of the IRC is ensured by T -periodicity along with the normalisation condition $\nabla_{x_0} \psi_k \cdot v_k = 1$. The iIRC gives a measure of the effect of an external input in driving the trajectory away from the limit cycle. Then the n -dimensional system (2.1) can be written as

$$\frac{d\theta}{dt} = \omega + \mathcal{Z}(\theta) \cdot g(t), \quad (2.14)$$

$$\frac{d\psi_k}{dt} = \kappa_k \psi_k + \mathcal{I}_k(\theta) \cdot g(t), \quad \text{for } k = 1, \dots, n-1. \quad (2.15)$$

In this system, the first variable determines the phase of the flow along the limit cycle, as in the equation (2.6), the remaining $n-1$ dimension and equations capture information about the transversal distance from the limit cycle along the k th eigenvector v_k , $k = 1, \dots, n-1$. As a result, this change of variables reflects the effect of an external drive on the oscillator's phase change by making use of the iPRC, and the change in its transversal distance to the limit cycle by using the iIRC. In practice, for Floquet multipliers λ_k close to zero, isostable coordinates ψ_k can be neglected since any perturbation in these directions decay rapidly, and these coordinates can be assumed to be zero. If all isostable coordinates are neglected, the system (2.14)-(2.15) recovers the standard phase reduction (2.6).

To calculate iIRCs, we can use the direct method applying perturbations $\Delta x_k \hat{k}$ at various locations along the limit cycle in the direction \hat{k} of the k th coordinate. We record the time and state values of crossings of the Γ_0 isochron, and use this data with the definition (2.10) to measure the isostable change $\Delta\psi = \psi_k(x^\gamma + \Delta x_k \hat{k}) - \psi_k(x^\gamma)$, which when divided by the magnitude of the perturbation results in the iIRC. Alternatively, the iIRC can be derived by solving equation (2.13) as a boundary value problem using a suitable numerical method, and details of such an approach can be found in [207].

Although the phase dynamics decouple from the isostable dynamics, the first-order accurate phase-amplitude reduction (2.14)-(2.15) provides a pow-

erful framework for improving the accuracy of phase only reduced dynamics (2.6) of oscillatory systems. One of the main characteristics of oscillators which enables reduction to a phase only system (2.6) is that they should stay close to the limit cycle; when the state moves away from the limit cycle, (2.6) becomes a poor approximation for the phase evaluation of the system. In cases where the external perturbation must be large, one can make use of equation (2.15) to limit the magnitude of the isostable coordinates in a way that the phase-reduced dynamics remains valid. In this case, the proposed reduced equations (2.14)-(2.15) set a moderately simplified framework within which further analysis can be achieved.

Here, the reduction (2.14)-(2.15) is referred to as a first-order accurate phase-amplitude reduction. In the next section, we will review how this reduction can be extended so that the additional information about the transversal dynamics toward the limit cycle does indeed result in an improved description of a reduced dynamics. We refer to this as a second-order accurate phase and isostable reduction. This is studied by Monga *et al.* [207], and Wilson and Ermentrout [325], and then applied to a thalamic neuron model [330], and a model for gene regulation [123], respectively. Latterly, this has been extended to an arbitrary order of accuracy, see for example [226, 323], though calculation of the reduced terms requires expensive numerical computations. This in turn has led to the development of so-called adaptive phase-amplitude reduction framework [322, 324] where isostable coordinates are kept small (and therefore the linear order approximation is sufficient) by continuously evolving the limit cycle the isostable is measured with respect to, against family of stable periodic orbits depending continuously on the parameter set that is varied. However, this method is based on the smoothness of the periodic solutions and thus we do not investigate this further here.

2.3.1 Phase and isostable reduction with second-order accuracy

As mentioned above, in a first order approximation, the phase and isostable dynamics given by (2.14)-(2.15) are uncoupled and therefore the phase dynamics of the equation (2.14) are same as those of equation (2.6). However, in some cases such as when a limit cycle is not strongly stable, it can be beneficial to utilise a second-order approximation to the phase and isostable dynamics to better understand how the system responds when it is perturbed. The computation of second and higher-order approximations of responses close to the periodic orbit has been investigated in [297, 299], which is effective for understanding perturbations actions from the limit cycle. Nevertheless, it is difficult to apply such strategies to systems which have already been perturbed from the periodic orbit, at least without explicit information of the state with respect to the periodic orbit. As we summarise below, isostable coordinates can be utilised to tackle this problem resulting in a closed set of equations for a second-order accurate phase-amplitude reduction. Originally, this reduction framework was given by Wilson and Ermentrout [325].

For locations near to the limit cycle, the gradient of the phase and isostable coordinates can be expanded as

$$\begin{aligned} \left. \frac{\partial \theta}{\partial x} \right|_{x^\gamma(\theta) + \Delta x} &= \left. \frac{\partial \theta}{\partial x} \right|_{x^\gamma(\theta)} + \left. \frac{\partial^2 \theta}{\partial x^2} \right|_{x^\gamma(\theta)} \Delta x + \mathcal{O}(\|\Delta x\|^2) \\ &= \mathcal{Z}(\theta) + H_{\theta, x^\gamma(\theta)} \Delta x + \mathcal{O}(\|\Delta x\|^2), \end{aligned} \quad (2.16)$$

$$\begin{aligned} \left. \frac{\partial \psi_k}{\partial x} \right|_{x^\gamma(\theta) + \Delta x} &= \left. \frac{\partial \psi_k}{\partial x} \right|_{x^\gamma(\theta)} + \left. \frac{\partial^2 \psi_i}{\partial x^2} \right|_{x^\gamma(\theta)} \Delta x + \mathcal{O}(\|\Delta x\|^2) \\ &= \mathcal{I}_k(\theta) + H_{\psi_k, x^\gamma(\theta)} \Delta x + \mathcal{O}(\|\Delta x\|^2), \quad k = 1, \dots, n-1. \end{aligned} \quad (2.17)$$

Here $H_{\theta, x^\gamma(\theta)}$ and $H_{\psi_k, x^\gamma(\theta)}$ are respectively the Hessian matrices of second derivatives of θ and ψ_k evaluated at $x^\gamma(\theta)$. Close to a periodic orbit, and using

Floquet theory [127, 157, 161], one can write

$$\Delta x(t) = \sum_{i=1}^n c_i \exp(\kappa_i t) \rho_i(t), \quad (2.18)$$

where c_i are constants determined by initial conditions, κ_i are Floquet exponents and $\rho_i(t) \in \mathbb{R}^n$ are T -periodic eigenfunctions that can be approximated according to

$$\rho_i(t) = \frac{[\varphi(t, \epsilon v_i + x_0) - \varphi(t, x_0)] \exp(-\kappa_i t)}{\epsilon}, \quad (2.19)$$

where v_i are the eigenvectors associated with the Floquet exponents κ_i , and $0 < \epsilon \ll 1$. Using the definition of isostables and as shown in [207, 325], one can establish that $c_i = \psi_i$, and then Δx in the system (2.16)-(2.17) can be obtained in terms of phase and isostable coordinates as

$$\Delta x(\theta, \psi_1, \dots, \psi_{n-1}) = \sum_{i=1}^{n-1} \psi_i p_i(\theta), \quad (2.20)$$

where $p_i(\theta(0) + \omega t) = \rho_i(t)$. Remembering the fact that $d\theta/dt = \partial\theta/\partial x \cdot dx/dt$, a second-order correction to the phase reduction can be obtained by combining (2.16), (2.20) and the perturbed dynamics (2.1). In a similar way, the relation $d\psi_k/dt = \partial\psi_k/\partial x \cdot dx/dt$, along with equations (2.17), (2.20) and (2.1), gives a second-order correction to the isostable dynamics. The second-order accurate phase-amplitude reduction is thus obtained as

$$\frac{d\theta}{dt} = \omega + \left(\mathcal{Z}(\theta) + \sum_{i=1}^{n-1} [\mathcal{B}^i(\theta) \psi_i] \right) \cdot g(t), \quad (2.21)$$

$$\frac{d\psi_k}{dt} = \kappa_k \psi_k + \left(\mathcal{I}_k(\theta) + \sum_{i=1}^{n-1} [\mathcal{C}_k^i(\theta) \psi_i] \right) \cdot g(t), \quad k = 1, \dots, n-1, \quad (2.22)$$

where $\mathcal{B}^i(\theta) \equiv H_{\theta, x^\gamma(\theta)} p_i(\theta)$ and $\mathcal{C}_k^i(\theta) \equiv H_{\psi_k, x^\gamma(\theta)} p_i(\theta)$. The system (2.21)-(2.22) contains second-order correction terms and is different from the previous reduced system (2.14)-(2.15). Here, the evaluation of phase dynamics explicitly

depends on the isostable coordinates.

In order to solve system (2.21)-(2.22), we need to know $H_{\theta, x^\gamma(\theta)}$ and $H_{\psi_k, x^\gamma(\theta)}$. To obtain these, we consider phase changes due to the perturbation from the limit cycle:

$$\Delta\theta = \nabla_{x^\gamma}\theta \cdot \Delta x + \frac{1}{2}\Delta x^\top H_{\theta, x^\gamma}\Delta x + \mathcal{O}(\|\Delta x\|^3). \quad (2.23)$$

If we consider a perturbed trajectory $x(t) = x^\gamma(t) + \Delta x(t)$, where Δx is a small perturbation to the limit cycle $x^\gamma(t)$ at time $t = 0$, then a second-order approximation to the evaluation of Δx is given by

$$\begin{aligned} \frac{d\Delta x(t)}{dt} = & Df(x^\gamma(t))\Delta x(t) + \frac{1}{2} \begin{bmatrix} \Delta x^\top(t)H_{1, x^\gamma(t)} \\ \Delta x^\top(t)H_{2, x^\gamma(t)} \\ \vdots \\ \Delta x^\top(t)H_{n, x^\gamma(t)} \end{bmatrix} \Delta x(t) \\ & + \mathcal{O}(\|\Delta x\|^3), \end{aligned} \quad (2.24)$$

where $H_{i, x^\gamma(t)} \equiv \nabla(\nabla f_i)|_{x^\gamma(t)}$ is the Hessian matrix of second partial derivatives of the i th component of f . By following a similar process of derivation to equation (2.7), we first take the time derivative of equation (2.23). Then we substitute $d\Delta x(t)/dt$ from equation (2.24) into the result. Thereafter we collect all $\|\Delta x\|^2$ terms to obtain (cf. [325])

$$\begin{aligned} \frac{dH_{\theta, x^\gamma(t)}}{dt} = & - \sum_{i=1}^n [\mathcal{Z}_i(x^\gamma(t)) H_{i, x^\gamma(t)}] \\ & - Df^\top(x^\gamma(t)) H_{\theta, x^\gamma(t)} - H_{\theta, x^\gamma(t)} Df(x^\gamma(t)), \end{aligned} \quad (2.25)$$

where $\mathcal{Z}_i(x^\gamma(t)) \equiv \partial\theta/\partial x_i|_{x^\gamma(t)}$. The solution of equation (2.25) can be found using T -periodicity along with the normalisation condition

$$- Df^\top(x^\gamma(t)) \nabla_{x^\gamma(t)}\theta = H_{\theta, x^\gamma(t)} f(x^\gamma(t)). \quad (2.26)$$

By starting with equation (2.7), this normalisation condition is obtained as follows

$$\begin{aligned} -Df(x^\gamma(t))^\top \nabla_{x^\gamma(t)} \theta &= \frac{d\nabla_{x^\gamma(t)} \theta}{dt} \\ &= \frac{\partial \nabla_{x^\gamma(t)} \theta}{\partial x} \frac{\partial x}{\partial t} \Big|_{x^\gamma(t)} = H_{\theta, x^\gamma(t)} f(x^\gamma(t)). \end{aligned} \quad (2.27)$$

That is to say, the variation in the iPRC derived according to adjoint equation (2.7) [i.e., the left-hand side of the equation (2.26)] for a perturbation from the limit cycle needs to be equal to the change derived by using $H_{\theta, x^\gamma(t)}$ [i.e., the right-hand side of the equation (2.26)].

As presented in [325], by using similar approaches for the deviation of $H_{\theta, x^\gamma(t)}$ (as shown above), we can show that $H_{\psi_k, x^\gamma(t)}$ is the periodic solution of

$$\begin{aligned} \frac{dH_{\psi_k, x^\gamma(t)}}{dt} &= \kappa_k H_{\psi_k, x^\gamma(t)} - \sum_{i=1}^n [\mathcal{I}_k^i(x^\gamma(t)) H_{i, x^\gamma(t)}] \\ &\quad - Df^\top(x^\gamma(t)) H_{\psi_k, x^\gamma(t)} - H_{\psi_k, x^\gamma(t)} Df(x^\gamma(t)), \end{aligned} \quad (2.28)$$

where $\mathcal{I}_k^i(x^\gamma(t)) \equiv \partial \psi_k / \partial x_i|_{x^\gamma(t)}$. This must be solved subject to both T -periodicity of the solution of equation (2.28) and the normalisation condition

$$(\kappa_k I - Df^\top(x^\gamma(t))) \nabla_{x^\gamma(t)} \psi_k = H_{\psi_k, x^\gamma(t)} f(x^\gamma(t)). \quad (2.29)$$

Similar to equation (2.27), this normalisation condition is obtained starting from equation (2.13) as follows:

$$\begin{aligned} \left(\kappa_k I - Df(x^\gamma(t))^\top \right) \nabla_{x^\gamma(t)} \psi_k &= \frac{d\nabla_{x^\gamma(t)} \psi_k}{dt} \\ &= \frac{\partial \nabla_{x^\gamma(t)} \psi_k}{\partial x} \frac{dx}{dt} \Big|_{x^\gamma(t)} \\ &= H_{\psi_k, x^\gamma(t)} f(x^\gamma(t)). \end{aligned} \quad (2.30)$$

Here we note that equation (2.25) depends upon information of the iPRC and that (2.28) depends upon knowledge of the iIRC. Nonetheless both of these can be found by using equations (2.7) and (2.13).

As discussed in [207, 320, 325], the calculation of the matrices $H_{\theta, x^\gamma(\theta)}$ and $H_{\psi_k, x^\gamma(\theta)}$ is computationally challenging. The expense of these computations increases with the square of the dimension of the system (2.1). For high dimensional systems such computational effort becomes a limiting factor for the proposed reduction. However, Wilson [320] proposed an alternative direct method which reduces the computational effort to derive the terms $\mathcal{B}^i(\theta)$ and $\mathcal{C}_k^i(\theta)$ in (2.21)-(2.22). Such a method is particularly useful when some of the isostable coordinates can be ignored because they have Floquet multipliers with small magnitude.

2.3.2 An alternative strategy for calculation of second-order terms

Due to the limitations stated above, here we will review an alternative strategy [320] to obtain the second-order terms $\mathcal{B}^i(\theta)$ and $\mathcal{C}_k^i(\theta)$ from equations (2.21) and (2.22) with less computational effort (proportional to the dimension of the system, rather than its square). We start by multiplying equation (2.25) by a perturbation from the limit cycle $\Delta x(t)$ and obtain

$$\begin{aligned} \frac{dH_{\theta, x^\gamma(t)}}{dt} \Delta x(t) &= - \sum_{j=1}^n [\mathcal{Z}_j(x^\gamma(t)) H_{j, x^\gamma(t)} \Delta x(t)] \\ &\quad - Df^\top(x^\gamma(t)) H_{\theta, x^\gamma(t)} \Delta x(t) \\ &\quad - H_{\theta, x^\gamma(t)} Df(x^\gamma(t)) \Delta x(t). \end{aligned} \tag{2.31}$$

Using the following observation

$$\begin{aligned} \frac{d}{dt} (H_{\theta, x^\gamma(t)} \Delta x(t)) &= \frac{d}{dt} (H_{\theta, x^\gamma(t)}) \Delta x(t) + H_{\theta, x^\gamma(t)} \frac{d}{dt} (\Delta x(t)) \\ &= \frac{d}{dt} (H_{\theta, x^\gamma(t)}) \Delta x(t) \\ &\quad + H_{\theta, x^\gamma(t)} Df(x^\gamma(t)) \Delta x(t) + \mathcal{O}(\|\Delta x\|^2), \end{aligned} \tag{2.32}$$

we can rewrite equation (2.31) as

$$\begin{aligned} \frac{d}{dt} (H_{\theta, x^\gamma(t)} \Delta x(t)) &= - \sum_{j=1}^n [\mathcal{Z}_j(x^\gamma(t)) H_{j, x^\gamma(t)} \Delta x(t)] \\ &\quad - Df^\top(x^\gamma(t)) H_{\theta, x^\gamma(t)} \Delta x(t). \end{aligned} \quad (2.33)$$

Here, we note that equation (2.33) is valid for any arbitrary small perturbation $\Delta x(t)$ from the limit cycle. In order to derive $\mathcal{B}^i(\theta)$, we choose $\Delta x(t) = \epsilon \exp(\kappa_i t) p_i(\theta(t))$ and substitute into equation (2.33). Then by utilising the equality $\mathcal{B}^i(\theta) = H_{\theta, x^\gamma(\theta)} p_i(\theta)$ we obtain

$$\begin{aligned} \frac{d}{dt} (\mathcal{B}^i(\theta(t)) \epsilon \exp(\kappa_i t)) &= - \sum_{j=1}^n [\mathcal{Z}_j(x^\gamma(t)) H_{j, x^\gamma(t)} p_i(\theta(t)) \epsilon \exp(\kappa_i t)] \\ &\quad - Df^\top(x^\gamma(t)) \mathcal{B}^i(\theta(t)) \epsilon \exp(\kappa_i t), \end{aligned} \quad (2.34)$$

which can be rearranged to yield

$$\begin{aligned} \frac{d}{dt} (\mathcal{B}^i(\theta(t))) &= - \sum_{j=1}^n [\mathcal{Z}_j(x^\gamma(t)) H_{j, x^\gamma(t)} p_i(\theta(t))] \\ &\quad - (Df^\top(x^\gamma(t)) + \kappa_i I) \mathcal{B}^i(\theta(t)). \end{aligned} \quad (2.35)$$

Then $\mathcal{B}^i(\theta(t))$ can be obtained by finding the T -periodic solution of equation (2.35) along with the normalisation condition

$$- \mathcal{Z}(\theta(t))^\top Df(x^\gamma(t)) p_i(\theta(t)) = f(x^\gamma(t))^\top \mathcal{B}^i(\theta(t)). \quad (2.36)$$

To obtain this normalisation condition we first transpose equation (2.26) and then multiply by $p_k(\theta(t))$. Starting from equation (2.28) and pursuing a similar technique, we obtain the relation

$$\begin{aligned} \frac{d}{dt} (H_{\psi_k, x^\gamma(t)} \Delta x) &= \kappa_k H_{\psi_k, x^\gamma(t)} \Delta x(t) - \sum_{j=1}^n [\mathcal{I}_k^j(x^\gamma(t)) H_{j, x^\gamma(t)} \Delta x(t)] \\ &\quad - Df^\top(x^\gamma(t)) H_{\psi_k, x^\gamma(t)} \Delta x(t). \end{aligned} \quad (2.37)$$

By rearranging equation (2.37), we find

$$\begin{aligned} \frac{d}{dt} (\mathcal{C}_k^i(\theta(t))) &= - \sum_{j=1}^n [\mathcal{I}_k^j(x^\gamma(t)) H_{j,x(t)} p_i(\theta(t))] \\ &\quad - (\mathrm{D}f^\top(x^\gamma(t)) + (\kappa_i - \kappa_k) I) \mathcal{C}_k^i(\theta(t)). \end{aligned} \quad (2.38)$$

Hence, the T -periodic solution of equation (2.38) gives $\mathcal{C}_k^i(\theta(t))$ with the normalisation condition

$$\mathcal{I}_k(\theta(t))^\top (\kappa_k I - \mathrm{D}f(x^\gamma(t))) p_i(\theta(t)) = f(x^\gamma(t))^\top \mathcal{C}_k^i(\theta(t)), \quad (2.39)$$

which is obtained by taking the transpose of equation (2.29) and multiplying it by $p_i(\theta(t))$.

In order to find the required second-order reduction terms $\mathcal{B}^i(\theta(t))$ and $\mathcal{C}_k^i(\theta(t))$ in system (2.21)-(2.22), utilising the alternative equations (2.35) and (2.38) is more convenient because the latter does not require full computation of the Hessians $H_{\psi_k, x^\gamma(t)}$ and $H_{\theta, x^\gamma(t)}$. In the following chapters we will implement this method for piecewise linear models and show how it simplifies, allowing more explicit calculations to be performed.

2.4 Networks of oscillators

In general, oscillatory systems are not isolated and may have rich connections and interactions occurring at different levels that can be quite complicated. Scientists from many different areas such as engineering, physics, biology, and sociology have studied collective behaviour of complex networks and emergent patterns due to various interactions between network elements [19, 239, 243]. Some famous examples are pendulum clocks, electronic circuits, coupled Josephson junctions, social networks, cardiac pacemakers, flashing fireflies, and neural oscillations in the human brain. The characterisation of complex networks depends on both their structural and dynamical properties.

Here, structure refers to the underlying topology of the network which determines the connectivity between the network elements (nodes), and dynamics refers to the time evolution of the individual oscillators, the interaction between individual nodes, and the emergent collective behaviour at the network level.

In many cases the governing equation of a network of N interacting oscillators can be written in the form

$$\frac{dx_i}{dt} = f_i(x_i) + \sigma g_i(x_1, x_2, \dots, x_N), \quad i = 1, \dots, N. \quad (2.40)$$

Here each node is described by $x_i \in \mathbb{R}^n$ and its intrinsic dynamics are determined by f_i . The coupling strength of the network is denoted by $\sigma \in \mathbb{R}$ and g_i comprises driving effects (state-dependent coupling) from the other nodes on the i th node. As in many approaches, here we assume that the coupling structure is pairwise [14, 37], that is the coupling function g_i can be decomposed into the sum of pairwise interactions. Thus the system (2.40) can be written as

$$\frac{dx_i}{dt} = f_i(x_i) + \sigma \sum_{j=1}^N w_{ij} G_{ij}(x_i, x_j), \quad (2.41)$$

where interactions G_{ij} are summed according to some weights $w_{ij} \in \mathbb{R}$ (some of which may be zero) that represent the strength of the coupling between the i th and j th node. Here, for illustration, we consider a simplified system of interacting limit-cycle oscillator where $G_{ij} = G$, and thus

$$\frac{dx_i}{dt} = f_i(x_i) + \sigma \sum_{j=1}^N w_{ij} G(x_i, x_j). \quad (2.42)$$

In the forthcoming subsections, first, we will revisit the ideas behind phase reduction of an oscillator network (by assuming the coupling strength to be sufficiently small) and how the reduced phase dynamics can be utilised to assess and predict network states and emergent collective dynamics. Then we will review phase-amplitude approach for coupled systems. Finally, we will describe

the master stability function technique [230] which can be explicitly used to investigate the effect of coupling strength on the stability of the synchronous state, and provide an example of networks of Stuart-Landau oscillators to illustrate this methodology.

2.4.1 Weakly coupled phase oscillators

In order to analyse the oscillatory dynamics of many real world networks, researchers from a variety of disciplines have used the theory of weakly coupled oscillators [94, 169, 270]. In terms of equation (2.40) this reduces to the dimension of the system from Nn to N , by considering only a set of network phases. Despite the dimension reduction, the phase description of network dynamics can often provide a comprehensive picture of numerous collective behaviours. In the literature, there are abundant studies; for example the books by Hoppensteadt and Izhikevich [137], Ermentrout and Terman [96] and Izhikevich [146], explore this reduction framework from a rigorous mathematical perspective. Various approaches and algorithms have been independently introduced by Malkin [137, 195], Neu [216], and Ermentrout and Kopell [94, 95] to obtain phase dynamics and *phase interaction functions* (see equation (2.48)) of coupled nonlinear oscillators.

Here following the method in Section 2.2, the phase model equation (2.6) can be extended to a system of interacting limit-cycle oscillators given by the dynamical equation (2.42), and the network's phase dynamics takes the form

$$\frac{d\theta_i}{dt} = \omega_i + \sigma \mathcal{Z}_i(\theta_i) \cdot \sum_{j=1}^N w_{ij} G(\theta_i, \theta_j), \quad i = 1, \dots, N, \quad (2.43)$$

where $G(\theta_i, \theta_j) = G(x_i^\gamma(\theta_i), x_j^\gamma(\theta_j))$, ω_i is the natural frequency of the i th oscillator, and $\theta_i \in [0, 2\pi)$. For each i , equation (2.43) behaves similarly to that of (2.6), however the perturbation term g in equation (2.6) is replaced by (the sum over) the coupling terms G which is now a function of phase variables.

Some of the first mathematical studies for deriving a phase dynamics of population of coupled oscillators were performed by Winfree [331] and Kuramoto [169]. The Winfree model, which is inspired by the synchronisation of biological oscillators, is composed of N globally coupled phase oscillators and is described by the network equations,

$$\frac{d\theta_i}{dt} = \omega_i + \frac{\sigma}{N} \mathcal{Z}(\theta_i) \cdot \sum_{j=1}^N \mathcal{P}(\theta_j), \quad (2.44)$$

where \mathcal{Z} represents a biologically realistic iPRC, \mathcal{P} specifies a pulsatile interaction function, and ω_i are random variables drawn from a distribution. In this model a separation of time scales assumption was used to characterise an oscillator by its phase on cycle (strongly attractive limit cycle) and amplitudes are neglected. By exploiting a mixture of analysis and numerics, Winfree found that a large population ($N \gg 1$) of interacting limit cycle oscillators was capable of macroscopic synchrony at a critical value of the variance of the frequency distribution. Following this, Kuramoto introduced a more analytically tractable model for phase oscillators with heterogeneous intrinsic frequencies with interactions mediated by the sine of phase differences. Moreover, he proposed an order parameter to quantify the overall collective synchrony of the population. A more detailed review of the Kuramoto model can be found in [2, 255].

Here for illustration we assume that all the oscillators are identical, and $\omega_i = \omega$ for all i . If the coupling is sufficiently weak, the natural way to obtain a phase-difference model from equation (2.43) is by averaging over one period of oscillation. To do so, we introduce relative phase variables ϕ_i as

$$\theta_i = \phi_i + \omega t, \quad (2.45)$$

where ϕ_i represent deviations from the unperturbed dynamics along the limit cycle with natural frequency ω . Then we can show the relative phases ϕ_i

evolves (slowly) in time according to

$$\frac{d\phi_i}{dt} = \sigma \mathcal{Z}(\phi_i + \omega t) \cdot \sum_{j=1}^N w_{ij} G(\phi_i + \omega t, \phi_j + \omega t), \quad (2.46)$$

with $0 < \sigma \ll 1$. This weak coupling assumption along with equation (2.46) enables the relative phases ϕ_i to capture the coupling effect entirely. To apply averaging effectively, the relative phases ϕ_i must evolve slowly so that over a period they do not change significantly. Actually, the small valued σ guarantees a slow variation in ϕ_i by keeping the effect of coupling small on the oscillator's intrinsic dynamics over the period $T = 2\pi/\omega$. Nevertheless, such small driving effects shall accumulate as time evolves and will contribute to emergent network dynamics, such as phase synchronisation. If we assume all oscillators lock to a synchronised state, this state will be sustained as time evolves on an order of $1/\sigma$, that, for $0 < \sigma \ll 1$, is considered longer than all other distinguishing timescales in the system. Over this time, the ωt term will experience a multitude of changes that are of order ω/σ . Thus, over a period T , the ϕ_i shall be approximately time independent. Thereafter, we can average the right-hand side of equation (2.46) over one period T by considering ϕ_i as constant. To explore this averaging procedure rigorously one can find details in [95, 130, 239, 265] and references therein.

The averaged dynamics along with the equation (2.45) results in the phase-difference model for each phase variables θ_i as

$$\frac{d\theta_i}{dt} = \omega + \sigma \sum_{j=1}^N w_{ij} H(\theta_j - \theta_i), \quad (2.47)$$

with the 2π -periodic phase interaction function (or coupling function)

$$H(\chi) = \frac{1}{2\pi} \int_0^{2\pi} \mathcal{Z}(s) \cdot G(s, \chi + s) ds. \quad (2.48)$$

For a further discussion about the derivation of the phase interaction functions

we refer the reader to [96, 169, 213, 270]. This theory has also been extended to more complex systems such as the Mackey–Glass delay equation [219], a spatially extended model that describes oscillatory convection in a cylindrical Hele–Shaw cell [159], and stochastic systems [339].

2.4.2 Phase locked states and stability

The collective dynamical behaviours of phase oscillators has been analysed for many different regular network structures. These include hierarchical networks [285], rings with uni-directional or bi-directional coupling, and linear arrays [14, 15, 37, 93, 94]. Weakly coupled networks of identical phase oscillators described by equation (2.47) can support many different phase-locked states, including synchrony and asynchrony. Following [15], we introduce a phase-locked (1 : 1) solution of the form $\theta_i(t) = \zeta_i + \Omega t$, where ζ_i is a constant phase and Ω is the collective frequency of the coupled oscillators. From the phase difference network model (2.47) we obtain

$$\Omega = \omega + \sigma \sum_{j=1}^N w_{ij} H(\zeta_j - \zeta_i), \quad i = 1, \dots, N. \quad (2.49)$$

After assigning some reference oscillator, these N equations can be used to determine the collective frequency Ω and $N - 1$ relative phases. In order to study the local stability of a phase-locked solution $\Phi = (\zeta_1, \dots, \zeta_N)$, we linearise the system (2.47) around Φ by setting $\theta_i(t) = \zeta_i + \Omega t + \Delta\theta_i(t)$ where $\Delta\theta_i(t)$ is a small perturbation and expand this to first order in $\Delta\theta_i(t)$ to obtain

$$\begin{aligned} \Omega + \frac{d\Delta\theta_i}{dt} &= \omega + \sigma \sum_{j=1}^N w_{ij} H(\zeta_j + \Delta\theta_j - \zeta_i - \Delta\theta_i) \\ &\simeq \omega + \sigma \sum_{j=1}^N w_{ij} [H(\zeta_j - \zeta_i) + H'(\zeta_j - \zeta_i) [\Delta\theta_j - \Delta\theta_i]], \end{aligned}$$

where $H'(\zeta) = dH(\zeta)/d\zeta$. Hence,

$$\begin{aligned}
\frac{d\Delta\theta_i}{dt} &= \sigma \sum_{j=1}^N w_{ij} H'(\zeta_j - \zeta_i) [\Delta\theta_j - \Delta\theta_i] \\
&= \sigma \left[\sum_{j=1}^N w_{ij} H'(\zeta_j - \zeta_i) \Delta\theta_j - \Delta\theta_i \sum_{j=1}^N w_{ij} H'(\zeta_j - \zeta_i) \right] \\
&\equiv \sigma \sum_{j=1}^N \hat{\mathcal{H}}_{ij}(\Phi) \Delta\theta_j,
\end{aligned} \tag{2.50}$$

where

$$\hat{\mathcal{H}}_{ij}(\Phi) = w_{ij} H'(\zeta_j - \zeta_i) - \delta_{ij} \sum_{k=1}^N w_{ik} H'(\zeta_k - \zeta_i). \tag{2.51}$$

The Jacobian matrix $\hat{\mathcal{H}}$ always has a zero eigenvalue with corresponding eigenvector $(1, \dots, 1)$ which points in the direction of the locked flow. The phase-locked solution is stable if all other eigenvalues have a negative real part. We note that the Jacobian is in graph-Laplacian form which combines both anatomy (through w_{ik}) and dynamics (through H'). Therefore the stability of phase-locked network states is effected by both network structure and the intrinsic dynamics of the individual oscillators.

2.4.3 Synchrony

Synchronisation, as an emerging phenomenon of networks of dynamically interacting oscillators, has fascinated researchers for many years. Synchronisation phenomena are ubiquitous in nature and have important roles in diverse scientific disciplines including physics, biology, chemistry, ecology, sociology, and technology [10, 86, 240]. Many studies relate to whether networks behave coherently or whether more complicated spatiotemporal patterns, such as cluster states can appear.

One of the classic examples of a phase-locked state that was discussed in Subsection 2.4.2 is synchrony where $\theta_1 = \theta_2 = \dots = \theta_{N-1} = \theta_N$ with $\dot{\theta}_i = \Omega$, $\forall i$. In this case, substitution into equation (2.47), shows that Ω must

satisfy the following condition

$$\Omega = \omega + \sigma H(0) \sum_{j=1}^N w_{ij}, \quad \forall i, \quad i = 1, \dots, N. \quad (2.52)$$

One trivial way for this to hold for all i is the condition $H(0) = 0$. This is the case for diffusive coupling, that is linear in the difference between two state variables so that $H(0) = 0$, or for $H(\theta) = \sin(\theta)$ (the Kuramoto model). Another way to guarantee the existence of synchronous solutions is if $\sum_{j=1}^N w_{ij} = \text{const}$, i.e. the sum is independent of i . This would be the scenario for global coupling where $w_{ij} = 1/N$, such that the network has permutation symmetry.

The existence of the synchronous solution implies that Jacobian matrix has the form $-\sigma H'(0)\mathcal{G}$ where \mathcal{G} is the graph-Laplacian whose entries are given by

$$\mathcal{G}_{ij} = \delta_{ij} \sum_k w_{ik} - w_{ij}. \quad (2.53)$$

In order to determine stability of the synchronous state we calculate eigenvalues of the Jacobian which are in the form

$$-\sigma H'(0)\lambda_i, \quad (2.54)$$

where λ_i are the eigenvalues of \mathcal{G} . We recall that \mathcal{G} has one zero eigenvalue, with the corresponding eigenvector $(1, 1, \dots, 1, 1)$. Thus if all the remaining eigenvalues of \mathcal{G} lie on one side of the imaginary axis then stability is determined by the sign of $\sigma H'(0)$. As an example of this situation we can consider a weighted connectivity matrix with all positive entries because the graph-Laplacian in this case would be positive semi-definite (minimum eigenvalue is zero). One more specific example is global coupling with $\mathcal{G}_{ij} = \delta_{ij} - N^{-1}$, with an $(N - 1)$ degenerate eigenvalue $+1$. As a result the synchronous solution will be stable under the condition $\lambda = -\sigma H'(0) < 0$. Here we note that stability of the synchronous state is independent of the coupling strength (though

will depend on the sign of σ). Thus, this approach cannot be directly used to predict any strong coupling instabilities since any change in the magnitude of σ (keeping the sign same) does not alter the sign of λ [15].

2.4.4 Coupled phase-amplitude oscillators

As we mentioned above, phase reduction is an important mechanism to track the timing of a limit cycle oscillation and has been widely used to understand the dynamics of weakly coupled oscillators. Although phase reduction is convenient to use in various application, it is only valid in close proximity to a limit cycle and as coupling strength increases its applicability deteriorates. Due to this limitation, there is a huge interest to develop new reduction methodologies to determine dynamical properties of coupled limit cycle systems where the weak coupling assumption is insufficient, see for example [43, 92, 247, 257, 275, 277, 319, 325, 326]. However, for n -dimensional systems, this is not an easy task because the derivation of accurate coupling functions requires consideration of dynamical evaluation through the $n - 1$ transversal coordinates to the limit cycle.

In order to examine the effect of coupling strength on the stability of emergent network dynamics, we first review the relevant original work by Wilson *et al.* [326], and Ermentrout *et al.* [92]. In both studies the phase-amplitude formalism is used to analyse bifurcations that arise as the coupling strength increases that standard phase reduction methods would fail to detect. We note that the theory presented in [92, 326] was implemented only for networks of two nodes and in the future chapter we will compare this theory against an *exact* master stability function approach.

Consider a network of N identical coupled oscillators in the form

$$\frac{dx_i}{dt} = f(x_i) + \sigma \sum_{j=1}^N w_{ij} G(x_i, x_j), \quad i = 1, \dots, N. \quad (2.55)$$

This system is similar to the equation (2.42), though here the oscillators are

identical ($f_i = f, \forall i$) and the decoupled dynamics ($\sigma = 0$) is determined by $dx(t)/dt = f(x)$, assumed to have a stable T periodic limit cycle $x^\gamma(t)$. For simplicity all of the $n - 2$ nontrivial Floquet multipliers are assumed to be close to zero (perturbations in these directions annihilate rapidly), and therefore only one isostable coordinate is needed per oscillator [325, 326]. We denote the corresponding Floquet exponent by $\kappa < 0$ and the corresponding eigenfunction by $p(t)$. We introduce phase coordinates θ_i and isostable (amplitude) coordinates ψ_i for each node, and set perturbed solutions $x_i(t) = x^\gamma(\theta_i(t)) + \psi_i(t)p(\theta_i(t))$, see equation (2.20). Then we let $g_i(t) \equiv \sum_{j=1}^N w_{ij}G(x_i, x_j)$ refer to the sum of coupling terms and exploit the isostable reduction theory which was introduced in Subsection 2.3.1 to find

$$\begin{aligned}\frac{d\theta_i}{dt} &= \omega + \sigma [\mathcal{Z}(\theta_i) + \psi_i \mathcal{B}(\theta_i)] \cdot g_i(t), \\ \frac{d\psi_i}{dt} &= \kappa \psi_i + \sigma [\mathcal{I}(\theta_i) + \psi_i \mathcal{C}(\theta_i)] \cdot g_i(t).\end{aligned}\tag{2.56}$$

These equations are similar to equations (2.21) and (2.22), and the functions $\mathcal{Z}, \mathcal{I}, \mathcal{B}, \mathcal{C}$ are calculated using the equation $dx(t)/dt = f(x)$ as described in Subsections 2.3.1 and 2.3.2. We expand the coupling function $G \equiv G(\alpha, \beta)$ (assuming ψ_i are small) as follows

$$\begin{aligned}G(x_i, x_j) &= G(x^\gamma(\theta_i(t)) + \psi_i p(\theta_i(t)), x^\gamma(\theta_j(t)) + \psi_j p(\theta_j(t))) \\ &\simeq G(x^\gamma(\theta_i), x^\gamma(\theta_j)) + \psi_i G_1(x^\gamma(\theta_i), x^\gamma(\theta_j)) p(\theta_i) \\ &\quad + \psi_j G_2(x^\gamma(\theta_i), x^\gamma(\theta_j)) p(\theta_j),\end{aligned}\tag{2.57}$$

where $G_1 = \partial G / \partial \alpha|_{x^\gamma(t)}$ and $G_2 = \partial G / \partial \beta|_{x^\gamma(t)}$. Using equation (2.56) along with the definition of g_i , and by preserving lowest order terms, we obtain

$$\begin{aligned}\frac{d\theta_i}{dt} &= \omega + \sigma \sum_{j=1}^N w_{ij} [h_1(\theta_i, \theta_j) + \psi_i h_2(\theta_i, \theta_j) + \psi_j h_3(\theta_i, \theta_j)], \\ \frac{d\psi_i}{dt} &= \kappa \psi_i + \sigma \sum_{j=1}^N w_{ij} [h_4(\theta_i, \theta_j) + \psi_i h_5(\theta_i, \theta_j) + \psi_j h_6(\theta_i, \theta_j)],\end{aligned}\tag{2.58}$$

where

$$\begin{aligned}
h_1(\theta_i, \theta_j) &= \mathcal{Z}(\theta_i) \cdot G(x^\gamma(\theta_i), x^\gamma(\theta_j)), \\
h_2(\theta_i, \theta_j) &= \mathcal{Z}(\theta_i) \cdot G_1(x^\gamma(\theta_i), x^\gamma(\theta_j)) p(\theta_i) \\
&\quad + \mathcal{B}(\theta_i) \cdot G(x^\gamma(\theta_i), x^\gamma(\theta_j)), \\
h_3(\theta_i, \theta_j) &= \mathcal{Z}(\theta_i) \cdot G_2(x^\gamma(\theta_i), x^\gamma(\theta_j)) p(\theta_j),
\end{aligned} \tag{2.59}$$

and

$$\begin{aligned}
h_4(\theta_i, \theta_j) &= \mathcal{I}(\theta_i) \cdot G(x^\gamma(\theta_i), x^\gamma(\theta_j)), \\
h_5(\theta_i, \theta_j) &= \mathcal{I}(\theta_i) \cdot G_1(x^\gamma(\theta_i), x^\gamma(\theta_j)) p(\theta_i) \\
&\quad + \mathcal{C}(\theta_i) \cdot G(x^\gamma(\theta_i), x^\gamma(\theta_j)), \\
h_6(\theta_i, \theta_j) &= \mathcal{I}(\theta_i) \cdot G_2(x^\gamma(\theta_i), x^\gamma(\theta_j)) p(\theta_j).
\end{aligned} \tag{2.60}$$

We note that the case $\psi_i = 0$ (neglecting the amplitude terms) is equivalent to the standard phase reduction given by equation (2.43). In reference to Subsection 2.4.1, we define a relative phase variable $\phi_i = \theta_i - \omega t$, and note that all the h_i functions are 2π -periodic. We then average (2.58) over one period T and introduce $H_i(y) = (1/2\pi) \int_0^{2\pi} h_i(s, y + s) ds$ (which is similar to the equation (2.48)). Following [92, 326], we consider a network of two nodes ($N = 2$), so that equation (2.58) can be reduced, by choosing $\chi \equiv \phi_2 - \phi_1$, to the form

$$\begin{aligned}
\frac{d\chi}{dt} &= \sigma [H_1(-\chi) - H_1(\chi) + \psi_1 (H_3(-\chi) - H_2(\chi)) \\
&\quad + \psi_2 (H_2(-\chi) - H_3(\chi))], \\
\frac{d\psi_1}{dt} &= \kappa\psi_1 + \sigma [H_4(\chi) + \psi_1 H_5(\chi) + \psi_2 H_6(\chi)], \\
\frac{d\psi_2}{dt} &= \kappa\psi_2 + \sigma [H_4(-\chi) + \psi_2 H_5(-\chi) + \psi_1 H_6(-\chi)].
\end{aligned} \tag{2.61}$$

Determining stability of the fixed points of (2.61) corresponds to assessing phase locked solutions of equation (2.58). To do so, first we find the fixed points of the system (2.61), and then calculate their Jacobians. If the real part of the eigenvalues of the Jacobian matrix are negative then a locked solution will be stable. We note that both fixed points and their corresponding

Jacobians depend on the coupling strength σ . In the case of a synchronous solution, $[\chi, \psi_1, \psi_2]^\top = [0, 0, 0]^\top$, stability is explicitly effected by any change in the magnitude of σ , though this would not effect stability in the phase only reduction, see equation (2.54). Illustrative numerical examples of this can be found in [92, 326]. In the next chapter we will tailor this technique to some PWL nonsmooth models.

2.4.5 Master stability function technique

In the previous subsections, we reviewed synchronisation in networks of oscillators by focusing on both phase only and phase-amplitude approaches. There is another convenient methodology to analyse the synchronous state of coupled identical systems of periodic oscillators which is exact for strong diffusive coupling. The original work by Pecora and Carroll [229] initiated this approach by introducing the master stability function formalism. The MSF technique is utilised to assess the stability of the synchronised state in terms of the spectral properties of the network connectivity matrix.

In order to introduce the MSF formalism, we start with an arbitrary connected network of N coupled identical oscillators. Each oscillator, represented by the state vector x_i , $i = 1, \dots, N$, in an m -dimensional space with isolated (uncoupled) dynamics governed by $dx_i/dt = f(x_i)$. The output for each node is determined by a vector function $H : \mathbb{R}^m \rightarrow \mathbb{R}^m$ (which can be linear or non-linear). For instance, for a three-dimensional system with $x = (x^{(1)}, x^{(2)}, x^{(3)})$, we can set $H(x) = (0, x^{(2)}, 0)$, which means that the oscillators are linearly coupled only through the $x^{(2)}$ -component. For a given coupling matrix with components w_{ij} and a coupling (global) strength σ , the dynamics of a network of N coupled identical oscillators, to which the MSF technique applies,

is described by

$$\begin{aligned}
\frac{dx_i}{dt} &= f(x_i) + \sigma \sum_{j=1}^N w_{ij} [H(x_j) - H(x_i)] \\
&= f(x_i) - \sigma H(x_i) \sum_{j=1}^N w_{ij} + \sum_{j=1}^N w_{ij} H(x_j) \\
&= f(x_i) - \sigma \sum_{j=1}^N \left(\delta_{ij} \sum_{k=1}^N w_{ik} - w_{ij} \right) H(x_j) \\
&\equiv f(x_i) - \sigma \sum_{j=1}^N \mathcal{G}_{ij} H(x_j). \tag{2.62}
\end{aligned}$$

Here, the matrix $\mathcal{G} \in \mathbb{R}^{N \times N}$ with entries \mathcal{G}_{ij} is identified as the graph-Laplacian (see equation (2.53)). By definition, the matrix \mathcal{G} has zero row-sum. The $N - 1$ constraints $x_1(t) = x_2(t) = \dots = x_N(t) = s(t)$ define the invariant *synchronisation manifold*, with $s(t)$ a solution in \mathbb{R}^m of the uncoupled system, that is $ds(t)/dt = f(s(t))$.

When all oscillators are initially set on the synchronisation manifold with identical initial conditions, they will always remain synchronised. In order to assess the stability of a synchronised state we perform a linear stability analysis by inserting a perturbed solution $x_i(t) = s(t) + \delta x_i(t)$ into equation (2.62) to obtain the variational equation

$$\frac{d\delta x_i}{dt} = Df(s)\delta x_i - \sigma DH(s) \sum_{j=1}^N \mathcal{G}_{ij} \delta x_j, \tag{2.63}$$

where $Df(s) \in \mathbb{R}^{m \times m}$ and $DH(s) \in \mathbb{R}^{m \times m}$ denote the Jacobian of $f(s)$ and $H(s)$ which are evaluated at the synchronous solution $s(t)$, respectively. If we introduce $U = (\delta x_1, \delta x_2, \dots, \delta x_N) \in \mathbb{R}^{mN}$, and use the tensor (or Kronecker) product \otimes for matrices, the variational equation can be written as

$$\frac{dU}{dt} = [I_N \otimes Df(s) - \sigma(\mathcal{G} \otimes DH(s))] U. \tag{2.64}$$

We can organise (right) normalised eigenvectors of \mathcal{G} into a matrix P such that

$P^{-1}\mathcal{G} = \Lambda P^{-1}$, with $\Lambda = \text{diag}(\lambda_1, \lambda_2, \dots, \lambda_N)$ where λ_η are the corresponding eigenvalues of \mathcal{G} for $\eta = 1, \dots, N$. By introducing a new variable Y according to the linear transformation $Y = (P \otimes I_m)^{-1}U$, we obtain a block diagonal system

$$\frac{dY}{dt} = [I_N \otimes Df(s) - \sigma(\Lambda \otimes DH(s))]Y, \quad (2.65)$$

where I_N is the $N \times N$ identity matrix. Hence, this results in a set of N decoupled m -dimensional equations parametrised by the eigenvalues of the graph-Laplacian:

$$\frac{d\xi_l}{dt} = [Df(s) - \sigma\lambda_l DH(s)]\xi_l, \quad l = 1, \dots, N, \quad (2.66)$$

where $Df(s)$ and $DH(s)$ are independent of the block label l . Since \mathcal{G} has the property of a zero row-sum, there is always a zero eigenvalue, say $\lambda_1 = 0$, with corresponding eigenvector $(1, 1, \dots, 1)$ which characterises a perturbation tangential to the synchronisation manifold. The remaining $N - 1$ transversal perturbations (in relation with the other $N - 1$ solutions of equation (2.66)) must damp out in order for the synchronous state to be stable. For a general matrix \mathcal{G} some eigenvalues λ_l may be complex. This might be the case for example when the coupling matrix is not symmetric. This leads us to consider the following system

$$\frac{d\xi}{dt} = [Df(s) - \mu DH(s)]\xi, \quad \mu \in \mathbb{C}, \quad (2.67)$$

where $\xi \in \mathbb{C}^m$. We observe that all the individual variational equations in the system (2.66) have the same structure as that of the system (2.67). The only difference between them is the parameter $\mu_l = \sigma\lambda_l$. In general, the equation (2.67) is known as *master variational equation*, and in order to determine stability of this equation, we calculate its largest Lyapunov exponent [130] as a function of μ . The resulting function is called the *master stability function*. More explicitly, for a given $s(t)$, the MSF is characterised as the function that

maps the complex number μ to the greatest Lyapunov exponent of equation (2.67). Note that if $s(t)$ is periodic, the MSF is defined as the function which maps the complex number μ to the greatest Floquet exponent of the system (2.67). The synchronised state of the network of coupled oscillators is stable if the MSF is negative at $\mu = \sigma \lambda_l$ where λ_l ranges over the eigenvalues of the matrix \mathcal{G} (excluding $\lambda_1 = 0$). When the MSF is computed for an oscillator, then to assess the stability of the synchronised state for arbitrary network one needs only to calculate the eigenvalues of the matrix \mathcal{G} [15].

It is clear that the Laplacian form of coupling in equation (2.62) guarantees the existence of the synchronous state. However, there are other forms that occur naturally. Consider for example the case:

$$\frac{dx_i}{dt} = f(x_i) + \sigma \sum_{j=1}^N w_{ij} H(x_j). \quad (2.68)$$

If we substitute $x_i(t) = s(t)$, $i = 1, 2, \dots, N$, into the equation (2.68), we find

$$\frac{ds}{dt} = f(s) + \sigma H(s) \sum_{j=1}^N w_{ij}. \quad (2.69)$$

The only way to guarantee that all oscillators have the same behaviour is to restrict $\sum_{j=1}^N w_{ij} = \text{constant}$ for all i . In terms of dynamical evaluation, a constant row sum means that if the motion is started on a synchronisation manifold with identical initial values, it remains in a synchronised state. In other words, the synchronised state is *flow invariant* which is a necessity to have synchronised motion. If the constant is zero, then the system is often referred to as *balanced* [72, 260, 262, 313]. If these row sums are not zero but a fixed constant for all i , the synchronised state changes as the coupling strength σ changes.

We also note that MSF framework can be applied to chaotic systems where instead of calculating Floquet exponents, one needs to calculate Lyapunov exponents [63, 229, 231]. Moreover, the MSF formalism can be generalised to

network settings where the coupling between nodes is characterised by some time delay [64, 172]. The synchronous solution is a special network state, particularly when compared to more unusual ones, like chimeras where asynchronous and synchronous states co-exist [54, 188]. The MSF approach works only to investigate stability of the synchronous states of networks of identical nodes, though can be extended to nearly identical units [296].

For a more detailed discussion regarding the use of the MSF formalism we refer the reader to [10, 15, 230, 243]. In the following subsection we provide an explicit example to show how to compute and implement the MSF technique for a smooth nonlinear system.

2.4.6 An illustrative example: a network of Stuart-Landau oscillators

The Stuart-Landau equation, that represents a normal form of the Andronov-Hopf bifurcation, is given by

$$\frac{dz}{dt} = (\eta_R + i\eta_I)z - (\alpha_R + i\alpha_I)|z|^2z, \quad (2.70)$$

where the state of the oscillator $z = x + iy = Re^{i\theta} \in \mathbb{C}$, with $x, y, R \in \mathbb{R}$ and $\theta \in [0, 2\pi)$. By using $z = Re^{i\theta}$, the system (2.70) can be transformed into polar coordinates

$$\begin{aligned} \frac{dR}{dt} &= \eta_R R - \alpha_R R^3, \\ \frac{d\theta}{dt} &= \eta_I - \alpha_I R^2, \end{aligned} \quad (2.71)$$

where $R = 0$ is the only stable fixed point when $\eta_R < 0$. Moreover, if $\alpha_R < 0$ the solutions may blow up in finite time, while if $\alpha_R = 0$ the equation for the radial variable reduces to a first-order linear equation. If $\eta_R > 0$, $R_0 = 0$ becomes unstable and there is a stable fixed point $R_+ = \sqrt{\eta_R/\alpha_R}$ (corresponding to a limit cycle with amplitude R_+). A periodic solution bifurcates when η_R crosses zero from below when $\alpha_R > 0$ and this is known as an Andronov-Hopf

bifurcation. The emergent periodic solution can be written in closed form $(x(t), y(t)) = R_+(\cos(\Omega t), \sin(\Omega t))$, $\Omega = \eta_I - \alpha_I R_+^2$. This allows substantial analytical progress to be made. In the literature, the analysis of the single Stuart-Landau model has been studied by many authors and results are well documented [104, 205, 224, 310]. A typical limit cycle solution is illustrated in Fig. 2.1.

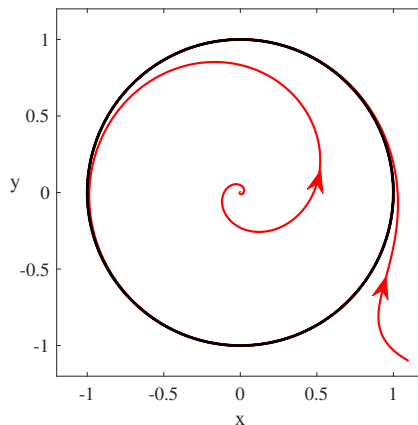


Figure 2.1: A limit cycle (black) of a Stuart-Landau oscillator and flows from different initial data (red), showing that the orbit is attracting. Parameters are $\alpha = 1$ and $\eta = 2$.

To better understand the complex dynamics of many real world coupled systems, network models of Stuart-Landau oscillators are often used. Applications have included systems of electronic oscillators [23], semiconductor lasers [41], chemical reaction-diffusion systems [144], and neural oscillators [8]. Recently, the synchronisation of both homogeneous and heterogeneous networks of Stuart-Landau oscillators has been studied in [104, 225, 234, 244, 263, 309, 310], where for instance, Salova and D’Souza [263] worked on properties of splay (asynchronous) states and cluster synchronisation, Panteley *et al.* [225] investigated synchronisation and other collective behaviours of networks of heterogeneous systems, Pereti and Fanelli [234] explored how to achieve synchronisation by allowing network plasticity over time, and Premalatha *et al.* [244] examined chimera states in linearly coupled networks of Stuart-Landau oscillators. Here we consider a network of N Stuart-Landau oscillators with

linear-coupling in the form

$$\begin{aligned} \frac{dz_n}{dt} &= (1 + i\eta)z_n - (1 + i\alpha)|z_n|^2 z_n \\ &+ \sigma \sum_{m=1}^N w_{nm} [z_m - z_n], \quad n = 1, \dots, N, \end{aligned} \quad (2.72)$$

where $z_n \in \mathbb{C}$, $\sigma \in \mathbb{R}$ is the global coupling strength and $w_{nm} \in \mathbb{R}$ are the entries of a coupling matrix. By introducing the complex representation $z_n = R_n e^{i\theta_n}$ we can transform the system (2.72) into

$$\begin{aligned} \frac{dR_n}{dt} &= R_n (1 - R_n^2) - \sigma \sum_m \mathcal{G}_{nm} R_m \cos(\theta_m - \theta_n), \\ \frac{d\theta_n}{dt} &= \eta - \alpha R_n^2 - \sigma \sum_m \mathcal{G}_{nm} \frac{R_m}{R_n} \sin(\theta_m - \theta_n), \end{aligned} \quad (2.73)$$

where \mathcal{G} is the graph Laplacian with components $\mathcal{G}_{nm} = -w_{nm} + \delta_{nm} \sum_l w_{nl}$. It is easy to show that the synchronous oscillatory solution with non-zero amplitude is given by $R_n = 1$ and $\theta_n = \Omega t$ with $\Omega = \eta - \alpha$. To assess the stability of synchronous state we consider a perturbed solution of the form $(R_n(t), \theta_n(t)) = (1 + \delta R_n(t), \Omega t + \delta \theta_n(t))$. The perturbations $\delta x_n = (\delta R_n, \delta \theta_n)$ evolves according to

$$\frac{d}{dt} \delta x_n = J \delta x_n - \sigma I_2 \sum_m \mathcal{G}_{nm} \delta x_m, \quad J = \begin{bmatrix} -2 & 0 \\ -2\alpha & 0 \end{bmatrix}, \quad (2.74)$$

where I_2 is 2×2 identity matrix. Using a basis in which \mathcal{G} is diagonal, this decouples into N two-dimensional variational Floquet problems

$$\frac{d}{dt} \xi = [J - \sigma \gamma I_2] \xi, \quad (2.75)$$

where γ are the eigenvalues of \mathcal{G} . The matrix $J - \sigma \gamma I_2$ is independent of time (a linear autonomous system) and the Floquet problem can be solved in terms of the matrix $M(\mu) = J - \mu I_2$. To do so we need to calculate eigenvalues of $e^{M(\mu)T}$ where $T = 2\pi/(\eta - \alpha)$. It is well known that if λ is an eigenvalue of $M(\mu)$ with

an eigenvector v , then $e^{\lambda T}$ is an eigenvalue of $e^{M(\mu)T}$ with the same eigenvector. The Floquet exponent of $e^{M(\mu)T}$ that corresponds to the Floquet multiplier $e^{\lambda T}$ is $\ln(e^{\lambda T})/T = \lambda$. Therefore the real part of λ corresponds to the real part of the Floquet exponent of $e^{M(\mu)T}$. Hence, the stability of the synchronous state is determined by the sign of the real part of λ . The MSF can be constructed as the real part of the largest eigenvalue of $M(\mu)$. The synchronous solution is stable if $\text{MSF}(\mu) < 0$ for all $\mu = \sigma\gamma$. The characteristic equation for the eigenvalues λ of $M(\mu)$ is given by $\det[J - (\lambda + \mu)I_2] = 0$. Thus $(\lambda + \mu)$ is an eigenvalue of J . The eigenvalues of J are easily calculated as 0 and -2 . Thus $\lambda = -\mu$ and $\lambda = -\mu - 2$, and the MSF is negative for $\text{Re } \mu > 0$.

In order to illustrate this result, we consider a ring network of 5 Stuart-Landau oscillators. For ease of numerical simulations instead of system (2.73), we use the following system by setting $z_n = x_n + iy_n$:

$$\begin{aligned}\frac{dx_n}{dt} &= x_n - \eta y_n - x_n(x_n^2 + y_n^2) + \alpha y_n(x_n^2 + y_n^2) - \sigma \sum_{m=1}^N \mathcal{G}_{nm} x_m, \\ \frac{dy_n}{dt} &= y_n + \eta x_n - y_n(x_n^2 + y_n^2) - \alpha x_n(x_n^2 + y_n^2) - \sigma \sum_{m=1}^N \mathcal{G}_{nm} y_m.\end{aligned}\tag{2.76}$$

Here we choose a connectivity matrix W with entries $[W]_{nm} = w_{nm}$ where

$$w_{nm} = \begin{bmatrix} 0 & 1 & 0 & 0 & 1 \\ 1 & 0 & 0.1 & 0 & 0 \\ 0 & 0.1 & 0 & 1 & 0 \\ 0 & 0 & 1 & 0 & 0.1 \\ 1 & 0 & 0 & 0.1 & 1.1 \end{bmatrix} \quad \text{and } n, m = 1, \dots, 5,\tag{2.77}$$

hence, the graph-Laplacian is

$$\mathcal{G} = \begin{bmatrix} 2 & -1 & 0 & 0 & -1 \\ -1 & 1.1 & -0.1 & 0 & 0 \\ 0 & -0.1 & 1.1 & -1 & 0 \\ 0 & 0 & -1 & 1.1 & -0.1 \\ -1 & 0 & 0 & -0.1 & 1.1 \end{bmatrix}.\tag{2.78}$$

All eigenvalues of the matrix \mathcal{G} are real with the smallest one equal to zero. As a result, the synchronous network state is linearly stable for $\sigma > 0$ because the MSF is negative for all arguments on the positive real half-line, see left plot in the Fig. 2.3 where we also indicate values of μ_l (γ of \mathcal{G}). The right plot of the Fig. 2.3 shows a direct numerical simulation and as we expect the synchronous network state is stable. To illustrate the theory, we replace the weights w_{23} and w_{32} of the connectivity matrix by $w_{23} = w_{32} = -0.1$. In this scenario, the MSF is negative for one of the μ_l , say when $l = p$, implying that the synchronous network state is unstable. Numerical simulations clearly show a variation of the values for x_n across the network, see Fig. 2.4. In Fig. 2.2, we show a snapshot of the network activity where in the stable case all nodes evolve together whereas in the unstable case they behave differently. To predict the shape of the emergent network pattern we can use the eigenvector that corresponds to the eigenvalue associated with p . As Fig. 2.5 depicts, the eigenvector mirrors very closely the obtained values of x_n .

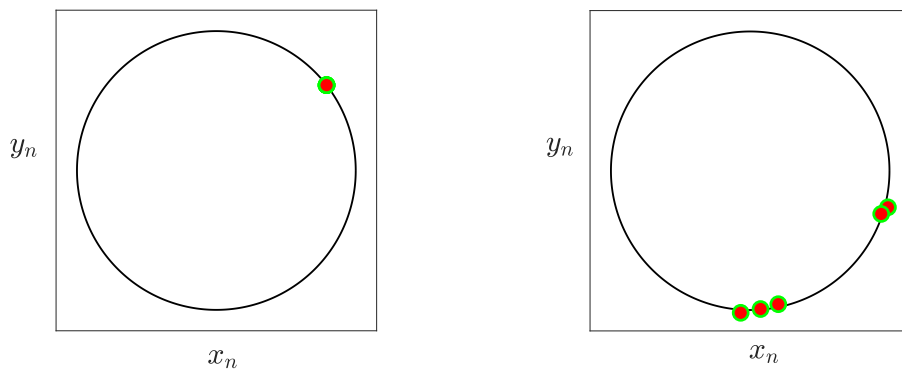


Figure 2.2: A typical snapshot of a simulation showing network activity of a linearly coupled ring network of five Stuart-Landau oscillators. The solid black line shows the synchronous orbit, whilst the red filled green circles show individual behaviours of oscillators. Left: Stable synchronous network state. All oscillators sit on top of each other. Right: Unstable synchronous network state. The oscillators behave differently. Node parameter values as in Fig. 2.1 and $\sigma = 1$. On the left panel \mathcal{G} is taken as in (2.78), and in the right panel we replaced weights w_{23} and w_{32} by $w_{23} = w_{32} = -0.1$.

In the following chapters we will adapt and apply the theory for smooth systems to treat nonsmooth systems at both the node and network levels for variety of biological and mechanical systems, from nodes to networks.

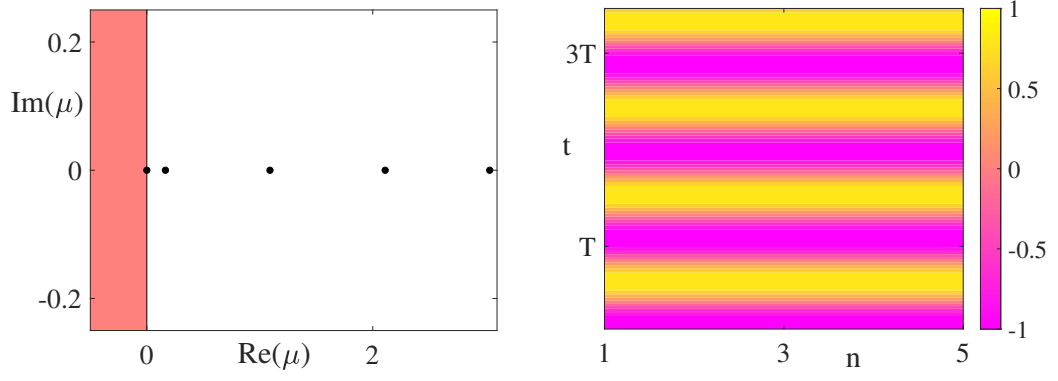


Figure 2.3: Left: MSF together with the values of μ_l (black dots) for a network of 5 oscillators. The white region indicates where the MSF is negative. Right: Space-time plot of the network activity of x_n . All parameter values are as in the left panel of Fig. 2.2.

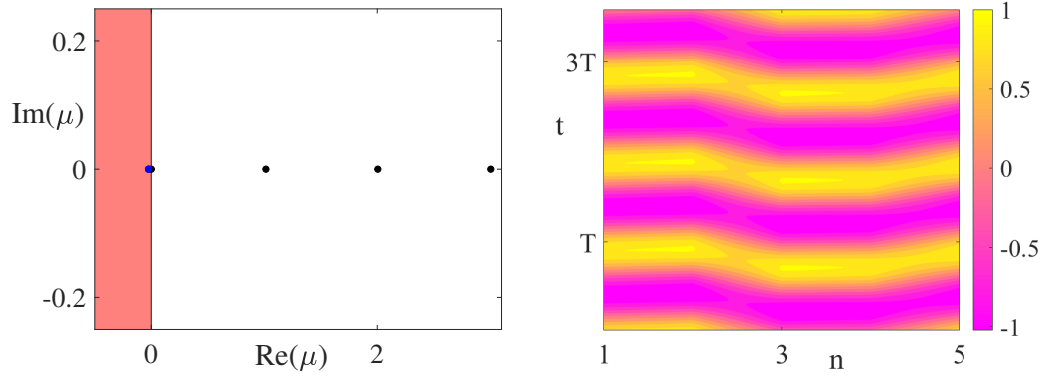


Figure 2.4: Left: MSF together with the values of μ_l (black blue dots) for a network of 5 oscillators, where we only change w_{23} and w_{32} to $w_{23} = w_{32} = -0.1$. Note that $\mu_k = -0.0245$ which corresponds to an unstable Floquet multiplier 1.1667 (represented by the blue dot). The white region represents where the MSF is negative. Right: Space-time plot of the network activity of x_n . All parameter values are as in the right panel of Fig. 2.2.

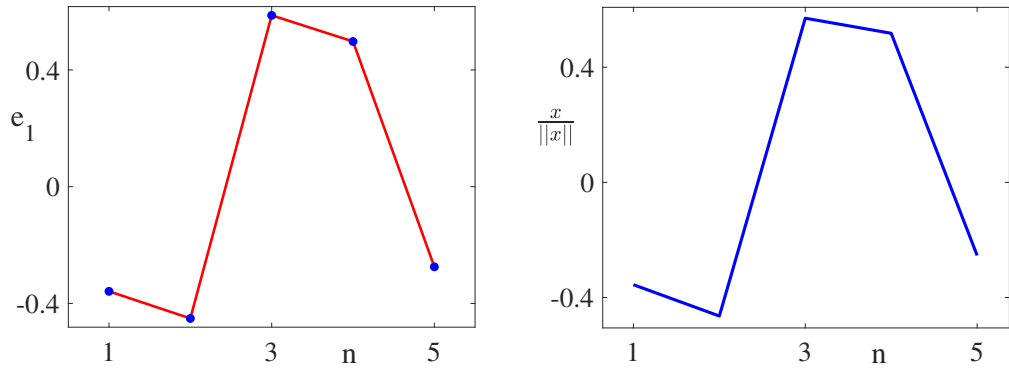


Figure 2.5: Left: The $n = 5$ components of the normalised eigenvector e_1 corresponding to the eigenvalue associated with μ_k in Fig. 2.4. Right: Normalised x_n as a function of n for a fixed time. All parameter values as in Fig. 2.4.

Chapter 3

Nonsmooth oscillators with piecewise dynamics

3.1 Introduction

Dynamical systems theory has a long and distinguished history and has been proven to be a very powerful tool to analyse and understand behavioural phenomena in a diverse range of problems in many different scientific fields including engineering, physics, medical science, economics, and biology to mention a few only [170, 235]. Many concepts of the classical theory rely on a smoothness of the underlying system, but this excludes a large number of concrete problems that arise in practice where nonsmooth phenomena play an important role, see for example the books [35, 81, 152, 168]. Therefore, it is vital to generalise concepts from smooth dynamical systems to cover nonsmooth ones, though almost always such a generalisation is non-trivial since problems of this kind are mathematically hard to handle.

Piecewise smooth (PWS) and piecewise linear (PWL) systems emerge in modelling of many important real world problems. PWL systems constitute an important class of nonsmooth models and are now commonplace in the applied sciences [51, 78, 81]. Some of the wide range of applications can be found in nonlinear engineering modelling, where certain processes are precisely modelled

by piecewise linear vector fields [242], mechanics, electronics, control theory, economics, ecology, and biology, see for example [42, 51, 66, 73, 81, 109, 111, 124, 180], and references therein. Indeed, the piecewise modelling approach has been used by physicists and engineers many years before it was formalised in rigorous mathematical terms [51, 242]. To the best of our knowledge, Andronov and co-authors [7] pioneered the investigation of piecewise linear systems from a formal perspective with their work “*Theory of Oscillations*” in the mid-sixties (whose Russian version was first released around the thirties).

Nonsmooth PWL systems can be characterised as the uniform limit of smooth nonlinearities, and therefore, the global dynamics of a large number of nonlinear models can sometimes be approximated by PWL models and vice-versa [54, 242]. Some applications of this can be found in [183, 333] where a qualitative agreement between two approaches is presented. It is also observed that the accuracy of approximated solutions depends on the fineness of the chosen piecewise linear caricature [49, 179]. Simply put, PWL modelling gives analytical insight to nonlinear models by dividing the phase space into different regions where trajectories evolve according to a linear dynamical system, and then patching solutions together to obtain the full flow. The main challenge during this process is the determination of the time-of-flight in each linear zone [242]. PWL modelling is common for dynamical systems with a discontinuous right hand side [100], such as in some gene regulatory networks where genes switch abruptly and a new set of linear rules are determined for protein production [112, 118]. Additionally, this approach can also be used to analyse discontinuous dynamical systems, for instance, impacting mechanical oscillators [25], and cardiac oscillators [303]. Interestingly, PWL systems can exhibit many different dynamical behaviours such as periodic solutions, limit cycles, heteroclinic loops, homoclinic loops, strange attractors, and chaos [47, 337], and even some more special bifurcations such as grazing or sliding [81].

In a mathematical neuroscience context, as famous examples of PWL

modelling, one may consider the McKean model [305], PWL Morris-Lecar (PML) model [52], and integrate-and-fire models [55, 306]. In Section 3.4 we provide model descriptions of the McKean model and the PML model, as well as show how to construct periodic orbits. We also review the absolute model that displays a nonsmooth Andronov-Hopf bifurcation, and the homoclinic loop model. We show how the period and the amplitude of the periodic orbits change under parameter variation, and for the McKean model we construct a bifurcation diagram to explore the parameter region where a stable periodic orbit co-exists with an unstable periodic orbit.

The organisation of the chapter is as follows. In Section 3.2 we introduce nonsmooth dynamical systems [81, 100, 121] and their natural classification. In Section 3.3 we consider a class of PWL systems with two linear zones and formulate the explicit construction process for periodic orbits. We then present the PWL models that we work with throughout Chapter 4. Finally, in Section 3.5, we give a discussion to emphasise the practicality and wide use of PWL modelling.

3.2 Nonsmooth dynamical systems and a classification

We consider nonsmooth dynamical systems (continuous-time) that can be described by a finite set (say N) of piecewise smooth ordinary differential equations, and introduce relevant terminology to make subsequent analysis clearer. Phase space is partitioned into N open sets R_i , $i = 1, \dots, N$, where the system is smooth in each of these R_i , so that

$$\frac{dx}{dt} = \begin{cases} f_1(x) & \text{if } x \in R_1, \\ f_2(x) & \text{if } x \in R_2, \\ \vdots & \\ f_N(x) & \text{if } x \in R_N. \end{cases} \quad (3.1)$$

Here $x \in R_i$, $R_i \subset \mathbb{R}^n$ and each vector field f_i is smooth. Across the boundaries Σ_{ij} between adjacent regions R_i and R_j , vector fields change abruptly and smoothness is lost. These non-empty discontinuity boundaries are called *switching manifolds* and can be defined using a smooth *indicator function* $h_{ij}(x) = 0$ when $x \in \Sigma_{ij}$. This is illustrated in Fig. 3.1. The piecewise-smooth flows $\varphi_i(t, x)$, $i = 1, \dots, N$, satisfy

$$\frac{d\varphi_i(t, x)}{dt} = f_i(\varphi_i(t, x)), \quad \varphi_i(0, x) = x, \quad x \in R_i, \quad (3.2)$$

generated by the vector fields $f_i(x)$ in each region R_i . The overall flow of the system is obtained by the composition of flows φ_i . Different classes of PWS systems can be characterised according to the different scenarios that take place when the overall flow φ intersects with the boundaries Σ_{ij} where switching between the regions R_i and R_j is governed by a *switching (jump) rule*. Following [81, 82, 180] we shall classify the nonsmooth dynamical systems of interest here into three different types depending upon their degree of discontinuity. In the following Table 3.1 we illustrate some typical shapes of periodic behaviours for planar systems. In a recent book, Glendinning *et al.* [121] presented both the historical and theoretical development of piecewise smooth systems together a wide variety of examples.

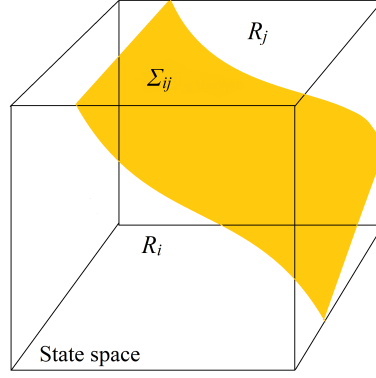


Figure 3.1: Schematic diagram showing the structure of the state space of a nonsmooth system. A non-empty smooth border Σ_{ij} between two adjacent regions R_i and R_j is called a switching manifold. In the region R_i system is governed by the vector field f_i until the flow $\varphi_i(t, x)$ reaches the switching manifold Σ_{ij} where a switching rule applies and then in the region R_j the flow $\varphi_j(t, x)$ evolves according to the vector field f_j .

1. PWS continuous systems. Systems with continuous state and continuous vector fields ($f_i(x) = f_j(x)$) but discontinuities in the first or higher derivatives of f , i. e. $\exists n \in \mathbb{Z}, n \geq 1$, such that $\partial^n f_i / \partial x^n \neq \partial^n f_j / \partial x^n$, across the switching manifolds Σ_{ij} . These systems have a degree of smoothness equal to two or higher, and have discontinuous Jacobians ($Df_i(x) \neq Df_j(x)$) across the switching manifolds.
2. Filippov systems. Systems with continuous state but discontinuous vector fields ($f_i(x) \neq f_j(x)$) across the switching surface. These systems have a degree of smoothness equal to one and are called Filippov systems [100]. The system described by the equation (3.1) does not define $f(x)$ if x is on Σ_{ij} . A description of the dynamics on the switching manifolds can be completed with the set-valued extension $F(x)$

$$\frac{dx}{dt} \in F(x) = \begin{cases} f_i(x) & \text{if } x \in R_i, \\ \overline{\text{co}} \{f_i(x), f_j(x)\} & \text{if } x \in \Sigma_{ij}, \\ f_j(x) & \text{if } x \in R_j. \end{cases} \quad (3.3)$$

where $\overline{\text{co}}(\mathcal{A})$ denotes the smallest closed convex set containing \mathcal{A} :

$$\overline{\text{co}}\{f_i(x), f_j(x)\} = \{\varsigma f_i(x) + (1 - \varsigma)f_j(x), \varsigma \in [0, 1]\}, \quad (3.4)$$

where ς is a parameter that defines the convex combination and has no physical meaning. The extension (or convexification) of a discontinuous system (3.1) into a convex differential inclusion (3.3) is known as the *Filippov convex method* [100]. If $\langle \nabla h_{ij}, f_i \rangle \langle \nabla h_{ij}, f_j \rangle < 0$ these systems may have *sliding* motion [149, 153] along a switching manifold such that $\dot{h}_{ij} = \nabla h_{ij} \cdot F = 0$. Note that we use $\langle \cdot, \cdot \rangle$ and \cdot interchangeably to denote the standard vector inner product. Then we can construct ς as

$$\varsigma = \frac{\nabla h_{ij} \cdot f_j}{\nabla h_{ij} \cdot (f_j - f_i)}. \quad (3.5)$$

3. Impulsive systems. Systems which have instantaneous discontinuities (jumps) in the solution at the switching boundaries Σ_{ij} which are governed by smooth jump operators

$$x^+ = \mathcal{J}_{ij}(x^-), \quad (3.6)$$

where x^- denotes state of the system just before the impact and x^+ denotes immediately thereafter. Here we consider switching manifolds that behave like hard constraints such that $\mathcal{J}_{ij} : \Sigma_{ij} \rightarrow \Sigma_{ij}$, i.e. the jump operator maps the set Σ_{ij} back to itself. These type of systems have degree of smoothness zero and are called *impulsive (or impacting)* systems. In the literature, \mathcal{J} is referred as an *impact rule (or law)* and the discontinuity boundaries Σ_{ij} are called *impact surfaces*. The event of a flow intersecting Σ_{ij} is referred to as an impacting event and the time of this event is named as the moment of impulsive action. Depending upon the properties of the jump operator \mathcal{J} , many different dynamics may be observed. In this thesis, we shall restrict our attention to linear jump

operators (matrices). To further understand the behaviour of impacting systems we refer the reader to [35, 36, 81, 82].

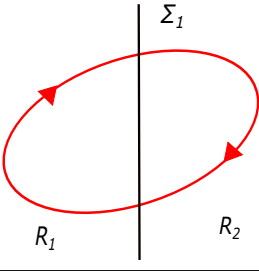
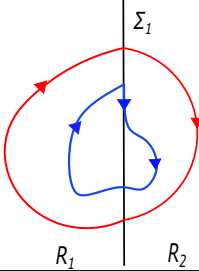
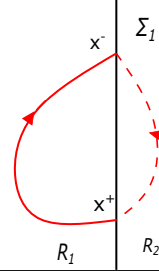
Nonsmooth dynamical systems		
Piecewise-smooth continuous systems	Filippov systems	Impulsive systems
An illustration	An illustration	An illustration
		
Example	Example	Example
Mechanical oscillators with a one-sided elastic support [180].	Mechanical systems with dry friction or visco-elastic supports [180].	Impacting systems [81] (e.g. Franklin Bells [84]).

Table 3.1: Classification of non-smooth dynamical systems with possible schematic illustration of some periodic orbits in \mathbb{R}^2 . The first column corresponds to non-smooth systems with continuous right hand side where both solutions and vector fields are continuous across the switching manifold Σ_1 between regions R_1 and R_2 . In this case we assume that the boundary Σ_1 is not simultaneously attracting (or repelling) from both sides, therefore all trajectories cross Σ_1 transversally and no sliding motion constrained to Σ_1 can arise. The second column addresses nonsmooth systems with discontinuous right hand side where solutions are continuous but vector fields discontinuous across the Σ_1 . Here it is possible to obtain both sliding (blue orbit) and transversal (red orbit) periodic solutions across the Σ_1 depending on the underling dynamics. The third column depict systems with discontinuities (jumps) in the state where x^- is the state immediately before the jump and x^+ immediately thereafter.

3.3 Planar piecewise linear models

Planar piecewise linear systems [88, 108, 274] whose dynamics are defined on two regions with a line of discontinuity have a simple tractable configuration,

though might have complex dynamical properties. Therefore, we start by considering the following systems with two zones described by $x = (v, w)^\top \in \mathbb{R}^2$ with

$$\frac{dx}{dt} = \begin{cases} f_1 \equiv A_1 x + b_1, & \text{if } x \in R_1, \\ f_2 \equiv A_2 x + b_2, & \text{if } x \in R_2, \end{cases} \quad (3.7)$$

where $A_{1,2} \in \mathbb{R}^{2 \times 2}$ are constant matrices and $b_{1,2} \in \mathbb{R}^2$ are constant vectors. The regions R_1 and R_2 are given as

$$R_1 = \{x \in \mathbb{R}^2 \mid h(x) > 0\} \quad \text{and} \quad R_2 = \{x \in \mathbb{R}^2 \mid h(x) < 0\}, \quad (3.8)$$

where we introduce an indicator function $h : \mathbb{R}^2 \rightarrow \mathbb{R}$ given by

$$h(x) = v - a, \quad (3.9)$$

so that switching events occur when $h(x) = 0$ which holds on the switching manifold $v = a$. If a fixed point exists in R_μ its stability is determined by the eigenvalues of A_μ , where $\mu \in \{1, 2\}$. We can easily calculate these eigenvalues $\lambda_\pm(A_\mu)$ using the well known formula for planar systems

$$\lambda_\pm(A) = \frac{\text{Tr}(A) \pm \sqrt{(\text{Tr}(A))^2 - 4 \det(A)}}{2}. \quad (3.10)$$

Then, each region of the model can be classified in the trace-determinant plane as saddle, attracting focus, repelling focus, attracting node, repelling node, and centre.

Planar PWL systems of the form (3.7) have been studied for many years due to the richness of their dynamical behaviours. Llibre *et. al* [186] studied existence and maximum number of limit cycles for discontinuous piecewise planar linear differential systems, and discussed the application of these to some physical problems. Freire *et. al* [107] considered continuous piecewise planar linear systems with two zones and proposed a canonical form that captures many interesting oscillatory behavior, and performed a bifurcation analysis.

As well as exhibiting almost all types of dynamics observed in smooth nonlinear systems, planar PWL systems may also support bifurcations that smooth systems do not [81, 82]. However, compared to smooth systems, knowledge of bifurcations in PWL systems is largely limited to specific examples and still needs further investigation. One of the reasons which precludes the development of results for PWL systems is the inability to generalise results for lower dimensional systems to higher dimensional systems. In particular, dimension reduction techniques are lacking, for example normal forms or centre manifold theory [51]. Nevertheless, we can still start to develop a picture of the theory of bifurcations in PWL systems by gathering results from the differential inclusions of Filippov [100], “C” bifurcations of Feigin [79, 99], and non-smooth equilibrium bifurcations of Andronov and co-workers [7]. Examples of well known bifurcations caused by discontinuities include grazing bifurcations, sliding bifurcations, and discontinuous saddle-node bifurcations [81, 134].

One of the main advantage of using PWL modelling is that we can derive closed form solutions for periodic orbits [242]. However, the analysis of such dynamics is not trivial because we need to match the different solution pieces obtained in separate linear regimes and this matching condition typically necessitates the explicit knowledge of *time-of-flights* (time spent by the flow in a zone of phase space before reaching the switching manifold) in each region. Essentially, we solve the system (3.7) in each of its linear zones using matrix exponentials and demand continuity of solutions to construct orbits of the full nonlinear flow. To clarify how to implement this, we denote a trajectory in zone R_μ by x^μ and solve (3.7) to obtain $x^\mu(t, t_0^\mu) = x(A_\mu, b_\mu; t, t_0^\mu)$ using the solution form

$$x(A, b; t, t_0) = G(A; t - t_0)x(t_0) + K(A; t - t_0)b, \quad (3.11)$$

where t_0 is the initial time, $t > t_0$, and

$$G(A; t) = e^{At}, \quad K(A; t) = \int_0^t G(A; s) ds = A^{-1}[G(A; t) - I_2], \quad (3.12)$$

where I_2 is the 2×2 identity matrix. If A has real eigenvalues λ_{\pm} (obtained from the formula (3.10)) such that $Aq_{\pm} = \lambda_{\pm}q_{\pm}$ with $q_{\pm} \in \mathbb{R}^2$, then $G(A; t)$ may be diagonalised and written in the computationally useful form $G(A; t) = \mathcal{P}e^{\Lambda t}\mathcal{P}^{-1}$, where $\Lambda = \text{diag}(\lambda_+, \lambda_-)$, $\mathcal{P} = [q_+, q_-]$ and $q_{\pm} = [(\lambda_{\pm} - a_{22})/a_{21}, 1]^{\top}$, where a_{ij} denote the entries of A with $i, j = 1, 2$. If A has complex eigenvalues $\lambda_{\pm} = \nu \pm iu$, then the corresponding complex eigenvectors q_{\pm} satisfies $Aq = (\nu \pm iu)q$, $q \in \mathbb{C}^2$. In this case, $G(A; t) = e^{\nu t}\mathcal{P}\mathcal{R}_{ut}\mathcal{P}^{-1}$, where

$$\mathcal{R}_{ut} = \begin{bmatrix} \cos(ut) & -\sin(ut) \\ \sin(ut) & \cos(ut) \end{bmatrix}, \quad P = [\text{Im}(q), \text{Re}(q)] = \begin{bmatrix} 0 & 1 \\ \hat{u} & \hat{\nu} \end{bmatrix}, \quad (3.13)$$

with $\hat{u} = u/a_{12}$ and $\hat{\nu} = (\nu - a_{11})/a_{12}$. We note that ν and u can be written using the invariance of trace and determinant as $\nu = (a_{11} + a_{22})/2$, $u = \sqrt{a_{11}a_{22} - a_{12}a_{21} - \nu^2}$.

Now, a closed orbit can be constructed from connecting two trajectories, starting from an initial data $x(0) = (a, w(0))^{\top}$, which lies on the switching surface, in each region according to

$$x(t) = \begin{cases} x^1(t, 0) & \text{if } t \in [0, T_1] \\ x^2(t, T_1) & \text{if } t \in (T_1, T] \end{cases}, \quad (3.14)$$

for some $T > T_1 > 0$. A periodic orbit can be obtained by requiring that x be T -periodic. Here T_{μ} , where $T_2 = T - T_1$, are the time-of-flights in the respective zones R_{μ} . To complete the procedure we must determine the

unknowns $(T_1, T_2, w^1(0))$ by simultaneously solving a system of three equations

$$a = v^1(T_1), \quad a = v^2(T_2), \quad w^2(T_2) = w^1(0). \quad (3.15)$$

This can be easily done using a numerical method for root finding such as `fsolve` in *Matlab* along with implementing matrix exponentials using `expm`. Alternatively, explicit calculations of $G(A; t)$ and $K(A; t)$ can easily be performed by explicit construction. Following [52], for real λ_{\pm} , entries of the matrix G are obtained as

$$\begin{aligned} G_{11}(t) &= \frac{1}{\lambda_+ - \lambda_-} \left\{ \lambda_+ e^{\lambda_+ t} - \lambda_- e^{\lambda_- t} - a_{22} [e^{\lambda_+ t} - e^{\lambda_- t}] \right\}, \\ G_{12}(t) &= -\frac{\lambda_+ - a_{22}}{\lambda_+ - \lambda_-} \frac{\lambda_- - a_{22}}{a_{21}} [e^{\lambda_+ t} - e^{\lambda_- t}], \\ G_{21}(t) &= \frac{a_{21}}{\lambda_+ - \lambda_-} [e^{\lambda_+ t} - e^{\lambda_- t}], \\ G_{22}(t) &= \frac{1}{\lambda_+ - \lambda_-} \left\{ \lambda_+ e^{\lambda_- t} - \lambda_- e^{\lambda_+ t} + a_{22} [e^{\lambda_+ t} - e^{\lambda_- t}] \right\}, \end{aligned} \quad (3.16)$$

while those of K are

$$\begin{aligned} K_{11}(t) &= \frac{1}{\lambda_+ - \lambda_-} \left\{ e^{\lambda_+ t} - e^{\lambda_- t} - a_{22} \left[\frac{e^{\lambda_+ t} - 1}{\lambda_+} - \frac{e^{\lambda_- t} - 1}{\lambda_-} \right] \right\}, \\ K_{12}(t) &= -\frac{\lambda_+ - a_{22}}{\lambda_+ - \lambda_-} \frac{\lambda_- - a_{22}}{a_{21}} \left[\frac{e^{\lambda_+ t} - 1}{\lambda_+} - \frac{e^{\lambda_- t} - 1}{\lambda_-} \right], \\ K_{21}(t) &= \frac{a_{21}}{\lambda_+ - \lambda_-} \left[\frac{e^{\lambda_+ t} - 1}{\lambda_+} - \frac{e^{\lambda_- t} - 1}{\lambda_-} \right], \\ K_{22}(t) &= \frac{1}{\lambda_+ - \lambda_-} \left\{ \frac{\lambda_+}{\lambda_-} [e^{\lambda_- t} - 1] - \frac{\lambda_-}{\lambda_+} [e^{\lambda_+ t} - 1] + a_{22} \left[\frac{e^{\lambda_+ t} - 1}{\lambda_+} - \frac{e^{\lambda_- t} - 1}{\lambda_-} \right] \right\}. \end{aligned} \quad (3.17)$$

In the case A has complex eigenvalues, these matrices are given by

$$G(t) = \frac{e^{\nu t}}{\hat{u}} \begin{bmatrix} \hat{u} \cos(ut) - \hat{\nu} \sin(ut) & \sin(ut) \\ -(\hat{\nu}^2 + \hat{u}^2) \sin(ut) & \hat{u} \cos(ut) + \hat{\nu} \sin(ut) \end{bmatrix}, \quad (3.18)$$

and

$$K(t) = \frac{1}{\hat{u}} \begin{bmatrix} \hat{u} K_r(t) - \hat{\nu} K_l(t) & K_l(t) \\ -(\hat{\nu}^2 + \hat{u}^2) K_l(t) & \hat{u} K_r(t) + \hat{\nu} K_l(t) \end{bmatrix}, \quad (3.19)$$

where

$$\begin{aligned} K_r(t) &= \frac{1}{\nu^2 + u^2} \{ \nu [e^{\nu t} \cos(ut) - 1] + u e^{\nu t} \sin(ut) \}, \\ K_l(t) &= \frac{1}{\nu^2 + u^2} \{ u [1 - e^{\nu t} \cos(ut)] + \nu e^{\nu t} \sin(ut) \}. \end{aligned} \quad (3.20)$$

Now we shall consider four different PWL models, each of these has oscillatory behaviour. For the first three models we will employ the above analysis to construct periodic orbits with two pieces where each piece lies on a different linear regime that are separated by one switching manifold, but in the final model we tailor this technique to a periodic orbit composed of four pieces over three distinct linear regimes slitted up by two switching manifolds.

3.4 Single neuron behaviour and the FitzHugh-Nagumo model

The excitable properties of neural cells are often analysed by examining their response to the injection of an external current. These responses depend on membrane conductance properties and the reversal potentials of the ions which are involved in generating the electrical response [53]. To better understand the behaviour of biological neural systems, the formulation of analytically tractable models has proven especially useful. The first mathematical description of neural activity given by Hodgkin and Huxley in 1952 [136] used a set of four coupled nonlinear ordinary differential equations. Most modern day description of biologically realistic nerves are based on extensions of the Hodgkin-Huxley (HH) model and have many parameters and nonlinearities. However, even the relatively simple HH model is mathematically intractable, in the sense that it does not admit to any (as yet) closed form solutions [163, 306]. Therefore, it is desirable to build simplified descriptions of neural activity, see for example [1, 101, 116, 209, 212, 253], using lower dimensional differential equations which includes some systematic reduction of the HH model to a planar system.

One can classify the dynamical structure of neural excitability for non-bursting cells as being either Type I or Type II. Type I excitability is obtained

when repetitive action potentials (periodic responses) are generated with an arbitrarily low frequency, whereas in Type II excitability, increasing input current produces repetitive action potentials with a non-zero frequency [163, 306]. Typically, in Type I systems periodic solutions emerge via a saddle-node on invariant circle (SNIC) bifurcation or a homoclinic bifurcation [146] and that of Type II systems arise through a Hopf bifurcation. The HH model has Type II dynamics and it is observed that alternative planar models can be implemented to fit firing rate responses and action potential shape [1]. The governing mathematical description of these planar models are in the form of two coupled nonlinear ordinary differential equations where one variable represents voltage and the other a gating variable. In general, the nullcline for the voltage variable of many excitable systems has a cubic shape [52].

The classical example of the reduced HH model is the FitzHugh-Nagumo model [101, 212] which retains many of the qualitative features of the HH system and has Type II excitability. Although the HH model was originally introduced to describe the squid giant axon, recent work has shown that the FHN model may provide a better qualitative description [50] despite being mathematically less complex. The governing equations for the FHN model are

$$\varepsilon \dot{v} = f(v) - w - w_0 + I, \quad \dot{w} = g(v, w), \quad (3.21)$$

where $f(v) = Cv(v - a)(1 - v)$ and $g(v, w) = v - \gamma w - v_0$. The variable v corresponds to membrane potential while w is associated with the refractory properties of a neural cell. The parameters $C > 0$, $0 < a < 1$, $\varepsilon > 0$, $w_0, v_0 \in \mathbb{R}$, and $\gamma > 0$ may be considered as combinations of the membrane reversal potentials and conductance properties whilst I is any externally injected input [53]. Nullclines of the reduced HH model [1] and FHN model have a common feature such that the v -nullcline ($\dot{v} = 0$) has a cubic shape and the w -nullcline ($\dot{w} = 0$) is a monotonically increasing function of the voltage variable. Moreover, the FHN model can capture slow-fast dynamics of

the Hodgkin–Huxley system for small ε [53, 101, 212]. Figure 3.2 illustrates a periodic orbit of the FHN model as well as the v (cubic shape) and w (linear) nullclines.

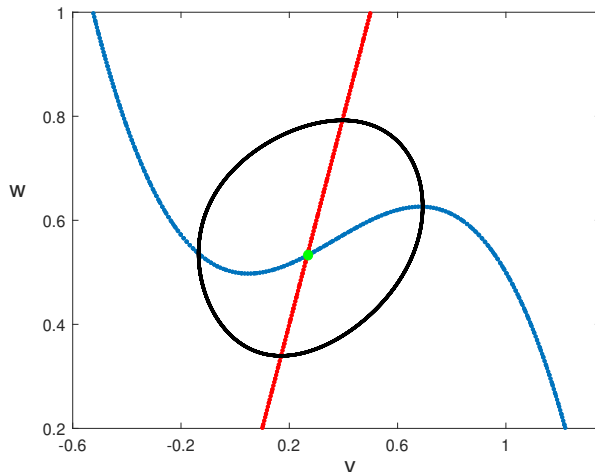


Figure 3.2: Phase plane for the FHN model, showing the v -nullclines (blue) and w -nullclines (red), as well as a periodic orbit (black). Parameters: $\varepsilon = 0.3$, $C = 1$, $w_0 = 0$, $I = 0.5$, $\gamma = 0.5$, $a = 0.1$ and $v_0 = 0$. The intersection of nullclines (crossing point of blue and red curves) gives an unstable equilibrium point. One can think of the cubic shaped v -nullcline composed of three pieces as left, middle, and right branches. It is observed that if the equilibrium point lies on the right (or left) branch of the v -nullcline, it is stable. Changing the parameter I causes the fixed point to pass through the maximum (minimum) value of the cubic curve, where a Hopf bifurcation occurs, giving rise to a stable periodic orbit (black).

Although the FHN model has a lower dimension and complexity than the HH model it is still hard to analyse due to the nonlinear function $f(v)$. This has motivated mathematical neuroscientists to introduce and study some PWL neural models by approximating $f(v)$ with nonsmooth or even discontinuous PWL caricatures. Even though nonlinear smooth planar models may be analysed by using some powerful geometric or numerical techniques [163], use of a PWL framework enables one to derive closed form analytical solutions that allows both qualitative and quantitative analysis of excitable systems.

3.4.1 The McKean model

A well known PWL approximation to the FHN model is the McKean model, introduced by Henry McKean [201]. The governing equations of a single McK-

can neuron model has the form

$$C\dot{v} = \rho(v) - w + I, \quad (3.22)$$

$$\dot{w} = g(v, w), \quad (3.23)$$

where $C > 0$, I is a constant input, and $\rho(v)$ is a PWL version of the cubic FHN nonlinearity $f(v)$ whilst $g(v, w)$ describes the linear behaviour of the gating variable w . There are two popular choices to replace the cubic polynomial $f(v)$. The first choice is substituting $f(v)$ by a PWL function $\rho(v)$ with three pieces. The second choice is a limiting case of the first one, for which the slope of the middle piece goes to infinity, obtained by substituting $f(v)$ with $\rho(v) = -v + \Theta(v - a)$, where Θ is the Heaviside step function ($\Theta(v) = 0, v < 0$ and $\Theta(v) = 1, v > 0$), and has been studied in [252, 254, 305, 306, 315]. Moreover, recently Rotstein, Coombes, and Gheorghe [259] performed a reduction of the FHN system, which is similar to that of McKean, by replacing $f(v)$ with a PWL function composed of four linear pieces, in order to examine an abrupt transition between small and large amplitude oscillations, giving rise to canard type solutions [75, 76].

Following the recently published paper by Coombes and Thul [54], in this section we consider a model of the form (3.22)-(3.23) with $C = 1$, $I = 0$, $\rho(v) = -\gamma v + \xi \Theta(v - a)$, and $g(v, w) = bw$, where γ, ξ and b are constants. This model has been shown [305] to reproduce essential features of the dynamics of the FHN model, including periodic solutions, and can be analysed using a PWL approach. We can write this model in the form (3.7) by substituting $A_1 = A_2 = A$, where

$$A = \begin{bmatrix} -\gamma & -1 \\ b & 0 \end{bmatrix}, \quad b_1 = \begin{bmatrix} \xi \\ 0 \end{bmatrix}, \quad b_2 = \begin{bmatrix} 0 \\ 0 \end{bmatrix}. \quad (3.24)$$

The vector field of the model is not defined on the switching manifold $\Sigma_1 = \{x \in \mathbb{R}^2 \mid h(x) = 0\}$, where $h(x) = v - a$. Using the Filippov convex method

[100], summarised in Section 3.2, we introduce a set-valued extension

$$\dot{x} \in f(x) = \begin{cases} f_1(x) & x \in R_1, \\ \overline{\text{co}}(\{f_1(x), f_2(x)\}) & x \in \Sigma_1, \\ f_2(x) & x \in R_2, \end{cases} \quad (3.25)$$

where

$$f_1 = \begin{bmatrix} -\gamma v - w + \xi \\ bv \end{bmatrix} \quad \text{and} \quad f_2 = \begin{bmatrix} -\gamma v - w \\ bv \end{bmatrix}, \quad (3.26)$$

such that $\mathbb{R}^2 = R_1 \cup \Sigma_1 \cup R_2$ and in this particular case,

$$\overline{\text{co}}(\{f_1(x), f_2(x)\}) = \{\zeta f_1 + (1 - \zeta)f_2, \quad \forall \zeta \in [0, 1]\}. \quad (3.27)$$

This system may have sliding motion along a switching manifold Σ_1 such that $\dot{h} = \nabla h \cdot f = 0$ where $\nabla h = (1, 0)$. Then we can construct ζ as

$$\zeta = \frac{\nabla h \cdot f_2}{\nabla h \cdot (f_2 - f_1)} = \frac{\gamma a + w}{\xi} \equiv \zeta(w), \quad (3.28)$$

where $w \in [-\gamma a, -\gamma a + \xi]$. The sliding motion along $v = a$ is governed by the vector field $f_s = \zeta(w)f_1 + (1 - \zeta(w))f_2$. This gives rise to

$$f_s = \begin{bmatrix} 0 \\ bv \end{bmatrix}, \quad (3.29)$$

so that only w varies during sliding (along $v = a$) on Σ_1 .

The equilibrium point, which occurs at $(v, w) = (0, 0)$, of the system lies in the region R_2 for $a > 0$. Using the formula (3.10), we can calculate the eigenvalues $\lambda_{\pm} = (-\gamma \pm \sqrt{\gamma^2 - 4b})/2$. This equilibrium point is stable for $b, \gamma > 0$, and globally attracting when $\gamma^2 - 4b > 0$. It is a focus for $\gamma^2 - 4b < 0$, and there is a possibility that a periodic solution may arise in this case. For a more detailed phase plane analysis and existence of periodic orbits (both sliding and transversal) we refer the reader to [54].

We observe that for some suitable parameter values, a stable periodic orbit may co-exist with the stable equilibrium point (attracting focus), separated by an unstable sliding periodic orbit. In the following Fig. 3.3, we illustrate this. Both periodic orbits are constructed using the technique described in Section 3.3. Since this model exhibits a co-existing stable and unstable periodic

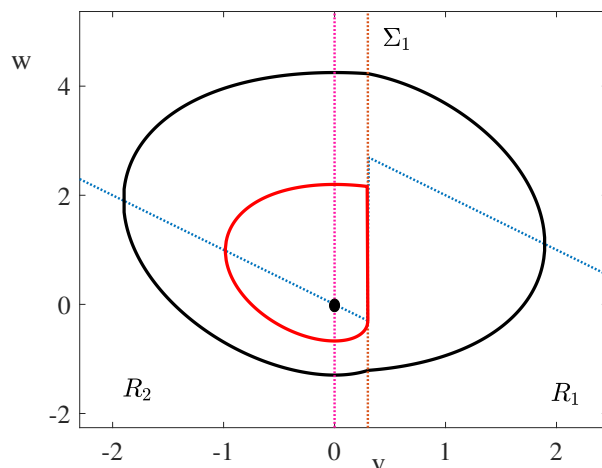


Figure 3.3: Periodic solutions of the McKean model. v -nullcline (blue-dotted line) and w -nullcline (purple-dotted line) and switching manifold Σ_1 (brown-dotted line). R_1 (R_2) represent the region where $v > a$ ($v < a$). A transversal stable periodic orbit given in black and an unstable sliding periodic orbit given in red. The stable equilibrium point (focus type) $(0,0)$ lies on the region R_2 indicated as a black filled circle. Parameters: $a = 0.3$, $b = 2$, $\gamma = 1$, $\xi = 3$.

solution (see Fig. 3.3), it is natural to expect a saddle node bifurcation of limit cycles (fold limit cycle bifurcation) under parameter variation. We illustrate this by constructing a bifurcation diagram in Fig. 3.4. If parameters a and b are chosen in the region S , then stable and unstable periodic orbits co-exists. These collide and annihilate each other when a and b are on the curve C_b . Tonnelier [305] has performed a more detailed bifurcation analysis for this model and proposed an alternative method (the harmonic balance method) to build periodic orbits. They obtained similar results as in Fig. 3.4 though they only managed to treat the stability of periodic orbits numerically. Here we have analysed the stability of periodic orbits analytically using the method that will be presented in Section 4.2 and used this to construct the bifurcation diagram in Fig. 3.4.

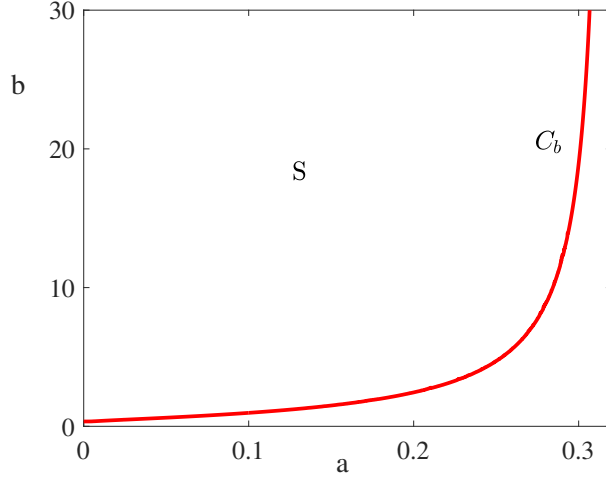


Figure 3.4: Bifurcation diagram of the McKean model in the plane (a, b) . In the region S a stable periodic orbit co-exists with an unstable periodic orbit. On the curve C_b solutions meet and annihilate via a saddle-node bifurcation of limit cycles. Parameters: $\gamma = 1$ and $\xi = 1$.

3.4.2 The absolute model

Similarly to the McKean model, the absolute model [54] has PWL dynamics but in this case the vector field changes continuously during the switching boundary crossing. The model has the form

$$\dot{v} = |v - a| - w, \quad (3.30)$$

$$\dot{w} = v - \bar{v} - d(w - \bar{w}), \quad (3.31)$$

where $|\cdot|$ is the absolute value function and the constants a, d, \bar{w}, \bar{v} satisfy the constraints $a \geq 0$, $0 < d < 1$, and $\bar{w} + (a - \bar{v})/d < 0$. This system may be transformed into to the form (3.7) with

$$A_1 = \begin{bmatrix} 1 & -1 \\ 1 & -d \end{bmatrix}, \quad A_2 = \begin{bmatrix} -1 & -1 \\ 1 & -d \end{bmatrix}, \quad (3.32)$$

and,

$$b_1 = \begin{bmatrix} -a \\ d\bar{w} - \bar{v} \end{bmatrix}, \quad b_2 = \begin{bmatrix} a \\ d\bar{w} - \bar{v} \end{bmatrix}. \quad (3.33)$$

We can easily calculate equilibrium point(s) by simultaneously solving the equation for the nullclines. In the region R_2 (where $v < a$), the equilibrium point is at $(v, w) = (da + \bar{v} - d\bar{w}, a - \bar{v} + d\bar{w})/(d + 1)$. The stability of this can be determined from the eigenvalues of A_2 :

$$\lambda_{\pm}(A_2) = \frac{-(1 + d) \pm i\sqrt{4 - (1 - d)^2}}{2}. \quad (3.34)$$

Thus, in R_2 , the equilibrium point is a stable focus. Nevertheless, in R_1 (where $v > a$), the equilibrium point is at $(v, w) = (d\bar{w} - \bar{v} + da, d\bar{w} - \bar{v} + a)/(d - 1)$ and stability is determined by the eigenvalues of A_1 :

$$\lambda_{\pm}(A_1) = \frac{1 - d \pm i\sqrt{4 - (1 + d)^2}}{2}. \quad (3.35)$$

This implies, in R_1 , the equilibrium point is an unstable focus. This observation indicates that the absolute model can exhibit a nonsmooth Andronov-Hopf bifurcation [152, 281, 282], that occurs when an equilibrium crosses a discontinuity surface. For the absolute model this happens when the equilibrium point shifts from R_1 to R_2 and the eigenvalues of the Jacobian jump across the imaginary axis. In Fig. 3.5 we illustrate a stable periodic orbit (arising through a nonsmooth Andronov-Hopf bifurcation) along with v and w nullclines. By changing the value of \bar{w} we move the equilibrium point (shown in Fig. 3.5 as a black dot) through the switching manifold. As \bar{w} is varied the period remains constant and the amplitude scales linearly. A short proof of this (perhaps counter-intuitive result) is given in Appendix B. We illustrate this result in Fig. 3.6, using direct numerical construction (confirming the theory).

3.4.3 A model with a homoclinic loop

As a last model of a planar PWL system with a single switching manifold ($h(x) = v - a$, with $a = 0$), we consider a system with a saddle point for $x \in R_2$ and an unstable focus for $x \in R_1$, with a vector field that crosses the

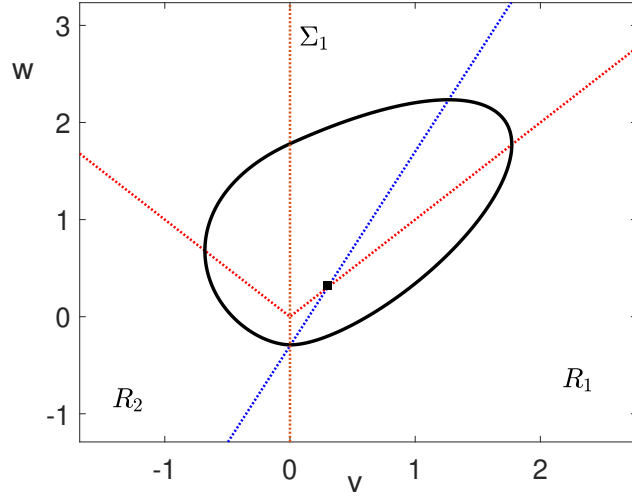


Figure 3.5: A stable periodic solution of the absolute model given in black. v -nullcline (red-dotted line) and w -nullcline (blue-dotted line) and switching manifold Σ_1 (brown-dotted line). R_1 (R_2) represent the region where $v > a$ ($v < a$). The unstable equilibrium point is in the zone R_1 and indicated as a filled circle. Parameters: $a = 0$, $\bar{w} = -0.1$, $\bar{v} = 0.1$, and $d = 0.5$.

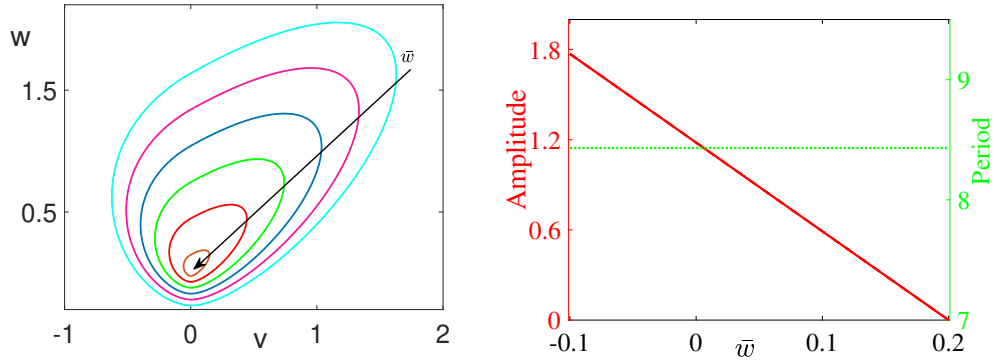


Figure 3.6: The absolute model. Left: Shape of the stable periodic orbits for $\bar{w} = -0.076, -0.026, 0.024, 0.075, 0.12, 0.17$. Right: Amplitude (period) of solution as a function \bar{w} colour in red (green). The period of oscillation remains constant and the amplitude changes linearly when $-0.1 < \bar{w} < 0.2$. The equilibrium point crosses the switching manifold when $\bar{w} \simeq 0.2$ where the periodic solution is lost. For $\bar{w} > 0.2$ the system only supports a stable equilibrium point in the left zone. Other parameters are as in Fig. 3.5.

switching boundary continuously. In this scenario, we may build a homoclinic orbit which tangentially touches the unstable and stable eigen-directions of the saddle point in R_2 , and is also able to enclose the unstable focus in R_1 . This model was first considered by Xu *et al.* [335] and then revisited in [54]. We consider a system in the form (3.7) whose dynamics has the form

$$A_1 = \begin{bmatrix} \tau_1 & -1 \\ \delta_1 & 0 \end{bmatrix}, \quad A_2 = \begin{bmatrix} \tau_2 & -1 \\ \delta_2 & 0 \end{bmatrix}, \quad b_1 = \begin{bmatrix} 0 \\ -1 \end{bmatrix} = b_2. \quad (3.36)$$

We observe that $\text{Tr } A_\mu = \tau_\mu$ and $\det A_\mu = \delta_\mu$ for $\mu \in \{1, 2\}$. Xu *et al.* [335] define a homoclinic orbit as degenerate if its limit equilibrium (corresponding to the saddle point) lies on the switching manifold; otherwise, it is nondegenerate. By following this paper (Theorem 13, p.17), let us denote $\lambda_\pm(A_2) = \lambda_\pm$ and $\lambda_\pm(A_1) = \bar{\alpha} \pm i\bar{\beta}$ with $\lambda_+ > 0 > \lambda_-$ and $\bar{\beta} > 0$, and write

$$\begin{aligned} \mathcal{A} = & \frac{1}{2} \ln \frac{\lambda_-^2 (\lambda_+^2 - 2\bar{\alpha}\lambda_+\bar{\alpha}^2 + \bar{\beta}^2)}{\lambda_+^2 (\lambda_-^2 - 2\bar{\alpha}\lambda_-\bar{\alpha}^2 + \bar{\beta}^2)} \\ & - \frac{\bar{\alpha}}{\bar{\beta}} \left(2\pi - \arctan \frac{\lambda_-\bar{\alpha} - (\bar{\alpha}^2 + \bar{\beta}^2)}{\lambda_-\bar{\beta}} - \arctan \frac{\bar{\alpha}^2 + \bar{\beta}^2 - \lambda_+\bar{\alpha}}{\lambda_+\bar{\beta}} \right), \end{aligned} \quad (3.37)$$

then a non-degenerate homoclinic orbit exists if and only if $\mathcal{A} = 0$. Furthermore, the existence of a limit cycle or a homoclinic orbit necessitates $\tau_1\tau_2 \leq 0$, see (Proposition 10, p.4), [335]. We illustrate an example of a periodic orbit near the homoclinic loop in Fig. 3.7 along with v and w nullclines. As the systems parameters move closer to the homoclinic case, the variation of period and amplitude of the periodic solutions are plotted in Fig. 3.8. We can also build a homoclinic loop when the system has a saddle point in R_2 and a centre ($\bar{\alpha} = 0$) in R_1 . In the later case, if we choose $\text{Tr } A_1 = 0 = \tau_1$, $\text{Tr } A_2 = 0 = \tau_2$, $\det A_1 = 1 = \delta_1$, and $\det A_2 = -1 = \delta_2$ then we find $\lambda_\pm = \pm 1$, $\bar{\alpha} = 0$ and $\bar{\beta} = 1$. Putting these values in (3.37) gives $\mathcal{A} = 0$. For this specific parameter set we also observe (numerically) that an infinite number of periodic orbits live inside the homoclinic orbit around a center.

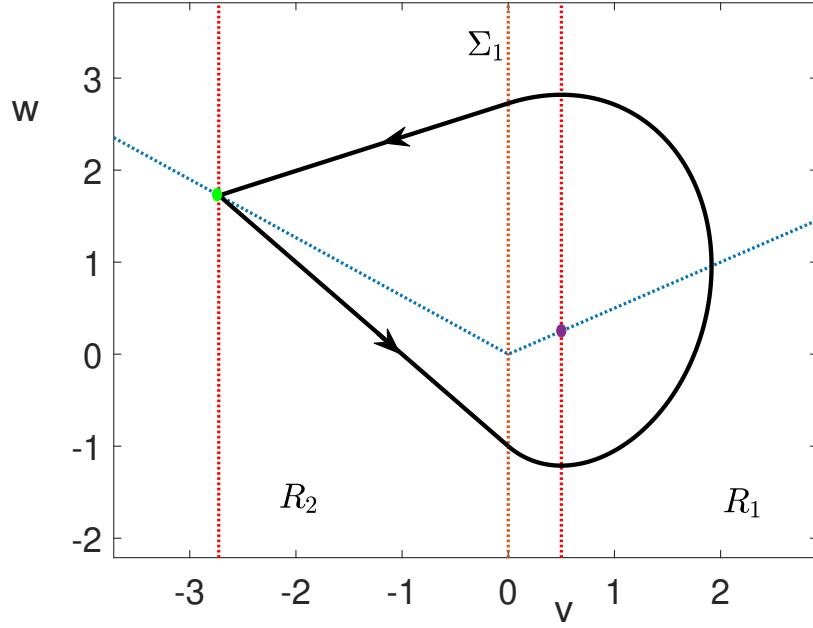


Figure 3.7: A stable periodic solution of the homoclinic model (near to a homoclinic bifurcation) is given in black. v -nullcline (blue-dotted line) and w -nullcline (red-dotted lines) and switching manifold Σ_1 (brown-dotted line). R_1 (R_2) represent the region where $v > a$ ($v < a$). The repelling focus (saddle point) is in the region R_1 (R_2) and indicated as a purple (green) filled circle. Parameters: $a = 0$, $\delta_1 = 2$, $\delta_2 = -0.3667$, $\tau_1 = 0.5$, $\tau_2 = -0.6333$.

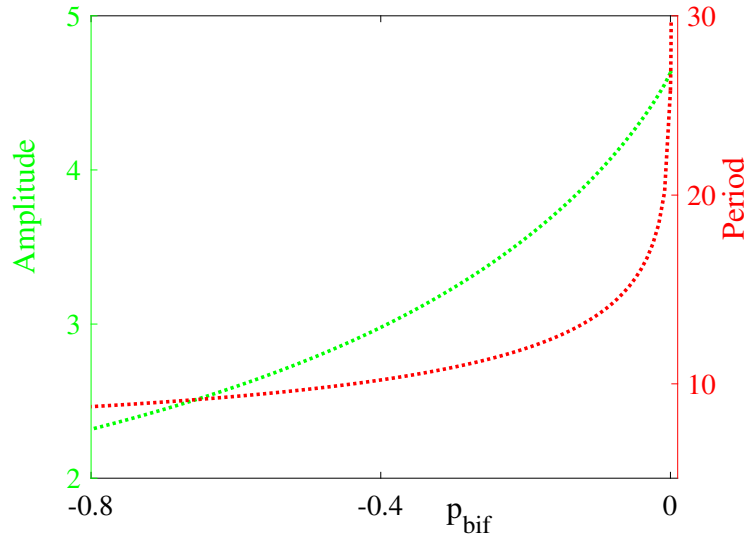


Figure 3.8: Period (red) and amplitude (green) of stable periodic orbits of the homoclinic model. The amplitude of the orbits approach that of the homoclinic loop, with increasing period. The entries of A_1 are $a_1^{11} = \tau_1 - p_{bif}/4$, $a_1^{12} = -1$, $a_1^{21} = \delta_1 - p_{bif}$, $a_1^{22} = 0$, and that of A_2 are $a_2^{11} = \tau_2 + p_{bif}$, $a_2^{12} = -1$, $a_2^{21} = \delta_2 + p_{bif}/2$, $a_2^{22} = 0$, and $-0.8 < p_{bif} < 0.00097$. Other parameters as in Fig. 3.7

3.4.4 Piecewise Linear Morris–Lecar model

Another well-studied biological neuron model for the production of action potentials is the Morris-Lecar model. Originally, in 1981 Cathy Morris and Harold Lecar designed this model to analyse the electrical activity in barnacle muscle fibres [209]. The proposed model is a two dimensional nonlinear conductance-based model, build on a reduced Hodgkin-Huxley formalism, however it still captures many important features of neuronal activity. The equations for the ML model have the form

$$C \frac{dv}{dt} = g_{Ca} M_{\infty}(v) (v_{Ca} - v) + g_L (v_L - v) + g_K w (v_K - v) + I, \quad (3.38)$$

$$\frac{dw}{dt} = \lambda(v) (w_{\infty}(v) - w), \quad (3.39)$$

where

$$M_{\infty}(v) = \frac{1}{2} [1 + \tanh((v - v_1)/v_2)], \quad (3.40)$$

$$w_{\infty}(v) = \frac{1}{2} [1 + \tanh((v - v_3)/v_4)], \quad (3.41)$$

$$\lambda(v) = \bar{\phi} \cosh((v - v_3)/(2v_4)). \quad (3.42)$$

Here, C is the membrane capacitance, v is the membrane potential, and I is the externally applied current (assumed to be constant). The parameters v_{Ca} , v_L , and v_K represent equilibrium potentials of calcium, leak current, and potassium, respectively, and g_{Ca} , g_L , and g_K denote the peak conductances of corresponding ionic currents. The variable w (recovery variable) captures the dynamics of the gating variables for both calcium and potassium, with M_{∞} and w_{∞} denoting voltage dependent gating functions and $\lambda(v)$ a voltage dependent rate. v_i , where $i = 1, \dots, 4$, are constant parameters that are chosen to fit voltage clamp data, and $\bar{\phi}$ is a constant (significantly depends on temperature of the cell).

Although the FHN model displays only Type II excitability, for suitable parameter values the ML model can exhibit both Type I and Type II be-

haviour, and Zhao and Gu have explored transitions between two classes in [344]. The ML model can support Hopf bifurcations, homoclinic bifurcations, and SNIC bifurcations, and for a more detailed bifurcation analysis we refer the reader to [96, 308]. Nevertheless, a lot of cortical neurons in mammals, for example pyramidal cells, are considered to have Type I excitability. Due to its rich dynamics the ML model is believed to be more realistic than the FHN model and has a widespread use in neurodynamics [163, 306]. We illustrate two different periodic orbits of the ML model in the Fig. 3.9, along with nullclines and fixed points. As the external input I decreases, the amplitude and period of periodic orbits grow and the orbit approaches the saddle point (magenta filled circle), leading to a homoclinic bifurcation where the orbit and saddle point collide.

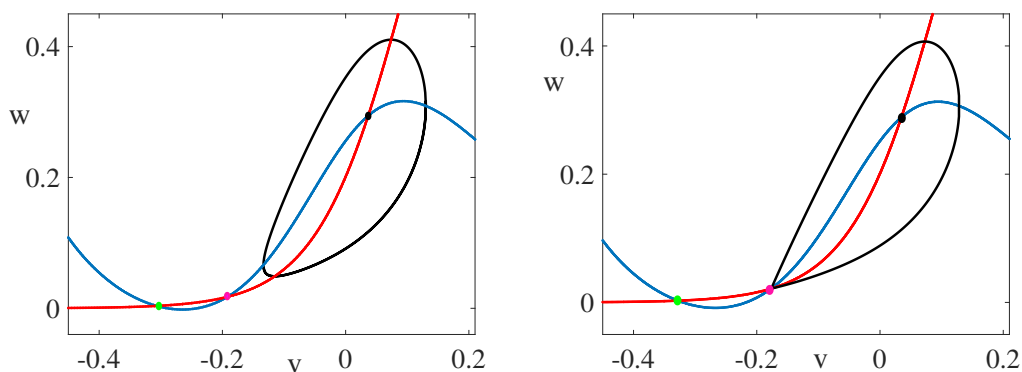


Figure 3.9: Phase plane of the Morris-Lecar model with stable periodic orbits in black. The voltage variable (v) nullcline is illustrated in blue and that of the gating variable (w) in red. The filled black circle shows an unstable fixed point, the filled magenta circle is a saddle point and the filled green circle is a stable fixed point. Parameters: $C = 4.92$, $g_L = 0.5$, $v_L = -0.5$, $g_K = 2$, $v_K = -0.7$, $g_{Ca} = 1$, $v_{Ca} = 1$, $v_1 = -0.01$, $v_2 = 0.15$, $v_3 = 0.1$, $v_4 = 0.145$ and $\bar{\phi} = 0.241$. Left: For $I = 0.075$ we obtain a periodic orbit away from saddle point with period $T \simeq 27.75$. Right: We decrease the value of I to 0.0692 and the orbit moves closer to saddle point while the amplitude and period increase.

Tonnelier and Gerstner [306] introduced a PWL reduction of the ML model to explore both qualitative description and quantitative analysis of Type I excitable systems in a simplified framework. Following this, Coombes [52] proposed another PWL caricature to this by using the model equations (3.22)-(3.23) with a continuous $\rho(v)$ (to approximate the cubic shape v -nullcline) in

the form

$$\rho(v) = \begin{cases} -v & \text{if } v < a/2, \\ v - a & \text{if } a/2 \leq v \leq (1+a)/2, \\ 1 - v & \text{if } v > (1+a)/2, \end{cases} \quad (3.43)$$

and a continuous choice of $g(v, w)$ (to approximate the quadratic shape w -nullcline) as

$$g(v, w) = \begin{cases} (v - \gamma_1 w + b^* \gamma_1 - b)/\gamma_1 & \text{if } v < b, \\ (v - \gamma_2 w + b^* \gamma_2 - b)/\gamma_2 & \text{if } v \geq b, \end{cases} \quad (3.44)$$

with the constraints $-a/2 < b^* < (1-a)/2$, $a/2 < b < (1+a)/2$, $\gamma_2 > 0$, and $\gamma_1 \in \mathbb{R}$. The ML model can also be caricatured by other natural choices such as choosing a discontinuous vector field for the gating variable w such as $g(v, w) = v - \gamma w + \Theta(v - b)$, which has been investigated in [306]. In Fig. 3.10, a stable periodic orbit is shown along with nullclines and fixed points for the PWL model defined by (3.22), (3.23), (3.43) and (3.44).

In order to construct periodic solutions, such as in Fig. 3.10, we used the formalism presented in Section 3.3. We break the periodic orbit into pieces such that each piece is governed by a linear equation. This is similar to the system (3.7), but this time, the orbit has four distinct pieces, labelled by $\mu = 1, 2, 3, 4$, over three linear regimes and transversally crosses two switching manifolds. Explicitly, we have

$$\frac{dx}{dt} = \begin{cases} A_1 x + b_1 & \text{if } x \in R_2, \\ A_2 x + b_2 & \text{if } x \in R_1, \\ A_3 x + b_3 & \text{if } x \in R_2, \\ A_4 x + b_4 & \text{if } x \in R_3, \end{cases} \quad (3.45)$$

where $R_1 = \{x \in \mathbb{R}^2 \mid v > (1+a)/2\}$, $R_2 = \{x \in \mathbb{R}^2 \mid b < v < (1+a)/2\}$ and

$R_3 = \{x \in \mathbb{R}^2 \mid a/2 < v < b\}$, and therefore

$$A_1 = \begin{bmatrix} 1/C & -1/C \\ 1/\gamma_2 & -1 \end{bmatrix}, \quad A_2 = \begin{bmatrix} -1/C & -1/C \\ 1/\gamma_2 & -1 \end{bmatrix}, \quad A_4 = \begin{bmatrix} 1/C & -1/C \\ 1/\gamma_1 & -1 \end{bmatrix}, \quad (3.46)$$

while

$$b_1 = \begin{bmatrix} (I - a)/C \\ b^* - b/\gamma_2 \end{bmatrix}, \quad b_2 = \begin{bmatrix} (1 + I)/C \\ b^* - b/\gamma_2 \end{bmatrix}, \quad b_4 = \begin{bmatrix} (I - a)/C \\ b^* - b/\gamma_1 \end{bmatrix}, \quad (3.47)$$

$A_3 = A_1$ and $b_3 = b_1$. The time-of-flight spent during each piece is denoted by T_μ , and the period of the orbit is $T = \sum_{\mu=1}^4 T_\mu$. To build a closed orbit we use boundary crossing values of the voltage variable ($v = b$ and $v = (1 + a)/2$), equation (3.11), and simply demand periodicity of the solution. Choosing initial data $x^1(0) = (b, w^1(0))^\top$ and enforcing continuity of solutions by using the matching conditions $x^{\mu+1}(0) = x^\mu(T_\mu)$ for $\mu = 1, 2, 3$, determines T_μ and $w(0)$ by the simultaneous solution of

$$\begin{aligned} v^1(T_1) &= \frac{1+a}{2}, \\ v^2(T_2) &= \frac{1+a}{2}, \\ v^3(T_3) &= b, \\ v^4(T_4) &= b, \\ w^1(0) &= w^4(T_4). \end{aligned} \quad (3.48)$$

In Fig. 3.11, we illustrate the shape, amplitude and period of the orbit by varying the external input I . Similar to the nonlinear case, the creation of low frequency oscillations is linked with homoclinic bifurcation. We observed that the amplitude and period of the periodic solution increases while I is decreasing, and the orbit collides with a saddle point. Other types of periodic orbits may be obtained, for example those that cross only $v = (1 + a)/2$ (built in the regions R_1 and R_2) or $v = b$ (built in the regions R_2 and R_3), or one that does not cross any of the switching manifolds. Euzebio and co-

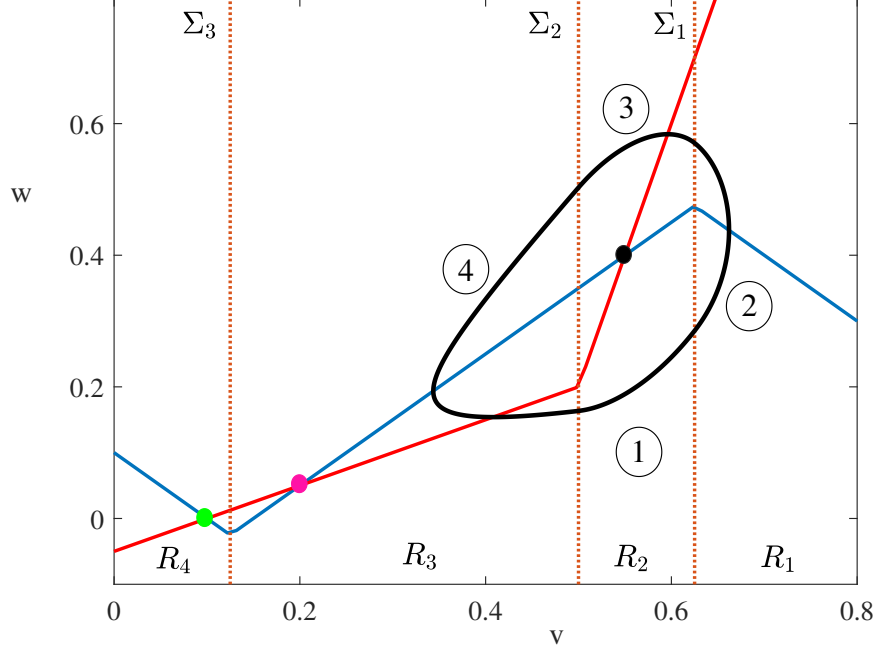


Figure 3.10: Phase plane of the piecewise linear Morris–Lecar model with a stable periodic orbit in black. Parameters [52]: $C = 0.825$, $I = 0.1$, $a = 0.25$, $b = 0.5$, $b^* = 0.2$, $\gamma_1 = 2$, and $\gamma_2 = 0.25$. The periodic orbit is composed of four pieces, where the first and third pieces are on R_2 , the second piece on R_1 , and the fourth piece on R_3 . v -nullcline (blue line) and w -nullcline (red line) and switching manifolds Σ_1 , Σ_2 , Σ_3 (brown-dotted lines). The nullclines are a piecewise approximation to the that of nonlinear model given in Fig. 3.9. The filled black circle shows an unstable fixed point, the filled magenta circle is a saddle point and the filled green circle is a stable fixed point (on region $R_4 = \{x \in \mathbb{R}^2 \mid v < a/2\}$).

workers [97] investigated bifurcations of piecewise linear differential systems with three zones with a particular focus on the PML model. They proposed some theorems to detect bifurcation of limit cycles for the PML model and introduced the concept of scabbard bifurcation which is linked with the shape of the bifurcating limit cycles. A scabbard bifurcation occurs when a limit cycle is born out of a continuum of equilibrium points.

3.5 Discussion

Although dynamical systems theory is well developed for smooth systems, it still needs further investigation for nonsmooth systems such as piecewise smooth and piecewise linear systems. These systems may arise in modelling of

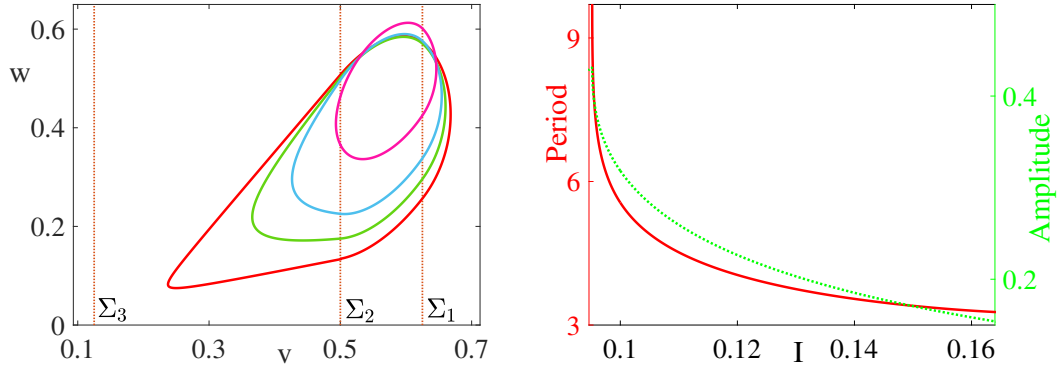


Figure 3.11: Piecewise linear Morris–Lecar model. Left: Shape of the stable periodic orbits for $I = 0.0945$ (red), $I = 0.0997$ (green), $I = 0.1031$ (aqua), and $I = 0.165$ (magenta). Right: Period (left axis in red) and amplitude (right axis in green) of solutions as a function of I , where I ranges from 0.1645 to 0.094. Other parameters as in Fig 3.10.

many important real world problems and are also utilised for phenomenological models in many different areas of applied sciences including engineering and biology. In addition to exhibiting almost all types of dynamics observed in smooth nonlinear systems, e.g. periodic solutions, limit cycles, heteroclinic and homoclinic orbits, and strange attractors, these systems may support bifurcations that smooth systems do not [81, 82].

Limit cycle oscillators with PWL dynamics are extensively studied in nonsmooth dynamical systems theory with a large number of applications in physics, engineering and biology, such as anti-lock braking systems [210], the PWL Hindmarsh–Rose model [26], gene regulatory networks [119], and some planar neuron models [52]. In general, for smooth nonlinear dynamical systems, this solution is not available in closed form whereas in the PWL case we can construct this quasi-analytically rather than relying on numerical evaluation. Bifurcation of oscillatory solutions for such nonsmooth systems have been studied by many researchers [51, 194, 279].

In a mathematical neuroscience context, PWL neural modelling is important and has a long history of use for understanding and investigating many interesting dynamical behaviours [55, 217]. Essentially, nonsmooth PWL models can be considered as the uniform limit of smooth nonlinearities and the global

dynamical behaviours of smooth models can be approximated by PWL models and vice-versa. PWL modelling allows to build explicit solutions of neuron models and this make further analysis easier. For example, here we have shown how to construct periodic solutions of the McKean model and the PML model, and explored how the period and amplitude of such solutions varies. Making use of a PWL modelling approach is not only practical to establish periodic solutions in closed form but also helps to construct response functions and understand the collective behaviour of coupled oscillatory systems which will be studied in later chapters.

Chapter 4

Stability and response of periodic orbits in PWL systems

4.1 Introduction

The adaptation or extension of results from smooth dynamical systems theory to nonsmooth systems is an appealing research area, and recently existence, uniqueness, stability, bifurcations, maximal number of limit cycles, and adaptation of Lyapunov functions for PWL systems has been studied by many authors, see for instance [40, 109, 110, 138, 182, 185, 187, 193, 345]. Here we modify standard Floquet theory [157, 161] to treat PWL systems [54, 81] for periodic solutions that are exposed to N switching events. This is achieved using the notion of saltation matrices that we build at each time of event. A saltation operator maps perturbations to the periodic orbits immediately before the switching event to immediately after, and have commonly been used for the study of nonsmooth systems [15, 180]. During the computation of Floquet exponents, the use of saltation matrices introduces a correction term (for example, see equation 4.9) to the Floquet exponent formula for determining stability.

Phase reduction theory is well developed for stable limit cycles of smooth dynamical systems and has been conveniently applied to many biological,

chemical and physical systems, particularly when exploring synchronisation, and entrainment phenomena [86, 96, 137, 332] and see Sections 2.2, 2.4. However, the application of this theory to nonsmooth dynamical systems is not trivial. The main reason for this is that the nonsmoothness of the vector fields at the switching boundaries impedes direct implementation of the adjoint equation (2.7) and further consideration is needed to compute discontinuities in the iPRC.

There are a few recent studies that have focused on this problem. For one dimensional systems, the phase normalisation condition is enough to derive the size of jump in the iPRC which relates the iPRC immediately before and after a switching event, but as the dimension of the system increases this problem becomes far more complicated, i.e. for n dimensional systems, n linearly independent equations are required to compute the iPRC uniquely. In [55], Coombes *et al.* derived the discontinuous iPRC for the planar PWL integrate-and-fire model by utilising normalisation conditions on both sides of a switching surface. In [52], Coombes also computed the iPRC for the PWL planar neuron models where the vector field changes continuously across the switching manifold (the vector field has the same value immediately before the switching event, on the switching manifold, and immediately after the switching event). For PWS systems, Park *et al.* [227], developed a jump operator for the iPRC by using the normalisation condition and equality of directional derivatives of the phase function in directions assigned by the vectors which span the tangential surface to the switching manifold at the point where the limit cycle and switching manifold intersect. They also found a relation between the saltation matrix for the variational equation and the jump operator of the iPRC. Using a similar method, Chartrand *et al.* [46] constructed the discontinuous iPRC for the resonate-and-fire model. In 2017, Shirasaka and co-workers [276], adapted phase reduction theory to hybrid dynamical systems (dynamical systems that contain both continuous and discrete state variables [5]) after rigorously defining an asymptotic phase function for such systems in

a suitable topology. They developed a jump operator to compute the size of discontinuity in the iPRC and deduced that this operator is the same as the inverse transpose of the saltation matrix. A special case of such systems was also considered by Ladenbauer *et al.* [173] where a discontinuous iPRC was built up for the exponential integrate-and-fire model. Ermentrout *et al.* [92] have computed iPRC of the Izhikevich neuron model by numerically solving the adjoint equation together with implementing the inverse transpose of a saltation matrix to construct the jump operator for the iPRC at the discontinuity boundary. Moreover, Wang *et al.* [317] produced the iPRC for some ad-hoc planar nonsmooth systems for a limit cycle with sliding dynamics by formulating a modified saltation matrix and then establishing relations between this matrix and the jump operator for the iPRC at the landing point where a sliding motion starts, and the liftoff point where the sliding terminates.

To overcome limitations of phase only reduction methods, for smooth systems, various analytical, computational and geometric techniques are proposed [131, 181, 275, 277, 297, 299, 319], including the phase-amplitude reduction theory [325, 328] reviewed in Section 2.3. Recently, Wilson [320] extended this phase-amplitude reduction formalism to treat PWS dynamical systems. Wilson also applied this theory to a nonsmooth model of cardiac myocytes to derive a discontinuous iPRC, iIRC, and second-order correction terms. In this recent approach, the theory simplifies in the case of PWL modelling, therefore in this thesis we used this reduction method. Moreover, we know that utilising caricature systems (a PWL or discontinuous model) instead of nonlinear models is found to be beneficial at the node level [177] and see Section 3.4, it has been shown that this is advantageous at network level as well [54, 174, 175, 217]. Therefore, in this chapter we will address the stability of the synchronous state in networks of PWL oscillators using coupled phase oscillator theory, the phase-amplitude network formalism, and the MSF methodology, in each case showing how to treat PWL systems. Each of the three are compared to numerical results and to each other.

The organisation of the chapter is as follows. In Section 4.2, by modifying Floquet theory, we show how to determine the stability of periodic orbits for planar PWL systems. In Section 4.3 and Section 4.4 we investigate the jump condition in the iPRC and iIRC using different approaches, and explicitly compute these for the models considered. In Section 4.5, we derive the general form for the second-order terms (necessary for the phase-amplitude reduction), \mathcal{B}, \mathcal{C} , for PWL systems along with an explicit calculation of them for the models considered. In Section 4.6, we show how to determine the stability of a synchronous network state. In Section 4.7, we test the stability of the synchronous state of the considered models by using all three methods, and then comparing these against numerical simulations to check the accuracy of the predicted results. Finally, in Section 4.8, we give a discussion highlighting the power of the PWL approach for circumventing the limitation of phase and phase-amplitude reductions.

4.2 Stability: Adaptation of Floquet theory

For smooth dynamical systems

$$\dot{x} = f(x), \tag{4.1}$$

where $x \in \mathbb{R}^n$, $f(x)$ is a continuously differentiable function, Floquet theory [235] is a popular and well-developed technique to study stability and bifurcations of periodic orbits. Let us denote Floquet multipliers and Floquet exponents of a periodic orbit $x^\gamma(t)$ with period T , by λ_i and κ_i , respectively, $i = 1, \dots, n$, where $\lambda_i = e^{\kappa_i T}$ holds. By following Perko [235], we revisit the useful result

$$\prod_{i=1}^n \lambda_i = \exp \left[\int_0^T \text{Tr}(Df(x^\gamma(t))) dt \right], \tag{4.2}$$

where $Df(x^\gamma(t))$ is the Jacobian of f evaluated along $x^\gamma(t)$. Essentially, he derives this result by using Liouville's theorem [235], which formulates the

determinant of the fundamental matrix (Wronskian) for a linearised system of the form $\dot{y} = Df(x^\gamma(t))y$.

For a planar system, with $x \in \mathbb{R}^2$, we can use this result and the fact that one of the Floquet multiplier is equal to one, which corresponds to perturbations along the periodic orbit, and show that the non-trivial Floquet exponent (κ_{smooth}) is

$$\kappa_{\text{smooth}} = \frac{1}{T} \int_0^T \nabla \cdot f(x^\gamma(t)) dt = \frac{1}{T} \int_0^T \text{Tr}(Df(x^\gamma(t))) dt. \quad (4.3)$$

The stability of periodic orbits can be determined from the sign of κ_{smooth} such that an orbit is stable if $\kappa_{\text{smooth}} < 0$ and unstable if $\kappa_{\text{smooth}} > 0$, see [235] for more details.

For dynamical systems with nonsmooth or even discontinuous vector fields, we can not directly make use of standard Floquet theory [157, 161]. Moreover, we must carefully study the effect of perturbing a periodic orbit in location where it crosses the switching boundaries. Here, we revisit the adaptation of standard theory to PWL systems [54, 81] of the form

$$\frac{dx}{dt} = \begin{cases} f_1(x) \equiv A_1x + b_1 & \text{if } x \in R_1, \\ f_2(x) \equiv A_2x + b_2 & \text{if } x \in R_2, \\ \vdots \\ f_N(x) \equiv A_Nx + b_N & \text{if } x \in R_N, \end{cases} \quad (4.4)$$

where $A_\mu \in \mathbb{R}^{n \times n}$, $b_\mu \in \mathbb{R}^n$, $\mu \in \{1, \dots, N\}$, and support a non sliding periodic orbit $x^\gamma(t)$ with N -pieces where each piece $x^{\gamma\mu}(t)$ is obtained by solving a linear dynamics over the region R_μ . Switching events are prescribed by some indicator functions $h_\mu(x)$, that occur when $h_\mu(x(t_\mu)) = 0$, at switching times t_μ . The state of the system immediately after the switch is given by $x(t_\mu^+) = \mathcal{J}_\mu(x(t_\mu^-))$ where $\mathcal{J}_\mu : \mathbb{R}^n \rightarrow \mathbb{R}^n$ is the switch rule, $t_\mu^\pm = \lim_{\Delta \rightarrow 0^+}(t_\mu \pm \Delta)$, and $x(t_\mu^-)$ denotes the state immediately before the event. Similar to the

construction of periodic orbits, we can evaluate the variational equation

$$\frac{d\delta x(t)}{dt} = A_\mu \delta x(t), \quad \text{for } \delta x(t) \in R_\mu, \quad (4.5)$$

where $\delta x(t)$ represents a perturbation to the periodic orbit, by solving this linear system in each region and mapping perturbations across the switching manifolds by making use of saltation matrices [105, 211]

$$\begin{aligned} S(t_\mu) &= D\mathcal{J}_\mu(x^\gamma(t_\mu^-)) \\ &+ \frac{[\dot{x}^\gamma(t_\mu^+) - D\mathcal{J}_\mu(x^\gamma(t_\mu^-))\dot{x}^\gamma(t_\mu^-)][\nabla_x h_\mu(x^\gamma(t_\mu^-))]^\top}{\nabla_x h_\mu(x^\gamma(t_\mu^-)) \cdot \dot{x}^\gamma(t_\mu^-)}. \end{aligned} \quad (4.6)$$

Note that a detailed derivation of formula (4.6) is given in Appendix A. Saltation operators are used to capture the evaluation of perturbations during the boundary crossing where either the solution or the vector field (or both) has a discontinuity. Some application of saltation matrices are reported by Muller [211] to calculate Lyapunov exponents of discontinuous systems, and Fredriksson and Nordmark [105] in the normal form derivation for impact oscillators. In recent years, they have been used to analyse both node and network behaviour of PWL or impacting oscillatory systems [54, 55, 217].

The evaluation of $\delta x(t)$ over one period is obtained as $\delta x(T) = \mathcal{M}\delta x(0)$ where \mathcal{M} is given by

$$\mathcal{M} = S_N G(A_N; T_N) \dots S_2 G(A_2; T_2) S_1 G(A_1; T_1). \quad (4.7)$$

Here T_μ denotes the time-of-flight in each region, $S_\mu \equiv S(t_\mu)$, and G is given in (3.12). The periodic orbit will be stable if all the nontrivial eigenvalues (Floquet multipliers), λ_k , $k = 1, \dots, n-1$, of the matrix \mathcal{M} have modulus less than unity or corresponding Floquet exponents $\kappa_k = \ln(\lambda_k)/T$ have negative real part. We note that one eigenvalue of \mathcal{M} is equal to 1 which corresponds perturbations along the periodic orbit.

In particular, for the absolute model, the homoclinic loop, and the McK-

ean model (see Section 3.4) we have $h_\mu(x) = v - a$, $\mu \in \{1, 2\}$, and the PML model $h_\mu(x) = v - b$, $\mu \in \{1, 4\}$ and $h_\mu(x) = v - (1 + a)/2$, $\mu \in \{2, 3\}$. The switching rule is $\mathcal{J}_\mu(x) = x$ (solution curves are continuous), and therefore $D\mathcal{J}_\mu = I_2$, where I_2 is 2×2 identity matrix. The saltation matrices are then explicitly given by

$$S(t_\mu) = \begin{bmatrix} \frac{\dot{v}^\gamma(t_\mu^+)}{\dot{v}^\gamma(t_\mu^-)} & 0 \\ \frac{(\dot{w}^\gamma(t_\mu^+) - \dot{w}^\gamma(t_\mu^-))}{\dot{v}^\gamma(t_\mu^-)} & 1 \end{bmatrix}. \quad (4.8)$$

The non-trivial Floquet exponent of these planar nonsmooth systems can then be calculated from the formula (see [54] for a similar description)

$$\kappa = \frac{1}{T} \sum_{\mu=1}^N \left[T_\mu \operatorname{Tr} A_\mu + \log \frac{\dot{v}^\gamma(t_\mu^+)}{\dot{v}^\gamma(t_\mu^-)} \right]. \quad (4.9)$$

The logarithmic term reflects the contribution of discontinuous switching in the vector field to the stability of an orbit. We note that if the vector field switches continuously (though may be nonsmooth), $S = I_2$ and therefore this logarithmic term reduces to zero. The derivation of Floquet exponent formula (4.9) is given in Appendix A. We can now use this formula (4.9) to calculate Floquet exponents [54] of above PWL models. For the McKean model, we find

$$\begin{aligned} \kappa &= \frac{1}{T} \left[-\gamma(T_1 + T_2) + \log \frac{\dot{v}^\gamma(T_1^+)}{\dot{v}^\gamma(T_1^-)} + \log \frac{\dot{v}^\gamma(T^+)}{\dot{v}^\gamma(T^-)} \right] \\ &= -\gamma + \frac{1}{T} \log \frac{(-\gamma a - w(T_1))(-\gamma a + \xi - w(T))}{(-\gamma a + \xi - w(T_1))(-\gamma a - w(T))}. \end{aligned} \quad (4.10)$$

This is plotted in Fig. 4.1-panel (a) for the stable periodic orbits ($\kappa < 0$). When $b = 0.9683$, a saddle-node bifurcation of periodic orbits is observed, see Fig. 3.4. For the absolute model, we have the expression

$$\begin{aligned} \kappa &= \frac{1}{T} [T_1(1 - d) + T_2(-1 - d)] \\ &= -d + \frac{2T_1 - T}{T}. \end{aligned} \quad (4.11)$$

We illustrate this in Fig. 4.1-panel (b) as a function of \bar{w} where κ switches to zero when a nonsmooth Andronov-Hopf bifurcation occurs. For the homoclinic model, formula (4.9) yields

$$\kappa = \frac{1}{T} (T_1\tau_1 + T_2\tau_2). \quad (4.12)$$

Finally, for the PML model, the Floquet exponent is

$$\begin{aligned} \kappa &= \frac{1}{T} \left[\left(-1 + \frac{1}{C}\right)(T_1 + T_3 + T_4) + T_2\left(-1 - \frac{1}{C}\right) \right] \\ &= -1 + \frac{T - 2T_2}{TC}. \end{aligned} \quad (4.13)$$

We compute this in Fig. 4.1-panel (c) as a function of the external drive I where large amplitude oscillation emerge via a homoclinic bifurcation. For systems with sliding periodic orbits, Bernardo *et al.* [81] proposed a formula for the saltation matrix, and Wang *et al.* [317] have derived saltation operators for some ad hoc PWL planar models.

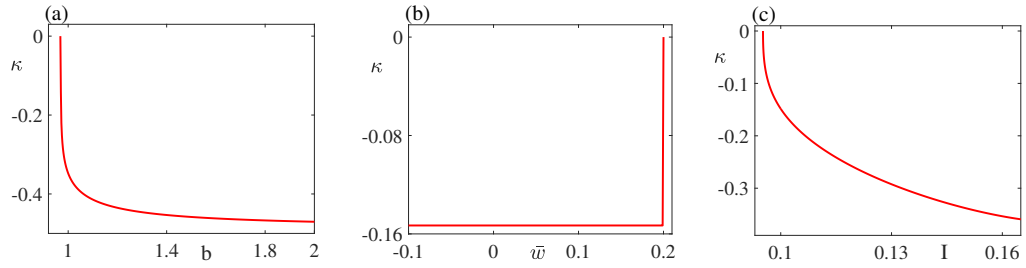


Figure 4.1: Plot of the Floquet exponent κ for the (stable) periodic orbits for the three PWL planar models. (a)-The McKean model. When $b = 0.9683$, stable and unstable periodic orbits annihilate each other via a saddle node bifurcation of periodic orbits, this bifurcation can be also seen in Fig. 3.4. Parameters: $a = 0.1$, $\gamma = 1$, $\xi = 1$ and $0.9683 \leq b \leq 2$. (b)-The absolute model. Stable periodic orbits have a constant κ for $-0.1 \leq \bar{w} < 0.2$ that suddenly reduces to zero when $\bar{w} \simeq 0.2$ where a nonsmooth Andronov-Hopf bifurcation occurs. Other parameters as in Fig 3.5. (c)-PML model. κ as a function of external input I , where large amplitude oscillations are first seen when $I = 0.094$. Other parameters are as in Fig 3.10.

4.3 Phase response curves for piecewise linear systems

As we introduced in Section 2.2, the iPRC is a periodic vector function which measures changes in timing of a limit cycle in response to infinitely small perturbations at each point along the cycle. Recall from Section 2.2 that for smooth systems, the iPRC ($\mathcal{Z}(t)$) can be found by solving the adjoint equation

$$\frac{d\mathcal{Z}(t)}{dt} = -Df(x^\gamma(t))^\top \mathcal{Z}(t), \quad (4.14)$$

subject to the normalisation condition $\mathcal{Z}^\top(0)f(x^\gamma(0)) = \omega$ with periodicity condition $\mathcal{Z}(t) = \mathcal{Z}(t + T)$, $T = 2\pi/\omega$. However, the adjoint method may not be directly used for nonsmooth systems without further consideration. For example, for some piecewise smooth systems the vector field may change discontinuously across the switching manifold and theretofore the Jacobian Df is not defined at all points along the limit cycle. Nevertheless, for PWL systems, $Df(x^\gamma(t))$ is piecewise constant, and similar to the construction of periodic solutions of the system (4.4), we can build a closed form solution for the adjoint equation. But, abrupt changes in the vector field on the discontinuity surface would lead to a discontinuous iPRC. Using the same labelling introduced for the periodic orbit of (4.4), within the interior of each subregion R_μ , the iPRC evolves according to

$$\frac{d\mathcal{Z}_\mu(t)}{dt} = -A_\mu^\top \mathcal{Z}_\mu(t), \quad (4.15)$$

where $A_\mu^\top = Df_\mu(x^\gamma(t))^\top$ is the transpose of the linearisation of the vector field f_μ evaluated along the $x^{\gamma_\mu}(t)$ portion of the limit cycle. The explicit solution of each subsystem is given by $\mathcal{Z}_\mu(t) = G(-A_\mu^\top; t - t_{\mu-1})\mathcal{Z}_\mu(t_{\mu-1})$ where $t_{\mu-1} \leq t < t_\mu$ and $\mathcal{Z}_\mu(t_{\mu-1})$ is the initial value on the boundary of each subregion. Now, we need to determine how the iPRC evolves across either side of a switching manifold. For brevity, at each switching event time t_μ , we denote \mathcal{Z}_μ^- for the iPRC vector immediately before the crossing, and \mathcal{Z}_μ^+ for

that of just after the crossing.

For one dimensional nonsmooth systems, such as the leaky integrate-and-fire (LIF) model or nonlinear integrate-and-fire (IF) models [55], the size of the discontinuity can be computed explicitly, because the normalisation condition $d\theta[x(t)]/dt = \omega$ at t_μ^+ yields one equation to find the unknown \mathcal{Z}_μ^+ immediately after the switching event. However, for n dimensional systems, the normalisation condition only gives one equation for n -unknowns. In particular, for planar systems we need one more equation to determine the jump in iPRC. To derive this we will summarise three different methods: (i) using the relation between jump operator of the variational equation and that of iPRC [227, 276], (ii) using the normalisation condition on either sides of the switching boundary [55], and (iii) using first principles along with linear matching conditions [227, 320]. All of these three methods give equivalent results though each has their own merit and practicality.

To derive the first method, let us consider an arbitrary state x^γ on the periodic orbit and a perturbed state $x^\gamma + \delta x$ where δx is an arbitrarily small perturbation. This gives a time-independent phase shift $\Delta\theta = \theta(x^\gamma + \delta x) - \theta(x^\gamma)$ such that this shift remains constant (since all isochrons have the same rotation rate) in time as the trajectories $x^\gamma(t)$ and $x^\gamma(t) + \delta x(t)$ starting from those two points evolve. Using a first order Taylor expansion of $\theta(x)$, we obtain

$$\Delta\theta = \theta(x^\gamma(t) + \delta x(t)) - \theta(x^\gamma(t)) \simeq \nabla_{x^\gamma(t)}\theta \cdot \delta x(t). \quad (4.16)$$

Hence, we deduce that

$$\mathcal{Z}(t) \cdot \delta x(t) = \text{const.} \quad (4.17)$$

holds both within the interior of each subregion R_μ and across the switching manifolds due to the continuity of $\Delta\theta$ [227, 317]. Therefore at any moment of switching event t_μ , we have

$$\langle \mathcal{Z}_\mu^-, \delta x^- \rangle = \langle \mathcal{Z}_\mu^+, \delta x^+ \rangle \quad (4.18)$$

where $\delta x^- = \delta x(t_\mu^-)$ and $\delta x^+ = \delta x(t_\mu^+)$. Then the saltation relation $\delta x^+ = S_\mu \delta x^-$ gives

$$\langle \mathcal{Z}_\mu^-, \delta x^- \rangle = \langle \mathcal{Z}_\mu^+, S_\mu \delta x^- \rangle = \langle S_\mu^\top \mathcal{Z}_\mu^+, \delta x^- \rangle, \quad (4.19)$$

and therefore

$$\langle \mathcal{Z}_\mu^- - S_\mu^\top \mathcal{Z}_\mu^+, \delta x^- \rangle = 0. \quad (4.20)$$

Since this holds for any arbitrary δx^- , we find $\mathcal{Z}_\mu^- - S_\mu^\top \mathcal{Z}_\mu^+ = 0$. As a result, we have the following relation between \mathcal{Z}_μ^- and \mathcal{Z}_μ^+

$$\mathcal{Z}_\mu^+ = (S_\mu^\top)^{-1} \mathcal{Z}_\mu^-, \quad (4.21)$$

where $(S_\mu^\top)^{-1}$ is the inverse of the transpose of S_μ . Shirasaka *et al.* [276] have rigorously shown this relation for hybrid dynamical systems with limit cycles by showing that the jump operator of the iPRC is equivalent to the transpose of the inverse of the saltation matrix. They then implemented this in an analytically tractable set of glued Stuart-Landau oscillators composed of two discrete states and a two-dimensional continuous state variable, and built the discontinuous iPRC using a direct numerical method and an adjoint method, showing that both methods agreed.

As a second method, by following a similar process presented in [55], we use the normalisation condition $\nabla_{x^\gamma(t)} \theta \cdot f_\mu(x^\gamma(t)) = \omega$ from either sides of the each switching manifolds. To observe this more explicitly, let us consider two regions R_μ and $R_{\mu+1}$. In order to determine the initial condition $\mathcal{Z}_\mu(t_{\mu-1}^+) = [z_\mu^1, z_\mu^2]^\top$ inside the region R_μ , we need to solve the following equations simultaneously

$$\begin{aligned} \langle \mathcal{Z}_\mu(t_{\mu-1}^+), [\dot{v}^\gamma(t_{\mu-1}^+), \dot{w}^\gamma(t_{\mu-1}^+)]^\top \rangle &= \omega, \\ \langle \mathcal{Z}_\mu(t_\mu^-), [\dot{v}^\gamma(t_\mu^-), \dot{w}^\gamma(t_\mu^-)]^\top \rangle &= \omega \end{aligned} \quad (4.22)$$

for z_μ^1 and z_μ^2 where $\mathcal{Z}_\mu(t_\mu^-) = G(-A_\mu^\top; T_\mu) \mathcal{Z}_\mu(t_{\mu-1}^+)$. Similarly, to determine the initial condition $\mathcal{Z}_{\mu+1}(t_\mu^+) = [z_{\mu+1}^1, z_{\mu+1}^2]^\top$ inside the region $R_{\mu+1}$, we need

to solve

$$\begin{aligned}\langle \mathcal{Z}_{\mu+1}(t_\mu^+), [\dot{v}^\gamma(t_\mu^+), \dot{w}^\gamma(t_\mu^+)]^\top \rangle &= \omega, \\ \langle \mathcal{Z}_{\mu+1}(t_{\mu+1}^-), [\dot{v}^\gamma(t_{\mu+1}^-), \dot{w}^\gamma(t_{\mu+1}^-)]^\top \rangle &= \omega\end{aligned}\tag{4.23}$$

for $z_{\mu+1}^1$ and $z_{\mu+1}^2$ where $\mathcal{Z}_{\mu+1}(t_{\mu+1}^-) = G(-A_{\mu+1}^\top; T_{\mu+1})\mathcal{Z}_{\mu+1}(t_\mu^+)$. Then the size of discontinuity at each t_μ is given by $\mathcal{Z}_{\mu+1}(t_\mu^+) - \mathcal{Z}_\mu(t_\mu^-)$. Coombes *et al.* [55] have obtained iPRCs for the planar PWL-IF model by using this approach for both regular and fast spiking orbits, as well as for bursting solutions.

Alternatively, assuming $\mathcal{R}^\top \mathcal{Z}_\mu^+ = \mathcal{Z}_\mu^-$ for some matrix \mathcal{R} , and using the normalisation condition, we have

$$\langle \mathcal{Z}_\mu^+, \dot{x}^\gamma(t_\mu^+) \rangle = \langle \mathcal{R}^\top \mathcal{Z}_\mu^+, \dot{x}^\gamma(t_\mu^-) \rangle = \langle \mathcal{Z}_\mu^+, \mathcal{R} \dot{x}^\gamma(t_\mu^-) \rangle,\tag{4.24}$$

and this gives

$$\langle \dot{x}^\gamma(t_\mu^+) - \mathcal{R} \dot{x}^\gamma(t_\mu^-), \mathcal{Z}_\mu^+ \rangle = 0.\tag{4.25}$$

Equation (4.25) holds for any arbitrary \mathcal{Z}_μ^+ , and therefore we have $\dot{x}^\gamma(t_\mu^+) = \mathcal{R} \dot{x}^\gamma(t_\mu^-)$. Now we will show the saltation matrix also satisfies $\dot{x}^\gamma(t_\mu^+) = S_\mu \dot{x}^\gamma(t_\mu^-)$. To do so, we use formula (4.6) and multiply it from the right by $\dot{x}^\gamma(t_\mu^-)$ to find

$$\begin{aligned}S(t_\mu) \dot{x}^\gamma(t_\mu^-) &= D\mathcal{J}_\mu(x^\gamma(t_\mu^-)) \dot{x}^\gamma(t_\mu^-) \\ &+ \frac{[\dot{x}^\gamma(t_\mu^+) - D\mathcal{J}_\mu(x^\gamma(t_\mu^-)) \dot{x}^\gamma(t_\mu^-)] [\nabla_x h_\mu(x^\gamma(t_\mu^-))]^\top \dot{x}^\gamma(t_\mu^-)}{\nabla_x h_\mu(x^\gamma(t_\mu^-)) \cdot \dot{x}^\gamma(t_\mu^-)} \\ &= D\mathcal{J}_\mu(x^\gamma(t_\mu^-)) \dot{x}^\gamma(t_\mu^-) + \dot{x}^\gamma(t_\mu^+) - D\mathcal{J}_\mu(x^\gamma(t_\mu^-)) \dot{x}^\gamma(t_\mu^-) \\ &= \dot{x}^\gamma(t_\mu^+).\end{aligned}\tag{4.26}$$

Hence, we obtain $\mathcal{R} = S_\mu$, and this implies the relation $\mathcal{Z}_\mu^+ = (S_\mu^\top)^{-1} \mathcal{Z}_\mu^-$ holds.

Therefore, the first and second methods are equivalent.

As a final method, we will revise the technique that has been proposed by Park *et al.* [227] and Wilson [320] to derive jump condition in the iPRC for n dimensional piecewise smooth systems with $n - 1$ dimensional switching surface Σ_μ that are transverse to $x^\gamma(t)$. This approach makes the following

assumptions: (i) The level sets of the phase function $\theta(x)$ (the isochronal surfaces) form a continuous foliation of an open neighbourhood of $x^\gamma(t)$. (ii) $\theta(x)$ is at least twice differentiable within the interior of each region R_μ . (iii) Each boundary Σ_μ is at least C^1 (continuously differentiable) in an open ball $B(p_\mu, R)$ centred at p_μ with radius R where p_μ the intersection point of Σ_μ and $x^\gamma(t)$. From this, it follows that at each crossing point p_μ there exists a tangent hyperplane Π spanned by an orthonormal set of $n - 1$ vectors w_i for $i = 1, \dots, n - 1$. (iv) Directional derivatives of $\theta(x)$ exist on Π in all tangential directions w_i and are identical from either side. Then, for each boundary crossing, using the assumption (iv) at crossing point $p_\mu \in \Sigma_\mu$, they derived following $n - 1$ equations

$$w_i \cdot \mathcal{Z}_\mu^- = w_i \cdot \mathcal{Z}_\mu^+, \quad i = 1, \dots, n - 1. \quad (4.27)$$

They obtained final equation from the normalisation condition at either side of switching manifold

$$f_\mu^-(x^\gamma(t_\mu^-)) \cdot \mathcal{Z}_\mu^- = \omega = f_\mu^+(x^\gamma(t_\mu^+)) \cdot \mathcal{Z}_\mu^+, \quad (4.28)$$

where f_μ^- is the vector field evaluated on the limit cycle immediately before a switching event and f_μ^+ that of thereafter. Hence, they got n equations to calculate each jump condition. Wilson [320], states that for all locations on Π the local directional derivative of the phase coordinate in all directions tangent to Π must be identical when approaching from either side, otherwise continuity would be violated. Here we note that, although this assumption guarantees the continuity of $\theta(x)$, in general, the asymptotic phase function will not necessarily be differentiable in the directions transverse to the switching boundary.

For the planar PWL models, we considered here, indicator functions are in the form $h_\mu(x) = v - c_\mu$, where c_μ is a constant, and therefore we have $w_1 =$

$[0, 1]^\top$. Then the equations (4.27)-(4.28) reduces to the system of equations

$$\begin{aligned} w_1 \cdot \mathcal{Z}_\mu^- &= w_1 \cdot \mathcal{Z}_\mu^+, \\ f_\mu^- \cdot \mathcal{Z}_\mu^- &= f_\mu^+ \cdot \mathcal{Z}_\mu^+, \end{aligned} \quad (4.29)$$

using these, at each boundary crossing, we have $C_\mu \mathcal{Z}_\mu^+ = D_\mu \mathcal{Z}_\mu^-$, where

$$C_\mu = \begin{bmatrix} \dot{v}^\gamma(t_\mu^+) & \dot{w}^\gamma(t_\mu^+) \\ 0 & 1 \end{bmatrix}, \quad D_\mu = \begin{bmatrix} \dot{v}^\gamma(t_\mu^-) & \dot{w}^\gamma(t_\mu^-) \\ 0 & 1 \end{bmatrix}. \quad (4.30)$$

This yields a linear jump condition in the form $\mathcal{Z}_\mu^+ = C_\mu^{-1} D_\mu \mathcal{Z}_\mu^-$. We also observe that

$$C_\mu^{-1} D_\mu = \begin{bmatrix} \frac{\dot{v}^\gamma(t_\mu^-)}{\dot{v}^\gamma(t_\mu^+)} & \frac{\dot{w}^\gamma(t_\mu^-) - \dot{w}^\gamma(t_\mu^+)}{\dot{v}^\gamma(t_\mu^+)} \\ 0 & 1 \end{bmatrix} = (S_\mu^\top)^{-1}. \quad (4.31)$$

This explicitly shows that first and last method give the same jump condition, as expected. Park *et al.* [227] applied this method to compute iPRCs of a piecewise constant model and a PWL Iris system.

The iPRCs of the McKean model, the absolute model, and the homoclinic model take the form

$$\mathcal{Z}(t) = \begin{cases} G(-A_1^\top; t) \mathcal{Z}(0), & 0 \leq t < T_1, \\ G(-A_2^\top; t - T_1) (S_1^\top)^{-1} G(-A_1^\top; T_1) \mathcal{Z}(0), & T_1 \leq t < T, \\ (S_2^\top)^{-1} G(-A_2^\top; T_2) (S_1^\top)^{-1} G(-A_1^\top; T_1) \mathcal{Z}(0), & t = T. \end{cases} \quad (4.32)$$

It remains to determine the initial condition $\mathcal{Z}(0) = [z_0^1, z_0^2]^\top$. To do so we use the normalisation condition at $t = 0$,

$$z_0^1 [a_{11}^1 a + a_{11}^1 w^1(0) + b_1^1] + z_0^2 [a_{21}^1 a + a_{22}^1 w^1(0) + b_2^1] = \frac{2\pi}{T}, \quad (4.33)$$

where a_{ij}^1 , $i, j = 1, 2$, and b_i^1 are entries of the matrix A_1 and the vector b_1 , respectively, along with the periodicity $\mathcal{Z}(0) = \mathcal{Z}(T)$. By introducing the 2×2

matrix

$$\Gamma^Z = (S_2^\top)^{-1}G(-A_2^\top; T_2)(S_1^\top)^{-1}G(-A_1^\top; T_1), \quad (4.34)$$

the periodicity condition $\mathcal{Z}(0) = \Gamma^Z \mathcal{Z}(0)$, gives the equation

$$[\Gamma_{11}^Z - 1]z_0^1 + \Gamma_{12}^Z z_0^2 = 0. \quad (4.35)$$

Then, using (4.33) and (4.35) we may write

$$\Psi^Z \begin{bmatrix} z_0^1 \\ z_0^2 \end{bmatrix} = \begin{bmatrix} \frac{2\pi}{T} \\ 0 \end{bmatrix}, \Psi^Z = \begin{bmatrix} a_{11}^1 a + a_{11}^1 w^1(0) + b_1^1 & a_{21}^1 a + a_{22}^1 w^1(0) + b_2^1 \\ \Gamma_{11}^Z - 1 & \Gamma_{12}^Z \end{bmatrix}$$

Then we can solve this using Cramer's rule, which gives

$$z_0^1 = \det(\Psi_1^Z) / \det(\Psi^Z) \quad \text{and} \quad z_0^2 = \det(\Psi_2^Z) / \det(\Psi^Z) \quad (4.36)$$

where

$$\Psi_1^Z = \begin{bmatrix} \frac{2\pi}{T} & a_{21}^1 a + a_{22}^1 w^1(0) + b_2^1 \\ 0 & \Gamma_{12}^Z \end{bmatrix}, \Psi_2^Z = \begin{bmatrix} a_{11}^1 a + a_{11}^1 w^1(0) + b_1^1 & \frac{2\pi}{T} \\ \Gamma_{11}^Z - 1 & 0 \end{bmatrix}.$$

Using a similar procedure, we can also construct the iPRCs for the PML model, by solving \mathcal{Z} over four subregions. Here we omit details of this by referring to [52] for a detailed discussion.

For the considered models, in Fig. 4.2 we illustrated plots of iPRCs constructed implementing the above technique. Moreover, in Fig. 4.3, we depict first order linear approximations to isochronal coordinates at various location around the limit cycles. For the homoclinic model, as the periodic orbit becomes closer to the homoclinic bifurcation, the sensitivity of the limit cycle to external perturbations increases, i.e. we need to choose small perturbations otherwise a perturbed solution will not converge to the limit cycle.

Using the relation $\mathcal{Z}(t) \cdot \delta x(t) = \text{const}$, we expect that components of the iPRC vector will increase and reach a peak in the vicinity of the homoclinic bifurcation. In Fig. 4.4, we plot the maximum value of the voltage component \mathcal{Z}_v of the iPRC under parameter variation of p_{bif} . We observe that as the limit cycle approaches to the homoclinic orbit, the maximum value of \mathcal{Z}_v increases quickly. For some particular values of p_{bif} , plots of the iPRCs and shape of the corresponding periodic orbits are shown in Fig. 4.5. As illustrated in panel (c) [homoclinic loop] and panel (d) [PML model] of Fig. 4.3, at locations on the limit cycle that are close to the saddle point, the phase coordinate system breaks down and a better or exact coordinate system is needed to avoid numerical discrepancies.

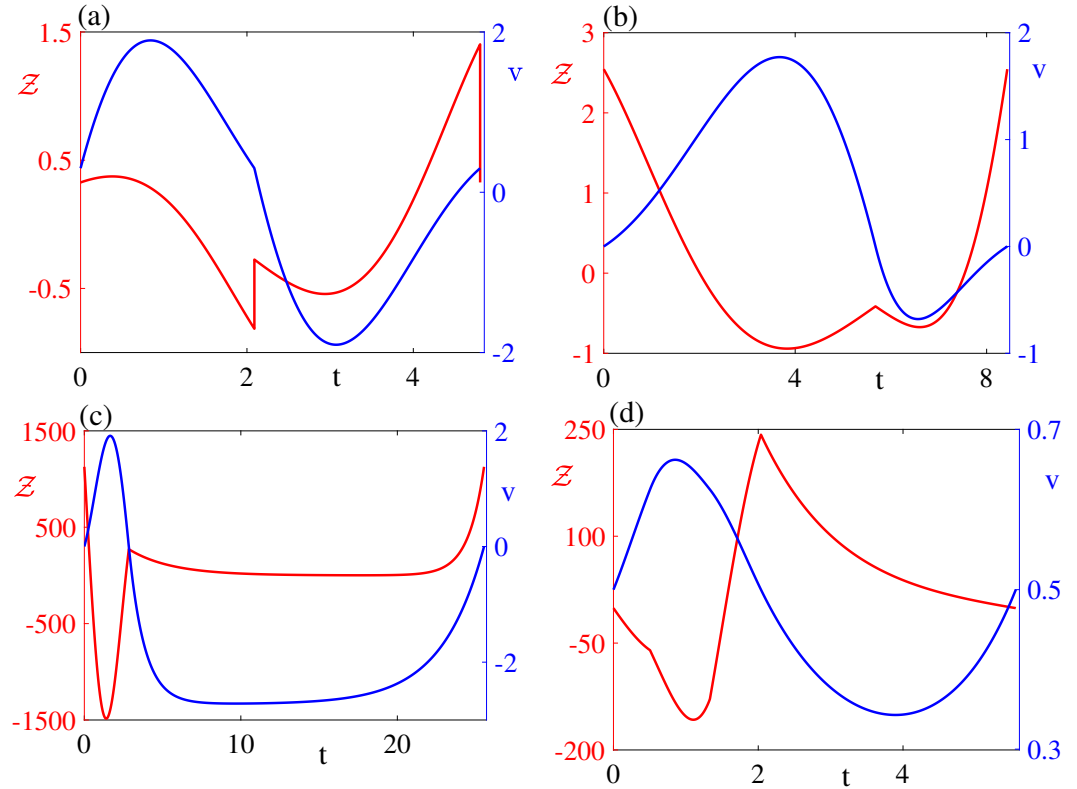


Figure 4.2: Plot of the iPRC (red) and underlying shape of the periodic v -component (blue). (a)-The McKean model with parameters as in Fig. 3.3. (b)-The absolute model with parameters as in Fig. 3.5. (c) Homoclinic loop with parameters as in Fig. 3.7. (d)-PML model with parameters as in Fig. 3.10.

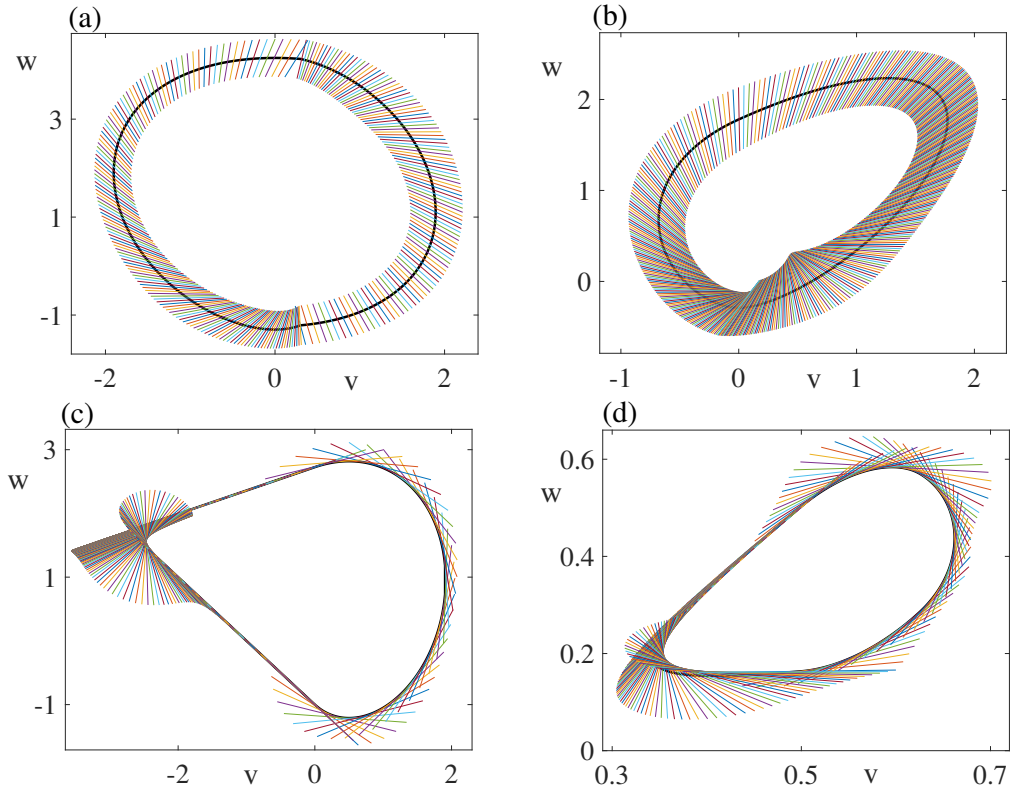


Figure 4.3: Illustration of first order linear approximations to isochronal coordinates at various locations around the limit cycles. (a)-The McKean model with parameters as in Fig. 3.3. (b)-The absolute model with parameters as in Fig. 3.5. (c) Homoclinic loop with parameters as in Fig. 3.7. (d)-PML model with parameters as in Fig. 3.10.

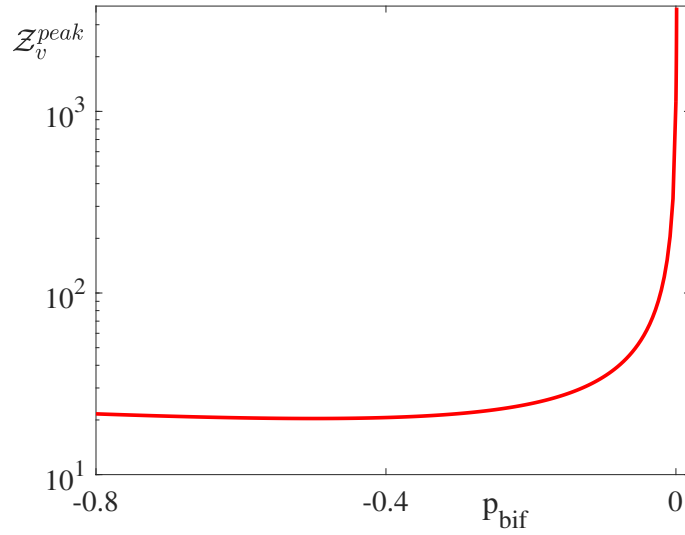


Figure 4.4: Peak values of the voltage components Z_v of the iPRC over parameter p_{bif} for the homoclinic model. As periodic orbit approaches to the homoclinic bifurcation, the maximum value of Z_v increases rapidly. Entries of A_1 , A_2 and p_{bif} values are defined as in Fig. 3.8, and other parameters as in Fig. 3.7.

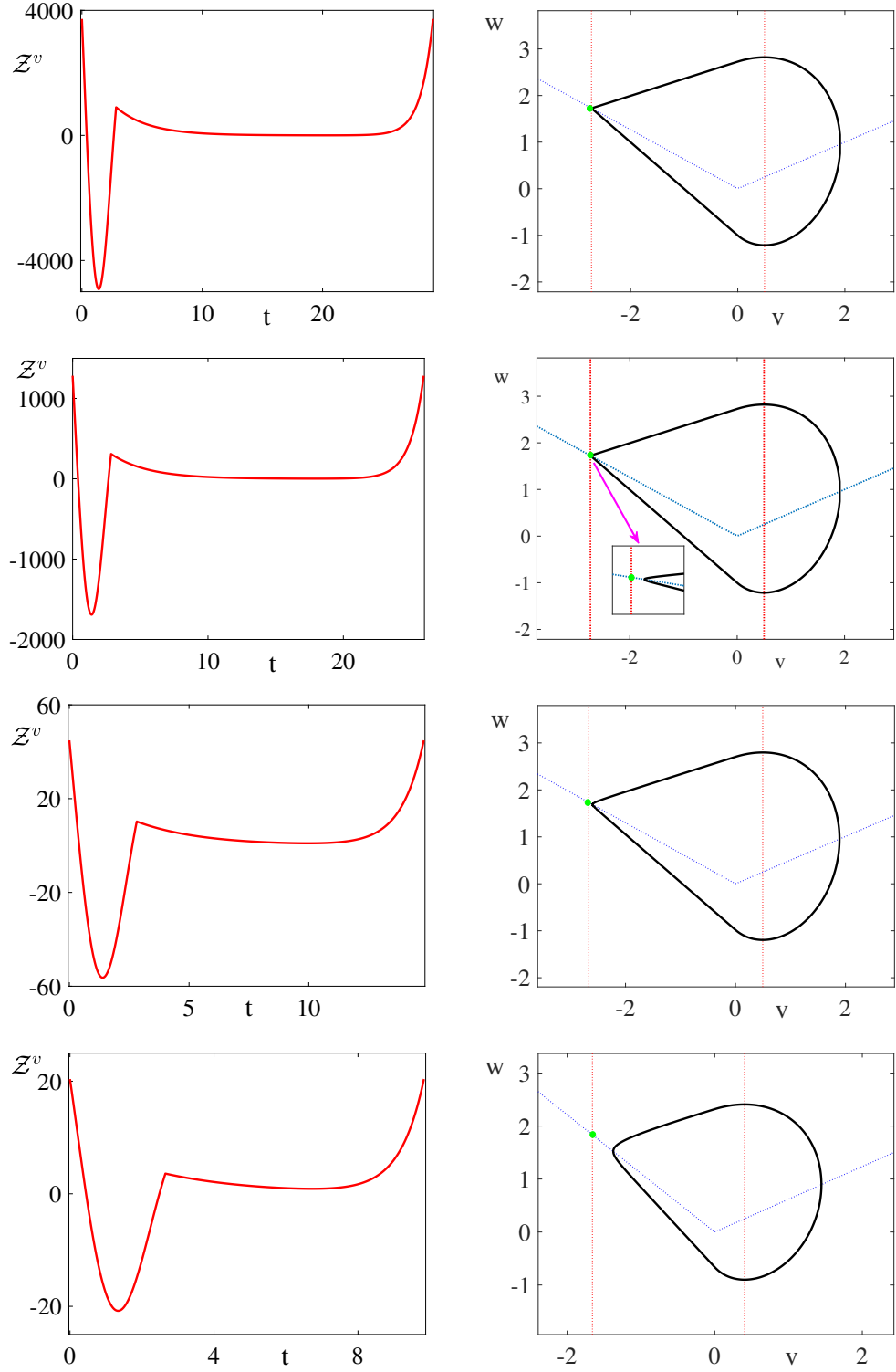


Figure 4.5: Shape of the homoclinic model iPRC in the homoclinic limit. The left column shows plots of the iPRC for the voltage component. The right column shows the corresponding limit cycle. Entries of A_1 and A_2 are defined as in Fig. 3.8. p_{bif} values from bottom to top: $p_{bif} = -0.4735$; -0.0653 ; 1.781×10^{-3} , and 0.97×10^{-3} . For the case $p_{bif} = 1.781 \times 10^{-3}$, we zoom in the dynamics around the homoclinic point. Other parameters as in Fig. 3.7.

4.4 Isostable response curves for piecewise linear systems

Referring back to Section 2.3, the iIRCs are periodic vector functions that give a quantification to the effect of an external perturbation in driving the trajectory away from the limit cycle and can be obtained by solving the adjoint equation (2.13). For nonsmooth systems, the adjoint equation (2.13) cannot be directly used and needs a more careful treatment. Here we will handle this problem for planar PWL systems which have only one non-trivial Floquet exponent, therefore, for simplicity of notation, in (2.13), we replace $\nabla_{x^\gamma} \psi_k \equiv \mathcal{I}_k(t)$ by $\mathcal{I}(t)$ and κ_k by κ . Using the same labelling introduced for the periodic orbit of (4.4), inside the each subregion R_μ , iIRC evolves according to

$$\frac{d\mathcal{I}_\mu(t)}{dt} = Q_\mu \mathcal{I}_\mu(t), \quad (4.37)$$

where $Q_\mu = (\kappa I_2 - A_\mu^\top)$. The explicit solution of each subsystem is given by $\mathcal{I}_\mu(t) = G(Q_\mu; t - t_{\mu-1}) \mathcal{I}_\mu(t_{\mu-1})$ where $t_{\mu-1} \leq t < t_\mu$ and $\mathcal{I}_\mu(t_{\mu-1})$ is the initial value at each subregion. Thereafter, we also need to determine how the iIRC evolves across either side of a switching manifold. For brevity, at each switching event time t_μ , we denote \mathcal{I}_μ^- for the iIRC vector immediately before the crossing, and \mathcal{I}_μ^+ for just after the crossing.

Now, we will revise the technique proposed by Wilson [320] to derive a jump condition in the iIRC for an n dimensional piecewise smooth systems with an $n - 1$ dimensional switching surface Σ_μ that is transverse to $x^\gamma(t)$. To obtain jump operator for the iIRC, Wilson made the following assumptions: (i) $\psi_k(x)$ are continuous for all k in an open neighbourhood of $x^\gamma(t)$. (ii) $\psi_k(x)$ for all k are at least twice differentiable within the interior of each subregion R_μ . (iii) Each boundary Σ_μ is at least C^1 (continuously differentiable) in an open ball $B(p_\mu, R)$ centred at p_μ with radius R where p_μ is the intersection point of Σ_μ and $x^\gamma(t)$. From this, it follows that at each crossing point p_μ there

exists a tangent hyperplane Π spanned by an orthonormal set of $n - 1$ vectors w_i for $i = 1, \dots, n - 1$. (iv) Directional derivatives of ψ_k for all k exist on Π in all tangential directions w_i and identical from either side. Similar to the approach for iPRC, Wilson [320] states that, directional derivatives of the ψ_k in all directions tangent to Π must be identical when approaching from either side, otherwise continuity of the ψ_k coordinate would be violated. Then, for planar PWL systems, at each boundary crossing point $p_\mu \in \Sigma_\mu$, we have

$$w_1 \cdot \mathcal{I}_\mu^- = w_1 \cdot \mathcal{I}_\mu^+. \quad (4.38)$$

Equation (2.12), gives the relation $\partial\psi/\partial x \cdot f(x) = \kappa\psi$, and using this, along with the continuity assumption of ψ , we have

$$f_\mu^-(x^\gamma(t_\mu^-)) \cdot \mathcal{I}_\mu^- = \kappa\psi^- = \kappa\psi^+ = f_\mu^+(x^\gamma(t_\mu^+)) \cdot \mathcal{I}_\mu^+, \quad (4.39)$$

where f_μ^- is the vector field evaluated on the limit cycle immediately before a switching event and f_μ^+ that thereafter. For the planar PWL models, we consider here, $h_\mu(x) = v - c_\mu$, where c_μ is a constant, and therefore $w_1 = [0, 1]^\top$. For this case equations (4.38)-(4.39) reduce to the system of equations

$$\begin{aligned} w_1 \cdot \mathcal{I}_\mu^- &= w_1 \cdot \mathcal{I}_\mu^+, \\ f_\mu^- \cdot \mathcal{I}_\mu^- &= f_\mu^+ \cdot \mathcal{I}_\mu^+. \end{aligned} \quad (4.40)$$

Using these, at each boundary crossing, we have $C_\mu \mathcal{I}_\mu^+ = D_\mu \mathcal{I}_\mu^-$, where C_μ and D_μ are the same as in (4.30). This results in a linear jump condition in the form $\mathcal{I}_\mu^+ = C_\mu^{-1} D_\mu \mathcal{I}_\mu^- = (S_\mu^\top)^{-1} \mathcal{I}_\mu^-$.

We can derive the same jump condition by considering an arbitrary point x^γ on the limit cycle and a perturbed state $x^\gamma + \delta x$ where δx is an arbitrarily small perturbation. The difference between the corresponding isostables is $\Delta\psi = \psi(x^\gamma + \delta x) - \psi(x^\gamma)$, where we note $\psi(x^\gamma) = 0$ (on the limit cycle the isostable value is always zero). Using equation (2.12), this difference evolves

according to $\frac{d\Delta\psi}{dt} = \kappa\Delta\psi$ in time as the trajectories $x^\gamma(t)$ and $x^\gamma(t) + \delta x(t)$ starting from those two points evolve. The continuity assumption of ψ implies $\Delta\psi$ is continuous at the switching boundary, i.e. $\Delta\psi^- = \Delta\psi^+$. Using a first order Taylor expansion, we find

$$\Delta\psi = \psi(x^\gamma(t) + \delta x(t)) - \psi(x^\gamma(t)) \simeq \nabla_{x^\gamma(t)}\psi \cdot \delta x(t). \quad (4.41)$$

Hence, at the time t_μ of a switching event, we have

$$\Delta\psi^- = \mathcal{I}_\mu^-(t_\mu^-) \cdot \delta x(t_\mu^-) = \mathcal{I}_\mu^+(t_\mu^+) \cdot \delta x(t_\mu^+) = \Delta\psi^+, \quad (4.42)$$

or equivalently,

$$\langle \mathcal{I}_\mu^-, \delta x^- \rangle = \langle \mathcal{I}_\mu^+, \delta x^+ \rangle. \quad (4.43)$$

Then the relation $\delta x^+ = S_\mu \delta x^-$ gives

$$\langle \mathcal{I}_\mu^-, \delta x^- \rangle = \langle \mathcal{I}_\mu^+, S_\mu \delta x^- \rangle = \langle S_\mu^\top \mathcal{I}_\mu^+, \delta x^- \rangle, \quad (4.44)$$

which implies

$$\langle \mathcal{Z}_\mu^- - S_\mu^\top \mathcal{Z}_\mu^+, \delta x^- \rangle = 0. \quad (4.45)$$

Since this holds for arbitrary δx^- , we obtain $\mathcal{I}_\mu^- - S_\mu^\top \mathcal{I}_\mu^+ = 0$. As a result, between \mathcal{I}_μ^- and \mathcal{I}_μ^+ , we have the relation

$$\mathcal{I}_\mu^+ = (S_\mu^\top)^{-1} \mathcal{I}_\mu^-. \quad (4.46)$$

As we expect, both methods gives the same jump condition. Therefore we can obtain jumps in iIRC using saltation matrices. The iIRCs of the McKean

model, the absolute model, and the homoclinic model are calculated form

$$\mathcal{I}(t) = \begin{cases} G(Q_1; t)\mathcal{I}(0), & 0 \leq t < T_1, \\ G(Q_2; t - T_1)(S_1^\top)^{-1}G(Q_1; T_1)\mathcal{I}(0), & T_1 \leq t < T, \\ (S_2^\top)^{-1}G(Q_2; T_2)(S_1^\top)^{-1}G(Q_1; T_1)\mathcal{I}(0), & t = T, \end{cases} \quad (4.47)$$

where we need to determine initial condition $\mathcal{I}(0) = [i_0^1, i_0^2]^\top$. To do so we use the normalisation condition,

$$i_0^1 \bar{v}^1 + i_0^2 \bar{v}^2 = 1, \quad (4.48)$$

where $\bar{v} = [\bar{v}^1, \bar{v}^2]^\top$ is the eigenvector associated with non-trivial Floquet multiplier $\bar{\lambda}$, and the periodicity condition $\mathcal{I}(0) = \mathcal{I}(T)$. By introducing the 2×2 matrix

$$\Gamma^I = (S_2^\top)^{-1}G(Q_2; T_2)(S_1^\top)^{-1}G(Q_1; T_1), \quad (4.49)$$

the periodicity condition $\mathcal{I}(0) = \Gamma^I \mathcal{I}(0)$ gives the equation

$$[\Gamma_{11}^I - 1]i_0^1 + \Gamma_{12}^I i_0^2 = 0. \quad (4.50)$$

Then, using (4.48) and (4.50) we may write

$$\Psi^I \begin{bmatrix} i_0^1 \\ i_0^2 \end{bmatrix} = \begin{bmatrix} 1 \\ 0 \end{bmatrix}, \quad \Psi^I = \begin{bmatrix} \bar{v}^1 & \bar{v}^2 \\ \Gamma_{11}^I - 1 & \Gamma_{12}^I \end{bmatrix}$$

Using Cramer's rule, we can solve this to yield

$$i_0^1 = \det(\Psi_1^I) / \det(\Psi^I) \quad \text{and} \quad i_0^2 = \det(\Psi_2^I) / \det(\Psi^I), \quad (4.51)$$

where

$$\Psi_1^I = \begin{bmatrix} 1 & \bar{v}^2 \\ 0 & \Gamma_{12}^I \end{bmatrix}, \quad \Psi_2^I = \begin{bmatrix} \bar{v}^1 & 1 \\ \Gamma_{11}^I - 1 & 0 \end{bmatrix}.$$

Likewise, the iIRC's for the PML model, can be constructed by solving \mathcal{I} over

four subregions. Here we omit the details of this. For the models considered, in Fig. 4.6 we give illustrative plots of iIRCs constructed implementing the above technique. In these plots, dots are obtained through direct numerical simulation of the original systems. To achieve this, say in the voltage component v , we first applied a perturbation in the form $\delta x(t) = [\delta v(t), 0]^\top$ at various locations along the limit cycle, and then at each of these locations we calculate the isostable change given by (4.41) where we obtain $\psi(x^\gamma(t) + \delta x(t))$ from (2.10) and recognise that $\psi = 0$ on the cycle. For the introduced $\delta x(t)$ using $\Delta\psi \simeq \nabla_{x^\gamma(t)}\psi \cdot \delta x(t)$ we find

$$\Delta\psi \simeq \left(\frac{\partial\psi}{\partial v}, \frac{\partial\psi}{\partial w} \right) (\delta v(t), 0)^\top = \mathcal{I}^v(t)\delta v(t), \quad (4.52)$$

hence, at each location, we approximate the voltage component of the iIRC as $\mathcal{I}^v(t) \simeq \Delta\psi/\delta v(t)$. In a similar way, one can compute the w -component of the iIRC by introducing perturbations of the form $\delta x(t) = [0, \delta w(t)]^\top$. Monga and Moehlis [206] computed the iIRC both numerically and analytically for a planar smooth homoclinic loop model, and found a good agreement between numerical and analytical approaches.

4.5 Second-order terms in response functions for piecewise linear systems

For smooth planar systems, the second-order accurate phase-amplitude description (2.21)-(2.22), reduces to

$$\frac{d\theta}{dt} = \omega + [\mathcal{Z}(t) + \mathcal{B}(t)\psi] \cdot g(t), \quad (4.53)$$

$$\frac{d\psi}{dt} = \kappa\psi + [\mathcal{I}(t) + \mathcal{C}(t)\psi] \cdot g(t), \quad (4.54)$$

where $\mathcal{B}(t) = H_{\theta, x^\gamma}p(t)$, $\mathcal{C}(t) = H_{\psi, x^\gamma}p(t)$, and the periodic function $p(t)$ can be obtained from (2.19). In this case, the evolution equation (2.35) of $\mathcal{B}(t)$

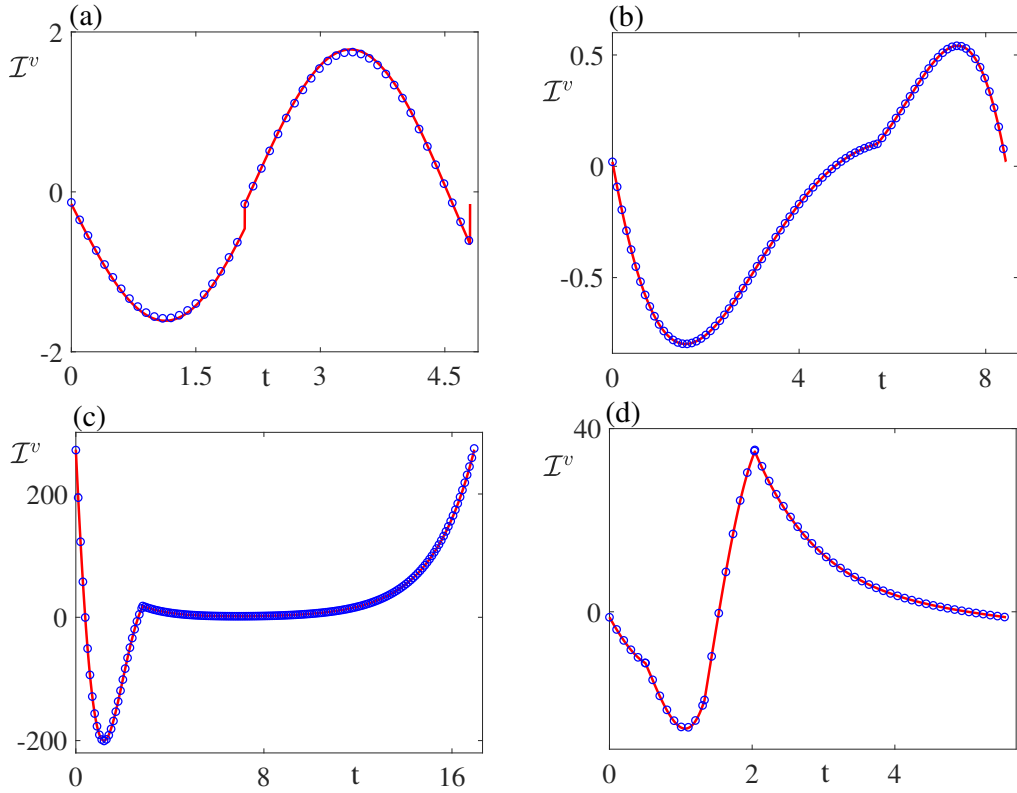


Figure 4.6: Illustration of v -components of the iRCs (red) where blue circles are obtained by direct numerical simulation of the original systems. (a)-The McKean model with parameters as in Fig. 3.3. (b)-The absolute model with parameters as in Fig. 3.5. (c) Homoclinic loop model with $\tau_2 = 0.64$ and other parameters as in Fig. 3.7. (d)-PML model with parameters as in Fig. 3.10. To test the adjoint method against to direct numerical simulation we choose $\delta v = 10^{-4}$. The theory and simulations show excellent agreement.

becomes

$$\frac{d}{dt}(\mathcal{B}(t)) = - \sum_{j=1}^2 [\mathcal{Z}^j(t) H_{j,x^\gamma} p(t)] - (Df^\top(x^\gamma(t)) + \kappa I_2) \mathcal{B}(t). \quad (4.55)$$

Hence, $\mathcal{B}(t)$ is obtained by finding the T -periodic solution of equation (4.55) along with the normalisation condition (2.36). For the $\mathcal{C}(t)$ term, following from equation (2.38), for planar systems we have

$$\frac{d}{dt}(\mathcal{C}(t)) = - \sum_{j=1}^2 [\mathcal{I}^j(t) H_{j,x^\gamma} p(t)] - Df^\top(x^\gamma(t)) \mathcal{C}(t), \quad (4.56)$$

where $\mathcal{I}^j(t) = \partial\psi / \partial x_j|_{x^\gamma}$. Then, the T -periodic solution of equation (4.56) along with the normalisation condition (2.39) gives $\mathcal{C}(t)$.

However, for PWL case, one has to be careful while evolving $\mathcal{B}(t)$, $\mathcal{C}(t)$, and $p(t)$ across the boundary crossing. For planar PWL systems in the form (4.4), by following the definition (2.19)-(2.20), the T -periodic eigenfunction $p(t)$ can be explicitly written as

$$p(t) = \begin{cases} e^{-\kappa t} e^{A_1 t} \bar{v}, & 0 \leq t < t_1, \\ e^{-\kappa t} e^{A_2(t-T_1)} S_1 e^{A_1 T_1} \bar{v}, & t_1 \leq t < t_2, \\ \vdots & \\ e^{-\kappa t} e^{A_N(t-T_{N-1})} \dots S_2 e^{A_2(T_2)} S_1 e^{A_1 T_1} \bar{v}, & t_{N-1} \leq t < T, \\ e^{-\kappa T} S_N e^{A_N(T_N)} \dots S_2 e^{A_2(T_2)} S_1 e^{A_1 T_1} \bar{v}, & t = T. \end{cases} \quad (4.57)$$

where \bar{v} is the eigenvector associated with non-trivial Floquet multiplier. For the PWL models considered, in Fig. 4.7, we illustrate the voltage component of the eigenfunction $p(t)$ along with the underlying v -component of the periodic orbit.

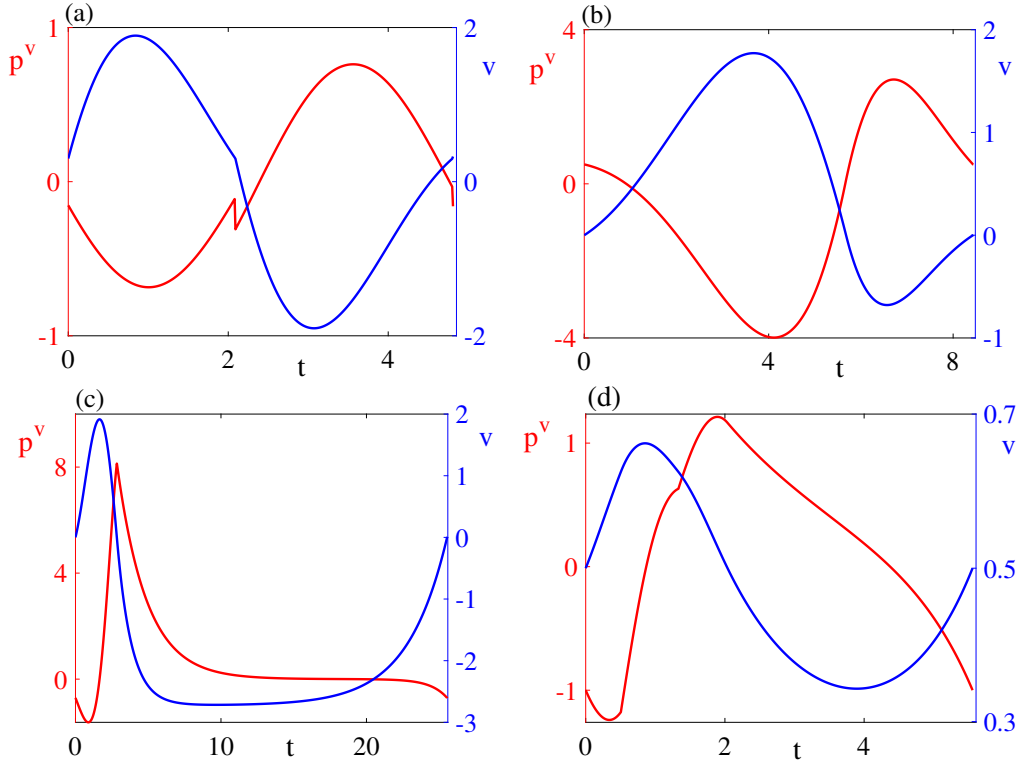


Figure 4.7: Plots of the v -component of the eigenfunction $p(t)$ (red-left axis) and underlying shape of the periodic v -component (blue-right axis). (a) The McKean model with parameters as in Fig. 3.3. (b) The absolute model with parameters values as in Fig. 3.5. (c) Homoclinic loop model with parameters as in Fig. 3.7. (d) PML model with parameters as in Fig. 3.10.

Moreover, we depict periodic orbits and eigenfunctions in the (u, w) plane in Fig. 4.8 where we also plot some level sets of isostable coordinates. In the following subsections, we will show how to compute $\mathcal{B}(t)$ and $\mathcal{C}(t)$ for planar PWL systems.

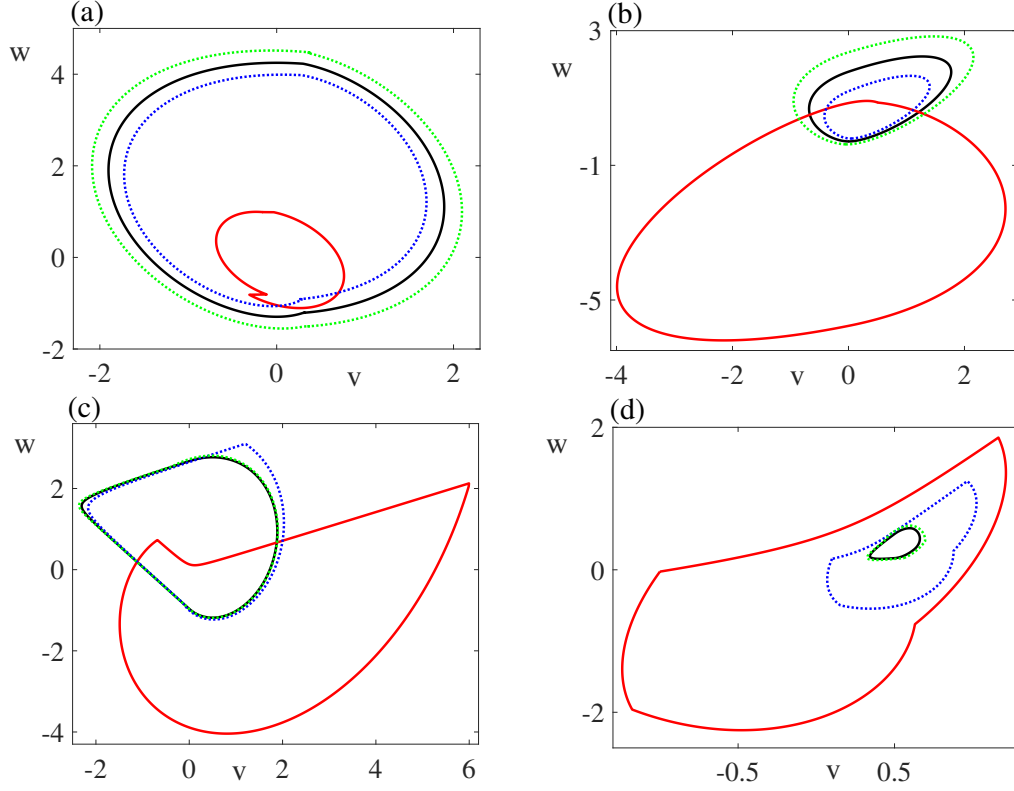


Figure 4.8: For each PWL model, plots of the eigenfunctions $p(t)$ and limit cycles $x^\gamma(t)$ are given in red and black, respectively. We illustrate two level sets of isostable coordinates, ψ_1, ψ_2 , by plotting perturbed solutions parametrised by $p(t)$ in the form $x(t) = x^\gamma(t) + \psi p(t)$ for a fixed ψ , where any point on these level sets approaches to limit cycle with a same rate. As expected, we observed that while $\psi \rightarrow 0$, $x(t) \rightarrow x^\gamma(t)$. We also calculated Floquet exponent σ of each model. (a) The McKean model that has $\sigma = -0.4705$ and eigenvector $\bar{v} = [-0.1536, 0.9881]^\top$. Isostable level sets are depicted for $\psi_1 = 0.3$ (blue) and $\psi_2 = -0.3$ (green), and parameters as in Fig. 3.3. (b) The absolute model that has $\sigma = -0.1534$ and eigenvector $\bar{v} = [0.5045, 0.8634]^\top$. Two isostable level sets $\psi_1 = 0.1$ (blue) and $\psi_2 = -0.1$ (green) are represented for parameters values as in Fig. 3.5. (c) Homoclinic loop model that has $\sigma = -0.4$ and eigenvector $\bar{v} = [-0.68266, 0.7307]^\top$. Isostable level set $\psi_1 = 0.2$ is given colour in blue and that of $\psi_2 = -0.06$ is in green. Here we choose $\tau_2 = -0.68$ and other parameters as in Fig. 3.7. (d) PML model that has $\sigma = -0.1458$ and eigenvector $\bar{v} = [-0.9997, -0.0254]^\top$, and level sets $\psi_1 = 0.4$ (blue) and $\psi_2 = -0.06$ (green) where parameters as in Fig. 3.10.

4.5.1 Computing $\mathcal{B}(t)$ for piecewise linear systems

For planar PWL systems, the Hessian matrices $H_{j,x^\gamma} = \nabla (\nabla f_j) |_{x^\gamma}$, $j = 1, 2$, are zero matrices, and therefore using a similar labelling introduced for the periodic orbit of (4.4), inside the each subregion R_μ , $\mathcal{B}(t)$ evolves according to

$$\frac{d}{dt}(\mathcal{B}_\mu(t)) = -(A_\mu^\top + \kappa I_2)\mathcal{B}_\mu(t), \quad (4.58)$$

By denoting $K_\mu = -(A_\mu^\top + \kappa I_2)$, we can explicitly write solution of each subsystem as $\mathcal{B}_\mu(t) = G(K_\mu; t - t_{\mu-1})\mathcal{B}_\mu(t_{\mu-1})$ where $t_{\mu-1} \leq t < t_\mu$ and $\mathcal{B}_\mu(t_{\mu-1})$ is the initial value at each subregion. Thereafter, we need to determine how $\mathcal{B}(t)$ evolves across a switching boundary. For brevity, at each switching event time t_μ , we denote \mathcal{B}_μ^- for $\mathcal{B}(t)$ which is evaluated immediately before the crossing, and \mathcal{B}_μ^+ for that of just after. Using equation (2.20), let us consider a perturbed solution in the form $x(t) = x^\gamma + \psi p(t)$, where $\psi = \mathcal{O}(\epsilon)$ has a small value, such that perturbed trajectory crosses the switching manifolds at the perturbed switching times $\tilde{t}_\mu = t_\mu + g_\mu(\psi)$ which are prescribed by the continuous indicator functions $h_\mu(x(t_\mu + g_\mu(\psi))) = 0$. In general, $g_\mu(\psi)$ will depend on the geometry of a switching surface and the displacement $\psi p(t)$. For the PWL models considered here, one can explicitly calculate $g_\mu(\psi)$ as follows. A first order Taylor expansion of $h_\mu(\tilde{x}(\tilde{t}_\mu))$ can be calculated as

$$\begin{aligned} h_\mu(\tilde{x}(\tilde{t}_\mu)) &= h_\mu(x(t_\mu + g_\mu(\psi))) = h_\mu(x^\gamma(t_\mu + g_\mu(\psi)) + \psi p(t_\mu + g_\mu(\psi))) \\ &\simeq h_\mu(x^\gamma(t_\mu^-) + \dot{x}^\gamma(t_\mu^-)g_\mu(\psi)) + \nabla_x h_\mu(x^\gamma(t_\mu^- + g_\mu(\psi))) \cdot \\ &\quad \psi p(t_\mu^- + g_\mu(\psi)) \\ &\simeq h_\mu(x^\gamma(t_\mu^-)) + \nabla_x h_\mu(x^\gamma(t_\mu^-)) \cdot \dot{x}^\gamma(t_\mu^-)g_\mu(\psi) + \nabla_x h_\mu(x^\gamma(t_\mu^-)) \cdot \psi p(t_\mu^-). \end{aligned} \quad (4.59)$$

Since $h_\mu(x^\gamma(t_\mu)) = 0 = h_\mu(\tilde{x}(\tilde{t}_\mu))$ then we have that

$$g_\mu(\psi) = -\frac{\nabla_x h_\mu(x^\gamma(t_\mu^-)) \cdot \psi p(t_\mu^-)}{\nabla_x h_\mu(x^\gamma(t_\mu^-)) \cdot \dot{x}^\gamma(t_\mu^-)} = -\frac{\psi p^v(t_\mu^-)}{\dot{v}^\gamma(t_\mu^-)}, \quad (4.60)$$

where $p^v(t)$ is the first component of $p(t)$. Equation (2.16) implies that immediately before the switching event we have

$$\begin{aligned} \frac{\partial \theta}{\partial x} \Big|_{x^\gamma(\tilde{t}_\mu^-) + \psi p(\tilde{t}_\mu^-)} &= \frac{\partial \theta}{\partial x} \Big|_{x^\gamma(\tilde{t}_\mu^-)} + \frac{\partial^2 \theta}{\partial x^2} \Big|_{x^\gamma(\tilde{t}_\mu^-)} \psi p(\tilde{t}_\mu^-) + \mathcal{O}(\epsilon^2) \\ &\simeq \mathcal{Z}_\mu(t_\mu^- + g_\mu(\psi)) + \psi \mathcal{B}_\mu(t_\mu^- + g_\mu(\psi)). \end{aligned} \quad (4.61)$$

A similar equation immediately after is obtained by evaluating (2.16) at $\tilde{t}_\mu^+ = t_\mu^+ + g_\mu(\psi)$. Using continuity of $\theta(x)$ and the above assumption (iv) for the phase function, while approaching from either side of the switching manifold, we have

$$\left(\frac{\partial \theta}{\partial x} \Big|_{x^\gamma(\tilde{t}_\mu^-) + \psi p(\tilde{t}_\mu^-)} \right) \cdot w_1 = \left(\frac{\partial \theta}{\partial x} \Big|_{x^\gamma(\tilde{t}_\mu^+) + \psi p(\tilde{t}_\mu^+)} \right) \cdot w_1, \quad (4.62)$$

or equivalently,

$$\begin{aligned} [\mathcal{Z}_\mu(t_\mu^- + g_\mu(\psi)) + \psi \mathcal{B}_\mu(t_\mu^- + g_\mu(\psi))] \cdot w_1 &= [\mathcal{Z}_\mu(t_\mu^+ + g_\mu(\psi)) \\ &\quad + \psi \mathcal{B}_\mu(t_\mu^+ + g_\mu(\psi))] \cdot w_1. \end{aligned} \quad (4.63)$$

Taylor expanding this in orders of ψ gives

$$\begin{aligned} &\left[\mathcal{Z}_\mu(t_\mu^-) + \left(\frac{d\mathcal{Z}_\mu}{dt} \Big|_{t=t_\mu^-} \right) g_\mu(\psi) + \psi \mathcal{B}_\mu(t_\mu^-) \right] \cdot w_1 \\ &= \left[\mathcal{Z}_\mu(t_\mu^+) + \left(\frac{d\mathcal{Z}_\mu}{dt} \Big|_{t=t_\mu^+} \right) g_\mu(\psi) + \psi \mathcal{B}_\mu(t_\mu^+) \right] \cdot w_1 + \mathcal{O}(\psi^2). \end{aligned} \quad (4.64)$$

Setting the $\mathcal{O}(\psi^0)$ terms equal on either side of this equation yields the relation given by (4.27). Using this along with normalisation conditions (see equation (4.28)) we can construct the jump operator for \mathcal{Z} at t_μ , which is exactly the same as given by equation (4.30). By collecting the $\mathcal{O}(\psi)$ terms in equation

(4.64) we obtain the following

$$\left[\left(\frac{d\mathcal{Z}_\mu}{dt} \Big|_{t=t_\mu^-} \right) g_\mu(\psi) + \psi \mathcal{B}_\mu^- \right] \cdot w_1 = \left[\left(\frac{d\mathcal{Z}_\mu}{dt} \Big|_{t=t_\mu^+} \right) g_\mu(\psi) + \psi \mathcal{B}_\mu^+ \right] \cdot w_1. \quad (4.65)$$

We may use equation (4.15) and (4.60) to rewrite (4.65) to obtain

$$\psi \left[\frac{p^v(t_\mu^-)}{\dot{v}^\gamma(t_\mu^-)} A_\mu^\top \mathcal{Z}_\mu^- + \mathcal{B}_\mu^- \right] \cdot w_1 = \psi \left[\frac{p^v(t_\mu^-)}{\dot{v}^\gamma(t_\mu^-)} A_{\mu+1}^\top \mathcal{Z}_\mu^+ + \mathcal{B}_\mu^+ \right] \cdot w_1. \quad (4.66)$$

In addition, the normalisation condition (2.36) holds on either sides of a switching manifold and therefore we have that

$$\mathcal{Z}_\mu^- \cdot (A_\mu p(t_\mu^-)) + f_\mu^- \cdot \mathcal{B}_\mu^- = 0 = \mathcal{Z}_\mu^+ \cdot (A_{\mu+1} p(t_\mu^+)) + f_\mu^+ \cdot \mathcal{B}_\mu^+. \quad (4.67)$$

Combining (4.67) and (4.66) we have that

$$\begin{aligned} \mathcal{B}_\mu^+ \cdot f_\mu^+ &= \mathcal{B}_\mu^- \cdot f_\mu^- + \mathcal{Z}_\mu^- \cdot (A_\mu p(t_\mu^-)) - \mathcal{Z}_\mu^+ \cdot (A_{\mu+1} p(t_\mu^+)) \\ \mathcal{B}_\mu^+ \cdot w_1 &= \mathcal{B}_\mu^- \cdot w_1 + \frac{p^v(t_\mu^-)}{\dot{v}^\gamma(t_\mu^-)} [A_\mu^\top \mathcal{Z}_\mu^- - A_{\mu+1}^\top \mathcal{Z}_\mu^+] \cdot w_1. \end{aligned} \quad (4.68)$$

Hence, the jump condition on \mathcal{B} during the transition across a switching manifold is

$$\mathcal{B}_\mu^+ = C_\mu^{-1} (D_\mu \mathcal{B}_\mu^- + \sigma_\mu) = (S_\mu^\top)^{-1} \mathcal{B}_\mu^- + C_\mu^{-1} \sigma_\mu, \quad (4.69)$$

where σ_μ is the following vector

$$\sigma_\mu = \begin{bmatrix} \mathcal{Z}_\mu^- \cdot (A_\mu p(t_\mu^-)) - \mathcal{Z}_\mu^+ \cdot (A_{\mu+1} p(t_\mu^+)) \\ \frac{p^v(t_\mu^-)}{\dot{v}^\gamma(t_\mu^-)} (A_\mu^\top \mathcal{Z}_\mu^- - A_{\mu+1}^\top \mathcal{Z}_\mu^+) \cdot (0, 1) \end{bmatrix}. \quad (4.70)$$

The $\mathcal{B}(t)$ of the McKean model, the absolute model, and the homoclinic model are calculated from

$$\mathcal{B}(t) = \begin{cases} G(K_1; t)\mathcal{B}(0), & 0 \leq t < T_1, \\ G(K_2; t - T_1)[(S_1^\top)^{-1}G(K_1; T_1)\mathcal{B}(0) + C_1^{-1}\sigma_1], & T_1 \leq t < T, \\ (S_2^\top)^{-1}(G(K_2; T_2)[(S_1^\top)^{-1}G(K_1; T_1)\mathcal{B}(0) + C_1^{-1}\sigma_1]) + C_2^{-1}\sigma_2, & t = T, \end{cases}$$

where we need to determine initial condition $\mathcal{B}(0) = [b_0^1, b_0^2]^\top$. To do so we use the normalisation condition (2.36),

$$b_0^1 \dot{v}^\gamma(0) + b_0^2 \dot{w}^\gamma(0) = -\mathcal{Z}(0)^\top Df(x^\gamma(0))p(0) \equiv \tilde{q}, \quad (4.71)$$

where $\tilde{q} \in \mathbb{R}$ and also use the periodicity condition $\mathcal{B}(0) = \mathcal{B}(T)$. By introducing $\Gamma^{B_1} \in \mathbb{R}^{2 \times 2}$ and $\Gamma^{B_2} \in \mathbb{R}^{2 \times 1}$ as follows

$$\Gamma^{B_1} = (S_2^\top)^{-1}G(K_2; T_2)(S_1^\top)^{-1}G(K_1; T_1), \quad (4.72)$$

$$\Gamma^{B_2} = (S_2^\top)^{-1}G(K_2; T_2)C_1^{-1}\sigma_1 + C_2^{-1}\sigma_2, \quad (4.73)$$

we can write

$$\mathcal{B}(0) = \Gamma^{B_1}\mathcal{B}(0) + \Gamma^{B_2}. \quad (4.74)$$

Hence, using (4.71) and (4.74) we have

$$\Psi^B \begin{bmatrix} b_0^1 \\ b_0^2 \end{bmatrix} = \begin{bmatrix} -\Gamma_1^{B_2} \\ \tilde{q} \end{bmatrix}, \quad \Psi^B = \begin{bmatrix} \Gamma_{11}^{B_1} - 1 & \Gamma_{12}^{B_1} \\ \dot{v}^\gamma(0) & \dot{w}^\gamma(0) \end{bmatrix}$$

Using Cramer's rule, we solve this to yield

$$b_0^1 = \det(\Psi_1^B) / \det(\Psi^B) \quad \text{and} \quad b_0^2 = \det(\Psi_2^B) / \det(\Psi^B), \quad (4.75)$$

where

$$\Psi_1^B = \begin{bmatrix} -\Gamma_1^{B_2} & \Gamma_{12}^{B_1} \\ \tilde{q} & \dot{w}^\gamma(0) \end{bmatrix}, \quad \Psi_2^B = \begin{bmatrix} \Gamma_{11}^{B_1} - 1 & -\Gamma_1^{B_2} \\ \dot{v}^\gamma(0) & \tilde{q} \end{bmatrix}.$$

Similarly, we can also build $\mathcal{B}(t)$ for the PML model, by solving \mathcal{B} over four subregions. To illustrate some examples, in Fig. 4.9, we plot $\mathcal{B}(t)$ for the McKean model and PML model.

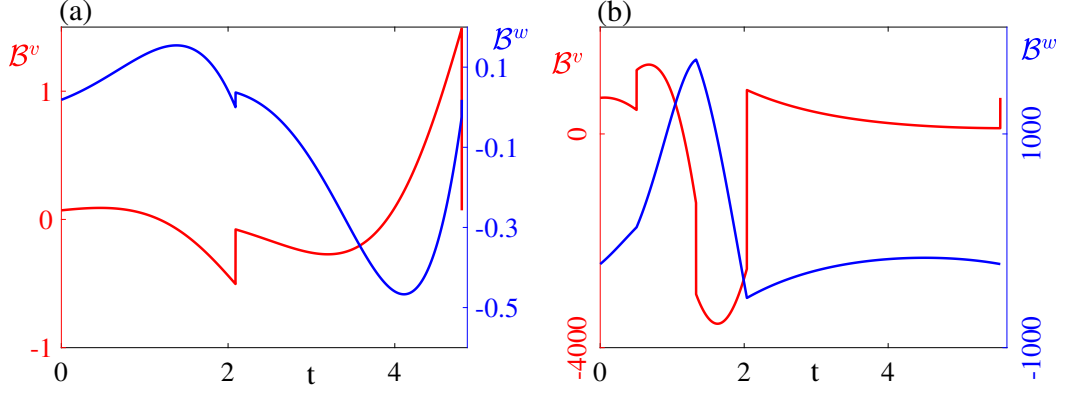


Figure 4.9: Plots of the v and w components of the function $\mathcal{B}(t)$ on the left and right y axis, respectively. (a) The McKean model with parameters as in Fig. 3.3. (b) PML model with parameters as in Fig. 3.10.

4.5.2 Computing $\mathcal{C}(t)$ for piecewise linear systems

For planar PWL systems, we use equation (4.56) and replace the Hessian matrices by zero matrices, therefore, inside the each subregion R_μ , $\mathcal{C}(t)$ evolves according to

$$\frac{d}{dt}(\mathcal{C}_\mu(t)) = -A_\mu^\top \mathcal{C}_\mu(t), \quad (4.76)$$

which is same as that of \mathcal{Z} . We can explicitly write the solution of each subsystem as $\mathcal{C}_\mu(t) = G(-A_\mu^\top; t - t_{\mu-1})\mathcal{C}_\mu(t_{\mu-1})$ where $t_{\mu-1} \leq t < t_\mu$ and $\mathcal{C}_\mu(t_{\mu-1})$ is the initial value at each subregion. Now, we need to determine how $\mathcal{C}(t)$ evolves across a switching surface. By following similar steps as for the calculation of $\mathcal{B}(t)$, and using (2.17), (4.60), along with continuity of ψ and assumption (iv) for the isostable coordinates we obtain

$$\begin{aligned} & \left[\mathcal{I}_\mu(t_\mu^-) + \left(\frac{d\mathcal{I}_\mu}{dt} \Big|_{t=t_\mu^-} \right) g_\mu(\psi) + \psi \mathcal{C}_\mu(t_\mu^-) \right] \cdot w_1 \\ &= \left[\mathcal{I}_\mu(t_\mu^+) + \left(\frac{d\mathcal{I}_\mu}{dt} \Big|_{t=t_\mu^+} \right) g_\mu(\psi) + \psi \mathcal{C}_\mu(t_\mu^+) \right] \cdot w_1 + \mathcal{O}(\psi^2). \end{aligned} \quad (4.77)$$

Setting the $\mathcal{O}(\psi^0)$ terms equal on either side of this equation yields the relation given by (4.38). Using this along with the normalisation condition (4.39), we can construct the jump matrix for \mathcal{I} at t_μ , which is exactly same as given in above Section 4.4. By collecting the $\mathcal{O}(\psi)$ terms in equation (4.77) we obtain the following

$$\left[\left(\frac{d\mathcal{I}_\mu}{dt} \Big|_{t=t_\mu^-} \right) g_\mu(\psi) + \psi \mathcal{C}_\mu^- \right] \cdot w_1 = \left[\left(\frac{d\mathcal{I}_\mu}{dt} \Big|_{t=t_\mu^+} \right) g_\mu(\psi) + \psi \mathcal{C}_\mu^+ \right] \cdot w_1. \quad (4.78)$$

We may use equation (4.37) and (4.60) to rewrite (4.78), to derive

$$\psi \left[\frac{p^v(t_\mu^-)}{\dot{v}^\gamma(t_\mu^-)} (A_\mu^\top - \kappa I_2) \mathcal{I}_\mu^- + \mathcal{C}_\mu^- \right] \cdot w_1 = \psi \left[\frac{p^v(t_\mu^-)}{\dot{v}^\gamma(t_\mu^-)} (A_{\mu+1}^\top - \kappa I_2) \mathcal{I}_\mu^+ + \mathcal{C}_\mu^+ \right] \cdot w_1. \quad (4.79)$$

Additionally, the normalisation condition (2.39) holds on either sides of a switching boundary and therefore we have that

$$\mathcal{I}_\mu^- \cdot [(\kappa I_2 - A_\mu) p(t_\mu^-)] - f_\mu^- \cdot \mathcal{C}_\mu^- = 0 = \mathcal{I}_\mu^+ \cdot [(\kappa I_2 - A_{\mu+1}) p(t_\mu^+)] - f_\mu^+ \cdot \mathcal{C}_\mu^+. \quad (4.80)$$

Using (4.80) and (4.79) we have that

$$\begin{aligned} \mathcal{C}_\mu^+ \cdot f_\mu^+ &= \mathcal{C}_\mu^- \cdot f_\mu^- + \mathcal{I}_\mu^+ \cdot [(\kappa I_2 - A_{\mu+1}) p(t_\mu^+)] - \mathcal{I}_\mu^- \cdot [(\kappa I_2 - A_\mu) p(t_\mu^-)] \\ \mathcal{C}_\mu^+ \cdot w_1 &= \mathcal{C}_\mu^- \cdot w_1 + \frac{p^v(t_\mu^-)}{\dot{v}^\gamma(t_\mu^-)} [(A_\mu^\top - \kappa I_2) \mathcal{I}_\mu^- - (A_{\mu+1}^\top - \kappa I_2) \mathcal{I}_\mu^+] \cdot w_1. \end{aligned} \quad (4.81)$$

Thus, the jump condition on \mathcal{C} during the transition across a switching boundary is

$$\mathcal{C}_\mu^+ = \mathcal{C}_\mu^{-1} (D_\mu \mathcal{C}_\mu^- + \rho_\mu) = (S_\mu^\top)^{-1} \mathcal{C}_\mu^- + \mathcal{C}_\mu^{-1} \rho_\mu, \quad (4.82)$$

where ρ_μ is the following vector

$$\rho_\mu = \begin{bmatrix} \mathcal{I}_\mu^+ \cdot [(\kappa I_2 - A_{\mu+1})p(t_\mu^+)] - \mathcal{I}_\mu^- \cdot [(\kappa I_2 - A_\mu)p(t_\mu^-)] \\ \frac{p^v(t_\mu^-)}{\dot{v}^\gamma(t_\mu^-)} [(A_\mu^\top - \kappa I_2)\mathcal{I}_\mu^- - (A_{\mu+1}^\top - \kappa I_2)\mathcal{I}_\mu^+] \cdot (0, 1) \end{bmatrix}. \quad (4.83)$$

The $\mathcal{C}(t)$ of the McKean model, the absolute model, and the homoclinic model are calculated from

$$\mathcal{C}(t) = \begin{cases} G(-A_1^\top; t)\mathcal{C}(0), & 0 \leq t < T_1, \\ G(-A_2^\top; t - T_1)[(S_1^\top)^{-1}G(-A_1^\top; T_1)\mathcal{C}(0) + C_1^{-1}\rho_1], & T_1 \leq t < T, \\ (S_2^\top)^{-1}(G(-A_2^\top; T_2)[(S_1^\top)^{-1}G(-A_1^\top; T_1)\mathcal{C}(0) + C_1^{-1}\rho_1]) + C_2^{-1}\rho_2, & t = T, \end{cases}$$

where we need to determine initial condition $\mathcal{C}(0) = [c_0^1, c_0^2]^\top$. To do so we need two equations and one of them is obtained from the normalisation condition (2.39) as

$$c_0^1 \dot{v}^\gamma(0) + c_0^2 \dot{w}^\gamma(0) = \mathcal{I}(0)^\top (\kappa I_2 - Df(x^\gamma(0))) p(0) \equiv \tilde{r}, \quad (4.84)$$

where $\tilde{r} \in \mathbb{R}$. By introducing $\Gamma^{C_1} \in \mathbb{R}^{2 \times 2}$ and $\Gamma^{C_2} \in \mathbb{R}^{2 \times 1}$:

$$\Gamma^{C_1} = (S_2^\top)^{-1}G(-A_2^\top; T_2)(S_1^\top)^{-1}G(-A_1^\top; T_1), \quad (4.85)$$

$$\Gamma^{C_2} = (S_2^\top)^{-1}G(-A_2^\top; T_2)C_1^{-1}\rho_1 + C_2^{-1}\rho_2, \quad (4.86)$$

and using periodicity condition $\mathcal{C}(0) = \mathcal{C}(T)$, we can write

$$\mathcal{C}(0) = \Gamma^{C_1}\mathcal{C}(0) + \Gamma^{C_2}. \quad (4.87)$$

Thus, (4.84), (4.87), and a similar calculation for $\mathcal{B}(t)$ give

$$c_0^1 = \det(\Psi_1^C) / \det(\Psi^C) \quad \text{and} \quad c_0^2 = \det(\Psi_2^C) / \det(\Psi^C), \quad (4.88)$$

where

$$\Psi^C = \begin{bmatrix} \Gamma_{11}^{C_1} - 1 & \Gamma_{12}^{C_1} \\ \dot{v}^\gamma(0) & \dot{w}^\gamma(0) \end{bmatrix}, \quad \Psi_1^C = \begin{bmatrix} -\Gamma_1^{C_2} & \Gamma_{12}^{C_1} \\ \tilde{r} & \dot{w}^\gamma(0) \end{bmatrix}, \quad \Psi_2^C = \begin{bmatrix} \Gamma_{11}^{C_1} - 1 & -\Gamma_1^{C_2} \\ \dot{v}^\gamma(0) & \tilde{r} \end{bmatrix}.$$

A similar procedure allows us to build $\mathcal{C}(t)$ for the PML model, by solving $\mathcal{C}(t)$ over four subregions. For illustrative purposes, in Fig. 4.10, we plot $\mathcal{C}(t)$ for the absolute model and the PML model. In these plots, dots are obtained through direct numerical simulation of the original systems. To clarify direct computation process, let us rewrite equation (2.17) for planar systems

$$\begin{aligned} \left. \frac{\partial \psi}{\partial x} \right|_{x^\gamma + \Delta x} &= \left. \frac{\partial \psi}{\partial x} \right|_{x^\gamma} + \left. \frac{\partial^2 \psi}{\partial x^2} \right|_{x^\gamma} \Delta x + \mathcal{O}(\|\Delta x\|^2) \\ &\simeq \mathcal{I}(t) + \psi_c \mathcal{C}(t), \end{aligned} \quad (4.89)$$

where $\Delta x = \psi_c p(t)$ for some fixed small ψ_c . Then we shall evaluate these, say in the w component, by choosing a perturbation in the form $\delta x = [0, \delta w]^\top$ at various locations along the cycle as follows.

$$\begin{aligned} \psi_c \mathcal{C}^w(t) &\simeq \lim_{\delta w \rightarrow 0} \frac{\psi(x^\gamma(t) + \Delta x(t) + \delta x) - \psi(x^\gamma(t) + \Delta x(t))}{\delta w} \\ &\quad - \lim_{\delta w \rightarrow 0} \frac{\psi(x^\gamma(t) + \delta x) - \psi(x^\gamma(t))}{\delta w} \\ &= \lim_{\delta w \rightarrow 0} \frac{\psi(x^\gamma(t) + \Delta x(t) + \delta x) - \psi(x^\gamma(t) + \Delta x(t)) - \psi(x^\gamma(t) + \delta x)}{\delta w}, \end{aligned}$$

where we know $\psi(x^\gamma(t)) = 0$. We may dividing both sides by ψ_c and approximate $\mathcal{C}^w(t)$, at each location, by

$$\mathcal{C}^w(t) = \frac{\psi(x^\gamma(t) + \Delta x(t) + \delta x) - \psi(x^\gamma(t) + \Delta x(t))}{\psi_c \delta w} - \frac{\mathcal{I}^w(t)}{\psi_c}, \quad (4.90)$$

where we can calculate $\psi(x^\gamma(t) + \Delta x(t) + \delta x)$ and $\psi(x^\gamma(t) + \Delta x(t))$ from formula (2.10), and $\mathcal{I}^w(t)$ has been approximated in equation (4.52). In a similar way one can calculate $\mathcal{C}^v(t)$ by choosing $\delta x = [\delta v, 0]^\top$.

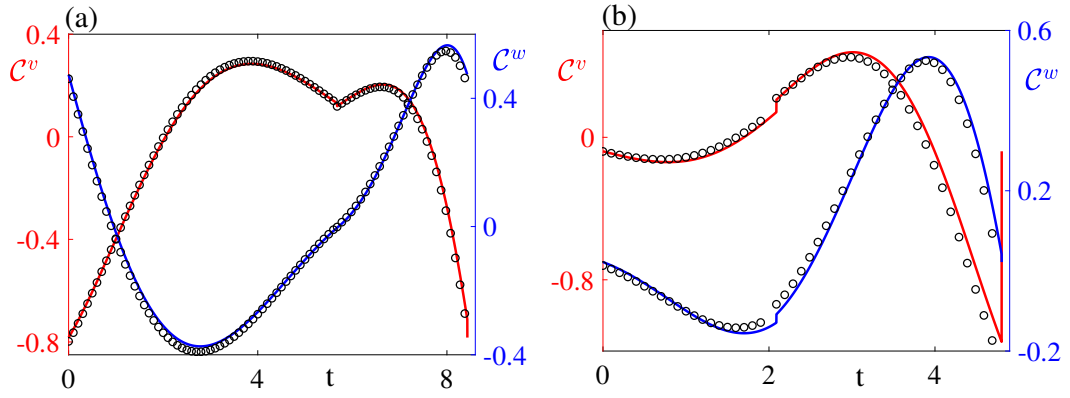


Figure 4.10: Plots of v and w components of the function $C(t)$ on the left and right y -axis, respectively. Black circles are obtained from direct numerical simulation. (a) The absolute model has parameters as in Fig. 3.5, we choose $\delta v = \delta w = 0.0001$, and $\psi_c = 0.01$. (b)-The McKean model with parameters as in Fig. 3.3, $\delta v = \delta w = 0.012$, and $\psi_c = 0.16$. Theory and direct numerical evaluation show a good agreement.

4.6 Synchronization of coupled oscillators with piecewise linear dynamics

The stability properties of the synchronous state in networks of piecewise linear oscillators has been studied in [52, 54, 227] where the authors used MSF, and weak coupling theory. Here we extend the phase-amplitude reduction, and MSF approach to treat networks of nonsmooth PWL oscillators.

For ease of exposition we shall focus on a network of two identical nodes. We shall consider diffusive coupling through the v component. This form of coupling is also referred as to gap junction coupling and has a common use in the context of biological neural networks [52, 55]. In this case, the network dynamics can be written in the form

$$\begin{aligned} \begin{bmatrix} \dot{v}_1 \\ \dot{w}_1 \end{bmatrix} &= \left(A_{\mu_1} \begin{bmatrix} v_1 \\ w_1 \end{bmatrix} + b_{\mu_1} \right) + \sigma \begin{bmatrix} v_2 - v_1 \\ 0 \end{bmatrix}, \\ \begin{bmatrix} \dot{v}_2 \\ \dot{w}_2 \end{bmatrix} &= \left(A_{\mu_2} \begin{bmatrix} v_2 \\ w_2 \end{bmatrix} + b_{\mu_2} \right) + \sigma \begin{bmatrix} v_1 - v_2 \\ 0 \end{bmatrix}, \end{aligned} \quad (4.91)$$

where each node evolves in the corresponding region R_{μ_i} , $i = 1, 2$, and $\mu_1, \mu_2 \in \{1, \dots, N\}$. Here we aim to determine the stability of the synchronous state

by implementing both the MSF approach and coupled phase-amplitude framework and comparing their results; the MSF being exact makes an interesting bench-mark for the phase-amplitude reduction.

4.6.1 Networks of two phase-amplitude units

Ermentrout *et. al* [92] employed second-order accurate phase-amplitude reduction formalism to analyse the stability of the synchronous state for a pair of synaptically coupled thalamic neurons [261]. Since, their model is a smooth one, they computed iPRC, iIRC, and second-order terms \mathcal{B} , \mathcal{C} numerically using the methods presented in Chapter 2. As we discussed above in Sections 4.3-4.5 (for piecewise linear oscillators) these terms may have discontinuities. Here we will extend the the work in [92] to treat piecewise linear oscillators. To do so, we first rewrite (4.91) in the phase-amplitude network setting form as follows

$$\begin{aligned}\frac{d\theta_i}{dt} &= \omega + \sigma [\mathcal{Z}(\theta_i) + \psi_i \mathcal{B}(\theta_i)] g_i(t), \\ \frac{d\psi_i}{dt} &= \kappa \psi_i + \sigma [\mathcal{I}(\theta_i) + \psi_i \mathcal{C}(\theta_i)] g_i(t), \quad i = 1, 2,\end{aligned}\tag{4.92}$$

where

$$\begin{aligned}g_1(t) &= [v_2(t) - v_1(t), 0]^\top, \\ g_2(t) &= [v_1(t) - v_2(t), 0]^\top.\end{aligned}\tag{4.93}$$

Here, the four periodic vector functions \mathcal{Z} , \mathcal{I} , \mathcal{B} and \mathcal{C} are all computed by using the PWL node dynamics as explained in Sections 4.3, 4.4, and Subsections 4.5.1, 4.5.2, respectively. Setting perturbed solutions around the periodic orbit by using equation (2.20), in the v -components, we have $v_i(t) = v^\gamma(\theta_i(t)) + \psi_i(t)p^v(\theta_i(t))$, and this gives

$$\begin{aligned}g_1(t) &= [v^\gamma(\theta_2(t)) + \psi_2(t)p^v(\theta_2(t)) - v^\gamma(\theta_1(t)) - \psi_1(t)p^v(\theta_1(t)), 0]^\top, \\ g_2(t) &= [v^\gamma(\theta_1(t)) + \psi_1(t)p^v(\theta_1(t)) - v^\gamma(\theta_2(t)) - \psi_2(t)p^v(\theta_2(t)), 0]^\top,\end{aligned}\tag{4.94}$$

where we assumed ψ_1 and ψ_2 are $\mathcal{O}(\epsilon)$ terms, and we obtained periodic function p from (4.57). We then put g_1 and g_2 into (4.92) and expand this by only

keeping terms to a leading order $\mathcal{O}(\epsilon^2)$, and find

$$\begin{aligned}
\dot{\theta}_1 = & \omega + \sigma [\mathcal{Z}^v(\theta_1) [v^\gamma(\theta_2) - v^\gamma(\theta_1)] + \psi_1 [\mathcal{B}^v(\theta_1) (v^\gamma(\theta_2) - v^\gamma(\theta_1)) \\
& - \mathcal{Z}^v(\theta_1) p^v(\theta_1)] + \psi_2 \mathcal{Z}^v(\theta_1) p^v(\theta_2)], \\
\dot{\psi}_1 = & \kappa \psi_1 + \sigma [\mathcal{I}^v(\theta_1) (v^\gamma(\theta_2) - v^\gamma(\theta_1)) + \psi_1 [\mathcal{C}^v(\theta_1) (v^\gamma(\theta_2) - v^\gamma(\theta_1)) \\
& - \mathcal{I}^v(\theta_1) p^v(\theta_1)] + \psi_2 \mathcal{I}^v(\theta_1) p^v(\theta_2)], \\
\dot{\theta}_2 = & \omega + \sigma [\mathcal{Z}^v(\theta_2) [v^\gamma(\theta_1) - v^\gamma(\theta_2)] + \psi_1 \mathcal{Z}^v(\theta_2) p^v(\theta_1) \\
& + \psi_2 [\mathcal{B}^v(\theta_2) (v^\gamma(\theta_1) - v^\gamma(\theta_2)) - \mathcal{Z}^v(\theta_2) p^v(\theta_2)]], \\
\dot{\psi}_2 = & \kappa \psi_2 + \sigma [\mathcal{I}^v(\theta_2) (v^\gamma(\theta_1) - v^\gamma(\theta_2)) + \psi_1 \mathcal{I}^v(\theta_2) p^v(\theta_1) \\
& + \psi_2 [\mathcal{C}^v(\theta_2) (v^\gamma(\theta_1) - v^\gamma(\theta_2)) - \mathcal{I}^v(\theta_2) p^v(\theta_2)]],
\end{aligned} \tag{4.95}$$

where $\mathcal{Z}^v, \mathcal{I}^v, \mathcal{B}^v$ and \mathcal{C}^v are the v component of the corresponding vectors.

Then by denoting

$$\begin{aligned}
h_1(\theta_1, \theta_2) &= \mathcal{Z}^v(\theta_1) (v^\gamma(\theta_2) - v^\gamma(\theta_1)), \\
h_2(\theta_1, \theta_2) &= \mathcal{B}^v(\theta_1) (v^\gamma(\theta_2) - v^\gamma(\theta_1)) - \mathcal{Z}^v(\theta_1) p^v(\theta_1), \\
h_3(\theta_1, \theta_2) &= \mathcal{Z}^v(\theta_1) p^v(\theta_2), \\
h_4(\theta_1, \theta_2) &= \mathcal{I}^v(\theta_1) (v^\gamma(\theta_2) - v^\gamma(\theta_1)), \\
h_5(\theta_1, \theta_2) &= \mathcal{C}^v(\theta_1) (v^\gamma(\theta_2) - v^\gamma(\theta_1)) - \mathcal{I}^v(\theta_1) p^v(\theta_1), \\
h_6(\theta_1, \theta_2) &= \mathcal{I}^v(\theta_1) p^v(\theta_2),
\end{aligned}$$

we may rewrite system (4.95) in the form

$$\begin{aligned}
\dot{\theta}_1 &= \omega + \sigma [h_1(\theta_1, \theta_2) + \psi_1 h_2(\theta_1, \theta_2) + \psi_2 h_3(\theta_1, \theta_2)], \\
\dot{\psi}_1 &= \kappa \psi_1 + \sigma [h_4(\theta_1, \theta_2) + \psi_1 h_5(\theta_1, \theta_2) + \psi_2 h_6(\theta_1, \theta_2)], \\
\dot{\theta}_2 &= \omega + \sigma [h_1(\theta_2, \theta_1) + \psi_2 h_2(\theta_2, \theta_1) + \psi_1 h_3(\theta_2, \theta_1)], \\
\dot{\psi}_2 &= \kappa \psi_2 + \sigma [h_4(\theta_2, \theta_1) + \psi_2 h_5(\theta_2, \theta_1) + \psi_1 h_6(\theta_2, \theta_1)].
\end{aligned} \tag{4.96}$$

Now we introduce rotating phase variables ϕ_j as $\theta_j = \phi_j + \omega t$ and substitute into (4.96), to obtain

$$\begin{aligned}
\dot{\phi}_1 &= \sigma [h_1(\phi_1 + \omega t, \phi_2 + \omega t) + \psi_1 h_2(\phi_1 + \omega t, \phi_2 + \omega t) \\
&\quad + \psi_2 h_3(\phi_1 + \omega t, \phi_2 + \omega t)], \\
\dot{\psi}_1 &= \kappa \psi_1 + \sigma [h_4(\phi_1 + \omega t, \phi_2 + \omega t) + \psi_1 h_5(\phi_1 + \omega t, \phi_2 + \omega t) \\
&\quad + \psi_2 h_6(\phi_1 + \omega t, \phi_2 + \omega t)], \\
\dot{\phi}_2 &= \sigma [h_1(\phi_2 + \omega t, \phi_1 + \omega t) + \psi_2 h_2(\phi_2 + \omega t, \phi_1 + \omega t) \\
&\quad + \psi_1 h_3(\phi_2 + \omega t, \phi_1 + \omega t)], \\
\dot{\psi}_2 &= \kappa \psi_2 + \sigma [h_4(\phi_2 + \omega t, \phi_1 + \omega t) + \psi_2 h_5(\phi_2 + \omega t, \phi_1 + \omega t) \\
&\quad + \psi_1 h_6(\phi_2 + \omega t, \phi_1 + \omega t)].
\end{aligned} \tag{4.97}$$

Since here ψ_1 , ψ_2 and σ are assumed to be $\mathcal{O}(\epsilon)$, ϕ_j evolves slowly, that is $\dot{\phi}_j \simeq 0$ which almost eliminates the explicit time dependence of ϕ_j over one period. However, such small deviations may accumulate over longer time and will affect the emergent network dynamics. Hence, over a single period of motion, we can set $\phi_j(s) \simeq \phi_j(t)$, $s \in [t, t + T]$. Moreover, we know all h_k , $k = 1, \dots, 6$, functions are T periodic, therefore, we can average these functions over period T . Then averaging each h_k over one period $T = 2\pi/\omega$ yields

$$\begin{aligned}
h_k(\phi_1 + \omega t, \phi_2 + \omega t) &\simeq \frac{1}{T} \int_0^T h_k(\phi_1 + \omega t, \phi_2 + \omega t) dt \\
&= \frac{1}{2\pi} \int_0^{2\pi} h_k(u, u + \phi_2 - \phi_1) du \\
&\equiv H_k(\phi_2 - \phi_1).
\end{aligned} \tag{4.98}$$

Averaging gives an approximation of (4.97) as [130, 265]

$$\begin{aligned}
\dot{\phi}_1 &= \sigma [H_1(\phi_2 - \phi_1) + \psi_1 H_2(\phi_2 - \phi_1) + \psi_2 H_3(\phi_2 - \phi_1)], \\
\dot{\psi}_1 &= \kappa \psi_1 + \sigma [H_4(\phi_2 - \phi_1) + \psi_1 H_5(\phi_2 - \phi_1) + \psi_2 H_6(\phi_2 - \phi_1)], \\
\dot{\phi}_2 &= \sigma [H_1(\phi_1 - \phi_2) + \psi_2 H_2(\phi_1 - \phi_2) + \psi_1 H_3(\phi_1 - \phi_2)], \\
\dot{\psi}_2 &= \kappa \psi_2 + \sigma [H_4(\phi_1 - \phi_2) + \psi_2 H_5(\phi_1 - \phi_2) + \psi_1 H_6(\phi_1 - \phi_2)].
\end{aligned} \tag{4.99}$$

Then by choosing $\chi \equiv \phi_2 - \phi_1$, these equations reduce to

$$\begin{aligned}\dot{\chi} &= \sigma [H_1(-\chi) - H_1(\chi) + \psi_1 (H_3(-\chi) - H_2(\chi)) + \psi_2 (H_2(-\chi) - H_3(\chi))], \\ \dot{\psi}_1 &= \kappa \psi_1 + \sigma [H_4(\chi) + \psi_1 H_5(\chi) + \psi_2 H_6(\chi)], \\ \dot{\psi}_2 &= \kappa \psi_2 + \sigma [H_4(-\chi) + \psi_2 H_5(-\chi) + \psi_1 H_6(-\chi)],\end{aligned}\tag{4.100}$$

where we can compute each H_k by evaluating the following integrals

$$\begin{aligned}H_1(\chi) &= \frac{1}{2\pi} \int_0^{2\pi} \mathcal{Z}^v(u) [v(u + \chi) - v(u)] du, \\ H_2(\chi) &= \frac{1}{2\pi} \int_0^{2\pi} (\mathcal{B}^v(u) [v(u + \chi) - v(u)] - \mathcal{Z}^v(u) p^v(u)) du, \\ H_3(\chi) &= \frac{1}{2\pi} \int_0^{2\pi} \mathcal{Z}^v(u) p^v(u + \chi) du, \\ H_4(\chi) &= \frac{1}{2\pi} \int_0^{2\pi} \mathcal{I}^v(u) [v(u + \chi) - v(u)] du, \\ H_5(\chi) &= \frac{1}{2\pi} \int_0^{2\pi} (\mathcal{C}^v(u) [v(u + \chi) - v(u)] - \mathcal{I}^v(u) p^v(u)) du, \\ H_6(\chi) &= \frac{1}{2\pi} \int_0^{2\pi} \mathcal{I}^v(u) p^v(u + \chi) du.\end{aligned}\tag{4.101}$$

In Appendix (C), Fig. C.1, Fig. C.2, Fig. C.3, and Fig. C.4 we illustrate the shape of H_1, H_3, H_4 , and H_6 , respectively. We choose to plot these functions since the stability of synchronous state explicitly depend on these, see (4.103), however the plots of H_2 and H_3 can be obtained from (4.101) similarly.

Determining the stability of the fixed points of (4.100) correspond to assessing the stability of phase locked solution of (4.92) or equivalently that of (4.91). To find fixed points, that satisfy $[\dot{\chi}, \dot{\psi}_1, \dot{\psi}_2]^\top = [0, 0, 0]^\top$, we shall first numerically calculate

$$\begin{aligned}\psi_1(\chi) &= \frac{-\sigma H_4(\chi)(\kappa + \sigma H_5(-\chi)) + \sigma^2 H_4(-\chi) H_6(\chi)}{(\kappa + \sigma H_5(-\chi))(\kappa + \sigma H_5(\chi)) - \sigma^2 H_6(\chi) H_6(-\chi)}, \\ \psi_2(\chi) &= \frac{-\sigma H_4(-\chi)(\kappa + \sigma H_5(\chi)) + \sigma^2 H_4(\chi) H_6(-\chi)}{(\kappa + \sigma H_5(\chi))(\kappa + \sigma H_5(-\chi)) - \sigma^2 H_6(-\chi) H_6(\chi)},\end{aligned}\tag{4.102}$$

$\chi \in [0, 2\pi]$, and then put these into the right hand side of $\dot{\chi}$. If the right hand side of $\dot{\chi}$ is also zero for a particular $\hat{q} = (\chi, \psi_1(\chi), \psi_2(\chi))$, then we

conclude \hat{q} is a fixed point of (4.100). Here we are particularly interested in the stability of synchronous solution which corresponds to $[\chi, \psi_1, \psi_2]^\top = [0, 0, 0]^\top$. By denoting $[\dot{\chi}, \dot{\psi}_1, \dot{\psi}_2]^\top \equiv F$, we can calculate the Jacobian of F at $[0, 0, 0]$ in the form

$$J_F = \begin{bmatrix} -2\sigma H_1'(0) & 2\sigma H_3(0) & -2\sigma H_3(0) \\ \sigma H_4'(0) & \kappa - \sigma H_6(0) & \sigma H_6(0) \\ -\sigma H_4'(0) & \sigma H_6(0) & \kappa - \sigma H_6(0) \end{bmatrix}, \quad (4.103)$$

where $H_k'(0) = [\partial H_k(\chi)/\partial \chi] |_{\chi=0}$. These terms can be calculated from equation (4.101), for example $H_1'(0) = (1/2\pi) \int_0^{2\pi} \mathcal{Z}^v(u) v'(u) du$. Then we can compute the eigenvalues of J_F

$$\begin{aligned} \lambda_1 &= \kappa, \\ \lambda_2 &= \frac{1}{2}(-2\sigma(H_1'(0) + H_6(0)) + \kappa) \\ &\quad + \frac{1}{2}\sqrt{((2\sigma(H_1'(0) - H_6(0)) + \kappa)^2 + 16\sigma^2 H_3(0) H_4'(0))}, \\ \lambda_3 &= \frac{1}{2}(-2\sigma(H_1'(0) + H_6(0)) + \kappa) \\ &\quad - \frac{1}{2}\sqrt{((2\sigma(H_1'(0) - H_6(0)) + \kappa)^2 + 16\sigma^2 H_3(0) H_4'(0))}. \end{aligned}$$

Hence, the synchronous solution is stable if all eigenvalues of λ_1, λ_2 and λ_3 have negative real part. Here we also observe that, if we keep only $\mathcal{O}(\epsilon)$ terms in the expansion (4.95), we obtain

$$\begin{aligned} \dot{\theta}_1 &= \omega + \sigma [\mathcal{Z}^v(\theta_1) (v^\gamma(\theta_2) - v^\gamma(\theta_1))], \\ \dot{\psi}_1 &= \kappa\psi_1 + \sigma [\mathcal{I}^v(\theta_1) (v^\gamma(\theta_2) - v^\gamma(\theta_1))], \\ \dot{\theta}_2 &= \omega + \sigma [\mathcal{Z}^v(\theta_2) v^\gamma(\theta_1) - v^\gamma(\theta_2)], \\ \dot{\psi}_2 &= \kappa\psi_2 + \sigma [\mathcal{I}^v(\theta_2) (v^\gamma(\theta_1) - v^\gamma(\theta_2))]. \end{aligned} \quad (4.104)$$

By following the above procedure, this will reduce to

$$\begin{aligned} \dot{\chi} &= \sigma [H_1(-\chi) - H_1(\chi)], \\ \dot{\psi}_1 &= \kappa\psi_1 + \sigma [H_4(\chi)], \\ \dot{\psi}_2 &= \kappa\psi_2 + \sigma [H_4(-\chi)]. \end{aligned} \quad (4.105)$$

In this case the Jacobian at $[0, 0, 0]$ will be

$$J_F^\epsilon = \begin{bmatrix} -2\sigma H_1'(0) & 0 & 0 \\ \sigma H_4'(0) & \kappa & 0 \\ -\sigma H_4'(0) & 0 & \kappa \end{bmatrix} \quad (4.106)$$

which has eigenvalues $\lambda_1^\epsilon = -2\sigma H_1'(0)$, and $\lambda_2^\epsilon = \kappa = \lambda_3^\epsilon$. Here we know that the Floquet exponent κ is negative (periodic orbit is stable), and therefore the stability of synchronous solution will be determined from the sign of $-2\sigma H_1'(0)$. In Section 2.4, using weak coupling theory (phase only reduction), we found that the stability of the synchronous state was determined from the sign of $-\sigma H'(0)\lambda_i$, (see equation (2.54)). The coupling matrix of the network setting (4.91) has the graph-Laplacian form

$$\mathcal{G} = \begin{bmatrix} w_{12} & -w_{12} \\ -w_{21} & w_{21} \end{bmatrix} = \begin{bmatrix} 1 & -1 \\ -1 & 1 \end{bmatrix}, \quad (4.107)$$

which has eigenvalues $\lambda_1 = 0$ and $\lambda_2 = 2$, and also from the corresponding definitions we know $H'(0) \equiv H_1'(0)$. Hence, as expected, the eigenvalues of J_F^ϵ and the formula given in equation (2.54) yield the same result. At this level of accuracy, in Fig. 4.11, for each PWL model we plot the phase interaction function $\mathcal{K}(\chi) = H_1(-\chi) - H_1(\chi)$. In both cases, variation of coupling strength σ does not effect the sign of λ_1^ϵ or $-\sigma H'(0)\lambda_i$, and therefore first order accurate reductions cannot uncover any effect of the variation of σ on stability (apart from a sign change). Both the second order reduction and MSF formalism enable this.

4.6.2 Master stability function approach

The MSF methodology cannot be directly applied to networks of nonsmooth oscillators. Here, we first review the technique that adapts the MSF to PWL systems given in [54], and then apply this method to the models considered in

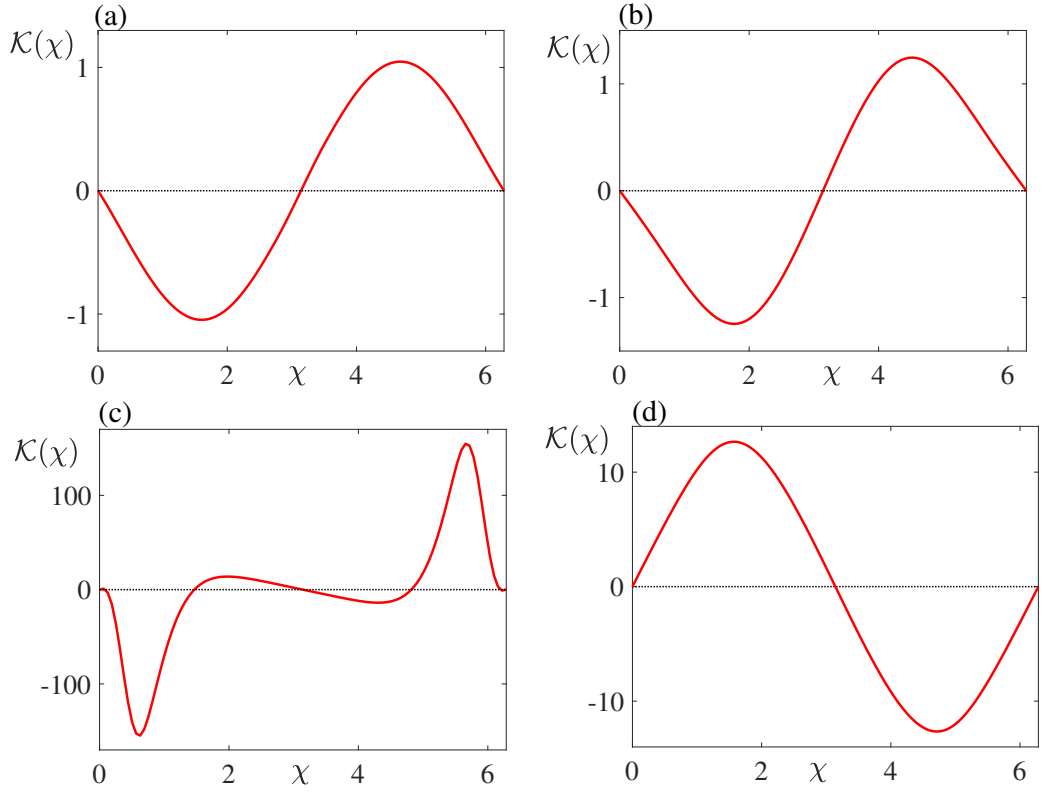


Figure 4.11: Phase interaction functions. (a)-The McKean model with parameters as in Fig. 3.3. (b)-The absolute model with parameters as in Fig. 3.5. (c) Homoclinic loop model with $\tau_2 = 0.64$ and other parameters as in Fig. 3.7. (d)-PML model with parameters as in Fig. 3.10.

this chapter. We aim to show how the stability of the synchronous solution changes under variation of the coupling strength in linearly coupled networks settings for systems of the type (4.91). In Section 2.4, we introduced the MSF technique for networks of smooth N identical m dimensional oscillators given in equation (2.62) and decoupled this into a set of m dimensional systems in the form (2.67) to assess the stability of synchronous state. For PWL systems of the form (4.4) with linear diffusive coupling both $Df(s)$ and $DH(s)$ are piecewise constant matrices. Therefore, in each subregion R_μ , (2.67) evolves according to

$$\frac{d\xi_\mu}{dt} = [A_\mu - \beta J]\xi_\mu, \quad \beta \in \mathbb{C}, \quad (4.108)$$

where $J = DH(s)$ and $\xi_\mu \in \mathbb{C}^m$. Then, we can solve this system using matrix exponentials, i.e. $\xi_\mu(t) = G(A_\mu - \beta J; t) \xi_\mu(0)$; where $G(A; t)$ is given by (3.12), though, we may need to be careful while evolving perturbations through the

switching manifolds. Using the previous notation from Subsection 2.4.5 where $U = (\delta x_1, \delta x_2, \dots, \delta x_N) \in \mathbb{R}^{Nm}$, at each event time t_μ , we can write $U^+ = (I_N \otimes S(t_\mu))U^-$. Then we may reuse the transformation $Y = (P \otimes I_m)^{-1}U$ to obtain

$$\begin{aligned}
Y^+ &= (P \otimes I_m)^{-1}U^+ = (P \otimes I_m)^{-1}(I_N \otimes S_\mu)U^- \\
&= (P \otimes I_m)^{-1}(I_N \otimes S_\mu)(P \otimes I_m)Y^- = (P^{-1} \otimes I_m^{-1})(I_N \otimes S_\mu)(P \otimes I_m)Y^- \\
&= (P^{-1}I_N) \otimes (I_m^{-1}S_\mu)(P \otimes I_m)Y^- = (I_N P^{-1}) \otimes (S_\mu I_m^{-1})(P \otimes I_m)Y^- \\
&= (I_N \otimes S_\mu)(P^{-1} \otimes I_m^{-1})(P \otimes I_m)Y^- = (I_N \otimes S_\mu)(P^{-1}P) \otimes (I_m^{-1}I_m)Y^- \\
&= (I_N \otimes S_\mu)(I_N \otimes I_m)Y^- = (I_N \otimes S_\mu)I_{Nm}Y^- \\
&= (I_N \otimes S_\mu)Y^-.
\end{aligned} \tag{4.109}$$

Hence, (4.109) has $m \times m$, N -block structure, and therefore the saltation operator acts on each block with $\xi(t_\mu^+) = S(t_\mu)\xi(t_\mu^-)$. Using the technique in Appendix A to treat perturbations across a switching boundary, after one period of motion (with N switching events), we have $\xi(T) = \Gamma\xi(0)$, where

$$\Gamma = S_N G(A_N - \beta J; T_N) \dots S_2 G(A_2 - \beta J; T_2) S_1 G(A_1 - \beta J; T_1). \tag{4.110}$$

For PWL systems, we see that all the individual variational equations, in the form (2.66), have the same structure as that of system (4.108). The only difference being the additional term $\beta_l = \sigma\lambda_l$. Therefore by choosing some reasonable value of β over the complex plane, we can determine the stability of (2.66) by checking this for each $\beta_l = \sigma\lambda_l$ over the MSF of (4.108). Alternatively, we can calculate Γ for each l , where we denote each of them by $\Gamma(l)$, and then, the synchronous state will be stable if the periodic solution of a single node is stable and the eigenvalues of $\Gamma(l)$ for $l = 2, \dots, n$ lie within the unit disc. Here, as an example, we consider the network setting (4.91) of planar PWL oscillators, for which the graph-Laplacian has eigenvalues $\lambda_1 = 0$ and $\lambda_2 = 2$

(see equation (4.107)). Then equation (4.108) reads

$$\frac{d\xi_\mu}{dt} = [A_\mu - 2\sigma J]\xi_\mu, \quad (4.111)$$

where $\xi_\mu \in \mathbb{R}^2$, and stability will be determined from the eigenvalues of $\Gamma(l)$, $l = 2$. In the next section, we will illustrate the MSF (network independent) for the McKean model, the absolute model, the homoclinic model, and the PML model. Then we will determine the stability of the synchronous state of (4.91) for each model under variation of coupling strength (σ).

4.7 Applications and comparisons

Here we examine the stability of the synchronous state using weak coupling theory, the second-order accurate phase-amplitude network formalism, and the MSF methodology. We compare results against the numerical simulations and explore the accuracy of each approach.

4.7.1 Networks of the McKean and absolute models

For the McKean and absolute models presented earlier, by using the node parameters as in Fig. 3.3 and Fig. 3.5, we find that the synchronous network state is stable for small σ (weak coupling) and also observed that this stability persists with increasing σ . All of the three methods give the same result, and these results show excellent agreement with numerical simulations. These results can be seen in Figs. 4.12 and 4.13.

4.7.2 Networks of piecewise linear Morris-Lecar model

For the PML model, phase-amplitude formalism and MSF approach predict that the synchronous state is unstable for small σ and that can restabilise by increasing σ . Using the MSF approach, the synchronous state is unstable for $0 \leq \sigma \leq 0.272$ and stable for $\sigma > 0.272$. However, using the phase amplitude network formalism, the synchronous state is predicted to be

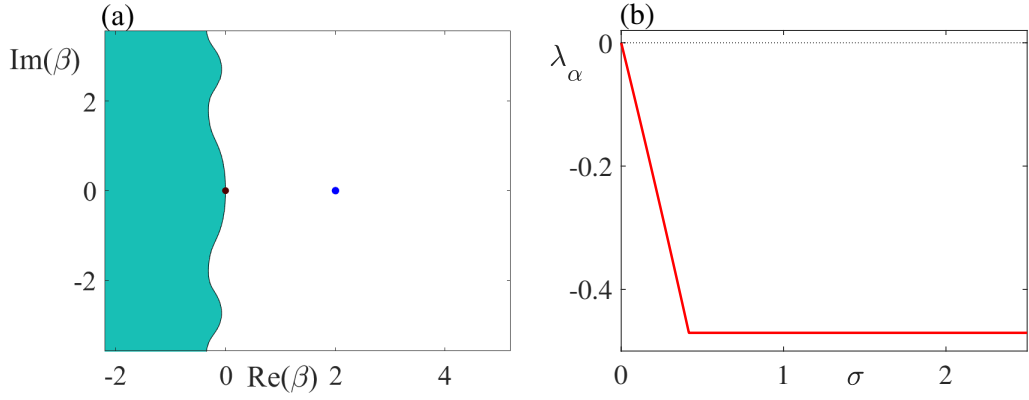


Figure 4.12: *Networks of the McKean model. (a)-MSF together with the values $\sigma\lambda_l$ where λ_l are eigenvalues of coupling matrix \mathcal{G} . We know that \mathcal{G} has eigenvalues $\lambda_1 = 0$ (brown dot) and $\lambda_1 = 2$ (blue dot where we choose $\sigma = 1$). Under σ variation, position of the blue dot changes along the x -axis. The MSF takes positive and negative values on green and white regions, respectively. For $\sigma > 0$, the MSF predicts that the synchronous state is always stable. (b)-Stability of the synchronous state using phase-amplitude network formalism. Here we plot the maximum of the real parts of the eigenvalues of the Jacobian matrix J_F , denoting this by λ_α , where $\lambda_\alpha = \max\{\text{Re}(\lambda_1), \text{Re}(\lambda_2), \text{Re}(\lambda_3)\}$, and $\sigma \in [0, 2.5]$. As seen in (b), λ_α is always negative, hence synchrony is always stable. In addition $H'_1(0) = 0.5363$ and therefore $\lambda_1^\epsilon = -2\sigma H'_1(0) = -1.0727\sigma$, thus from weak coupling theory, we conclude that the synchronous state is always stable for $\sigma > 0$. Direct numerical simulations confirm that the synchronous network state is always stable. Node parameters as in Fig. 3.3.*

unstable for $0 \leq \sigma \leq 0.2071$ and stable for $\sigma > 0.2071$. In addition to this, $H'_1(0) = -6.2766$, and therefore using weak coupling theory, we derive $\lambda_1^\epsilon = -2\sigma H'_1(0) = 12.5533\sigma$, which is positive for $\sigma > 0$, and this implies synchronous state is always unstable for positive coupling strength. We performed direct numerical simulations and observed that the synchronous state is unstable for $0 \leq \sigma \leq 0.272$ and stable for $\sigma > 0.272$, which exactly agrees with MSF result. Hence, in this case, although the phase amplitude network formalism gave a better result than weak coupling theory, it is still insufficient to detect the bifurcation point precisely. These results can be seen in Figs. 4.14 and 4.15.

4.7.3 Networks of the homoclinic (loop) model

For the homoclinic (loop) model, we consider two cases. As a first case, by choosing $\tau_2 = -0.68$, we constructed a periodic orbit that is not very close to the homoclinic limit (this can be thought as a smoothed homoclinic loop). In the network setting, by using the MSF method, the synchronous state is

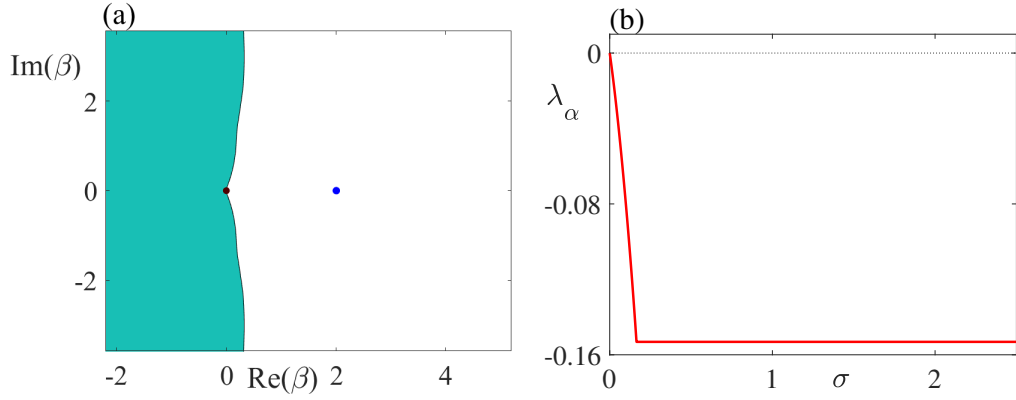


Figure 4.13: *Networks of the absolute model. (a)-MSF together with the values $\sigma\lambda_l$ where λ_l are eigenvalues of coupling matrix \mathcal{G} . We know that \mathcal{G} has eigenvalues $\lambda_1 = 0$ (brown dot) and $\lambda_1 = 2$ (blue dot where we choose $\sigma = 1$). Under σ variation, the position of blue dot moves along the x -axis. The MSF takes positive and negative values on green and white regions, respectively. For $\sigma > 0$, the MSF predicts that the synchronous state is always stable. (b)-Stability of the synchronous state using phase-amplitude network formalism. Here we plot the maximum of the real parts of the eigenvalues of the Jacobian matrix J_F , denoting this by λ_α , where $\lambda_\alpha = \max\{\text{Re}(\lambda_1), \text{Re}(\lambda_2), \text{Re}(\lambda_3)\}$, and $\sigma \in [0, 2.5]$. As seen in (b), λ_α is always negative, hence the synchronous state is always stable. In addition $H'_1(0) = 0.3038$ and therefore $\lambda_1^\epsilon = -2\sigma H'_1(0) = -0.6077\sigma$, thus from weak coupling theory, we would predict that synchrony is always stable for positive σ . We also performed direct numerical simulations and confirmed that the synchronous state is always stable. Node parameters as in Fig. 3.5.*

stable when $0 \leq \sigma \leq 0.2719$, and unstable if $0.2719 < \sigma \leq 0.5527$, it then restabilise for $0.5527 < \sigma$. In this case, using phase-amplitude network formalism, the synchronous state is stable when $0 \leq \sigma \leq 0.00696$, and unstable if $0.00696 < \sigma$, and stays unstable with increasing values of σ . Moreover, $H'_1(0) = 0.0966$, and therefore $\lambda_1^\epsilon = -2\sigma H'_1(0) = -0.1932\sigma$, thus from weak coupling theory, the synchronous state is always stable for positive σ . We depict these results in Fig. 4.16. We also performed direct numerical simulations and find that the MSF method shows an excellent agreement with actual simulation, see Fig. 4.17. Hence, as compared with weak coupling theory, although the phase-amplitude network formalism detects a bifurcation point, it still does not detect this point precisely. As a second case, we consider node parameter as in Fig. 3.7 which is close to homoclinic limit. In the network setting of this case, by using the MSF method, we find that the synchronous state is unstable when $0 \leq \sigma \leq 0.0395$, and stable if $0.0395 < \sigma \leq 0.0439$, then unstable for

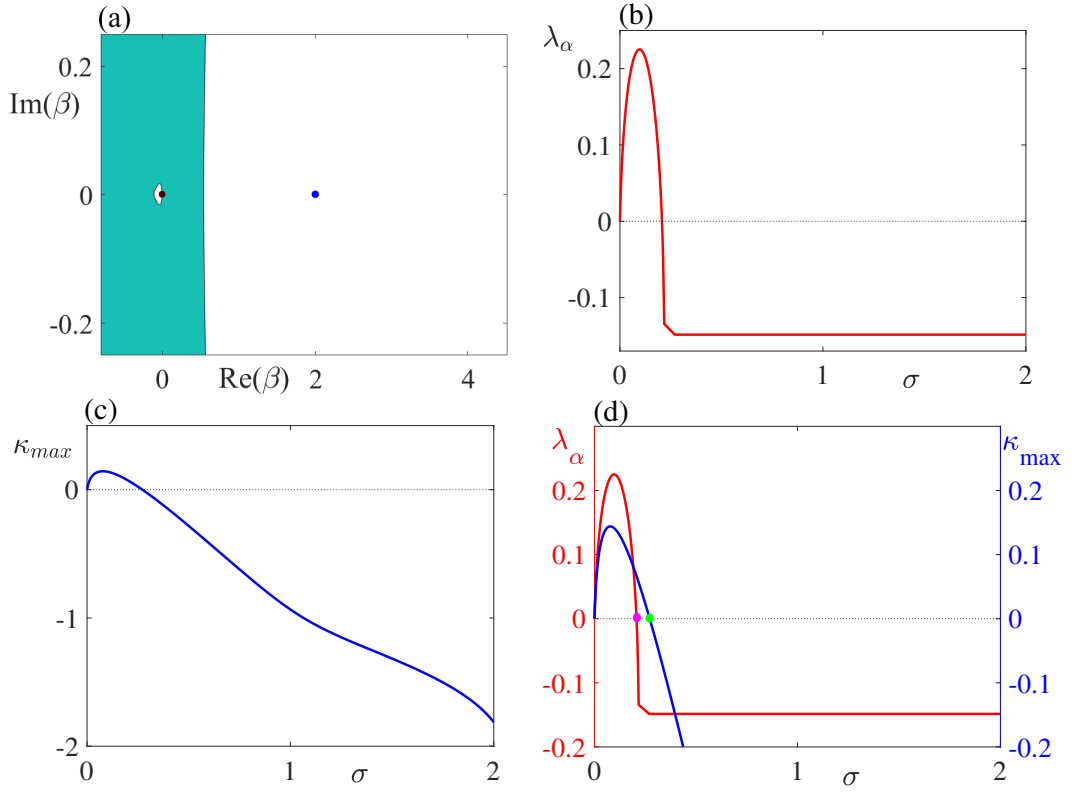


Figure 4.14: Networks of the PML model. (a)- The MSF together with the values $\sigma\lambda_l$ where λ_l are eigenvalues of coupling matrix \mathcal{G} with eigenvalues $\lambda_1 = 0$ (brown dot) and $\lambda_1 = 2$ (blue dot where we choose $\sigma = 1$). Under σ variation, the position of blue dot moves on the x -axis. The MSF takes positive and negative values on green and white regions, respectively. For this particular \mathcal{G} : the synchronous state is unstable when $0 \leq \sigma \leq 0.272$ and stable if $\sigma > 0.272$. This is explicitly shown in panel (c), where we depict the maximum real part of the Floquet exponents (κ_{max}) by directly using (4.111). b)-Stability of the synchronous state using phase amplitude network formalism. We plot the maximum of the real parts of the eigenvalues of the Jacobian matrix J_F , denoting this by λ_α , where $\lambda_\alpha = \max\{\text{Re}(\lambda_1), \text{Re}(\lambda_2), \text{Re}(\lambda_3)\}$, and $\sigma \in [0, 2]$. As shown in panel (b), λ_α is positive when $\sigma \in [0, 0.2071]$, hence the synchronous state is unstable, and negative for $\sigma > 0.2071$ so the synchronous state is stable. To compare these two approaches, in panel (d), we illustrate the bifurcation points on the same figure where blue curve with green dot and red curve with magenta dot correspond to the MSF approach and the phase-amplitude formalism, respectively. In addition $H'_1(0) = -6.2766$ and therefore $\lambda_1^\epsilon = -2\sigma H'_1(0) = 12.5533\sigma$, thus from weak coupling theory, we conclude that synchrony is always unstable for positive σ . We also performed direct numerical simulations in Fig. 4.15, and find that the MSF approach gives the exact result. Node parameters as in Fig. 3.10.

$0.0439 < \sigma \leq 1.178$, and again stable for $1.178 < \sigma \leq 2.226$, and then unstable for any $2.226 < \sigma$. In this case, by using the phase-amplitude network formalism, we find that the synchronous state is always unstable for positive values of σ . Moreover, $H'_1(0) = -3.8424$, and therefore $\lambda_1^\epsilon = -2\sigma H'_1(0) = 7.6848\sigma$. Thus from weak coupling theory, we would conclude that the synchronous

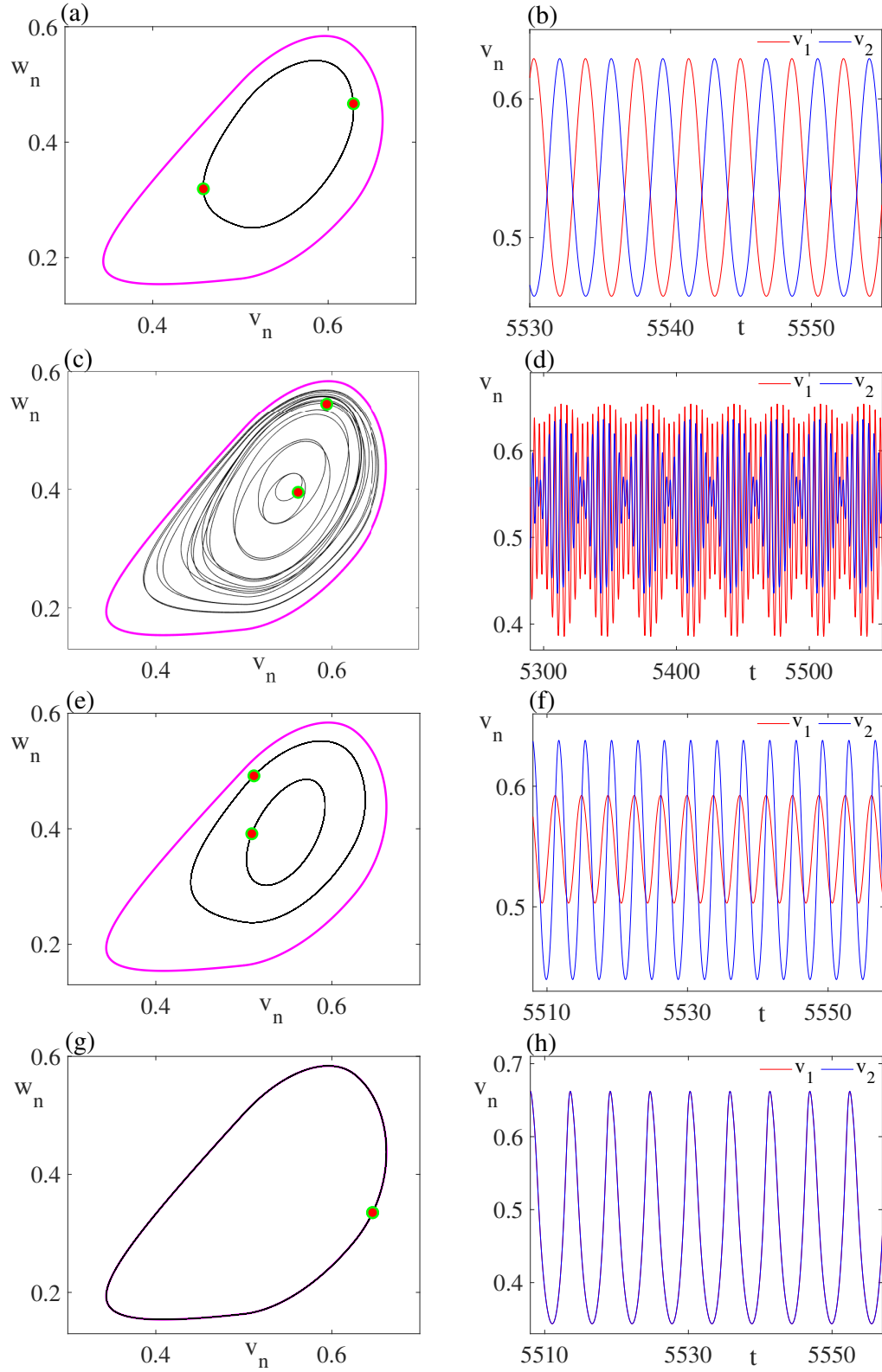


Figure 4.15: Direct numerical simulations of PML networks for different σ values. (a,b)- $\sigma = 0.1$. (c,d)- $\sigma = 0.18$. (e,f)- $\sigma = 0.25$. And (g,h)- $\sigma = 0.28$. In the left panels (a, c, e, g) we plot network activity in the (v, w) plane, and in the right panels we plot v_1 and v_2 components against time t . For all $\sigma \geq 0.272$ the synchronous network state is always stable, and for $\sigma < 0.272$ we observe different patterns. Node parameters as in Fig. 3.10 and \mathcal{G} is given by (4.107).

state is always unstable when $0 < \sigma$. We also performed direct numerical simulations and find that the MSF method is in excellent agreement, and the other methods not so. We illustrate these results in Figs. 4.16, 4.18, and 4.19. Finally, we test the accuracy of these methods when the periodic orbit moves away from the homoclinic case, by choosing $-0.7 \leq \tau_2 \leq -0.6333$, and find that both phase-amplitude network formalism and weak coupling theory fail to detect bifurcation points precisely. We show this using Fig. 4.20.

4.8 Discussion

In this chapter we have studied three methods to investigate the stability properties of the synchronous state of networks of identical PWL oscillators, namely weakly coupling theory, the phase-amplitude network formalism, and the MSF approach. Although the weak coupling theory of oscillators is a powerful tool and has been applied to a variety of problems across many different areas of science [14, 137, 270], as we have shown above, it fails to reflect the effect of coupling strength variation on the stability of the synchronous state. In order to improve the accuracy of the standard first-order phase reduction technique, various researchers have proposed higher order approximation to compute isochronal coordinates more accurately, such as in [297, 299]. However, it is important to also consider the dynamical evolution of the perturbed system in the transversal directions to the limit cycle, and this can be done by introducing amplitude coordinates. Many approaches have been proposed for smooth systems to tackle this problem, see for example, [43, 181, 319].

Recently, Wilson and Moehlis [328] introduced a new phase-amplitude reduction framework that defines amplitude coordinates using Floquet theory. Then, they improved this to a second-order accurate phase-amplitude reduced system in [325]. Moreover, Wilson [320] extended this technique to piecewise smooth systems by showing how to compute discontinuity conditions for the first and second order terms of the phase and amplitude coordinates. These studies, initially, have been done at node level. Ermentrout *et al.* [92],

extended this framework to a network of two identical synaptically coupled thalamic neuron models. They showed that there are interesting bifurcations that are not captured by a phase only reduction. Wilson [326] made a similar observation for a pair of coupled complex Ginzburg-Landau oscillators. In these two recent works, network units are prescribed by smooth systems, and here we have extended this methodology to a network setting where nodes have PWL oscillatory dynamics. This has enabled us to compute higher order reduction terms in closed form, and therefore higher order coupling functions more accurately.

We have confirmed predicted results from theory against the actual numerical simulations for a variety of networks. For McKean and absolute systems both weak coupling theory and phase-amplitude network formalism give the same stability result for the synchronous state, and this is in agreement with numerical simulations. However, for the PML network, weak coupling theory predicts that synchrony is unstable for $\sigma > 0$ though the phase-amplitude formalism predicts that it is unstable until $\sigma = 0.2071$ and stable for all larger σ . Simulations suggest that synchrony is unstable until $\sigma = 0.272$ and stable for all larger σ . In comparison the MSF approach for nonsmooth systems is in excellent agreement, both qualitatively and quantitatively, predicting $\sigma = 0.272$ as a bifurcation point. We obtained similar results for the homoclinic loop network model, as summarised in Fig. 4.20.

Some interesting patterns, even at the level of networks of two nodes, have been observed for the PML model, see Fig. 4.15. The phase-amplitude network formalism may be useful to test stability of these states as shown in [92]. Hence, the PWL modelling approach is beneficial for both phase only reduction and the phase-amplitude formalism since it allows one to compute the terms $i\text{PRC}$, $i\text{IRC}$, \mathcal{B} and \mathcal{C} quasi-analytically, rather than relying on expensive numerical computations. Moreover, the MSF methodology gives exact results for determining the stability of the synchronous state in networks of PWL units without approximation or reduction.

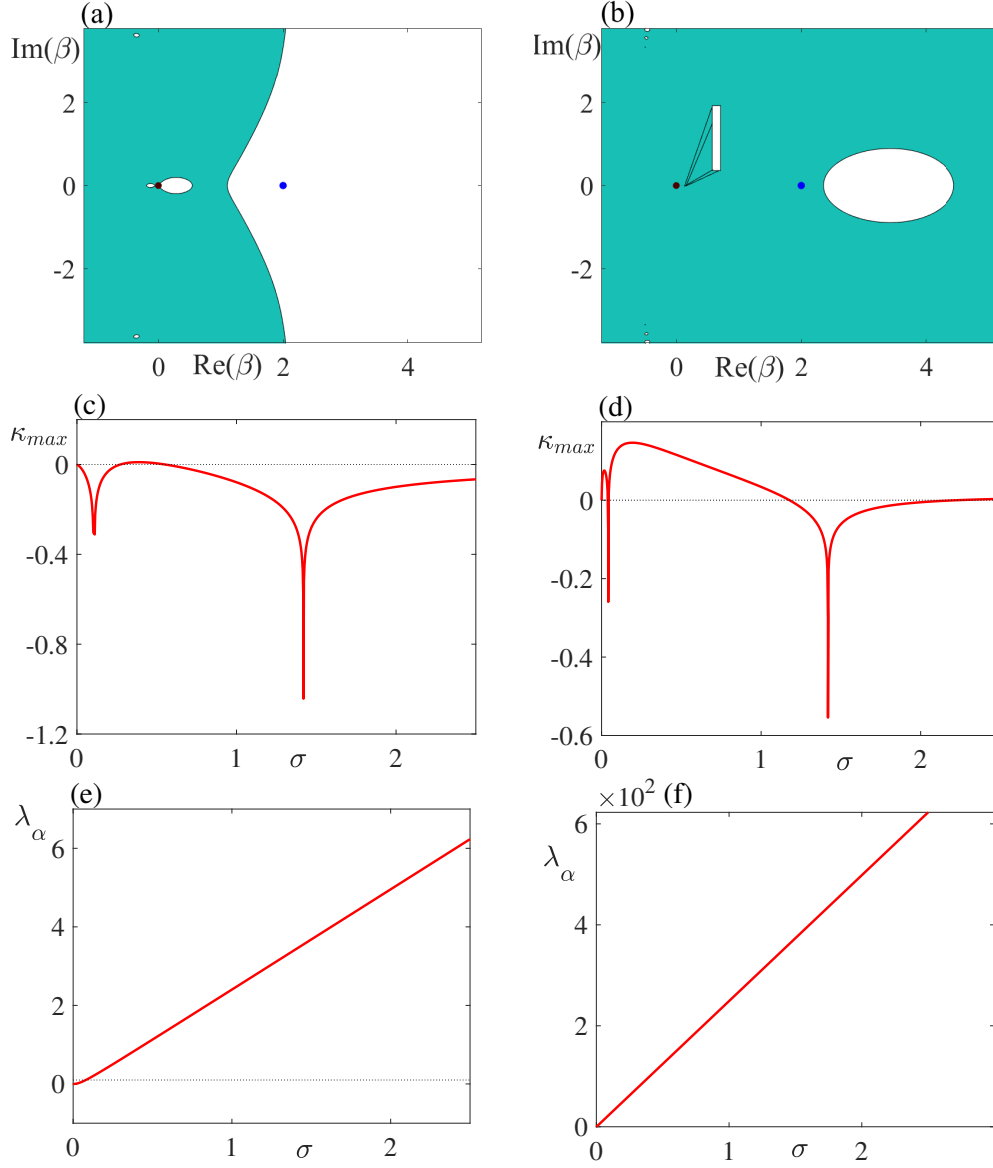


Figure 4.16: Networks of the homoclinic loop model. Plots in the left column belong to a smoothed loop ($\tau_2 = -0.68$), and that of the right column belongs to the original homoclinic loop. (a,b)- MSF together with the values $\sigma\lambda_i$ where λ_i are eigenvalues of coupling matrix \mathcal{G} with eigenvalues $\lambda_1 = 0$ (brown dot) and $\lambda_1 = 2$ (blue dot where we choose $\sigma = 1$). In the green and white zones the MSF is positive and negative, respectively. Under σ variation, the position of blue dot moves along the x -axis. In panel (b), to show MSF is negative for $0.0395 < \sigma \leq 0.0439$, we show a zoom of this area. In panel (c,d), we plot the maximum real part of the Floquet exponents (κ_{max}) to show the MSF results more explicitly. In panel (e,f), we test the stability of the synchronous state using the phase-amplitude network formalism. Here we plot the maximum of the real parts of the eigenvalues of the Jacobian matrix J_F , denoting this by λ_α , where $\lambda_\alpha = \max\{\text{Re}(\lambda_1), \text{Re}(\lambda_2), \text{Re}(\lambda_3)\}$, and $\sigma \in [0, 2.5]$. In addition to these, for smoothed loop, $H'_1(0) = 0.0966$ and therefore $\lambda_1^\epsilon = -2\sigma H'_1(0) = -0.1932\sigma$, thus from weak coupling theory, we would conclude that synchrony is always stable for positive σ . For the original homoclinic loop, $H'_1(0) = -3.8424$ and therefore $\lambda_1^\epsilon = -2\sigma H'_1(0) = 7.6848\sigma$, thus from weak coupling theory, we would conclude that synchrony is always unstable for $\sigma > 0$. We also performed direct numerical simulations and found that the MSF approach was in excellent agreement with actual network activity. Other node parameters as in Fig. 3.7.

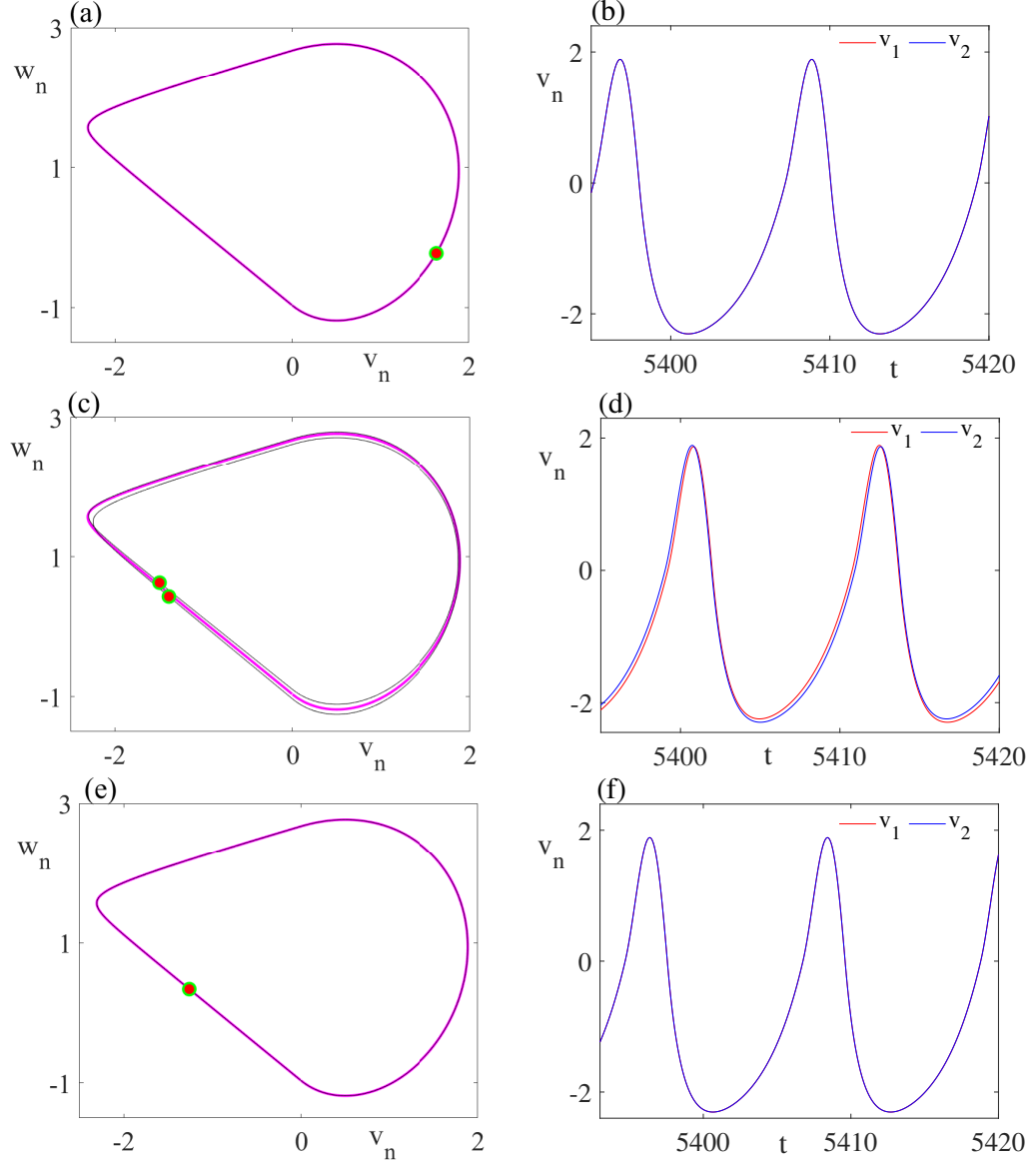


Figure 4.17: Direct numerical simulations of networks of the smoothed homoclinic loop for different σ values. (a,b)- $\sigma = 0.1$ (c,d)- $\sigma = 0.5$, and (e,f)- $\sigma = 0.6$. In the left panels (a, c, e) we plot network activity in the (v, w) plane and in the right panels (b,d,f) we plot v_1 and v_2 components against time t . Node parameters as in Fig. 3.7 with $\tau_2 = -0.68$ and \mathcal{G} is given in (4.107).

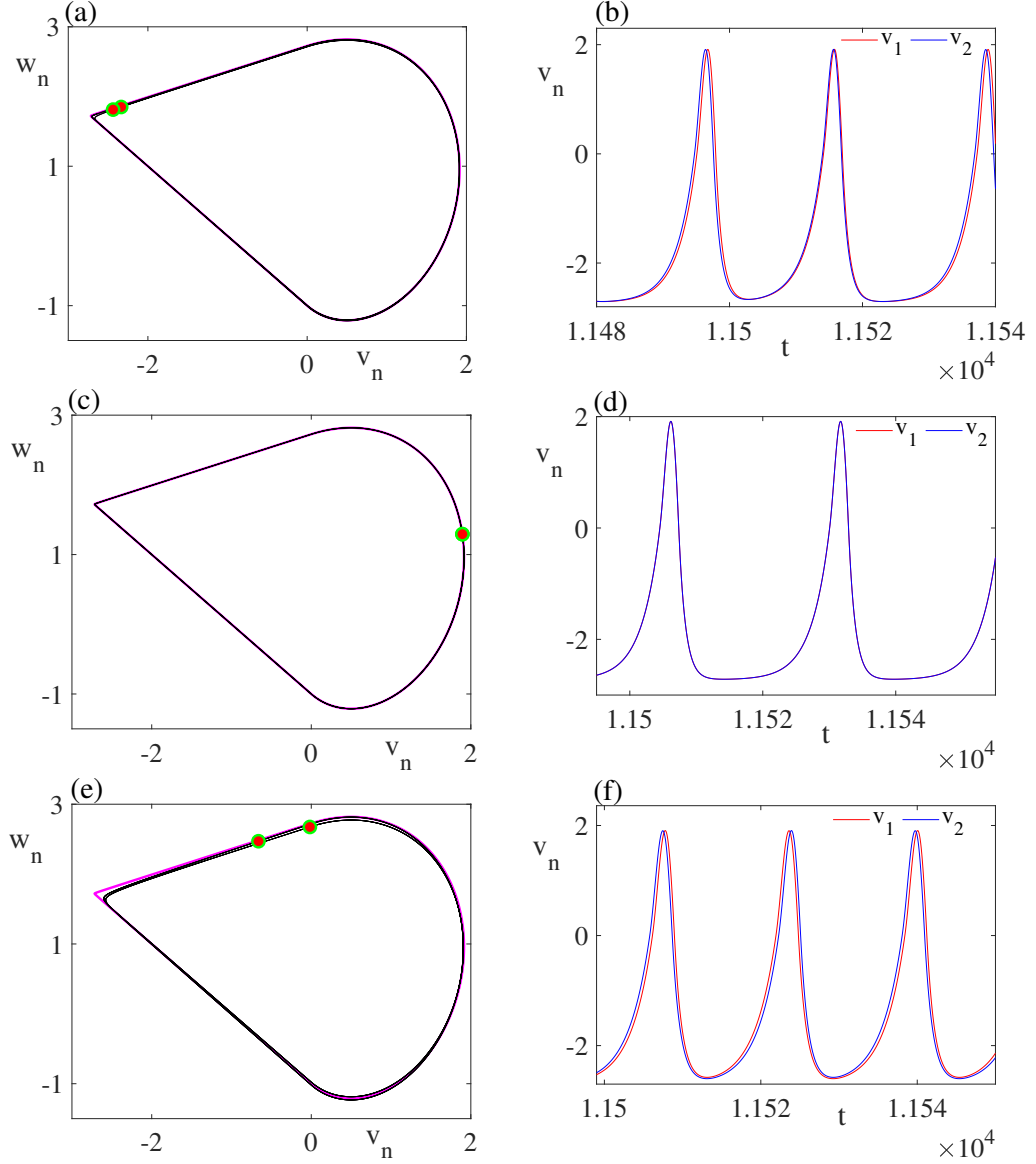


Figure 4.18: Direct numerical simulations of networks of the homoclinic loop (given in Fig. 3.7) for different σ values. (a,b)- $\sigma = 0.02$ (c,d)- $\sigma = 0.041$, and (e,f)- $\sigma = 0.08$. In the left panels (a, c, e) we plot network activity in the (v, w) plane and in the right panels (b,d,f) we plot v_1 and v_2 components against time t . \mathcal{G} is given in (4.107)

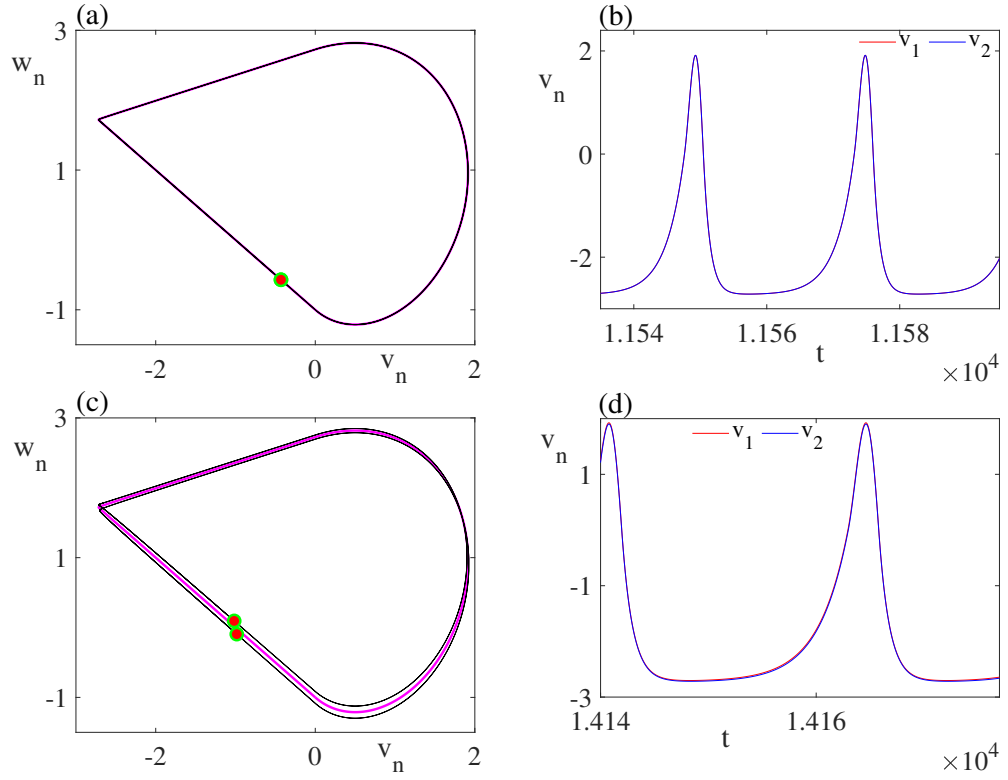


Figure 4.19: Direct numerical simulations of networks of the homoclinic loop for different σ values. (a,b)- $\sigma = 2$, and (c,d)- $\sigma = 2.6$. In the left panels (a,c) we plot network activity in the (v, w) plane and in the right panels (b,d) we plot v_1 and v_2 components against time t . Node parameters as in Fig. 3.7 and \mathcal{G} is given in (4.107).

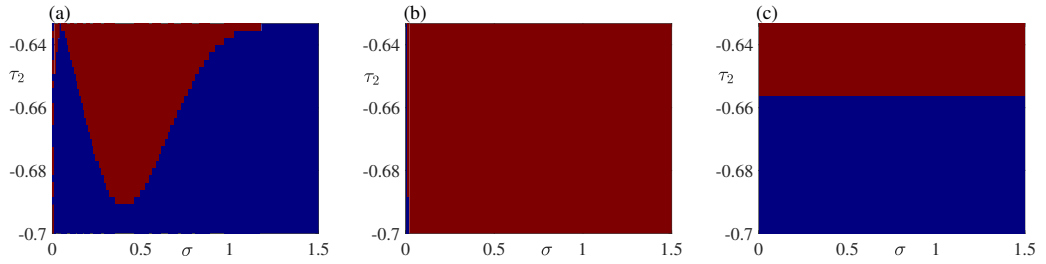


Figure 4.20: Stability of the synchronous state of networks of the homoclinic loop model. Here we compare three methods by choosing $\tau_2 \in [-0.7, -0.6333]$ and $\sigma \in [0, 1.5]$. On blue and dark red regions the synchronous state is stable and unstable, receptively. (a) MSF approach. (b) Phase amplitude network formalism. (c) Weak coupling theory. We compare these result against direct network simulations and find that the MSF approach agrees very well with simulations. Other node parameters as in Fig. 3.7 and \mathcal{G} is given by (4.107).

Chapter 5

Networks of Franklin bells

5.1 Introduction

The history of the Franklin bell is long and well established. Although named after the American scientist Benjamin Franklin it was in fact invented by the Scottish Benedictine monk Andrew Gordon in Erfurt, Germany, around 1742. The bell converts electrical energy into mechanical energy in the form of a repeating mechanical motion and forms the basis for many modern day bell-chimes, from security alarms to school bells. Franklin made use of Gordon's idea by connecting one bell to his pointed lightning rod, attached to a chimney, and a second bell to the ground. One of his letters contains the following description [103]

In September 1752 I erected an Iron Rod to draw the Lightning down into my House, in order to make some Experiments on it, with two bells to give Notice when the Rod should be electrified. A contrivance obvious to every Electrician.

The original Franklin bell was composed of a pair of bells located a certain distance apart and one conductive metal ball hanging between them from an insulating string. It operates when one of the bells receives an electrical discharge as a weather cloud crosses above the lightning rod connected to that

bell while the other bell conducts the discharge to the ground. The shuttling behaviour of the metallic ball between bells produces the chime and allows the detection of lightning. This is a prototypical example of an impact oscillator.

In recent years, a considerable amount of research has been devoted to the development of efficient techniques to analyse the dynamical behaviours of impacting systems. This has been motivated in part by challenges arising in control theory, population dynamics, chemistry, physics, biotechnologies, economics, industrial robotics, to name but a few [44, 81, 82, 264, 280, 336]. Indeed, many real world systems can be characterised by instantaneous jumps or switches in behaviour, which may be created by impulsive interactions. In contrast to smooth dynamical systems, the analysis of such nonsmooth systems is relatively underdeveloped. This is even more true at the network level. Thus, it is of interest to either adapt techniques from the theory of smooth dynamical systems or to develop entirely new ones, as in Chapter 4. We do so here with a focus on synchronous periodic states in Franklin bell networks of arbitrary topology. For some demonstrations of Franklin bell networks we refer the reader to the growing number of videos that are being increasingly used in scientific outreach activities [251]. We have made our own (using aluminium drink cans and a hand operated electric generator) and see [268] for a link to a video.

Since synchrony is a common behaviour seen in networks of oscillators with graph-Laplacian coupling (of which diffusive coupling is a classic example), and arises in many different areas [10, 11, 218, 231, 240, 241, 291, 316, 340, 342], Pecora and Carroll [229, 231] developed a network Floquet theory that can be diagonalised in the basis of the eigenvectors of the network connectivity matrix. This means that the stability of the synchronous orbit can be assessed in terms of a set of lower dimensional Floquet problems parameterised by the (possibly complex) eigenvalues of the network connectivity matrix, see Subsection 2.4.5 for more details. Recently, this method has been extended to treat diffusively coupled networks of nonsmooth Filippov type [100] and

integrate-and-fire piecewise linear oscillator models [54, 174, 217], making use of saltation operators. These have been widely used in the nonsmooth dynamical systems community to treat the linearised evolution of small perturbations through switching manifolds [211] and see Section 4.2.

As well as developing the mathematical techniques for handling a truly nonsmooth Franklin bell network, we further introduce a new form of *smoothing* that circumvents the need for constructing saltation operators. At heart, this technique introduces a virtual linear dynamical system that smoothly connects the orbits before and after impact. The duration of this virtual trajectory (that bridges the impact) is chosen as a control parameter δ . In the limit that δ tends to zero the propagator for this virtual system recovers the saltation rule. Thus working with small but finite δ we may treat the Franklin bell network solely as a smooth system. As expected the MSF for the nonsmooth network and the smoothed network show excellent agreement for small δ .

The organisation of the chapter is as follows. In Section 5.2, we provide a detailed description of a model for a single Franklin bell. We show how to construct periodic orbits and use the modified Floquet theory from Section 4.2 to assess solution stability. We use this to determine the bifurcation diagram as a function of the restitution of the ball velocity upon impact with the bell. In Section 5.3, we present the new smoothing technique and show that it recovers the saltation operators previously constructed. Then in Section 5.4 we use the MSF technique to determine the stability of synchronous network states, for both smooth and nonsmooth networks. Numerical examples are presented in Section 5.5 and shown to be in excellent agreement with theory. Finally in Section 5.6 we discuss the results in this chapter and natural extensions of the work presented.

The results of this chapter have been published in [269].

5.2 Model description and periodic orbits

In its simplest form the Franklin bell can be regarded as an electro-mechanical system consisting of two oppositely charged parallel plates (representing the metal bells) with a conductive particle (metal ball) which travels between them. This is suspended from an insulating wire hanging midway between the two plates. The polarisation of the plates is maintained by a battery, such that the constant electric field between them generates an electrostatic force that causes the ball to move. Upon impact with a plate the ball reverses direction and moves toward the opposite plate. In this way a periodic impacting rhythm can be generated. This is illustrated in Fig. 5.1. To formulate a mathematical

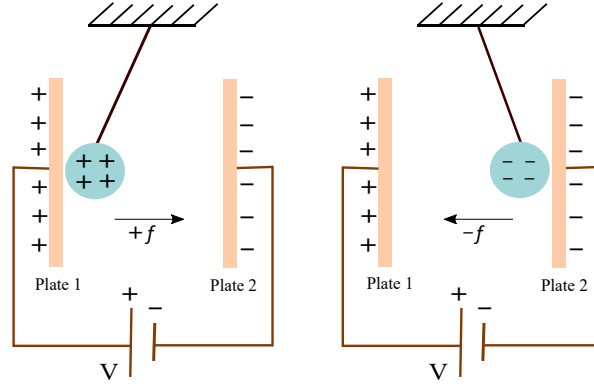


Figure 5.1: A sketch of the electro-mechanical idealisation of a single Franklin bell. Here a battery generates a constant voltage V across the circuit. An initially stationary ball, hanging midway between the two charged plates, will have a charge distribution that is positive on its right-hand side and negative on its left hand side. Left: An initial push to the left will cause a stationary ball to be attracted to the left-hand plate. Upon impact it will exchange charge with the plate and develop a net positive charge distribution. The ball and plate will then both have positive charge and repel each other. Right: The repulsive force from the left will cause an impact of the ball with the right-hand plate, where it can collect negative charge. The negatively charged metal ball will then be repelled from the negatively charged plate, and will move to the left. Thus a repetitive impacting oscillation can develop. This is the basis for chiming in a Franklin bell.

description of this idealised process we consider the metallic plates to be placed at the positions $u = \pm a$, with $u \in \mathbb{R}$. The ball that travels between the plates is governed by the dynamics of a forced damped simple harmonic (pendulum) oscillator. The direction of the forcing is determined by the sign of the charge carried by the ball at the instant before impact and is reversed after impact.

The magnitude of this force is determined by the sum of the repelling and attracting electrostatic forces, and will be assumed to be a constant denoted by f . Thus we are led to the equations of motion for a single Franklin bell as

$$\ddot{u} + \gamma_1 \dot{u} + \gamma_2 u = \text{sgn}(\dot{u})f, \quad \text{if } t \neq t_i, \quad (5.1)$$

$$\dot{u}(t_i^+) = -k\dot{u}(t_i^-), \quad \text{if } t = t_i. \quad (5.2)$$

Here u , \dot{u} , and \ddot{u} are the position, velocity, and acceleration of the particle at time t , respectively. The damping coefficient is given by $\gamma_1 > 0$, $\gamma_2 > 0$ sets the natural frequency of the pendulum, and $k \in \mathbb{R}^+$ is the coefficient of restitution upon impact. The *impact* times t_i are determined implicitly from the conditions $u(t_i) = \pm a$, $i \in \mathbb{Z}$. The dramatic change in velocity at impact is governed by equation (5.2), where $\dot{u}(t_i^-)$ represents the velocity of the ball immediately before $t = t_i$ and $\dot{u}(t_i^+)$ immediately thereafter, that is $\dot{u}(t_i^\pm) = \lim_{t \rightarrow t_i^\pm} \dot{u}(t)$. It is clear from the equation (5.1) that the right hand side of the system changes discontinuously upon impact. Moreover, the system is *impulsive* because of the velocity jump at the impact times. Thus, we consider the basic Franklin bell model as a state-dependent impulsive system with discontinuous changes in the vector field at impact times. Models of this type exist in many in real world scenarios [80, 105, 184, 211, 336], and are exemplified by impact oscillators. Thus, it is natural to analyse the Franklin bell as a state-dependent impacting system [25, 105].

It is first sensible to examine the fixed point structure of the model. Introducing $v = \dot{u}$ and denoting $x = (u, v)^\top$, then (5.1) and (5.2) can be written in a state-space form as

$$\dot{x} = Ax + f_e, \quad \text{if } t \neq t_i, \quad (5.3)$$

$$x(t_i^+) = \mathcal{J}(x(t_i^-)), \quad \text{if } t = t_i, \quad (5.4)$$

where

$$A = \begin{bmatrix} 0 & 1 \\ -\gamma_2 & -\gamma_1 \end{bmatrix}, \quad f_e = \begin{bmatrix} 0 \\ f \end{bmatrix} \text{sgn}(v), \quad (5.5)$$

and $\mathcal{J}(x) = (u, -kv)^\top$. As well as the *jump* rule \mathcal{J} for describing what happens at impact it is convenient to introduce two indicator functions $h = h_\pm(x) = u \pm a$ that determine the times of impact according to $h(x(t_i)) = 0$.

From (5.3) the stability of any equilibrium points is determined by the eigenvalues of the matrix A . These are easily calculated as $\lambda_\pm = (-\gamma_1 \pm \sqrt{\gamma_1^2 - 4\gamma_2})/2$. Remembering that γ_1 and γ_2 are both positive, we see that if a fixed point exists then it is stable (being a node for $\gamma_1^2 - 4\gamma_2 \geq 0$ and a focus otherwise). Formally, equilibrium points can be calculated as $(u, v) = (\pm f/\gamma_2, 0)$. Consequently if $|f| < \gamma_2|a|$ then both fixed points will be between the two plates, and otherwise they will be *virtual* (lying outside of the physically accessible region). This latter case will guarantee the existence of impacts, and is the one we focus on for the rest of the chapter since it is a necessary condition for the existence of periodic orbits, and hence *chiming* in a Franklin bell.

5.2.1 Construction and stability of periodic solution

In general it is very hard to find closed form solutions for periodic orbits in nonlinear dynamical systems. However, since (5.3) is a piecewise linear system, it can be solved exactly in regions of phase space where $v > 0$ and $v < 0$, respectively, and solutions glued together to construct periodic orbits. Consider now a periodic motion that starts at $t = 0^+$ at Plate 1 (see Fig. 5.1) and returns to the same point after a period Δ . Let us denote the time-of-flight for the trajectory from $u = -a$ to $u = a$ with $v > 0$ by Δ_1 . Using formulation (3.11), an explicit form for this trajectory can be constructed with initial data $(u(0^+), v(0^+)) = (-a, v_0)$ as:

$$\begin{bmatrix} u(t) \\ v(t) \end{bmatrix} = e^{At} \begin{bmatrix} -a \\ v_0 \end{bmatrix} + A^{-1} (e^{At} - I_2) \begin{bmatrix} 0 \\ f \end{bmatrix}, \quad 0 < t \leq t_1. \quad (5.6)$$

The impact time t_1 is determined by the condition $u(t_1^-) = a$, and the time-of-flight is simply $\Delta_1 = t_1$. An application of the jump rule can then be used to determine new initial data for the trajectory in the region where $v < 0$. This yields

$$\begin{bmatrix} u(t_1^+) \\ v(t_1^+) \end{bmatrix} = \begin{bmatrix} a \\ -kv(t_1^-) \end{bmatrix}. \quad (5.7)$$

Denoting the time-of-flight for the trajectory from $u = a$ to $u = -a$ with $v < 0$ by Δ_2 , then the corresponding trajectory is

$$\begin{bmatrix} u(t) \\ v(t) \end{bmatrix} = e^{A(t-t_1)} \begin{bmatrix} a \\ v(t_1^+) \end{bmatrix} - A^{-1} (e^{A(t-t_1)} - I_2) \begin{bmatrix} 0 \\ f \end{bmatrix}, \quad t_1 < t \leq t_1 + \Delta_2. \quad (5.8)$$

The impact time t_2 is determined by the condition $u(t_2^-) = -a$, and the time-of-flight is simply $\Delta_2 = t_2 - t_1$. An application of the jump rule at time t_2 then gives $(u(t_2^+), v(t_2^+)) = (-a, -kv(t_2^-))$, and for the orbit to be periodic this must match the initial data $(u(0^+), v(0^+)) = (-a, v_0)$. Thus a periodic orbit, parametrised by (t_1, t_2, v_0) , will exist if there is a solution to the three simultaneous nonlinear algebraic equations (similar to (3.15))

$$a = u(t_1), \quad -a = u(t_2), \quad v_0 = -kv(t_2^-). \quad (5.9)$$

If a solution exists then the period of oscillation for a periodic orbit with $x(t) = x(t + \Delta)$ is given by $\Delta = \Delta_1 + \Delta_2$.

To determine the stability of the periodic solution we follow the approach given in Section 4.2. After one period of oscillation a perturbation $\delta x(t)$ to the periodic orbit will have evolved according to the formula $\delta x(\Delta) = Q\delta x(0)$ where

$$Q = S(t_2)e^{A\Delta_2}S(t_1)e^{A\Delta_1}, \quad (5.10)$$

and

$$S(t) = \begin{bmatrix} -k & 0 \\ k \frac{\dot{v}(t^-)}{\dot{u}(t^-)} + \frac{\dot{v}(t^+)}{\dot{u}(t^-)} & -k \end{bmatrix}. \quad (5.11)$$

In (5.10), the saltation operator $S(t)$ given by (5.11) is used to map perturbations across the impact manifolds (where $u = \pm a$). Thus, the periodic orbit will be stable if the eigenvalues of Q lie within the unit disc. Since for a planar system one of the Floquet multipliers is equal to one (corresponding to tangential perturbations along the orbit) there is only one non-trivial eigenvalue of Q to consider. If we denote this by $e^{\kappa\Delta}$ and use the result that $\det Q = e^{\kappa\Delta} \times 1$, then we have that

$$\kappa = \frac{1}{\Delta} \log \det Q = -\gamma_1 + \frac{4}{\Delta} \log k. \quad (5.12)$$

A periodic orbit will be stable if $\kappa < 0$. Thus if $k < 1$ then all periodic orbits must be stable. However if the coefficient of restitution were taken to be greater than one (corresponding to injecting energy into the system at impact) then it would be possible for unstable periodic orbits to exist. An example of a co-existing stable and unstable periodic orbit for $k > 1$ is shown in Fig. 5.2. Here a stable periodic orbit is encircled by a an unstable periodic orbit with a large amplitude.

A bifurcation diagram, summarising the properties of periodic orbits under variation in the coefficient of restitution k is shown in Fig. 5.3. Here we see that for $k < 1$ there is only one stable periodic orbit, whilst for $k > 1$ a new unstable period orbit of large amplitude can be created. With increasing k , it is ultimately destroyed in a saddle-node bifurcation of periodic orbits. Mechanically, the case with $k > 1$ corresponds to energy being pumped into the system at impact, as in many pinball machines, and is often referred to as *active impact* [245].

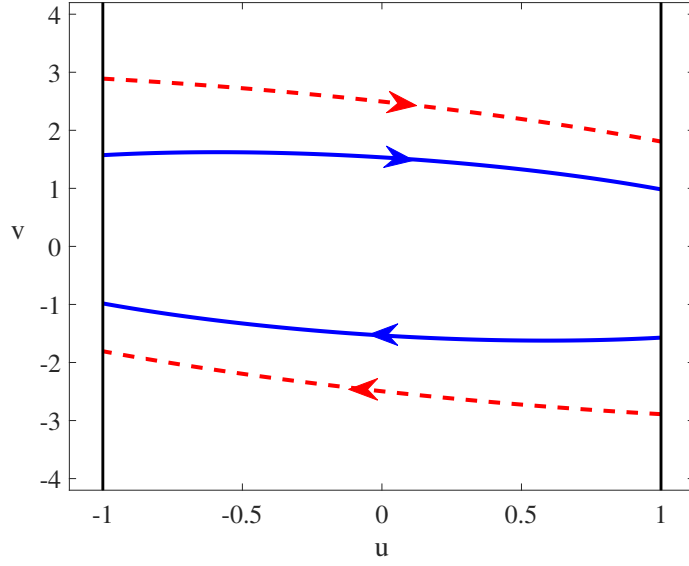


Figure 5.2: Limit cycles of the Franklin bell model described by equations (5.1) and (5.2). The impact manifolds (representing Plates 1 and 2 in Fig. 5.1) are fixed with the choice $a = \pm 1$. The red dashed and blue solid curves shown an unstable and stable periodic orbit for $k = 1.6$. Other parameters are $\gamma_1 = \gamma_2 = 0.9$, $f = 0.93$.

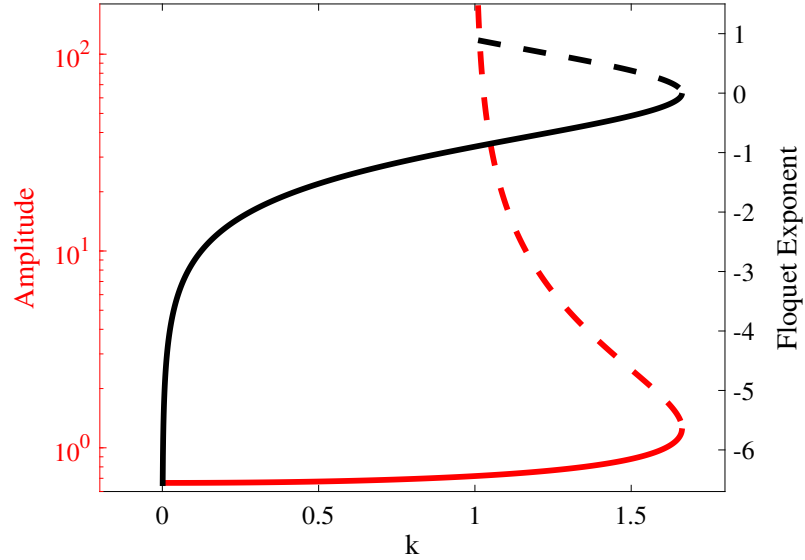


Figure 5.3: Bifurcation diagram for limit cycles of the Franklin bell model given by equations (5.1) and (5.2). Parameters are the same as that for Fig. 5.2. For $k \leq 1$ there is only one stable periodic orbit. At $k = 1$ an unstable orbit with infinitely large amplitude is born whose amplitude decreases with a further increase in k . For $k > 1$ stable and unstable periodic orbits co-exist until $k \simeq 1.663$ where they are lost in a saddle-node bifurcation of periodic orbits. The amplitude of the stable periodic orbit is always less than that of the unstable orbit. Black solid (dashed) and red solid (dashed) curves represent Floquet exponents and the amplitude of stable (unstable) periodic orbits respectively.

5.3 A piecewise linear smoothing technique

Although the nonsmooth system can be treated rigorously with the use of saltation operators it is of interest to consider a *smoothed* version of the model, which can be analysed with more traditional techniques. The choice of smoothing is somewhat arbitrary and one may consider a variety of approaches and a discussion can be found in Jeffrey [151]. If the model is written using potentials, then the nonsmooth system has an infinitely steep potential at the two plates, which could be replaced by a potential function with finite but steep gradient at the plates. Instead here we choose to append new dynamical rules at the end plates (and the regions beyond them), remove the strict impact condition, and allow trajectories to cross through the switching manifolds. We now envisage trajectories, beyond the plates, that smoothly connect to those within the plates. If the latter are determined by the original nonsmooth system then this effectively provides a smoothing. Preserving the shape of an orbit this does not preserve its proper duration as further time is needed to traverse the region outside the plates. If the time-of-flight could be reduced to zero outside the plates then this would recover the truly nonsmooth trajectory. Here we show that this can be achieved with a simple choice of linear dynamical system outside the plates.

The formal description of the smoothed model is written by augmenting the original model, given by (5.1) and (5.2), in the following way:

$$\frac{dx}{dt} = \begin{cases} Ax + f_e, & \text{if } |u| \leq a \\ A_R x + f_R, & \text{if } u > a \\ A_L x + f_L, & \text{if } u < -a \end{cases} \quad , \quad (5.13)$$

for as yet undetermined matrices $A_{R,L} \in \mathbb{R}^{2 \times 2}$ and vectors $f_{R,L} \in \mathbb{R}^2$. Each of the two new linear dynamical system is thus determined by six unknown parameters (four for $A_{R,L}$ and two for $f_{R,L}$). These can be computed from

matching conditions at the points where $u = \pm a$ such that the solution for x and \dot{x} is continuous and respects the rule for restitution. For example if we denote the value of x when $u = +a$ by $x(t_i)$ then we would require $A_R x(t_i) + f_R = A x(t_i) + f_e$ (two equations), $x(t_i + \delta t) = \mathcal{J}(x(t_i))$ (two equations), and $A_R x(t_i + \delta t) + f_R = A x(t_i + \delta t) + f_e$ (two equations). This gives a total of six equations for six unknowns, parameterised by the time-of-flight δt . The equation for $x(t)$ can be determined explicitly using matrix exponentials, as in Eq. (5.6) and Eq. (5.8), using the matrix A or $A_{R,L}$ as appropriate. The six simultaneous nonlinear equations can be solved numerically. Similarly we may match at $u = -a$ and obtain a similar system of equations (under the interchange of labels R to L). An illustration of this process is given in Fig. 5.4.

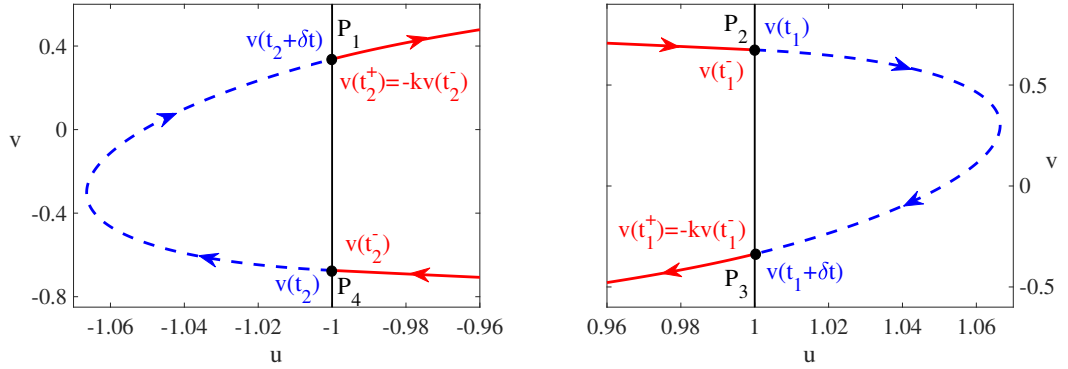


Figure 5.4: A visualisation of a smoothed trajectory. Parameters are the same as Fig. 5.2, with $k = 0.5$ and $\delta t = 0.5$. The trajectory in solid red coincides with that of the nonsmooth system described by Eq. (5.3) and Eq. (5.4). The trajectories in dashed blue are those from the augmented linear dynamical system, see Eq. (5.13), and are constructed to match those in red at the points P_1, \dots, P_4 in a C^1 fashion.

In Fig. 5.5 we show two examples of trajectories constructed by patching together matrix exponential solutions in the regions $u < -a$, $|u| \leq a$, and $u > a$, subject to the smoothing process described above. As we take δt smaller and smaller we find that the smooth trajectory approaches that of the nonsmooth system, as expected. The stability of periodic orbits in the smoothed system can be easily determined using the fact that the non-trivial Floquet exponent is given simply by $\kappa = \Delta^{-1} \int_0^\Delta \text{Tr } D(s) ds$, where $D(s)$ represents the

Jacobian along the periodic orbit. Due to the piecewise linear nature of the model this reduces to $\kappa = \Delta^{-1} \sum_{i=1}^4 \Delta_i \text{Tr } A_i$, see Section 4.2 for the details of this. Here $A_1 = A_3 = A$, $A_2 = A_R$, $A_4 = A_L$ and $\Delta = \Delta_1 + \Delta_2 + \Delta_3 + \Delta_4$, where Δ_1, Δ_3 are the times-of-flight in the region $|u| \leq a$ and $\Delta_2 = \Delta_4 = \delta t$ in the regions where $|u| > a$. Moreover, the propagators in the regions $u < -a$ and $u > a$, $\exp(A_L t)$ and $\exp(A_R t)$ respectively, approximate the relevant saltation matrices. The numerical evidence for this is provided in Fig. 5.6, where we compare the components of $S(t_1)$ (see Eq. (5.11)) with those of $\exp(A_R \delta t)$.

Although δt is under our control it is not guaranteed that this time-of-flight can be made arbitrarily small. Here, we have only provided numerical evidence that this is the case, and have not provided a formal proof. Rather we have presented a practical method for smoothing systems with hard impacts, obviating the need for the construction of saltation matrices. In the next section we show how to treat networks of interacting Franklin bells, with both hard and smoothed impacts.

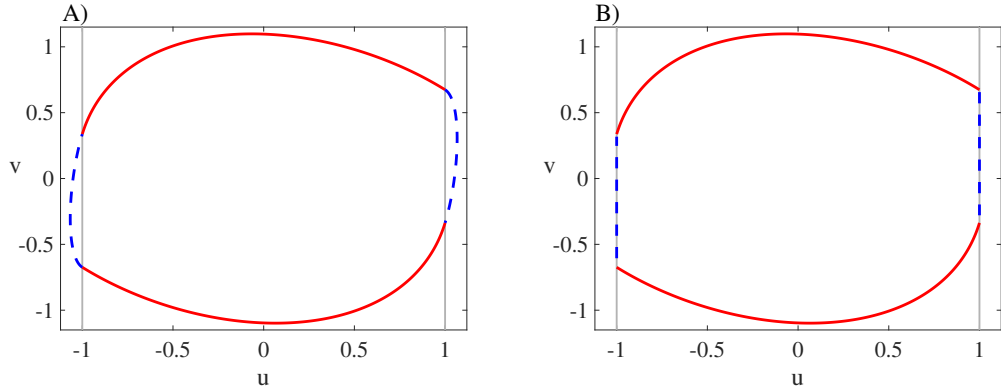


Figure 5.5: *Stable periodic orbits of the continuous PWL model (5.13). Parameters: $k = 0.5$, $\gamma_1 = \gamma_2 = 0.9$, $f = 0.93$, and $a = \pm 1$. The trajectories in solid red are those of the nonsmooth model, and those in dashed blue those of the augmented model. In A) the time-of-flight is $\delta t = 0.5$ and in B) $\delta t = 0.0004$. As δt is made smaller and smaller the smoothed model has trajectories that approach more closely those of the nonsmooth model.*

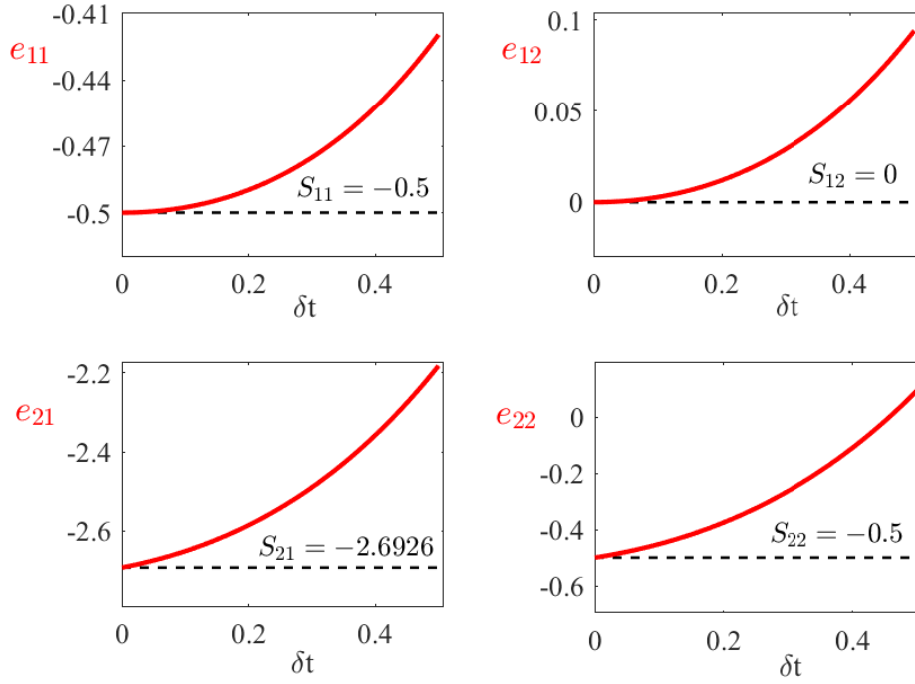


Figure 5.6: A plot of the components e_{ij} of the propagator $\exp(A_R \delta t)$ as δt goes to zero where $i, j = 1, 2$ (solid red lines). The black dashed line corresponds to the value of the component in the saltation matrix $S(t_1)$. All parameter values as in Fig. 5.5.

5.4 A Franklin bell network

A Franklin bell network can easily be constructed by serial extension of the network shown in Fig. 5.1. One simply hangs more metal balls from a cross-bar and inserts a metal bell between each suspended ball. Other topologies are, of course, possible which leads us to the consideration of general Franklin bell networks. The vertices of such a network can be represented by the bell-ball-bell combination and network edges by the interactions between them. From a modelling perspective the interactions between nodes are mediated by the vibrations communicated through the cross-bar. This is very reminiscent of a system of Huygens clocks [141], albeit where the clocks are impact oscillators rather than smooth limit-cycle oscillators. There is now a vast literature on the study of the latter, see for example [86], though far less work has been done on networks of impact oscillators. The exception to this perhaps being the recent work of Shiroky and Gendelman [278] who examined a linear array of Franklin bell oscillators. They analysed the properties of localised states

(breathing modes), whereby only one of the network nodes made repetitive impacts. The stability and bifurcation of these localised states was determined using a Fourier-based Floquet theory adapted to cope with local impulsive (Dirac-delta) effects. Thorin *et al.* [302] have also considered a similar problem, and most recently James *et al.* [148] have highlighted some of the many open problems in the study of impact oscillator networks. Here we focus on globally periodic synchronous impacting behaviour and show how to augment techniques from the network science of smoothy coupled limit cycles to treat impact oscillators. Moreover, by exploiting the PWL nature of a Franklin bell network between impacts we show how to readily construct the MSF. This is a powerful tool for determining the stability of a synchronous orbit in a network of *arbitrary* topology.

We begin by describing the construction of the MSF for an impulsive nonsmooth Franklin bell network, and then indicate how to perform the same calculation for a smoothed system.

5.4.1 Master stability function for a nonsmooth Franklin bell network

Consider an impacting Franklin bell network with N identical nodes labelled by $n = 1, 2, \dots, N$, with interactions mediated by linear coupling between ball displacements (representing the vibrational coupling through a crossbar). In this case we have a network dynamics governed by the equation

$$\ddot{u}_n + \gamma_1 \dot{u}_n + \gamma_2 u_n + \sigma \sum_{m=1}^N w_{nm} (u_m - u_n) = \text{sgn}(\dot{u}_n) f, \quad \text{if } t \neq t_{n_i}, \quad (5.14)$$

$$\dot{u}_n(t_{n_i}^+) = -k \dot{u}_n(t_{n_i}^-), \quad \text{if } t = t_{n_i}, \quad (5.15)$$

where t_{n_i} represents the i th impacting event time of the n th node, implicitly determined by $u_n(t_{n_i}) = \pm a$. The parameter σ represents a global coupling strength, whilst the specific influence of node m on node n is determined

by the value w_{nm} . The network structure is effectively encoded by a matrix with elements w_{nm} . The model equations (5.14)-(5.15), or variants thereof, also arise naturally when considering mechanical vibro-impact chain systems [114, 115, 128, 233]. It is convenient to write the network model in first order form by introducing the state vector $x_n = (u_n, v_n)^\top$ (where $v_n = \dot{u}_n$) so that

$$\dot{x}_n = F(x_n) + \sigma \sum_{m=1}^N w_{nm} [H(x_m) - H(x_n)], \quad \text{if } t \neq t_{n_i}, \quad (5.16)$$

$$x_n(t_{n_i}^+) = g(x_n(t_{n_i}^-)), \quad \text{if } t = t_{n_i}. \quad (5.17)$$

Here $H : \mathbb{R}^2 \rightarrow \mathbb{R}^2$ describes the form of interaction between the components of nodes and for the (linear) case considered here it is given simply by $H(u, v) = (0, u)^\top$. The vector field $F : \mathbb{R}^2 \rightarrow \mathbb{R}^2$ is the single node dynamics prescribed by $F(x_n) = Ax_n + f_{e_n}$, with A as in Eq. (5.5) and $f_{e_n} = (0, f)^\top \text{sgn}(v_n)$.

From the form of coupling in Eq. (5.16) it is apparent that if $x_m = x_n$ for all pairs (m, n) then the coupling has no effect and the network reduces to an uncoupled system of individual Franklin bells. Thus if an individual bell can oscillate then a synchronous network state defined by the $N - 1$ constraints $x_1(t) = x_2(t) = \dots = x_N(t) = s(t)$ is guaranteed to exist, where $s(t) = (u(t), v(t))^\top$ is the periodic orbit of an isolated node. The techniques for constructing this are precisely those of section 5.2.1. The network impact times are also inherited directly from the periodic orbit of an isolated node so that $t_{1_i} = t_{2_i} = \dots = t_{N_i} = t_i$, for $i = 1, 2$.

To determine the stability of the synchronous network state it is first convenient to rewrite Eq. (5.16) using the graph-Laplacian \mathcal{G} given by (2.53). The network dynamics between impacts then takes the succinct form

$$\dot{x}_n(t) = F(x_n(t)) - \sigma \sum_{m=1}^N \mathcal{G}_{nm} H(x_m). \quad (5.18)$$

If we now consider a small perturbation to the synchronous orbit by writing

$x_n(t) = s(t) + \delta x_n(t)$ then we obtain the variational equation

$$\frac{d}{dt}\delta x_n = DF(s(t))\delta x_n - \sigma DH(s(t)) \sum_{m=1}^N \mathcal{G}_{nm}\delta x_m, \quad (5.19)$$

where $DF(s(t))$ and $DH(s(t))$ are the Jacobian matrices of $F(s(t))$ and $H(s(t))$. The PWL nature of the network model means that these can be explicitly calculated as

$$DF(s(t)) = A \quad \text{and} \quad DH(s(t)) = \begin{bmatrix} 0 & 0 \\ 1 & 0 \end{bmatrix}. \quad (5.20)$$

Using the technique presented in Section 2.4.5, we reduce (5.19) to a block diagonal form where in each block we have a 2×2 linear dynamical system parametrised by the eigenvalues of the graph-Laplacian:

$$\frac{d}{dt}\xi_l = (A - \sigma\lambda_l DH)\xi_l, \quad l = 1, \dots, N, \quad (5.21)$$

where $\xi_l(t) \in \mathbb{C}^2$. Then the evolution of the perturbations through the impacting manifolds can be obtained using the same approach as in Sections 5.2.1 since saltation acts blockwise (see Section 4.6.2). Thus solutions of the set of Floquet equations given by Eq. (5.21) are in the form $\xi_l(\Delta) = Q(l)\xi_l(0)$, $l = 1, \dots, N$, where

$$Q(l) = S(t_2)e^{A_l\Delta_2}S(t_1)e^{A_l\Delta_1}, \quad A_l = A - \sigma\lambda_l DH. \quad (5.22)$$

One of the eigenvalues of the graph-Laplacian is zero (which we fix with the choice $\lambda_1 = 0$), with corresponding eigenvector $(1, 1, \dots, 1)/\sqrt{N}$ tangential to the periodic orbit. Thus the synchronous state will be stable if all the other eigenvalues of $Q(l)$, $l = 2, \dots, N$ lie within the unit disc, and the periodic orbit of an isolated node is stable. Since this argument is valid for an arbitrary graph-Laplacian it is useful to consider a Floquet problem obtained from Eq. (5.22)

under the replacement $\sigma\lambda_l \rightarrow \eta \in \mathbb{C}$, so that $Q(l) \rightarrow \mathcal{Q}(\eta)$ where $\eta_l \equiv \sigma\lambda_l$ and

$$\mathcal{Q}(\eta) = S(t_2) \exp[(A - \eta DH)\Delta_2] S(t_1) \exp[(A - \eta DH)\Delta_1]. \quad (5.23)$$

Then the MSF can be computed independently of the network choice and then used to assess the stability of the synchronous state in an arbitrary network, simply by determining where the spectrum of the graph-Laplacian lies in relation to the MSF.

We note that it is also natural to consider the stability of the synchronous state in networks of identically coupled limit cycle oscillators using weakly coupled phase oscillator theory. Doing so would give rise to a Kuramoto type network model. The Jacobian determining the stability of the synchronous state would have eigenvalues $-\sigma H'(0)\lambda_l$, where $H(t)$ is a derived Δ -periodic phase interaction function, and see Chapter 2 for a further discussion. In this case, the stability of the synchronous state is independent of the strength of interaction (though will depend on the network graph-Laplacian and the sign of σ). Thus, it cannot be used to predict any *strong coupling* instabilities, whereas the MSF approach can. Moreover, we may consider to use the phase-amplitude network formalism presented in Section 4.6.1 but it gets more complicated and computationally expensive for networks of N nodes since the number of interaction functions increases. Also, as we observed in Section 4.7, it is less accurate than the MSF approach to detect bifurcation points or even sometimes insufficient to detect them.

5.4.2 Master stability function for a smoothed Franklin bell network

The argument above shows how the MSF, originally developed for the study of smooth systems, can be modified for the use of nonsmooth systems using saltation operators. We can also sidestep the need to use saltation operators using the smoothing technique described in section 5.3. In essence, this leads

to the replacement of the saltation operators by propagators $\exp[A_{L,R}\delta t]$ for some fixed small δt with $A_{L,R}$ determining the augmented dynamics in the region where $|u_n| > a$. In this case the MSF can be constructed in an almost identical fashion to that of section 5.4.1 under the replacement of Eq. (5.23) by

$$\begin{aligned} \mathcal{Q}(\eta) = & \exp[(A_L - \eta DH)\delta t] \exp[(A - \eta DH)\Delta_2] \\ & \times \exp[(A_R - \eta DH)\delta t] \exp[(A - \eta DH)\Delta_1]. \end{aligned} \quad (5.24)$$

A comparison of the MSF for the nonsmooth and smoothed model is shown in Fig. 5.7. The white region indicates where the MSF is negative. It can be seen that as δt is chosen to be smaller and smaller that the agreement between the two MSFs becomes closer and closer.

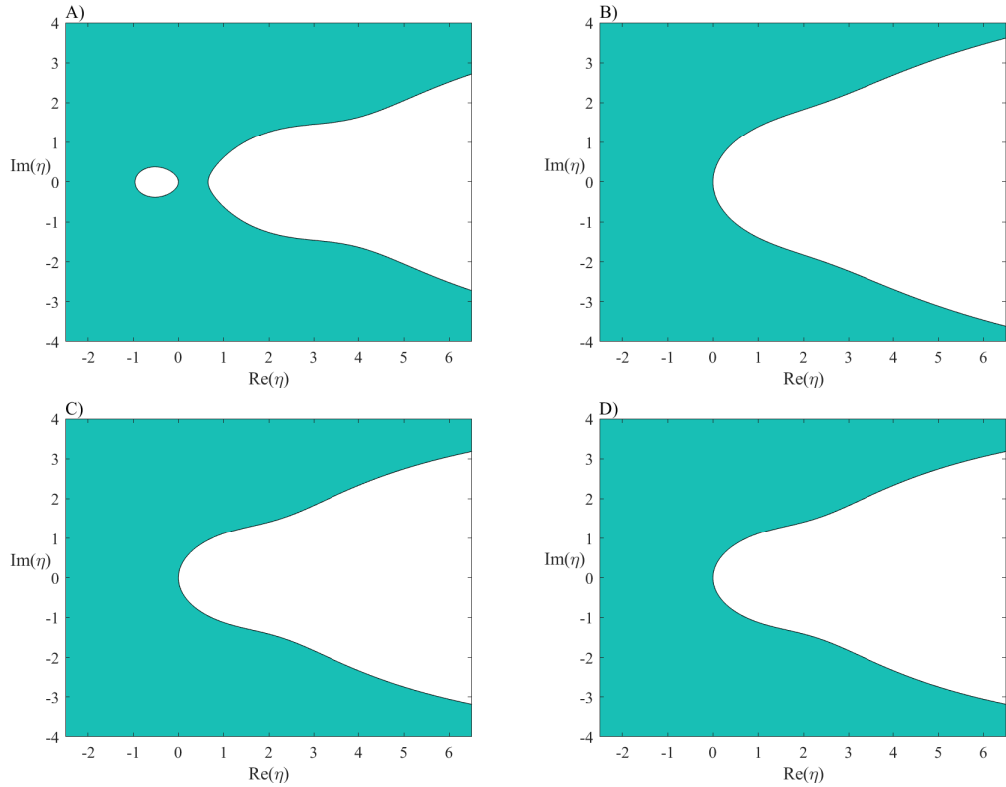


Figure 5.7: A comparison of the MSF between the smoothed and nonsmooth system. Panels A), B), and C) are for the smoothed system and panel D) for the nonsmooth system. A) $\delta t = 1$, B) $\delta t = 0.5$, and C) $\delta t = 0.0004$. The white region indicates where the MSF is negative. Parameters are the same as Fig. 5.5. As $\delta t \rightarrow 0$ there is increasing agreement between the MSF of the smoothed model and that of the nonsmooth model.

5.5 Examples

In the following we will illustrate the above concepts with two kinds of network. We begin with an undirected ring network, for which the symmetric coupling strength between nodes n and m is given by

$$w_{nm} = c_n(\delta_{n,m-1} + \delta_{N-n+1,1}) + c_{n-1}\delta_{n,m+1} + c_N\delta_{1,N-m+1} \quad (5.25)$$

$$n, m = 1, 2, \dots, N,$$

where c_n , $n = 0, 1, \dots, N$ is non-zero. Due to symmetry, all eigenvalues of the matrix W (with components $[W]_{nm} = w_{nm}$) are real. For a network of regular springs, i.e. when $c_n > 0$ for $0 \leq n \leq N$, this entails that the eigenvalues of the graph-Laplacian are all larger or equal to zero. As a consequence, the synchronous network state is linearly stable since the MSF is negative for all arguments on the positive real half-line, see Fig. 5.7D. In Fig. 5.8A, we superimpose the η_l ($\sigma\lambda_l \equiv \eta_l$) for a network of 15 nodes where $c_n = 1$ if n is odd and $c_n = 0.1$ if n is even, while Fig. 5.8B shows results from direct numerical simulations. As expected, the synchronous network state is stable.

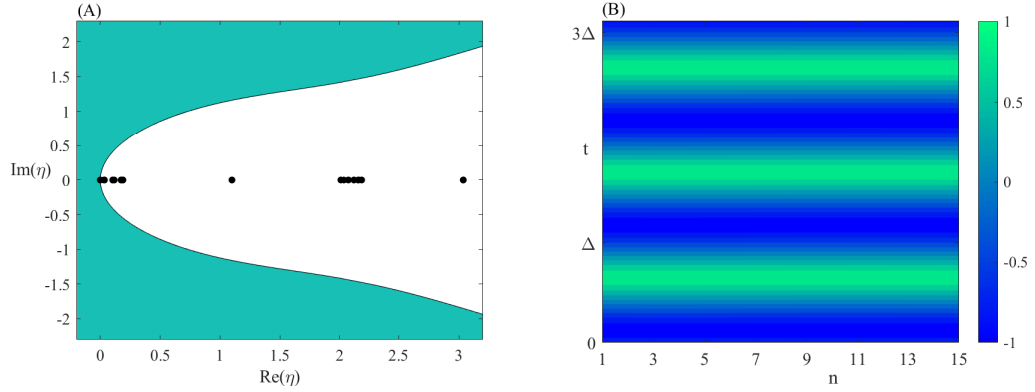


Figure 5.8: (A) MSF together with the values of η_l (black dots) for a network of 15 nodes, where $c_n = 1$ if n is odd and $c_n = 0.1$ if n is even. (B) Space-time plot of the network activity of u_n . All parameter values as in Fig. 5.5 and $\sigma = 1$.

It is now instructive to change one of the spring constants c_n in the above network to a negative value, which represents a repulsive spring. When we choose $c_2 = -0.1$, we obtain the results depicted in Fig. 5.9. In this case, the MSF is negative for one of the η_l , say η_k , indicating that the synchronous

network state is unstable. Indeed, numerical simulations clearly show a modulation of the values for u_n across the network, see Fig. 5.9B.

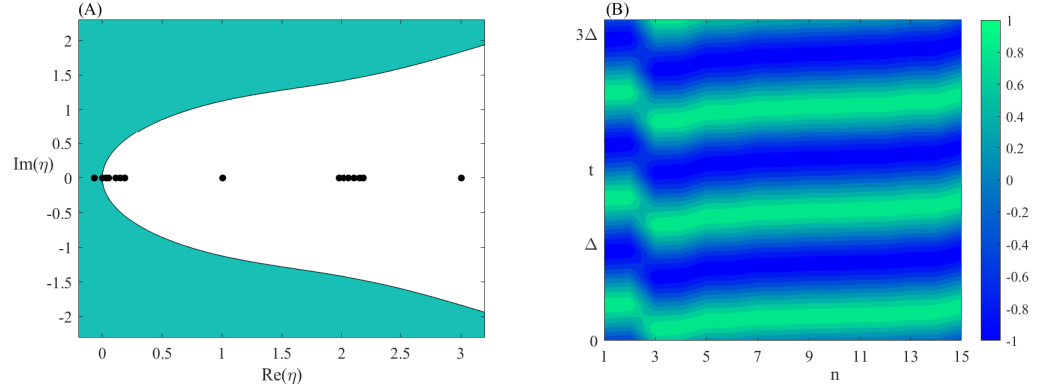


Figure 5.9: (A) MSF together with the values of η_l (black dots) for a network of 15 nodes, where $c_n = 1$ if n is odd and $c_n = 0.1$ if n is even, except for $c_2 = -0.1$. Note that $\eta_k = -0.0665$. (B) Space-time plot of the network activity of u_n . All parameter values as in Fig. 5.5 and $\sigma = 1$.

To predict the shape of the emergent network pattern, we can make use of the eigenvector that corresponds to the eigenvalue associated with η_k . As Fig. 5.10 illustrates, the eigenvector resembles very closely the observed values of u_n . Note how well the eigenvector captures the large peak and the small oscillations of the network state.

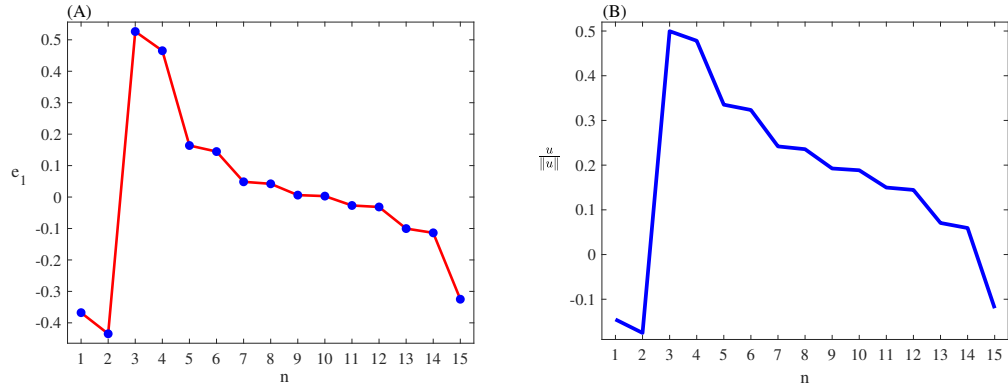


Figure 5.10: (A) Normalised eigenvector corresponding to the eigenvalue associated with η_k in Fig. 5.9. (B) Normalised u as a function of n for a fixed time across the network. All parameter values as in Fig. 5.9.

We can now move away from real eigenvalues of W by considering the directed network shown in Fig. 5.11. The coupling strengths are given by

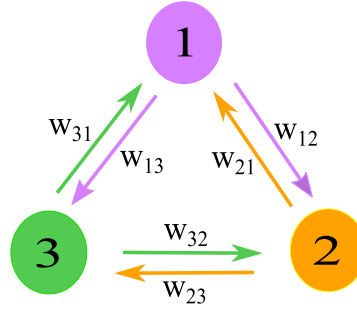


Figure 5.11: Architecture of the directed ring network.

$$w_{nm} = \mu \begin{bmatrix} 0 & 1 & 1 \\ -1 & 0 & 3 \\ 2 & -2 & 0 \end{bmatrix} \quad \text{and} \quad n, m = 1, 2, 3, \quad (5.26)$$

where μ is a real number, resulting in complex eigenvalues for W , hence we can test the theory for such cases. If we choose $\mu^{-1} = 2.1$ the MSF is negative at the corresponding values of η_i , indicating that the synchronous network state is stable (see Fig. 5.12A). Numerical simulations plotted in Fig. 5.12B confirm the results from the linear stability analysis. Here, we plot the time evolution of the v component of all three nodes, i.e. v_1 , v_2 and v_3 . Because of synchrony, the curves overlap and we can see only one trajectory.

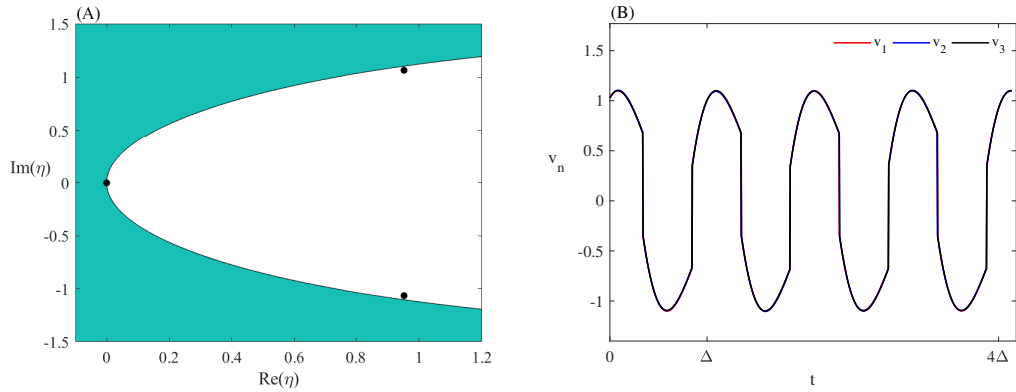


Figure 5.12: (A) MSF together with the values of η_i (black dots) for the directed network shown in Fig. 5.11 for $\mu^{-1} = 2.1$. (B) Time evolution of v_1 , v_2 and v_3 . All parameter values as in Fig. 5.5 and $\sigma = 1$.

When we change μ^{-1} to 1.9 we obtain a pair of complex conjugates η_i that lie in the green region in Fig. 5.13A. Here, the MSF is positive, which means that the synchronous network state is unstable. This can also be seen

in Fig. 5.13B, where we plot trajectories for v_1 , v_2 and v_3 from numerical simulations. In contrast to Fig. 5.12B, all three trajectories can be clearly distinguished. Note that the emergent pattern can be predicted from the real eigenvector that is associated with the pair of complex eigenvalues η_l , see Figs. 5.14. This is an example of a strong coupling instability.

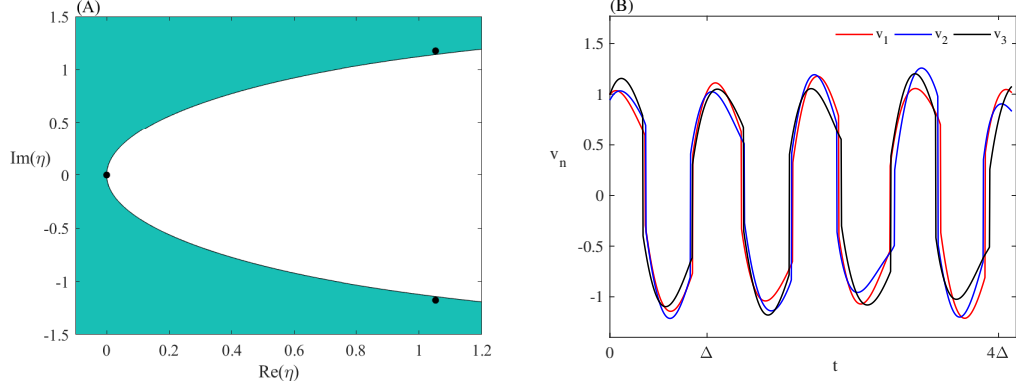


Figure 5.13: (A) MSF together with the values of η_l (black dots) for the directed network shown in Fig. 5.11 for $\mu^{-1} = 1.9$. (B) Time evolution of v_1 , v_2 and v_3 . All parameter values as in Fig. 5.5 and $\sigma = 1$.

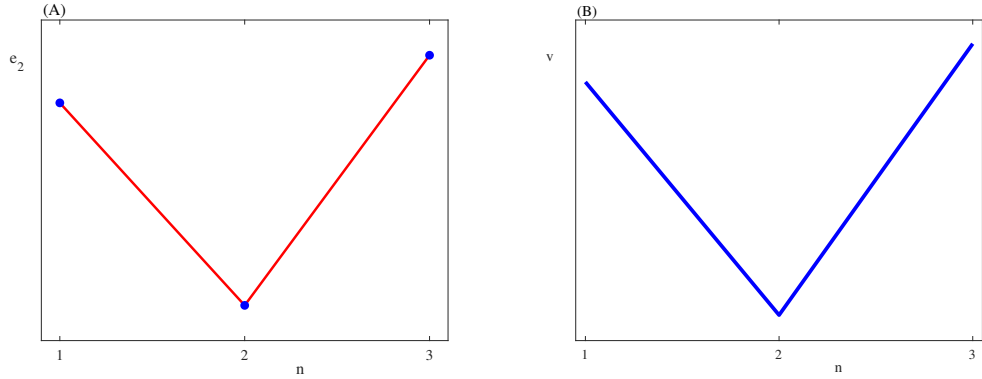


Figure 5.14: (A) Real part of the eigenvector corresponding to eigenvalues associated with the complex η_k in Fig. 5.13. (B) v as a function of n for a fixed time across the network. All parameter values as in Fig. 5.5 and $\sigma = 1$.

5.6 Discussion

Since their inception, Franklin bells have provided the blueprint for numerous electro-mechanical impact oscillators [13, 84, 145, 162]. In its original incarnation, a Franklin bell consisted of two bells between which a metal ball was

suspended. The regular chime of a Franklin bell results from the periodic motion of the metal ball between the two bells. Upon impact, the metal ball loses some of its energy, which is captured by a restitution coefficient $k < 1$. In this regime, only one periodic orbit of the underlying dynamical system (5.3) and (5.4) exists, which is linearly stable (see Fig. 5.3). As we increase k past one, an unstable solution emerges, which eventually collides with the stable periodic orbit in a saddle node bifurcation. A restitution coefficient larger than one corresponds to an active impacting surface where energy is transferred into the metal ball instead of it being lost from it [113, 245, 312].

For constructing periodic solutions, the nonsmooth character of the governing equations does not pose any difficulties. Indeed, we can construct solutions between impacts and then glue them together. Since the system in (5.3) and (5.4) is piecewise linear, solutions are given explicitly in terms of exponential functions. To assess linear stability, we use saltation matrices to propagate perturbations through the impacting manifolds. One could now argue that at a microscopic scale, the dynamics of Franklin bells are actually smooth and the nonsmooth character only emerges due to the coarse-grained use of a restitution coefficient. Motivated by this notion, we developed a novel smoothing technique, which is based on supplementing the original dynamical system with two additional parts that describe the dynamics for $u > a$ and $u < -a$. In each region, we prescribe a linear dynamical system whose coefficients are uniquely determined by demanding that the new pieces of the orbit connect to the existing parts in a C^1 fashion and satisfy the restitution condition. What we need to prescribe, however, is the time-of-flight δt in these two regions. In other words, once we impose a time-of-flight, all coefficients are fixed. The advantage of this approach is that we can explore how the smooth dynamical system approaches the nonsmooth one by reducing δt . As Fig. 5.5 illustrates, letting δt go to zero reduces the propagator in the regions $u < -a$ and $u > a$ to the saltation matrices of the nonsmooth system, highlighting the consistency of our new technique.

The above discussion about smooth versus nonsmooth representations ties into the discourse on *hard impact modelling* (particle exposed to a rigid constraint) and *soft impact modelling* (particle exposed to an elastic constraint) [27]. Inelastic models are based on Newton’s law of impact and use two main assumptions; (i) the interaction time with the rigid constraint is infinitely small and (ii) that energy dissipation is characterised by a constant restitution coefficient. Explicitly, a restitution coefficient refers to the ratio of post- and pre-impact velocities. In this modelling regime the rigid particle collides with the stiff constraint and none of them are deformed during the collision. On the other hand, soft modelling assumes a finite non-zero contact time and a penetration of the constraint by the colliding body. In this modelling philosophy, the hard impacting constraint is replaced with a spring–damper support or cushioned as it is common in engineering. Elastic impact modelling can be used to analyse different types of spring–damper support systems, which can be either linear or nonlinear [67, 155, 191, 192, 272]. Interpolating between these two scenarios is the case in which an elastic body impacts on a rigid surface, which again leads to a nonzero interaction time [61].

While we use the time-of-flight δt to control the transition from smooth to nonsmooth dynamics, applications in engineering typically adjust the parameters of the spring–damper system. Naturally, these two approaches are equivalent. Shaw and Holmes [274] observed that as the stiffness of the cushioned constraint approaches infinity, collision times go to zero and the system becomes an inelastic impact oscillator. Further evidence for this equivalence is provided in Ing et al. [142, 143]. The findings in [27, 156] also demonstrate that the smooth system approaches the nonsmooth one for large spring–damper stiffnesses. In addition, these studies show how the dynamics of the two systems diverges for softer spring–dampers. This is attributed to the growing influence of external forces, such as gravity, and is consistent with the idea of larger impact times, since only then have these external forces sufficient time to interact.

Having investigated a single Franklin bell, we next turned to networks of N Franklin bells with arbitrary topology. Crucially, each node of the network corresponds to a Franklin bell, and nodes are coupled via springs. Our work contrasts that in Shiroky and Gendelman [278], where in a linear chain only the central node was a Franklin bell, whilst the remaining nodes were classical non-impacting pendula. Our interest was in the linear stability of the synchronous network state. The existence of synchrony is guaranteed due to the linear coupling between Franklin bells. For linear stability, we employed the MSF approach [229], which reduces the complexity of the linear stability analysis from investigating a $2N$ -dimensional system of coupled equations to N two-dimensional systems. As Fig. 5.7 illustrates, the MSF for the nonsmooth model is well approximated by the one for the smoothed dynamics. However, as we make the time-of-flight δt in the additional regions $|u| > a$ larger, the topology of the MSF changes. A new bubble emerges around the origin, and the extended white region of stability shifts to the right, cf. Figs. 5.7A and 5.7D. For a ring network of standard springs, i.e. with positive spring constants, the MSF predicts that synchrony is stable, which is confirmed by direct numerical simulations (Fig. 5.8). By changing the spring constant of one of the springs in the network to a repulsive value, one η_l crosses into the green region where the MSF is positive, indicating that the synchronous network state is unstable (Fig. 5.9). This highlights the fact that subtle changes to the network parameters can have drastic consequences for the network dynamics. Close to the onset of instability, only one η_l crosses into the region where the MSF is positive. In this case, the eigenvector associated with the corresponding eigenvalue provides a good estimator for the emergent network state as illustrated by Fig. 5.10. For the examples above, all eigenvalues of the connectivity matrix W are real. By changing the topology of the network, the eigenvalues of the graph-Laplacian may also become complex. Again, the MSF predicts correctly the linear stability of the synchronous state, see Figs. 5.12 and 5.13.

While we focussed our analysis on Franklin bells, the present study more generally furthers our understanding of networks comprised of nodes with non-smooth dynamics. To date, discontinuous and nonsmooth dynamical systems have mostly been studied in isolation. Yet, networks are ubiquitous across engineering and the natural and social sciences. It is therefore desirable to expand our toolbox from individual to interacting nonsmooth dynamical systems, as recently advocated by Coraggio *et al.* [58] for piecewise-smooth systems, with applications in seismology and load balancing in power grids. As we have illustrated, concepts such as saltation matrices, which are useful at the node level, carry over to the network level and expand the applicability of central techniques for smooth dynamical systems, such as the MSF, to nonsmooth systems. A possible extension of this work can be achieved by adding time delays [292]. Moreover, the techniques used here could be adopted to vibro-impact energy harvesting systems [3, 341] to test the efficiency at the network level, and our smoothing method could be useful for the investigation of new materials such as elastic support for fenders [283, 284].

Chapter 6

Piecewise linear neural mass models

6.1 Introduction

The brain is the most complicated organ in the body with a complex architecture and rich dynamics involving approximately 10^{10} neurons and 10^{14} synapses. It is responsible for many vital functions, including learning, action, cognition, and perception [200]. The structure and function of the brain have been studied for hundreds of years; yet still there are many interesting dynamical phenomena that remain a mystery such as precise description of memory storage and retrieval. Although neural activity in the human brain is a hard task to understand, it is important to explore this in order to better treat disorders such as epilepsy [96]. Computational and mathematical models are useful for gaining insight wider fundamental mechanisms of the brain, and naturally complement experimental approaches. In a mathematical model one can easily explore effects of parameter variation but this is very difficult and expensive or even impossible in a real experimental environment. The main weakness of mathematical models is that in general they are simplification or idealisation of real behavior. However, it is expected that a well-defined mathematical model could give proper insight into brain activities. There are

various kinds of mathematical models for brain activity. These models can have different levels of description, ranging from microscopic (single neuron activity) through mesoscopic to macroscopic levels. Single neuron modelling is important because the transmission of information (action potentials) in the brain starts at that level (between neurons via axons and synapses). Famous examples of the single neuron modelling are the Hodgkin-Huxley model [135], the FitzHugh-Nagumo model [101, 212] and the McKean model [201], see Chapter 3 for more details. Mesoscopic models (typically 10^6 neurons) explain how neural elements interact to yield emergent behaviour at the level of microcolumns and cortical columns. And macroscopic models give information about whole brain dynamics and interactions between large-scale neural systems such as the thalamus, brain stem, and cortical regions [69].

The behavior of biological neural cells is often explored by examining the response of their cell membrane potential to the injection of an external current. When the postsynaptic potential reaches a threshold value, the neuron produces an impulse or spike. These responses, called action potentials (typically $\sim 100\text{mV}$ amplitude and 1ms duration), are partially dependent upon membrane conductance properties, and are the units of information transmission at the interneuron level. This information is thought to be encoded in terms of the frequency of the action potentials, called firing rate, and in the timing of action potentials [53, 69].

It is well known that brain functions such as cognitive, motor, and sensory functions are implemented by large groups of interacting neurons [65, 200]. A common way to model this is to simulate a large network of synaptically interacting single neuron models. Although this is a useful way to understand network behaviour it requires a lot of expensive computations. Another drawback of large simulations is that they may involve a large number of parameters. Therefore it could be very difficult to see the influence of parameter changes. These reasons have lead researchers to use mesoscopic and macroscopic models to examine large scale brain dynamics. These models usually describe average

activity of a large group of neurons and are less detailed than single neuron models. Despite this they can often generate activity consistent with human neuroimaging studies. Being computationally less expensive and having fewer parameters makes analysis easier and therefore, mesoscopic and macroscopic models studies are significantly important to better understand brain activities. One of the famous classes of mesoscopic models is called a neural mass model [106].

Neural mass models generate brain rhythms using the notion of population firing rates, aiming to side-step the need for large scale simulations of more realistic networks of spiking neurons. Although they are not derived from detailed conductance based models they can be motivated by a number of phenomenological arguments [56], and typically take the form of systems of nonlinear ordinary differential equations. Neural mass models are a key component of the Virtual Brain project that aims to deliver the first simulation of the human brain based on individual large-scale connectivity [266]. Such large-scale brain network models are especially relevant to understanding resting state networks [34], whereby different regions of the brain’s sensorimotor system oscillate slowly and synchronously in the absence of any explicit task.

The Wilson-Cowan model is one of the most well-known neural mass models for modelling the activity of cortex, and for a historical perspective see [59, 134]. It describes the dynamics of two interacting populations of neurons, one of which is excitatory and the other inhibitory. Interactions are mediated between the populations with the use of a nonlinear sigmoidal firing rate function. In its most simple incarnation it consists of two nonlinear ODEs, and as such has been widely studied using techniques from phase-plane analysis and numerical bifurcation theory. Since the 1970s there has been a large amount of attention devoted to the analysis of these models and their application in neuroscience [77, 178, 220, 334].

It is important to note that from a mathematical modelling perspective all neural mass models to date are essentially low dimensional coupled ODEs with

a sigmoidal firing rate nonlinearity, exemplified by the Wilson-Cowan model. Given their relevance to large scale brain dynamics it is highly desirable to develop mathematical techniques for the analysis of Wilson-Cowan style neural mass models at the large network level. Here we advocate for the replacement of smooth sigmoidal nonlinearities in neural mass models by more tractable functions, including piecewise linear and piecewise constant functions. We refer to Chapter 3 for the advantages of using PWL neural modelling [55, 217].

In this chapter, first in Sections 6.2 and 6.3 we introduce the model for an isolated Wilson-Cowan node with a PWL firing rate. The description of dynamical states with reference to switching manifolds becomes very useful [54], see Section 3.3. Making use of the techniques from Chapter 3, we show how matrix exponentials can be used to patch together a periodic orbit, and that Floquet theory simplifies considerably to yield explicit formulas for determining solution stability. Next in Section 6.4 we consider a network of PWL Wilson-Cowan nodes, with nodes arranged along a ring with distance-dependent interactions. This particular choice of coupling guarantees the existence of the synchronous state. We then develop a linear stability analysis of this state and show that this leads to a tractable variational problem of a very similar type to that for the single node, albeit now parameterised by the eigenvalues of the connectivity matrix. We use this to determine instabilities that can lead to the formation of spatio-temporal network patterns. Then in Section 6.5 we consider the case that the firing rate is a Heaviside function, for which the techniques developed for studying PWL systems break down. Once again periodic orbits can be constructed using matrix exponentials, although standard Floquet theory must be now augmented to cope with the evolution of linearised perturbations through the switching manifolds, see Section 4.2. However, at the network level (Section 6.6) the stability of the synchronous state is much harder to determine than for the continuous model. Here we show the ideas from the study of Glass networks [90, 117, 118] developed by Edwards [89] are particularly useful, and that stability is strongly influenced

by the temporal order in which network components cross switching manifolds, and that this in turn is determined by the choice of initial perturbation. Finally in Section 6.7 we conclude with an overview of the new results about synchrony in networks of neural mass models, and discuss the natural extension of this work to treat non-synchronous states.

The results of this chapter have been published in [57].

6.2 The Wilson-Cowan model

For their activity-based neural mass model Wilson and Cowan [329, 330] distinguished between excitatory and inhibitory sub-populations. This seminal (space-clamped) model can be written succinctly in terms of the pair of coupled differential equations:

$$\frac{du}{dt} = -u + F(I_u + w^{uu}u - w^{uv}v), \quad \tau \frac{dv}{dt} = -v + F(I_v + w^{vu}u - w^{vv}v), \quad (6.1)$$

Here $u = u(t)$ is a temporal coarse-grained variable describing the proportion of excitatory cells firing per unit time at the instant t . Similarly the variable v represents the activity of an inhibitory population of cells. The constants $w^{\alpha\beta}$, $\alpha, \beta \in \{u, v\}$, describe the weight of all synapses from the α th population to cells of the β th population, and τ is a relative time-scale.

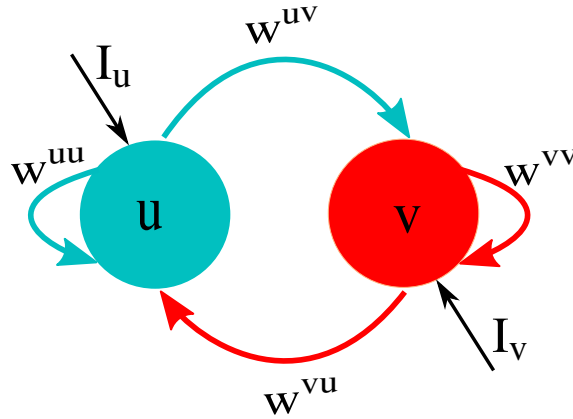


Figure 6.1: Schematic diagram of the Wilson-Cowan model.

The nonlinear function F describes the expected proportion of neurons receiving at least threshold excitation per unit time, and is often taken to have a sigmoidal form. Here the terms I_α represent external inputs (that could be time varying). For a historical perspective on the Wilson-Cowan model see [77], and for a more recent reflection by Cowan see [60].

6.3 A piecewise linear reduction

In order to reduce the model to a mathematically tractable form we consider the choice of a PWL firing rate function given by

$$F(x) = \begin{cases} 0 & x \leq 0 \\ \epsilon^{-1}x & 0 < x < \epsilon \\ 1 & x \geq \epsilon \end{cases} \quad (6.2)$$

Some different illustrations of firing rate functions are shown in Fig. 6.2.

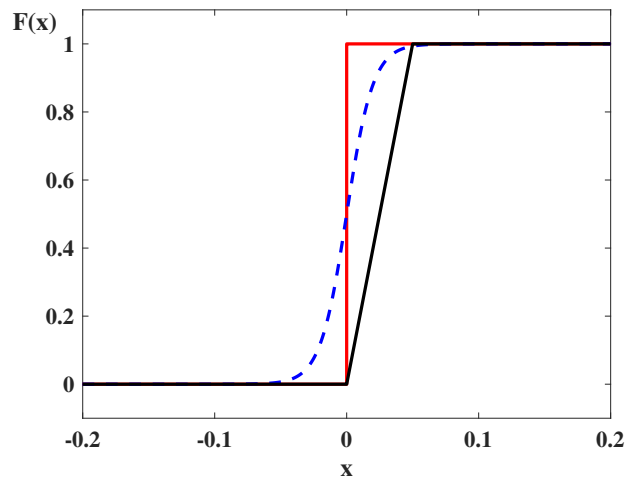


Figure 6.2: *Firing rate functions. PWL (black), sigmoidal (blue) and Heaviside (red).*

For appropriate choices of parameters the Wilson-Cowan model, with the firing rate given by (6.2), can support stable oscillations. An example is shown in Fig. 6.3, where we also plot the four switching manifolds defined by the

condition that arguments to the function F in (6.1) take on the values zero and ϵ .

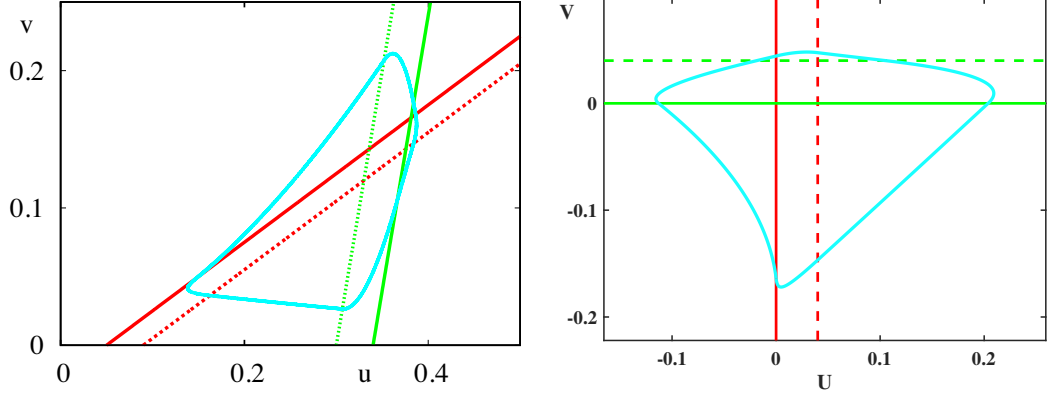


Figure 6.3: *Left: Phase plane for the Wilson-Cowan model with a PWL firing rate, showing a stable periodic orbit. Parameters: $\epsilon = 0.04$, $\tau = 0.6$, $I_u = -0.05$, $I_v = -0.3$, $w^{uu} = 1$, $w^{vu} = 2$, $w^{uv} = 1$, and $w^{vv} = 0.25$. The straight lines in red and green show the switching manifolds, where $I_u + w^{uu}u - w^{vu}v = 0, \epsilon$ and $I_v + w^{uv}u - w^{vv}v = 0, \epsilon$ respectively. Right: Same periodic orbit in the transformed coordinate plane (U, V) . The straight lines in red and green show the switching manifolds, where $U = 0, \epsilon$ and $V = 0, \epsilon$ respectively.*

Away from the switching manifolds the dynamics governing the evolution of trajectories is linear, and may be constructed using matrix exponentials. To simplify further analysis it is first convenient to introduce new variables (U, V) such that $u = (w^{vu}(V - I_v) - w^{vv}(U - I_u))/|W|$, where $|W| = \det W$, and $v = (w^{uu}(V - I_v) - w^{uv}(U - I_u))/|W|$, as well as the matrices

$$W = \begin{bmatrix} w^{uu} & -w^{vu} \\ w^{uv} & -w^{vv} \end{bmatrix}, \quad J = \begin{bmatrix} 1 & 0 \\ 0 & 1/\tau \end{bmatrix} \quad A = -WJW^{-1}. \quad (6.3)$$

With these choices (6.1) transforms to

$$\frac{d}{dt} \begin{bmatrix} U \\ V \end{bmatrix} = A \begin{bmatrix} U - I_u \\ V - I_v \end{bmatrix} + WJ \begin{bmatrix} F(U) \\ F(V) \end{bmatrix}. \quad (6.4)$$

In the representation (6.4) we see that the four switching manifolds are simply defined by $U = 0$, $U = \epsilon$, $V = 0$, and $V = \epsilon$. The periodic orbit shown in

Fig. 6.3 (encircling an unstable fixed point) crosses each of these manifolds twice, so that the periodic trajectory is naturally decomposed into eight separate pieces. On each piece we shall denote the time-of-flight for a trajectory to travel from one switching manifold to another by Δ_i , $i = 1, \dots, 8$, so that the period of the orbit is given by $\Delta = \sum_{i=1}^8 \Delta_i$. As an explicit example of how to construct a trajectory between two switching manifolds, consider the region where $0 \leq U \leq \epsilon$ and $V < 0$. In this case the solution of (6.4) is given by

$$\begin{bmatrix} U(t) \\ V(t) \end{bmatrix} = e^{A_+(\epsilon)t} \begin{bmatrix} U(0) \\ V(0) \end{bmatrix} - A_+^{-1}(\epsilon) (e^{A_+(\epsilon)t} - I_2) A \begin{bmatrix} I_u \\ I_v \end{bmatrix}, \quad t \geq 0, \quad (6.5)$$

where

$$A_+(\epsilon) = \left(A + \epsilon^{-1} W J \begin{bmatrix} 1 & 0 \\ 0 & 0 \end{bmatrix} \right). \quad (6.6)$$

It is a simple matter to write down the trajectories in each of the remaining regions of phase space visited by a periodic orbit. We may then use these matrix exponential formulas to *patch* together solutions, setting the origin of time in each region such that *initial* data in one region comes from *final* data from a trajectory in a neighbouring region. We shall denote the periodic orbit by (\bar{U}, \bar{V}) such that $(\bar{U}(t), \bar{V}(t)) = (\bar{U}(t + \Delta), \bar{V}(t + \Delta))$. If we consider initial data with $(\bar{U}(0), \bar{V}(0)) = (U_0, 0)$ then the eight times-of-flight and the unknown U_0 are determined self-consistently by the nine equations $\bar{V}(\Delta_1) = \epsilon$, $\bar{U}(\Delta_2) = \epsilon$, $\bar{U}(\Delta_3) = 0$, $\bar{V}(\Delta_4) = \epsilon$, $\bar{V}(\Delta_5) = 0$, $\bar{U}(\Delta_6) = 0$, $\bar{U}(\Delta_7) = \epsilon$, $\bar{V}(\Delta_8) = 0$, and $\bar{U}(\Delta_8) = U_0$. The numerical solution of this nonlinear algebraic system of equations can be used to construct periodic orbits such as the one shown in Fig. 6.3. This system is also support an unstable periodic orbit and we depict this together with the stable one in Fig. 6.4.

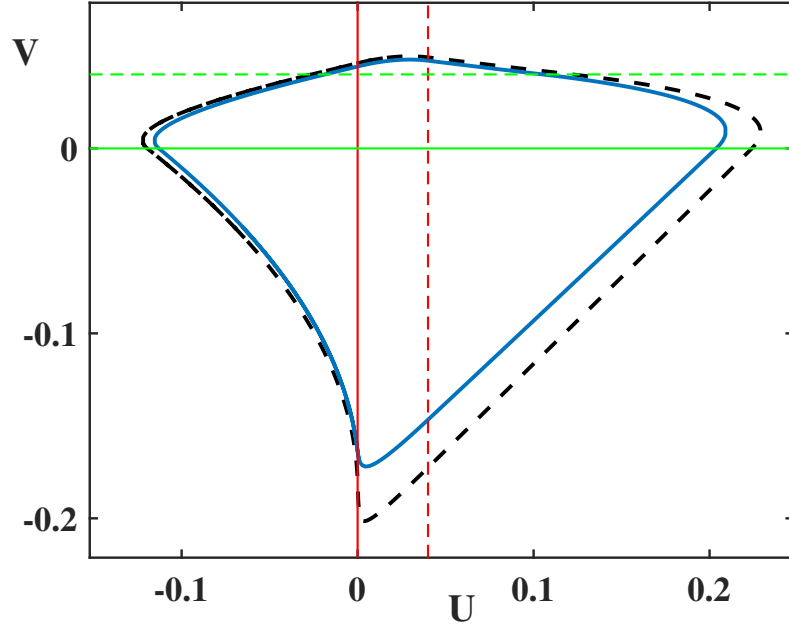


Figure 6.4: A plot of the stable periodic orbit (blue), and an unstable periodic orbit (dashed black). Parameters and switching manifolds as in Fig. 6.3.

Note that the construction of periodic orbits that do not cross all of the switching manifolds can similarly be performed (requiring the simultaneous solution of fewer equations). To determine stability we use results from Section 4.2, denoting non-trivial Floquet exponent by κ , for the PWL Wilson-Cowan model we have that

$$\kappa = \frac{1}{\Delta} \sum_{i=1}^8 \Delta_i \text{Tr } A_i, \quad (6.7)$$

where $A_2 = A_4 = A_6 = A_8 = A$, $A_3 = A_7 = A_+(\epsilon)$, and $A_1 = A_5 = A_-(\epsilon)$, where

$$A_-(\epsilon) = \left(A + \epsilon^{-1} W J \begin{bmatrix} 0 & 0 \\ 0 & 1 \end{bmatrix} \right). \quad (6.8)$$

Thus a periodic orbit is stable if $\kappa < 0$. In Fig. 6.5 we present a plot of κ as a function of τ , to show that the periodic solution in Fig. 6.3 is stable. Given the above method to construct and determine the stability of a periodic orbit, we next show how to extend this approach to treat synchronous solutions in networks of Wilson-Cowan oscillators.

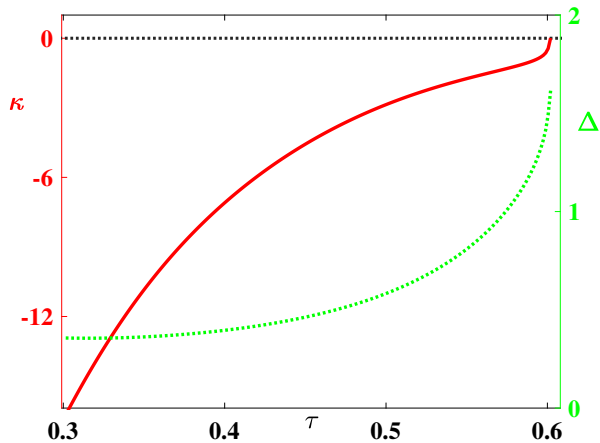


Figure 6.5: A plot of the non-trivial Floquet exponent for the PWL Wilson-Cowan model (left axis), as a function of the relative time-scale τ , with the period of the orbit also shown (right axis). Parameters as in Fig. 6.3. Periodic orbits emerge via a supercritical Hopf bifurcation as τ increases through $\tau_{\text{Hopf}} \simeq 0.3$. We see that the branch of periodic orbits shown is stable, with stability decreasing to zero as the solution is lost with increasing τ . This loss of existence occurs because of a grazing bifurcation (coincident with a saddle-node bifurcation of periodic orbits, see Fig. 6.4) at $\tau_{\text{graze}} \sim 0.6$ whereby part of the trajectory develops a point of inflection on the switching manifold $v = (I_u + w^{uu}u)/w^{vu}$ (red solid line in Fig. 6.3), such that beyond bifurcation the trajectory does not cross the switching manifold and instead is attracted to the stable fixed point at $(u, v) = (0, 0)$.

6.4 A piecewise linear Wilson-Cowan network

The study of coupled oscillator networks in biology, physics, and engineering is now commonplace. Two particularly well known tools for studying patterns of phase-locked states and their instabilities are the theory of weakly coupled oscillators [169], and the master stability function [229], see Chapter 2 for more details. The MSF approach (for identical oscillators) does not require any restriction on coupling strength. Therefore, here we favour the MSF approach and show it simplifies considerably for a PWL choice of firing rate function (though the numerical evolution of a system of dynamical equations, arising from a Floquet variational problem, must be performed). This allows us to improve upon previous mathematical studies of Wilson-Cowan networks, such as those by Campbell and Wang [39] (who treated networks with nearest neighbour coupling and established the condition for synchrony), Ueta and Chen [311] (who performed a numerical bifurcation analysis for small networks),

and Ahmadizadeh *et al.* [4] (who used perturbation techniques and numerics to study synchrony in networks with diffusive coupling).

We consider a network of Wilson-Cowan nodes given by

$$\frac{du_i}{dt} = -u_i + F \left(I_u + \sum_{j=1}^N \mathcal{W}_{ij}^{uu} u_j - \sum_{j=1}^N \mathcal{W}_{ij}^{vu} v_j \right), \quad (6.9)$$

$$\tau \frac{dv_i}{dt} = -v_i + F \left(I_v + \sum_{j=1}^N \mathcal{W}_{ij}^{uv} u_j - \sum_{j=1}^N \mathcal{W}_{ij}^{vv} v_j \right), \quad i = 1, \dots, N, \quad (6.10)$$

subject to the constraints $\sum_{j=1}^N \mathcal{W}_{ij}^{uu} = w^{uu}$, $\sum_{j=1}^N \mathcal{W}_{ij}^{vu} = w^{vu}$, $\sum_{j=1}^N \mathcal{W}_{ij}^{uv} = w^{uv}$, and $\sum_{j=1}^N \mathcal{W}_{ij}^{vv} = w^{vv}$ for all i . These *row-sum* constraints are natural for networks arranged on a ring, and guarantee the existence of a synchronous orbit $(u_i(t), v_i(t)) = (u(t), v(t))$ for all $i = 1, \dots, N$, where $(u(t), v(t))$ is given by the solution of (6.1).

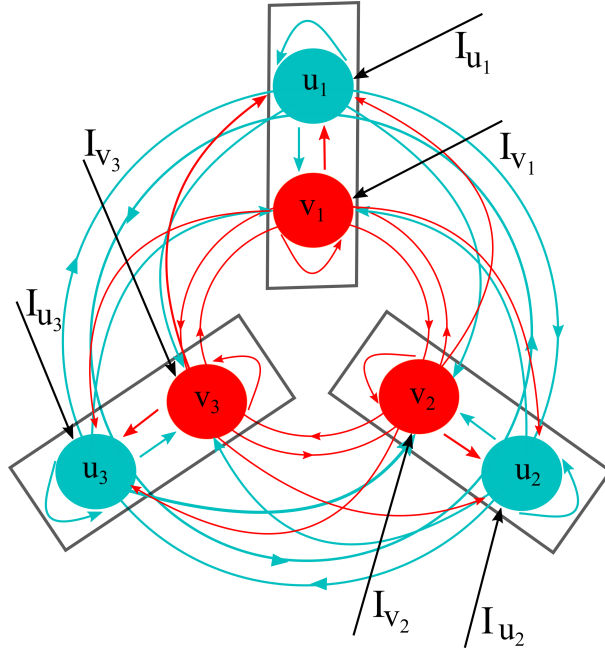


Figure 6.6: Architecture of a network of Wilson-Cowan consisting of 3 nodes. Excitatory (inhibitory) cells are represented by blue (red) circles with corresponding interactions and external inputs.

It is now convenient to introduce a vector notation for the coupled system with $X = (u_1, v_1, u_2, v_2, \dots, u_N, v_N) \in \mathbb{R}^{2N}$ and consider a change of variables $Y = \mathcal{W}X + C$, where $C = \mathbf{1}_N \otimes (I_u, I_v)$, and

$$\mathcal{W} = \mathcal{W}^{uu} \otimes \begin{bmatrix} 1 & 0 \\ 0 & 0 \end{bmatrix} - \mathcal{W}^{vu} \otimes \begin{bmatrix} 0 & 1 \\ 0 & 0 \end{bmatrix} + \mathcal{W}^{uv} \otimes \begin{bmatrix} 0 & 0 \\ 1 & 0 \end{bmatrix} - \mathcal{W}^{vv} \otimes \begin{bmatrix} 0 & 0 \\ 0 & 1 \end{bmatrix}. \quad (6.11)$$

Here the symbol \otimes denotes the usual tensor product for matrices, and $\mathbf{1}_N$ is an N -dimensional vector with all entries equal to unity. This means that the switching manifolds can be succinctly described by $Y_i = 0$ and $Y_i = \epsilon$, and the dynamics takes the form

$$\frac{d}{dt}Y = \mathcal{A}(Y - C) + \mathcal{W}\mathcal{J}F(Y), \quad (6.12)$$

where

$$\mathcal{J} = I_N \otimes J, \quad \mathcal{A} = -\mathcal{W}\mathcal{J}\mathcal{W}^{-1}, \quad (6.13)$$

where J is given by (6.3) and I_N is the $N \times N$ identity matrix. If we denote the synchronous solution by $\bar{Y}(t) = (\bar{U}(t), \bar{V}(t), \bar{U}(t), \bar{V}(t), \dots, \bar{U}(t), \bar{V}(t))$ and consider small perturbations such that $Y = \bar{Y} + \delta Y$, then these evolve according to

$$\frac{d}{dt}\delta Y = \mathcal{A}\delta Y + \mathcal{W}\mathcal{J}DF(\bar{Y})\delta Y, \quad (6.14)$$

where $DF(\bar{Y})$ is the Jacobian of F evaluated along the periodic orbit.

Given the constraints on the matrices $\mathcal{W}^{\alpha\beta}$, with $\alpha, \beta \in \{u, v\}$ it is natural to take these to be circulant matrices with $\mathcal{W}_{ij}^{\alpha\beta} = \mathcal{W}_{|i-j|}^{\alpha\beta}$. In this case the normalised eigenvectors of $\mathcal{W}^{\alpha\beta}$ are given by $e_p = (1, \omega_p, \omega_p^2, \dots, \omega_p^{N-1})/\sqrt{N}$, where $p = 0, \dots, N-1$, and $\omega_p = \exp(2\pi ip/N)$ are the N th roots of unity. The corresponding complex eigenvalues are given by $\nu^{\alpha\beta} = \nu^{\alpha\beta}(p)$ where

$$\nu^{\alpha\beta}(p) = \sum_{\mu=0}^{N-1} \mathcal{W}_{\mu}^{\alpha\beta} \omega_p^{\mu}. \quad (6.15)$$

If we introduce the matrix of eigenvectors $P = [e_0 \ e_1 \ \dots \ e_{N-1}]$, then we have

that

$$\begin{aligned}
& (P \otimes I_2)^{-1} \mathcal{W}(P \otimes I_2) = \\
& (P^{-1} \otimes I_2)(W^{uu} \otimes \begin{bmatrix} 1 & 0 \\ 0 & 0 \end{bmatrix})(P \otimes I_2) - (P^{-1} \otimes I_2)(W^{vu} \otimes \begin{bmatrix} 0 & 1 \\ 0 & 0 \end{bmatrix})(P \otimes I_2) \\
& + (P^{-1} \otimes I_2)(W^{uv} \otimes \begin{bmatrix} 0 & 0 \\ 1 & 0 \end{bmatrix})(P \otimes I_2) - (P^{-1} \otimes I_2)(W^{vv} \otimes \begin{bmatrix} 0 & 0 \\ 0 & 1 \end{bmatrix})(P \otimes I_2) \\
& = (P^{-1}W^{uu}P) \otimes (I_2 \begin{bmatrix} 1 & 0 \\ 0 & 0 \end{bmatrix} I_2) - (P^{-1}W^{vu}P) \otimes (I_2 \begin{bmatrix} 1 & 0 \\ 0 & 0 \end{bmatrix} I_2) \\
& + (P^{-1}W^{uv}P) \otimes (I_2 \begin{bmatrix} 1 & 0 \\ 0 & 0 \end{bmatrix} I_2) - (P^{-1}W^{vv}P) \otimes (I_2 \begin{bmatrix} 1 & 0 \\ 0 & 0 \end{bmatrix} I_2) \\
& = \Lambda^{uu} \otimes \begin{bmatrix} 1 & 0 \\ 0 & 0 \end{bmatrix} - \Lambda^{vu} \otimes \begin{bmatrix} 0 & 1 \\ 0 & 0 \end{bmatrix} + \Lambda^{uv} \otimes \begin{bmatrix} 0 & 0 \\ 1 & 0 \end{bmatrix} - \Lambda^{vv} \otimes \begin{bmatrix} 0 & 0 \\ 0 & 1 \end{bmatrix} \\
& = \text{diag}(\Lambda(0), \Lambda(1), \dots, \Lambda(N-1)) \equiv \Lambda, \tag{6.16}
\end{aligned}$$

where $\Lambda^{\alpha\beta} = \text{diag}(\nu^{\alpha\beta}(0), \nu^{\alpha\beta}(1), \dots, \nu^{\alpha\beta}(N-1))$, and

$$\Lambda(p) = \begin{bmatrix} \nu^{uu}(p) & -\nu^{vu}(p) \\ \nu^{uv}(p) & -\nu^{vv}(p) \end{bmatrix}, \quad p = 0, 1, \dots, N-1. \tag{6.17}$$

Moreover, it is easy to establish that in the above notation

$$\begin{aligned}
& (P \otimes I_2)^{-1} \mathcal{A}(P \otimes I_2) = (P \otimes I_2)^{-1} (-\mathcal{W} \mathcal{J} \mathcal{W}^{-1}) (P \otimes I_2) \\
& = -(P \otimes I_2)^{-1} \mathcal{W}(P \otimes I_2)(P \otimes I_2)^{-1} (I_N \otimes J) \mathcal{W}^{-1}(P \otimes I_2) \\
& = -\Lambda((P^{-1}I_N) \otimes (I_2J)) \mathcal{W}^{-1}(P \otimes I_2) \\
& = -\Lambda(I_N \otimes J)(P^{-1} \otimes I_2^{-1}) \mathcal{W}^{-1}(P \otimes I_2) \\
& = -\Lambda(I_N \otimes J)(P \otimes I_2)^{-1} \mathcal{W}^{-1}(P \otimes I_2) = -\Lambda(I_N \otimes J) \Lambda^{-1}. \tag{6.18}
\end{aligned}$$

If we now consider perturbations of the form $\delta Z = (P \otimes I_2)^{-1} \delta Y$ then from

(6.14) we find that the linearised dynamics is described by the system

$$\begin{aligned}
\frac{d}{dt}\delta Z &= (P \otimes I_2)^{-1} \mathcal{A}(P \otimes I_2) \delta Z + (P \otimes I_2)^{-1} \mathcal{W} \mathcal{J} D F(\bar{Y})(P \otimes I_2) \delta Z \\
&= -\Lambda(I_N \otimes J) \Lambda^{-1} \delta Z + (P \otimes I_2)^{-1} \mathcal{W}(P \otimes I_2)(P \otimes I_2)^{-1} \mathcal{J} D F(\bar{Y})(P \otimes I_2) \delta Z \\
&= -\Lambda(I_N \otimes J) \Lambda^{-1} \delta Z + \Lambda(P \otimes I_2)^{-1} \mathcal{J} D F(\bar{Y})(P \otimes I_2) \delta Z \\
&= -\Lambda(I_N \otimes J) \Lambda^{-1} \delta Z + \Lambda(P \otimes I_2)^{-1} (I_N \otimes J)(I_N \otimes D)(P \otimes I_2) \delta Z \\
&= -\Lambda(I_N \otimes J) \Lambda^{-1} \delta Z + \Lambda((I_N \otimes J)(P \otimes I_2)^{-1})((P \otimes I_2)(I_N \otimes D)) \delta Z \\
&= \Lambda(I_N \otimes J) [-\Lambda^{-1} + (I_N \otimes D)] \delta Z.
\end{aligned} \tag{6.19}$$

Here $D \in \mathbb{R}^{2 \times 2}$ is the Jacobian of $(F(\bar{U}), F(\bar{V}))$, and is a piecewise constant matrix that is only non-zero if $0 < \bar{U}(t) < \epsilon$ or $0 < \bar{V}(t) < \epsilon$. In the former case $[DF]_{11} = \epsilon^{-1}$ with all other entries zero, and in the latter case $[DF]_{22} = \epsilon^{-1}$ with all other entries zero. We see that (6.19) has a block structure where the dynamics in each of N 2×2 blocks is given by

$$\frac{d}{dt}\xi = [A(p) + \Lambda(p)JD]\xi, \quad p = 0, \dots, N-1, \quad \xi \in \mathbb{C}^2, \tag{6.20}$$

with $A(p) = -\Lambda(p)J\Lambda^{-1}(p)$. Thus, comparing to (6.4), we see that the variational equation for the network is identical to that for a single Wilson-Cowan unit with W replaced by $\Lambda(p)$. We note that for $p = 0$ the variational problem is identical to that for an isolated node since $\Lambda(0) = W$ (using $\nu^{\alpha\beta}(0) = \sum_{\mu=0}^{N-1} \mathcal{W}_\mu^{\alpha\beta} = w^{\alpha\beta}$). Thus to determine the stability of the synchronous state we only have to consider a set of N two dimensional variational problems. Exploiting the fact that between switching manifolds the variational problem defined by (6.20) is time-independent we may construct a solution in a piecewise fashion from matrix exponentials and write $\xi(t) = \exp[(A(p) + \Lambda(p)JD)t]\xi(0)$. We may then build up a perturbed trajectory over one period of oscillation in the form $\xi(\Delta) = \Gamma(p)\xi(0)$, where

$\Gamma(p) \in \mathbb{R}^{2 \times 2}$ is given by

$$\Gamma(p) = e^{A(p)\Delta_8} e^{A_+(p;\epsilon)\Delta_7} e^{A(p)\Delta_6} e^{A_-(p;\epsilon)\Delta_5} e^{A(p)\Delta_4} e^{A_+(p;\epsilon)\Delta_3} e^{A(p)\Delta_2} e^{A_-(p;\epsilon)\Delta_1}, \quad (6.21)$$

where

$$A_+(p; \epsilon) = \left(A(p) + \epsilon^{-1} \Lambda(p) J \begin{bmatrix} 1 & 0 \\ 0 & 0 \end{bmatrix} \right), \quad (6.22)$$

and

$$A_-(p; \epsilon) = \left(A(p) + \epsilon^{-1} \Lambda(p) J \begin{bmatrix} 0 & 0 \\ 0 & 1 \end{bmatrix} \right). \quad (6.23)$$

Thus if a periodic orbit of an isolated Wilson-Cowan node is stable then the synchronous network solution will be stable provided all the eigenvalues of $\Gamma(p)$, for $p = 0, \dots, N-1$, lie in the unit disc (excluding the one that arises from time-translation invariance, with a value +1). For a fixed value of p one of three bifurcations is possible, namely a tangent instability defined by $\det(\Gamma(p) - I_2) = 0$, a period-doubling instability defined by $\det(\Gamma(p) + I_2) = 0$, and a Neimark-Sacker bifurcation defined by $\det \Gamma(p) = 1$. If there is a $p = p_c$ such that one of these instabilities occurs then the excited network state will correspond to the eigenvector $\text{Re } e_{p_c}$.

6.4.1 Example: a ring network

By way of illustration of the above theory let us consider a network of Wilson-Cowan nodes arranged on a ring with an odd number of nodes. Introducing a distance between nodes indexed by i and j as $\text{dist}(i, j) = \min(|i-j|, N-|i-j|)$, we can define a set of exponentially decaying connectivity matrices according to

$$\mathcal{W}_{ij}^{\alpha\beta} = w^{\alpha\beta} \frac{e^{-\text{dist}(i,j)/\sigma_{\alpha\beta}}}{\sum_{j=0}^{N-1} e^{-\text{dist}(0,j)/\sigma_{\alpha\beta}}}. \quad (6.24)$$

Thus we have a set of four circulant matrices parametrised by the four spatial scales $\sigma_{\alpha\beta}$ that respect the row-sum constraints $\sum_{j=1}^N \mathcal{W}_{ij}^{\alpha\beta} = w^{\alpha\beta}$. In Fig. 6.7

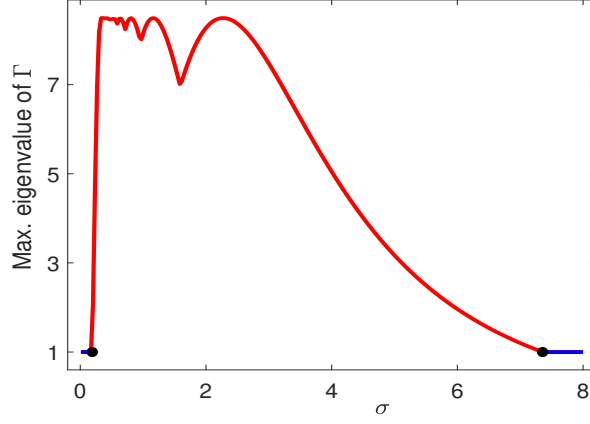


Figure 6.7: A plot of the absolute value of the maximum eigenvalue of $\Gamma(p)$ for $p = 0, \dots, N - 1$ for a Wilson-Cowan ring network, with spatial scales $\sigma_{\alpha\beta} = \sigma$ for all α, β , and $N = 31$. Here $\sigma \in [0.01, 8]$ and other parameters as in Fig. 6.3. Blue (red) piece corresponds to (un)stable synchronous solution for the varying σ . First (second) black dot for $\sigma \simeq 0.190724$ ($\sigma \simeq 7.356$) indicates a change from stable (unstable) to unstable (stable).

we show a plot of the absolute value of the maximum eigenvalue of $\Gamma(p)$ for $p = 0, \dots, N - 1$ with $\sigma_{\alpha\beta} = \sigma$ for all α, β varied over a finite interval to detect bifurcation points of network instabilities. We observed that for small coupling strength (σ) values the synchronous state is stable until $\sigma \simeq 0.190724$, and unstable if $\sigma \in (0.190724, 7.356)$, then restabilise for $\sigma \geq 7.356$.

In Fig. 6.8 we show a plot of the eigenvalues of $\Gamma(p)$ for $p = 0, \dots, N - 1$ for two different parameter choices. In one case all of the eigenvalues (excluding the one arising from time-translation invariance) lie within the unit disc, whilst in the other one leaves the unit disc along the negative real axis. This latter scenario predicts an instability of the synchronous state, and is consistent with direct numerical simulations. Moreover, by studying the spectrum under parameter variation we can find the value of $p = p_c$ which goes unstable first. In Fig. 6.9 we show time courses (obtained by direct numerical simulation) for the components $u_i(t)$ of the emergent network state just beyond the point of instability, as well as a plot of the real part of the spatial eigenvector e_{p_c} . We see that the spatial pattern of the network state is well predicted by e_{p_c} , suggesting that the bifurcation is supercritical.

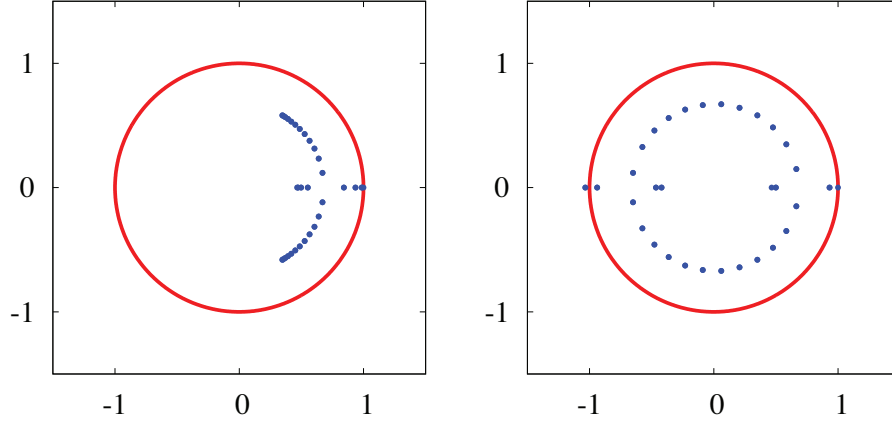


Figure 6.8: Spectral plots in the complex plane for a Wilson-Cowan ring network, with spatial scales $\sigma_{\alpha\beta} = \sigma$ for all α, β , and $N = 31$. Other parameters as in Fig. 6.3. Left: $\sigma = 0.15$, and the synchronous solution is predicted to be linearly stable. Right: $\sigma = 0.191$, and the synchronous solution is predicted to be linearly unstable.

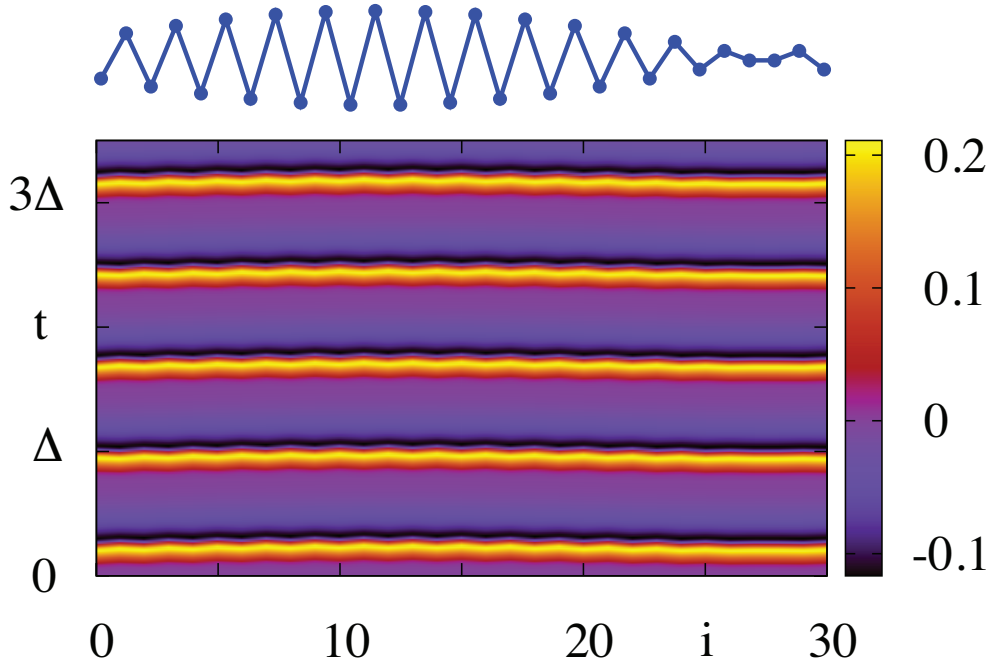


Figure 6.9: Direct numerical simulation of a Wilson-Cowan ring network, with $N = 31$, just beyond the point of synchronous instability where $\sigma = 0.191$. Other parameters as in Fig. 6.3. Here we plot the components $u_i(t)$ in a space-time plot. The shape of the unstable mode e_{p_c} , with $p_c = 16$ (and also $p_c = 17$ because of a degeneracy) is depicted in blue at the top of the figure. The bifurcation point of the linear instability is found to be in excellent agreement with simulations, with the spatial pattern of the emergent network state predicted by e_{p_c} .

6.5 The Heaviside world

In a recent paper Harris and Ermentrout [134] considered a single Wilson-Cowan population with a Heaviside nonlinearity, where the firing rate in (6.1) takes the form $F(x) = \Theta(x)$, where $\Theta(x) = 0$ for $x < 0$ and $\Theta(x) = 1$ for $x > 0$. The choice of a Heaviside firing rate has been very popular in mathematical neuroscience ever since the seminal work of Amari (for neural field models), as nicely exemplified by his recent article on the “Heaviside World” [6]. A case in point is the work of Laing and Chow [176] for understanding binocular rivalry. They considered a neural mass network model with recurrent excitation, cross-inhibition, adaptation, and synaptic depression and showed that the use of a Heaviside nonlinearity allowed the explicit calculation of the dominance durations of perceptions. A more recent use of the Heaviside firing rate has been by McCleney and Kilpatrick [199] for neural activity models with spike rate adaptation to understand the dynamics of up-down states. Using techniques from Filippov systems and differential inclusions Harris and Ermentrout made a study of periodic orbits for a Heaviside firing rate using a boundary value problem approach. Here we show that we can recover their results using the matrix exponential approach of Section 6.3. Moreover, we also extend their work on a single node by showing how to determine the stability of periodic orbits using a nonsmooth version of Floquet theory.

In the representation (6.4), with $F = \Theta$, we see that there are two switching manifolds defined by $U = 0$ and $V = 0$. If we introduce the indicator functions $h_1(U, V) = U$ and $h_2(U, V) = V$ then we can define these manifolds (lines in this case) as

$$\Sigma_i = \{(U, V) \in \mathbb{R}^2 \mid h_i(U, V) = 0\}. \quad (6.25)$$

These switching manifolds naturally divide the plane into *four* sets. We denote these by $D_{++} = \{(U, V) \mid U \geq 0, V \geq 0\}$, $D_{+-} = \{(U, V) \mid U \geq 0, V \leq 0\}$,

$D_{--} = \{(U, V) \mid U \leq 0, V \leq 0\}$, and $D_{-+} = \{(U, V) \mid U \leq 0, V \geq 0\}$. If we denote the elements of A by A_{ij} , $i = 1, 2$ and $j = 1, 2$, where

$$A = -\frac{1}{|W|} \begin{bmatrix} w^{vu}w^{uv}/\tau - w^{uu}w^{vv} & w^{uu}w^{vu}(1 - 1/\tau) \\ w^{vv}w^{uv}(1/\tau - 1) & w^{uv}w^{vu} - w^{uu}w^{vv}/\tau \end{bmatrix} \quad (6.26)$$

where $|W| = w^{vu}w^{uv} - w^{uu}w^{vv}$ and then the U -nullclines are given by

$$V = I_v - \frac{A_{11}(U - I_u)}{A_{12}} + \frac{1}{A_{12}} \begin{cases} -w^{uu} + w^{vu}/\tau & (U, V) \in D_{++} \\ -w^{uu} & (U, V) \in D_{+-} \\ 0 & (U, V) \in D_{--} \\ w^{vu}/\tau & (U, V) \in D_{-+} \end{cases}, \quad (6.27)$$

and the V -nullclines are given by

$$V = I_v - \frac{A_{21}(U - I_u)}{A_{22}} + \frac{1}{A_{22}} \begin{cases} -w^{uv} + w^{vv}/\tau & (U, V) \in D_{++} \\ -w^{uv} & (U, V) \in D_{+-} \\ 0 & (U, V) \in D_{--} \\ w^{vv}/\tau & (U, V) \in D_{-+} \end{cases}. \quad (6.28)$$

An example set of nullclines is shown in Fig. 6.10.

To discuss fixed points and their stability it is first necessary to complete the description of the dynamics on the switching manifolds. We do this using the Filippov convex method (see Section 3.2) and extend our discontinuous system into a convex differential inclusion. The Filippov extension of (6.4) is

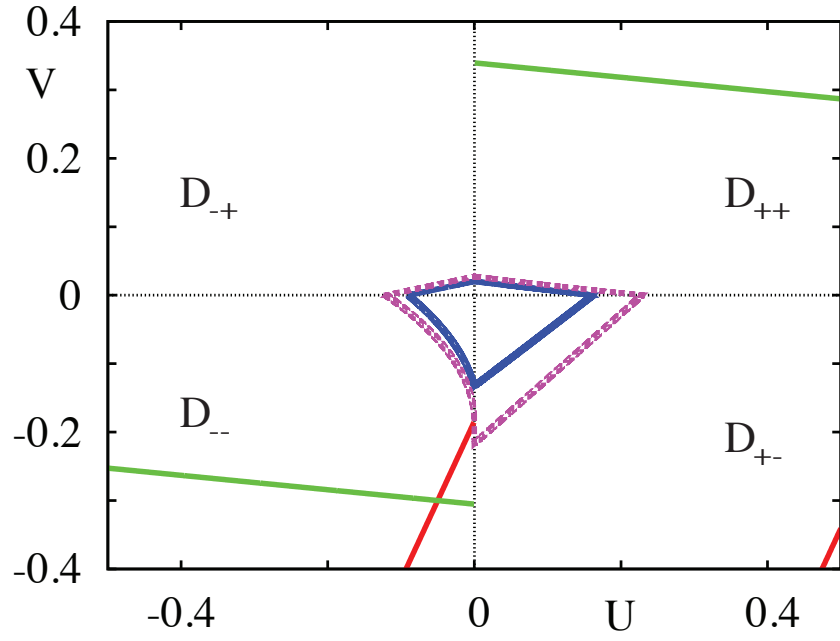


Figure 6.10: Phase plane for a Wilson-Cowan node with a Heaviside firing rate (transformed coordinates), showing the U -nullclines (red) and V -nullclines (green), as well as a stable periodic orbit (blue), and an unstable periodic sliding orbit (dashed magenta). Parameters (excluding ϵ) as in Fig. 6.3.

then

$$\frac{d}{dt} \begin{bmatrix} U \\ V \end{bmatrix} \in F(U, V) = \begin{cases} F_{++}(U, V) & (U, V) \in D_{++} \\ \overline{\text{co}}(\{F_{++}, F_{+-}\}, \kappa_1) & (U, V) \in D_{++} \cap D_{+-} \\ F_{+-}(U, V) & (U, V) \in D_{+-} \\ \overline{\text{co}}(\{F_{+-}, F_{--}\}, \kappa_2) & (U, V) \in D_{+-} \cap D_{--} \\ F_{--}(U, V) & (U, V) \in D_{--} \\ \overline{\text{co}}(\{F_{--}, F_{-+}\}, \kappa_3) & (U, V) \in D_{--} \cap D_{-+} \\ F_{-+}(U, V) & (U, V) \in D_{-+} \\ \overline{\text{co}}(\{F_{-+}, F_{++}\}, \kappa_4) & (U, V) \in D_{-+} \cap D_{++} \end{cases}, \quad (6.29)$$

where $F_{\alpha\beta}(U, V) = A[U - I_u, V - I_v]^T + b_{\alpha\beta}$ for $\alpha, \beta \in \{+, -\}$ and

$$b_{++} = \begin{bmatrix} w^{uu} - w^{vu}/\tau \\ w^{uv} - w^{vv}/\tau \end{bmatrix}, \quad b_{+-} = \begin{bmatrix} w^{uu} \\ w^{uv} \end{bmatrix}, \quad (6.30)$$

and

$$b_{--} = \begin{bmatrix} 0 \\ 0 \end{bmatrix}, \quad b_{-+} = \begin{bmatrix} -w^{vu}/\tau \\ -w^{vv}/\tau \end{bmatrix}. \quad (6.31)$$

Remembering $\overline{\text{co}}(\{f, g\}, \kappa) = \kappa f + (1 - \kappa)g$ with $\kappa \in [0, 1]$ is the closed convex hull of all values between f and g . A sliding solution may exist along a switching manifold such that $\dot{h}_i = \nabla h_i \cdot F = 0$. The functions κ_j , $j = 1, \dots, 4$, are chosen to ensure that $\dot{h}_i = 0$ along any switching manifold. See Section 3.2 and reference therein to find more detailed discussion about sliding phenomena. For example if a sliding solution exists along the line $U = 0$ for $V < 0$ then we would construct κ_2 using $\nabla h_1 = (1, 0)$ and $F(0, V) = \kappa_2 F_{+-}(0, V) + (1 - \kappa_2)F_{--}(0, V)$ yielding

$$\kappa_2 = \frac{(1, 0) \cdot F_{--}(0, V)}{(1, 0) \cdot (F_{--}(0, V) - F_{+-}(0, V))}. \quad (6.32)$$

As illustrated in Fig. 6.10 it is possible for two nullclines to intersect and create a fixed point (U_{ss}, V_{ss}) . In the example shown this occurs for $U < 0$ and $V < 0$, so that $(U_{ss}, V_{ss}) = (I_u, I_v)$. Linear stability analysis shows that this is a stable node (with eigenvalues of A , namely -1 and $-1/\tau$). Moreover, this system also supports *pseudo* equilibria where either a nullcline touches a switching manifold, or two switching manifolds intersect. A thorough exploration of the pseudo equilibria of (6.1) can be found in [134]. Here we shall simply focus on the pseudo equilibrium at $(U_{ss}, V_{ss}) = (0, 0)$, and characterise its stability by considering trajectories around this point. In fact given the PWL nature of the dynamics it is sensible to consider the construction of periodic orbits, and determine the stability of the pseudo equilibrium in terms of the stability of encircling small amplitude orbits.

6.5.1 Periodic orbits and their stability

A non-sliding periodic orbit around $(0, 0)$ can be constructed in terms of the times-of-flight in each region $D_{\alpha\beta}$. If we denote these four times by the symbols

$\Delta_{\alpha\beta}$ then the period of the orbit is given by $\Delta = \Delta_{++} + \Delta_{-+} + \Delta_{--} + \Delta_{+-}$.

We may then use a matrix exponential solution:

$$\begin{bmatrix} U(t) \\ V(t) \end{bmatrix} = e^{At} \begin{bmatrix} U(0) \\ V(0) \end{bmatrix} + (I_2 - e^{At}) \left[\begin{bmatrix} I_u \\ I_v \end{bmatrix} - A^{-1} W J \begin{bmatrix} H(U) \\ H(V) \end{bmatrix} \right], \quad t \geq 0. \quad (6.33)$$

to patch together solutions, setting the origin of time in each region such that *initial* data in one region comes from *final* data from a trajectory in a neighbouring region. We shall denote the periodic orbit by (\bar{U}, \bar{V}) such that $(\bar{U}(t), \bar{V}(t)) = (\bar{U}(t + \Delta), \bar{V}(t + \Delta))$. To indicate which region we are considering we shall simply add $\alpha\beta$ subscripts to the formula in (6.33). In this way a periodic orbit that visits all four regions in turn can be parameterised by the five unknowns $\bar{U}_{++}(0)$, $\bar{V}_{++}(\Delta_{++})$, $\bar{U}_{-+}(\Delta_{-+})$, $\bar{V}_{--}(\Delta_{--})$, $\bar{U}_{+-}(\Delta_{+-})$, and $\Delta_{\alpha\beta}$. These are determined self-consistently by the five equations $\bar{U}_{++}(\Delta_{++}) = 0$, $\bar{V}_{-+}(\Delta_{-+}) = 0$, $\bar{U}_{--}(\Delta_{--}) = 0$, $\bar{V}_{+-}(\Delta_{+-}) = 0$, and $\bar{U}_{+-}(\Delta_{+-}) = \bar{U}_{++}(0)$. To determine the stability of such an orbit we may use the results from Section 4.2. In essence, different from the PWL case, we need to treat the propagation of perturbations through a switching manifold using a saltation matrix, such that $Y(T^+) = \lim_{\epsilon \searrow 0} Y(T + \epsilon) = SY(T)$, where $Y = (U, V)$ denotes the vector state of the system and S is the saltation matrix that acts at time T . Saltation matrices can be derived in a number of ways (see Sections 4.2, 5.3), and in the context of the PWL model discussed in Section 6.3, we can obtain the relevant matrices by considering the approximation $\Theta(x) = \lim_{\epsilon \rightarrow 0} F(x)$. To see this we introduce the vector $\bar{Y}(t) = (\bar{U}(t), \bar{V}(t))$ and linearise the equations of motion (6.4) by considering $Y(t) = \bar{Y}(t) + \delta Y(t)$, for small perturbations $\delta Y(t) = (\delta U, \delta V)$. The linearised equations of motion are given by

$$\frac{d}{dt} \delta Y = [A + W J D F(\bar{Y}(t))] \delta Y. \quad (6.34)$$

Here $DF(\bar{Y}(t))$ is the piecewise constant matrix described after (6.19). Consider for example the time-of-flight, $t_1(\epsilon)$, between $U = \epsilon$ and $U = 0$. For small

ϵ we may estimate $t_1(\epsilon)$ using the result that $U(t) \simeq U(t_0) + \dot{U}\Big|_{t=t_0}(t - t_0)$, giving $t_1(\epsilon) = -\epsilon / \dot{U}\Big|_{t=\Delta_{++}}$. The corresponding change in state across this small time interval can be obtained by integrating (6.34) to give

$$\delta Y(T^+) - \delta Y(T) = \lim_{\epsilon \rightarrow 0} \int_T^{T+t_1(\epsilon)} WJ \begin{bmatrix} \epsilon^{-1} & 0 \\ 0 & 0 \end{bmatrix} \delta Y(t) dt. \quad (6.35)$$

Thus we obtain $\delta Y(T^+) = S_1 \delta Y^-$, with the saltation matrix S_1 given by

$$S_1 = I_2 - \frac{1}{\dot{U}(\Delta_{++})} WJ \begin{bmatrix} 1 & 0 \\ 0 & 0 \end{bmatrix}. \quad (6.36)$$

The other saltation matrices (describing the passage through ϵ -neighbourhoods of $U = 0$ and $V = 0$) are constructed in a similar fashion, and found to be

$$\begin{aligned} S_2 &= I_2 - \frac{1}{\dot{V}(\Delta_{-+})} WJ \begin{bmatrix} 0 & 0 \\ 0 & 1 \end{bmatrix}, \\ S_3 &= I_2 + \frac{1}{\dot{U}(\Delta_{--})} WJ \begin{bmatrix} 1 & 0 \\ 0 & 0 \end{bmatrix}, \\ S_4 &= I_2 + \frac{1}{\dot{V}(\Delta_{+-})} WJ \begin{bmatrix} 0 & 0 \\ 0 & 1 \end{bmatrix}. \end{aligned} \quad (6.37)$$

It is straightforward to check that the saltation matrices (6.36)-(6.37) are equivalent to those defined by (4.6). We now pass to the limit $\epsilon = 0$, to treat the Heaviside firing rate. Between switching events the perturbations evolve according to $\exp(A(t - T))\delta Y(T^+)$, for $t > T$, where $\delta Y(T^+)$ is the perturbation at the switching time. Thus after one period of oscillation we may put this all together to obtain

$$\delta Y(\Delta) = \Gamma \delta Y(0), \quad \Gamma = S_4 e^{A\Delta_{+-}} S_3 e^{A\Delta_{--}} S_2 e^{A\Delta_{-+}} S_1 e^{A\Delta_{++}}. \quad (6.38)$$

The periodic orbit will be stable if the eigenvalues of Γ lie within the unit disc. Remember that one of the Floquet multipliers is equal to one, corresponding to perturbations along the periodic orbit. Let us denote the other eigenvalue by $e^{\kappa\Delta}$ and use the results from Section 4.2 to get

$$\kappa = -\left(1 + \frac{1}{\tau}\right) + \frac{1}{\Delta} \log \frac{\dot{\bar{V}}(\Delta_{+-}^+) \dot{\bar{U}}(\Delta_{--}^+) \dot{\bar{V}}(\Delta_{-+}^+) \dot{\bar{U}}(\Delta_{++}^+)}{\dot{\bar{V}}(\Delta_{+-}) \dot{\bar{U}}(\Delta_{--}) \dot{\bar{V}}(\Delta_{-+}) \dot{\bar{U}}(\Delta_{++})}. \quad (6.39)$$

A periodic orbit will be stable provided $\kappa < 0$. We shall say that the pseudo-equilibria at $(0,0)$ is unstable (stable) if it is enclosed by a stable (unstable) periodic orbit of arbitrarily small amplitude. We shall say that there is a *pseudo-Hopf* bifurcation at $(0,0)$ when the pseudo-equilibrium changes stability, namely when $\kappa = 0$. A plot of $\kappa = \kappa(\tau)$ is shown in Fig. 6.11 for the parameters of Fig. 6.5. This shows a similar behaviour as for the steep PWL firing rate function though in this case the stable periodic orbits appear via a supercritical Hopf bifurcation for a larger value of τ . In essence we may regard the second term on the right hand side of (6.39) as a correction term to standard Floquet theory to cope with the nonsmooth nature of the Heaviside firing rate.

6.5.2 An unstable periodic sliding orbit

The Wilson-Cowan node can also support an unstable periodic orbit that has a component which slides along the switching manifold $U = 0$ for $V \in [V_1, V_2]$, as depicted in Fig. 6.10. The points $V_{1,2}$ are easily calculated by determining the points at which the U -nullclines touch the switching manifold where $U = 0$, and are found to be $V_1 = (A_{11}I_u + A_{12}I_v - w^{uu})/A_{12}$ and $V_2 = V_1 + w^{uu}/A_{12}$. In reverse time initial data close to a sliding trajectory would be attracted to it. Thus we can think of constructing an unstable periodic sliding orbit, of the type shown in Fig. 6.10, by breaking it into five pieces. All pieces of this orbit are constructed similarly to before (see above), except the component

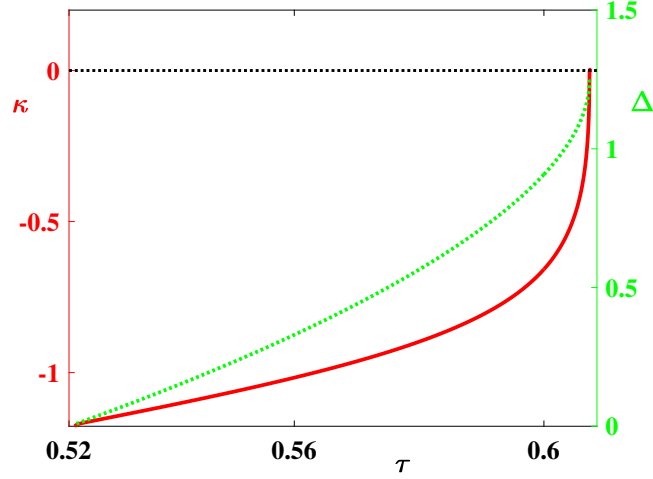


Figure 6.11: A plot of the non-trivial Floquet exponent for the Wilson-Cowan model with a Heaviside firing rate (left axis and colour in red), as a function of τ , with the period of the orbit also shown (right axis and colour in green). Parameters as in Fig. 6.10. Periodic orbits emerge via a supercritical Hopf bifurcation as τ increases through $\tau_{\text{Hopf}} \sim 0.5239$. We see that the stable periodic orbit grows as τ increases to zero and terminates at a saddle-node bifurcation of periodic orbits at $\tau \sim 0.6074$ where it intersects with the larger, shrinking unstable periodic orbit. Beyond the bifurcation the trajectory is attracted to the stable fixed point at $(U_{ss}, V_{ss}) = (I_u, I_v)$.

that slides. Using the Filippov method and equation (6.32) we find $\kappa_2 = (A_{11}I_u - A_{12}V + A_{12}I_v)/w^{uu}$, with the sliding dynamics prescribed by

$$\frac{d}{dt} \begin{bmatrix} U \\ V \end{bmatrix} = \begin{bmatrix} 0 & 0 \\ 0 & A_{22} - A_{11}w^{uv}/w^{uu} \end{bmatrix} \begin{bmatrix} U \\ V \end{bmatrix} + \begin{bmatrix} 0 \\ b_s \end{bmatrix}, \quad (6.40)$$

where $b_s = -A_{12}I_u - A_{22}I_v + (A_{11}I_u + A_{12}I_v)w^{uv}/w^{uu}$. In backward time the periodic sliding orbit shown in Fig. 6.10 would slide up along $U = 0$ until the point $V = V_2$, where it would leave the switching manifold.

We now turn our attention to networks built from Wilson-Cowan nodes with a Heaviside firing rate.

6.6 A network of Heaviside Wilson-Cowan nodes

As we have shown in Section 6.5 the replacement of a sigmoidal firing rate by

a Heaviside function can lead to highly tractable models for which substantial analytical results can be obtained (with the use of matrix exponentials and saltation matrices). However, at the network level the mathematical differences between the treatment of smooth and nonsmooth firing rates are considerably amplified relative to those at the single node level. At the node level it is well known that regarding the Heaviside function as the steep limit of a sigmoidal function can lead to arbitrarily many different non-equivalent dynamical systems. This is simply due to the non-uniqueness of the singular limits by which smooth functions may tend towards discontinuities. For a recent perspective on this issue see the work of Jeffrey [150]. Thus there is no reason to assume that taking the limit $\epsilon \rightarrow 0$ for the PWL network considered in Section 6.4 will be relevant to a Wilson-Cowan network with a Heaviside nonlinearity. Namely the approximation of a Heaviside function by a continuous function such that $\Theta(x) = \lim_{\epsilon \rightarrow 0} F(x)$, where $F(x)$ is given by (6.2), may have little utility given that pointwise convergence need not imply distributional convergence.

We now return to the network introduced in Section 6.4, but replace the dynamics of each node with the Heaviside limit studied in the previous section. For the following analysis, it is convenient to rewrite (6.12) as

$$\frac{d}{dt}Y = \mathcal{A}(Y - \mathcal{F}(Y)), \quad \mathcal{F}(Y) = C - \mathcal{A}^{-1}\mathcal{W}\mathcal{J}\Theta(Y). \quad (6.41)$$

The network model (6.12), with a Heaviside nonlinearity, is reminiscent of a so-called *Glass* network originally introduced for the study of biochemical networks that are dominated by switch-like behaviour [117, 118], though here the model has two-time scales. For a nice survey of periodic and aperiodic behaviour in Glass networks we recommend the article by Edwards [89], and for the application to gene networks see Edwards and Glass [90].

The synchronous network state is given by (6.33) (remembering the row-sum constraint on the network connections). To study its linear stability we consider values of the perturbed network state Y that are close to the syn-

chronous network state at the unperturbed crossing times. Let \bar{T}_i denote the time that the synchronous state moves between one of the four quadrants (as illustrated in Fig. 6.10). We then make the ansatz that the perturbed network state Y can be expressed with respect to the synchronous orbit at one of the switching times \bar{T}_i and write $Y(t) = \bar{Y}(\bar{T}_i) + \delta Y(t)$ with t in the neighbourhood of \bar{T}_i .

We first construct the saltation matrix through a switch, indexed by $i = 1, \dots, 4$. Suppose that the k th crossing occurs at a perturbed crossing time $T_{i,k}$. The network states at two consecutive crossings are related via

$$Y(T_{i,k+1}) = e^{A(T_{i,k+1}-T_{i,k})}Y(T_{i,k}) + (I_{2N} - e^{A(T_{i,k+1}-T_{i,k})}) \mathcal{F}(Y(T_{i,k}^+)). \quad (6.42)$$

This equation is obtained by integrating (6.41) using the observation that \mathcal{F} is constant between crossings. By linearising (6.42) we can relate the perturbations between crossing events as

$$\delta Y(T_{i,k+1}) = \delta Y(T_{i,k}) + Y^{i,k} \delta T_{i,k}, \quad (6.43)$$

where $Y^{i,k} = \mathcal{A}(\bar{Y}(\bar{T}_i) - \mathcal{F}(Y(T_{i,k}^+)))$ and $\delta T_{i,k} = T_{i,k+1} - T_{i,k}$. For the node that crosses at $T_{i,k+1}$, the corresponding component of $\delta Y(T_{i,k+1})$, say at position m , vanishes, since $Y_m(T_{i,k+1}) = \bar{Y}_m(\bar{T}_i)$ (namely the m th component of the perturbed trajectory equals the m th component of the synchronous orbit). Here, $m \in \{1, 3, \dots, 2N-1\}$ or $m \in \{2, 4, \dots, 2N\}$, depending on whether the crossing occurs along the V or U axis. We then see from (6.43) that

$$\delta T_{i,k} = -\frac{\delta Y_m(T_{i,k})}{Y_m^{i,k}}. \quad (6.44)$$

At this point, m is still unknown. However, since m corresponds to the node that crosses before any of the other remaining nodes do so, we find it by minimising (numerically) (6.44) over the possible values of m , and we denote it by m_k . When we combine (6.43) and (6.44), we find that

$\delta Y(T_{i,k+1}) = \Gamma_{i,k} \delta Y(T_{i,k})$ with

$$\Gamma_{i,k} = I_{2N} - \frac{Y^{i,k} e_{m_k}^\top}{Y_{m_k}^{i,k}}, \quad (6.45)$$

where e_m is the m th canonical basis vector in \mathbb{R}^{2N} . The saltation matrix for each of the four switches is then given by

$$L_i = \Gamma_{i,N-1} \Gamma_{i,N-2} \cdots \Gamma_{i,1}, \quad i = 1, \dots, 4. \quad (6.46)$$

The ordering of matrix multiplications in (6.46) is determined by the iterative minimisation of the perturbations given by (6.44).

In the next step, we analyse how a perturbed network state is propagated between saltation events. Let T_i^+ denote the time when the last node crosses between quadrants. Here, the superscript makes explicit that all nodes have crossed into the next quadrant. The next network event occurs when one of the nodes crosses into the subsequent quadrant. This happens at a time T_{i+1}^- , where the superscript indicates that only one node has crossed. We will make the ansatz that $T_i^+ = \bar{T}_i + \delta T_i^+$ and $T_{i+1}^- = \bar{T}_{i+1} + \delta T_{i+1}^-$. We see from (6.41) that

$$Y(T_{i+1}^-) = e^{A(T_{i+1}^- - T_i^+)} Y(T_i^+) + \left(I_{2N} - e^{A(T_{i+1}^- - T_i^+)} \right) \mathcal{F}(Y(T_i^+)), \quad (6.47)$$

from which we obtain after linearisation

$$\delta Y(T_{i+1}^-) = e^{A \Delta_i} \left(\delta Y(T_i^+) - \bar{Y}'(\bar{T}_i^+) \delta T_i^+ \right) + \bar{Y}'(\bar{T}_{i+1}^-) \delta T_{i+1}^-, \quad (6.48)$$

where we have used the fact that $\mathcal{F}(Y(T_i^+)) = \mathcal{F}(Y(T_{i+1}^-))$, since \mathcal{F} is constant between crossing events. Here $\bar{Y}'(t)$ denotes the differential of $\bar{Y}(t)$ with respect to t . As above, the component of $\delta Y(T_{i+1}^-)$ that corresponds to the node that switches first, say at position m , vanishes. Taking the m th component of

(6.48) then yields an expression for the perturbation of the crossing time

$$\delta T_{i+1}^- = -\frac{f_m^i}{\bar{Y}'_m(\bar{T}_{i+1}^-)}, \quad (6.49)$$

where the vector $f^i \in \mathbb{R}^{2N}$ is given by $e^{A\Delta_i} \left(\delta Y(T_i^+) - \bar{Y}'(\bar{T}_i^+) \delta T_i^+ \right)$. We again find the value of m by minimising (6.49) over all admissible values of m and refer to it as m_i . This leads to $\delta Y(T_{i+1}^-) = \Gamma_i \delta Y(T_i^+)$ with

$$\Gamma_i = \left(G_i - \frac{\bar{Y}'(\bar{T}_{i+1}^-)}{\bar{Y}'_{m_i}(\bar{T}_{i+1}^-)} e_{m_i}^T G_i \right), \quad (6.50)$$

and

$$G_i = e^{A\Delta_i} \left(I_{2N} - \frac{\bar{Y}'(\bar{T}_i^+) e_1^T \delta T_i^+}{\delta Y_1(T_i^+)} \right). \quad (6.51)$$

Taken together, we obtain after one period

$$\delta Y(T_4^+) = \Psi \delta Y(0), \quad \Psi = L_4 \Gamma_4 L_3 \Gamma_3 L_2 \Gamma_2 L_1 \Gamma_1. \quad (6.52)$$

The matrices Γ_i act to propagate perturbations across a quadrant, and the L_i propagate perturbations through a switch. At first sight, the definition of G_i suggests that we have introduced a dependence of Γ_i on $\delta Y(0)$ through the inclusion of $\delta Y(T_i^+)$. This dependence can be avoided by noting that $\delta T_i^+ = \delta T_i^- + \sum_k \delta T_{i,k}$ and the repeated use of (6.44), (6.45) and (6.49). The drawback of this approach is that the resultant operator does not lend itself to an interpretation of successive propagations and saltations, nor is it numerically advantageous. Moreover, this operator would only remove the *explicit* dependence of Ψ on $\delta Y(0)$. The minimisation steps that are necessary to determine the order in which nodes switch already leads to an *implicit* dependence of Ψ on $\delta Y(0)$. Changing $\delta Y(0)$ can lead to a different order of switching, and since matrix multiplication does not commute, Ψ can be different for different $\delta Y(0)$. This has profound implications for asserting linear stability. The usual argument that the eigenvalues of Ψ determine linear stability does not hold

anymore. To see this, consider the propagation of $\delta Y(0)$ over multiple periods, i.e.

$$\delta Y^{(1)} = \Psi^{(0)} \delta Y(0), \quad \delta Y^{(2)} = \Psi^{(1)} \delta Y^{(1)}, \quad \delta Y^{(3)} = \Psi^{(2)} \delta Y^{(2)}, \quad \dots \quad (6.53)$$

so that

$$\delta Y^{(m)} = \Psi^{(m-1)} \Psi^{(m-2)} \dots \Psi^{(0)} \delta Y(0). \quad (6.54)$$

The eigenvalues of $\Psi^{(i)}$ and $\Psi^{(j)}$ can be different for $i \neq j$. For some value of i $\Psi^{(i)}$ may have all eigenvalues in the unit disc, whilst for another value of i there may be some eigenvalues outside the unit disc. Over one period, perturbations can therefore grow or shrink. This entails that for a product of operators as in (6.54), $\delta Y^{(m)}$ may be smaller than $\delta Y^{(0)}$, although some $\Psi^{(i)}$ might have some eigenvalues that lie outside the unit disc. Instead of looking at the eigenvalues of individual $\Psi^{(i)}$, we could have studied the eigenvalues of the product of operators in (6.54). We would have come to the same conclusion since eigenvalues of the product operator move into and out of the unit disc as we increase m .

Figures 6.12 and 6.13 illustrate the dependence of the spectra on random initial conditions $\delta Y(0)$. In both figures, the left panel shows the spectra for initial conditions when all eigenvalues of $\Psi^{(0)}$ lie within the unit disc. The middle panel displays spectra with some eigenvalues outside the unit disc, and the right panel is a blowup of the middle panel around the unit disc. For Fig. 6.12, we chose a value of σ such that the synchronous orbit of the PWL network, with a small values of $\epsilon = 0.001$, is linearly stable. We observe that the eigenvalues of the Heaviside network cluster around those of the PWL network. While it appears that the majority of synchronous solutions are stable (for this parameter choice), some initial conditions lead to eigenvalues outside the unit disc. When zooming into the unit disc, we see some degree of clustering, although this is not as pronounced as for the stable solutions.

For larger values of σ , the synchronous state of the PWL network becomes

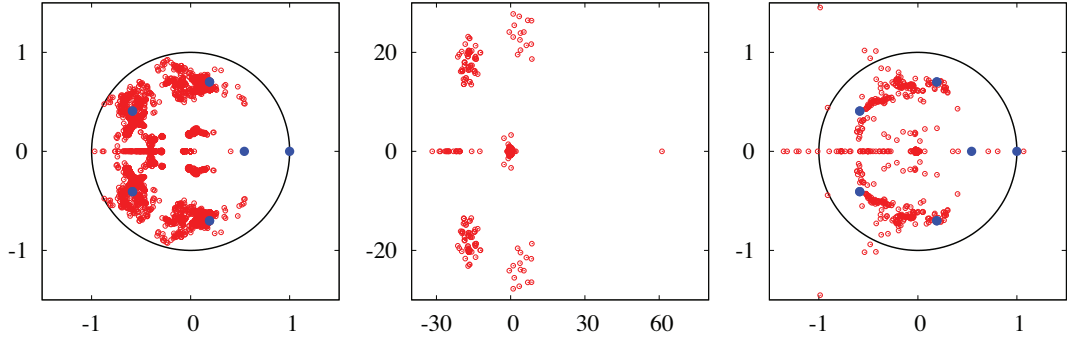


Figure 6.12: Spectral plots for a Heaviside Wilson-Cowan ring network with spatial scales $\sigma_{\alpha\beta} = 0.215$ for all α, β , and $N = 5$. We sampled 2000 random initial conditions, and eigenvalues are shown as open red circles. The filled blue circles are the eigenvalues of the PWL network with the same parameter values and $\epsilon = 0.001$. (Left) Spectra for initial conditions that lead to eigenvalues that all fall into the unit disc. (Middle) Spectra for initial conditions that lead to eigenvalues outside the unit disc. (Right) Blow-up of the the middle panel around the unit disc. Other parameters as in Fig. 6.3.

unstable (for small ϵ). The left panel of Fig. 6.13 shows that the eigenvalues of the Heaviside network that all fall into the unit disc exhibit only a weak association with the eigenvalues of the PWL network. In addition, it seems that more initial conditions lead to unstable synchronous solutions than stable ones. This mirrors the behaviour in Fig. 6.12, where the majority of initial conditions gives rise to stable solutions. The blow-up in the right panel of Fig. 6.13 illustrates that the eigenvalues of the Heaviside network form clusters around those of the PWL network. While the notion of linear stability in terms of eigenvalues of the propagator is lost for the Heaviside network, it appears that the clustering of these eigenvalues reflects the stability of the PWL system, at least for small values of ϵ (where the PWL firing rate becomes more switch like).

6.7 Discussion

In this chapter we have shown that the combination of two popular approaches in dynamical systems, namely PWL modelling of low dimensional oscillators and the MSF, can be combined to give insight into the behaviour of network states in neural mass network models. This is natural for this type of system

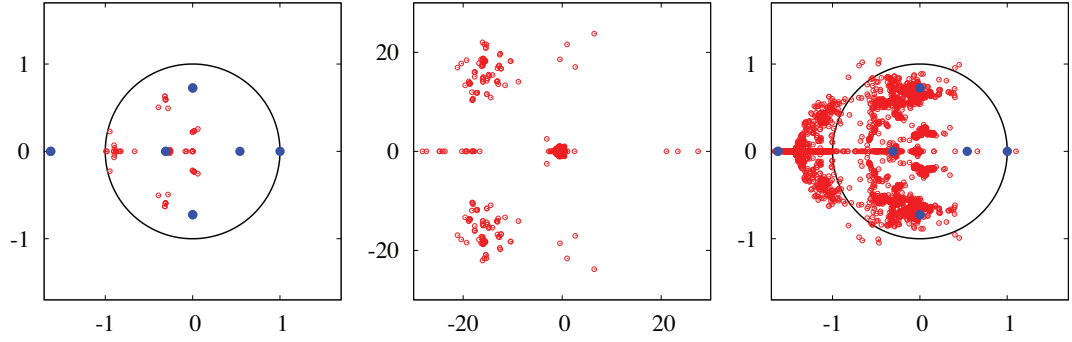


Figure 6.13: Spectral plots for a Heaviside Wilson-Cowan ring network with spatial scales $\sigma_{\alpha\beta} = 0.23$ for all α, β , and $N = 5$. We sampled 2000 random initial conditions, and eigenvalues are shown as open red circles. The filled blue circles are the eigenvalues of the PWL network with the same parameter values with $\epsilon = 0.001$. (Left) Spectra for initial conditions that lead to eigenvalues that all fall into the unit disc. (Middle) Spectra for initial conditions that lead to eigenvalues outside the unit disc. (Right) Blow-up of the the middle panel around the unit disc. Other parameters as in Fig. 6.3.

since the sigmoidal nonlinearity, ubiquitous throughout neuroscience modelling of large scale brain dynamics, is well caricatured by a PWL reduction. We have focused here on the bifurcation of the synchronous network state, and shown how this can be determined in terms of a set of low-dimensional Floquet problems, each of which can be solved using simple linear algebra. In essence the PWL aspect of the model allows the variational problem for stability to be solved without recourse to the numerical solution of an ordinary differential equation. Closed form solutions are *patched* together, and although this may appear inelegant at first sight, it does lead to explicit formulas for Floquet exponents at the single node level, and is easily cast into algorithmic form for accurate numerical computations at the network level. This nicely highlights the benefits of PWL modelling. Importantly the approach advocated here is not just limited to the construction and stability of the synchronous state. Pecora *et al.* [232] and Sorrentino *et al.* [291] have recently extended the MSF approach to treat more exotic states making extensive use of tools from computational group theory. Thus the work presented here is readily extended to treat non-synchronous states, such as clusters, and for a further discussion see [217]. From a neuroscience perspective it would also be important to treat

delays, arising from the finite propagation speed of action potentials relaying signals between distinct brain regions [70]. In this case we would hope to exploit the growing body of knowledge on PWL dynamics with time delay, as exemplified by [271].

From a mathematical perspective we have also seen that there is an important difference between the analysis of a high gain continuous PWL sigmoid and that of a discontinuous switch-like Heaviside firing rate. Although this can be facilitated with the use of saltation matrices (to propagate perturbations through switching manifolds) there is no MSF style approach that reduces the study of synchrony to a set of sub-network Floquet problems. Moreover, in contrast to the linear stability analysis of continuous systems, there is now a new challenge of addressing the temporal order in which perturbations to network states pass through a switching manifold. To treat this we have made use of ideas originally developed for Glass networks [89], though note that similar issues of *ordering* also arise in the analysis of pulse-coupled systems [122, 160, 304]. In essence the analysis of a Wilson-Cowan network with a Heaviside firing rate must be performed carefully, and with non-standard tools, as its behaviour can differ from that of a similar network with a high gain PWL sigmoid.

Chapter 7

The two process model for sleep-wake regulation

7.1 Introduction

Sleep is necessary for human beings to maintain a healthy mind and functioning body. During sleep, many systems in the body enter an anabolic state, and this allows recovery of the nervous, muscular, and immune systems [24, 248]. A *good* sleep also helps restoration of the brain, wound healing, reducing pain perception, restoring energy, and improving concentration [132, 294]. Sleep disorders such as insomnia, sleep apnoea, hypersomnia, sleepwalking, and bruxism result in poor sleep quality or mistimed sleep [17]. Sleep is related with many health problems [190], including psychotic disorders and depression [301], diabetes [273], obesity [45], and cardiovascular disease [290]. The significant association between sleep and health issues necessitates a good understanding of the sleep-wake regulation process, and many properties of sleep are still not fully understood.

Mathematical models have been utilised as a powerful instrument to explore biological mechanisms of sleep-wake regulation and circadian rhythms for many years. Most classical models have at least a pair of oscillators and often focus on the circadian rhythm forced by the suprachiasmatic nucleus (SCN),

the need to sleep after being awake for a period of time, cyclic transitions between rapid eye movement (REM) and nonrapid eye movement (NREM) sleep types (per oscillation is nearly 90 minutes), and a sleep inertia rule, see for example [17, 102, 166, 197, 198, 295]. The two process model [32, 62] is a simple nonsmooth dynamical system, that can nonetheless capture many essentials of the sleep-wake cycle. Recent developments have allowed a better understanding of the neuronal systems that regulate sleep-wake mechanisms [267] and more advanced neuronal models have been introduced [167, 300], including the Phillips-Robinson (PR) model [236]. The PR model is based on the interaction between wake boosting neurons and sleep boosting neurons that are modulated by circadian and homeostatic processes, is physiologically motivated [238]. It is also capable of describing the effects of caffeine, shift work, and sleep deprivation on the sleep-wake cycle [246].

By using multiple timescale analysis Skeldon *et. al* [286] have shown that the PR model can be reduced to the two process model. The link between the PR model and the two process model allows one to describe some properties of the two process model more physiologically [30]. Moreover, there is an association between the two process model and other more general neuronal models, and that link has been investigated in [287]. Hence, exploring the dynamics of the two process model helps to better understand sleep-wake regulation and provides a clearer framework to explain some features of more complex neuronal models.

To explain the sleep-wake cycle, the two process model introduces two interacting oscillatory activities: a circadian process (sleep independent) and a homeostatic process (sleep dependent). A circadian process is a rhythm that repeats approximately every 24 hours. A homeostatic sleep process is a biochemical adjustment within the body to keep physiological sleep requirements within sensible bounds. The homeostatic process represents sleep pressure that increases monotonically during wakefulness and decreases monotonically during sleep. The lower and upper boundaries of sleep pressure are regulated by

the circadian oscillation. Transition from sleep states to wake states happen at the lower boundary and switching from wake states to sleep states occur at the upper boundary. Examples of these are shown in Fig 7.2 for different sleep-wake patterns.

Although the two process model is a relatively simple model it exhibits many different sleep-wake patterns [62]. Nakao *et. al* [214, 215] have framed this model as a one-dimensional map with *gaps* and linked this to a circle map (utilising immanent periodicity of the circadian activity). Bailey *et. al* [18] performed a detailed bifurcation analysis for the model [16, 74, 154]. They also discussed the biological relevance of model parameters and how different solutions can be associated with sleep-wake patterns of babies and adults. Here we review and extend results from [18] by considering analytical ODE modelling with switches and nonsmooth Floquet theory. Moreover, we show that the original map-based analysis of the two process model is recovered using an approach that treats nonsmooth flows. The main reason to reproduce and extend results of [18] is as a basis for the future network studies (say involving two interacting sleepers- common in co-habitation).

The organisation of the chapter is as follows. In Section 7.2 we introduce the two process model by presenting it as an ODE system with switches (namely a nonsmooth flow). We then define periodic orbits and present relevant one dimensional maps. In Section 7.3, we give a construction of periodic orbits. We then show how to determine the stability of periodic solutions with an adaptation of Floquet theory, and also perform a linear stability analysis of the maps of switching event times around such orbits. Utilising techniques for nonsmooth systems, we derive a formula to compute Lyapunov exponents, shedding light on where different solution patterns exist in parameter space. We also show that the model may support super-stable periodic solutions. In Section 7.4 we perform a bifurcation analysis and build Arnol'd tongue boundaries by examining both saddle-node bifurcations of periodic orbits and grazing bifurcations. In Section 7.5, we review how social factors influence human sleep

dynamics including partners sharing the same bed, and discuss a phenomenological network version of the two process model. Finally, In Section 7.6, we give a discussion of the work presented in the chapter.

7.2 Model description and periodicity

The two process model is a fascinating and ostensibly simple prototype of PWL modelling whose rich and complicated dynamical behaviours exemplify many interesting phenomenon, see for example [74]. This model characterise the timing and structure of sleep as the interaction of circadian and homeostatic process evolution. To describe the combination of these two oscillatory processes as continuous flows we consider the following model formulation:

$$\dot{x}(t) = \begin{cases} \frac{-x(t)}{\tau_w} + \frac{1}{\tau_w}, & \text{if } \dot{x}(t) > 0 \text{ and } x(t) \leq H^+(t), \\ \frac{-x(t)}{\tau_s}, & \text{if } \dot{x}(t) < 0 \text{ and } x(t) \geq H^-(t), \end{cases} \quad (7.1)$$

$$(7.2)$$

with the circadian processes

$$H^+(t) = H_0^+ + a \sin(2\pi t), \quad (7.3)$$

$$H^-(t) = H_0^- + a \sin(2\pi t). \quad (7.4)$$

Here $x(t)$ represents the homeostatic sleep pressure and oscillates between the upper ($H^+(t)$) and lower ($H^-(t)$) threshold. We define $x_w(t, t_0^w)$ as the homeostatic sleep pressure during wake, which starts at $t = t_0^w$ with the initial value $x_w(t_0^w)$, and $x_s(t, t_0^s)$ as the homeostatic sleep pressure during sleep, which starts at $t = t_0^s$ with the initial value $x_s(t_0^s)$. Then the explicit solution for $x_w(t, t_0^w)$ can be calculated as follows

$$\begin{aligned} x_w(t, t_0^w) &= x_w(t_0^w) e^{-(t-t_0^w)/\tau_w} + \frac{1}{\tau_w} \int_{t_0^w}^t e^{-(t-s)/\tau_w} ds \\ &= 1 - [1 - x_w(t_0^w)] e^{-\frac{t-t_0^w}{\tau_w}}. \end{aligned} \quad (7.5)$$

Similarly, we can obtain the solution for $x_s(t, t_0^s)$ as

$$x_s(t, t_0^s) = x_s(t_0^s) e^{-\frac{(t-t_0^s)}{\tau_s}}. \quad (7.6)$$

If initially the homeostatic sleep pressure starts on either threshold, these initial values satisfy $H^-(t_0^w) = x_w(t_0^w)$ and $H^+(t_0^s) = x_s(t_0^s)$ on the lower and upper threshold, respectively. We denote switching event times on the lower threshold by T_{2i} and that of on the upper by T_{2i+1} where $i \in \mathbb{Z}$, $T_{2i} = \inf\{t \mid x(t) = H^-(t); t \geq T_{2i-1}\}$ and $T_{2i+1} = \inf\{t \mid x(t) = H^+(t); t \geq T_{2i}\}$. This model contains five parameters (see [17] for a detailed discussion on physiological relevance, restrictions and derivation of the model parameters). The parameter a is the circadian amplitude, τ_s and τ_w are time constants which determine the rate of change of homeostatic sleep pressure during sleep and wake, respectively. Borbely *et. al* [31] have investigated how to approximate these time constants in relation with human monophasic/polyphasic sleep-wake patterns by using some experimental data. $H^+(t)$ and $H^-(t)$ have period 1 that symbolise one day, and H_0^+ and H_0^- are the mean values of them, respectively. We note that biological constraints require a monotonically decreasing x_s and a monotonically increasing x_w . Wake and sleep homeostatic pressures asymptote to 1 and 0, respectively, and therefore stay in the interval $(0, 1)$. These restrictions yield $\tau_s > 0$, $\tau_w > 0$, and

$$a < H_0^- < H_0^+ < 1 - a. \quad (7.7)$$

Nakao *et. al* [214, 215] have shown that the dynamics of the two process model can be studied using one dimensional maps with discontinuities. Using this observation, Bailey *et. al* [18] introduced three different one dimensional maps in terms of switching event times to study periodic orbits and their bifurcations. These are: (i)– the down map $T_d : \mathbb{R} \rightarrow \mathbb{R}$ from upper to lower threshold, i.e. a map that takes a point $(H^+(t_0), t_0)$ on the upper threshold and maps it into the

next point on the lower threshold. (ii)– the up map $T_u : \mathbb{R} \rightarrow \mathbb{R}$ from lower to upper threshold. Therefore, $T_d(t_0)$ and $T_u(t_0)$ are the first times greater than t_0 such that $x_s(T_d(t_0), t_0) = H^-(T_d(t_0))$ and $x_w(T_u(t_0), t_0) = H^+(T_u(t_0))$ hold. (iii)– the map from upper threshold into itself (composition of the down and up maps) $T_s : \mathbb{R} \rightarrow \mathbb{R}$ where $T_s(t_0) = T_u(T_d(t_0))$. The upper and lower thresholds are one day periodic (see equations (7.3) and (7.4)), hence all three maps have the following property

$$T_j(t_0 + 1) = T_j(t_0) + 1, \quad j = d, u, s. \quad (7.8)$$

Examples of these maps are illustrated in Fig. 7.1. In panel (c) the diagonal line helps to see fixed points of the map $T_s(t_0)$ (corresponding to periodic solutions), e.g. here the two process model has a stable periodic orbit.

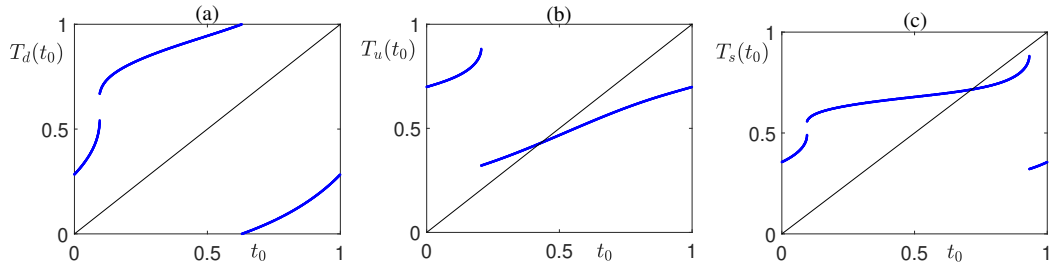


Figure 7.1: Illustrative examples of $T_j \bmod 1$ for $j = d; u; s$, showing behaviour similar to [18]. Parameters: $\tau_w = 0.75$, $\tau_s = 0.25$, $H_0^+ = 0.75$, $H_0^- = 0.1562$, and $a = 0.08675$.

Bailey *et. al* [18] have shown that the map T_s is monotonic for a large regions of the parameter plane, and in these regions T_s can be considered as the degree 1 lift of a circle map on the interval $[0, 1]$. Thus the map has a unique rotation number, which is independent of t_0 [228, 249], given by

$$\rho(T_s) = \lim_{n \rightarrow \infty} \frac{T_s^n(t_0) - t_0}{n}. \quad (7.9)$$

If the rotation number $\rho(T_s)$ is rational, then the map has periodic solutions [158, 249]. The model has various types of periodic orbits and these can be characterised as having p sleep-wake episodes in q days. Thus, t_0 yields a (p, q)

periodic orbit if $T_s^p(t_0) = t_0 + q$ where $(T_s^j(t_0) - t_0) \notin \mathbb{N}$ for $j = 1, \dots, p-1$. The monotonicity of T_s and relation (7.8) give that the set $T_s([0, 1])$ will be accommodated in an interval of length 1. Hence, if T_s has a (p, q) periodic solution, the greatest common divisor of p and q will be 1 and the theory of monotonic circle maps implies that the function T_s has rational rotation number $\rho(T_s) = q/p$, (cf. [12, 18]). We demonstrate some examples of (p, q) periodic orbits in Fig 7.2.

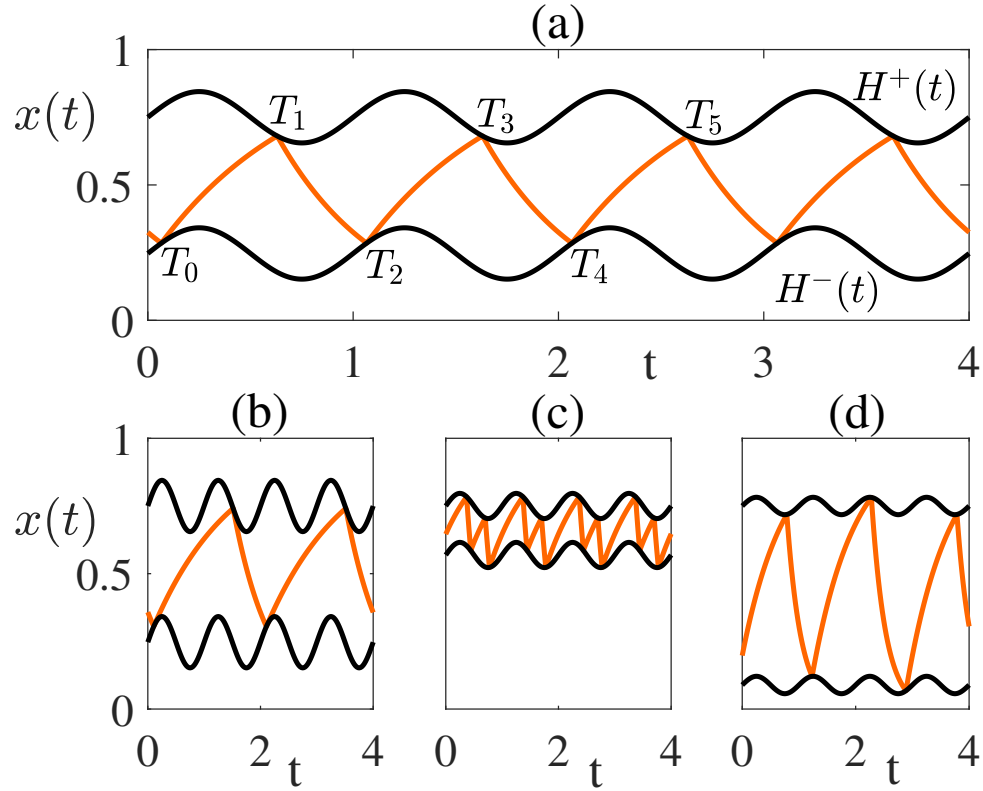


Figure 7.2: Periodic solutions of the two process model (in [18] similar orbits are presented with different parameters). (a)- A (1,1) periodic orbit (one sleep-wake episode in one day). The homeostatic sleep pressure (shown in light brown) increases during wake and decreases during sleep. The upper and lower thresholds are shown in black. Switching from wakefulness (sleep) to sleep (wakefulness) takes place at upper (lower) threshold crossing. Parameters: $\tau_w = 0.70$, $\tau_s = 0.5$, $H_0^+ = 0.75$, $H_0^- = 0.2469$, and $a = 0.09478$. (b)- A (1,2) periodic orbit (one sleep-wake episode in two days). Parameters: $\tau_w = 1.426$, $\tau_s = 0.6634$, $H_0^+ = 0.75$, $H_0^- = 0.2469$, and $a = 0.09478$. (c)- A (2,1) periodic orbit (two sleep-wake episodes in one day). Parameters: $\tau_w = 0.75$, $\tau_s = 0.25$, $H_0^+ = 0.75$, $H_0^- = 0.569$, and $a = 0.04659$. (d)- A (2,3) periodic orbit (two sleep-wake episodes in three days). Parameters: $\tau_w = 0.75$, $\tau_s = 0.25$, $H_0^+ = 0.75$, $H_0^- = 0.08883$, and $a = 0.03213$.

7.3 Construction and stability of periodic orbits

Daan *et. al* [62] have shown that the two process model can describe a wide range of sleep-wake periodic pattern. Using the methodology presented in Section 3.3, we can explicitly construct any (p, q) periodic solution. Here we will show the construction of a $(1, 1)$ periodic orbit, but a similar method can be implemented to build any (p, q) periodic orbit.

A $(1, 1)$ periodic solution has period $\Delta = 1$ and contains one wake episode and one sleep episode. To build this let us consider a solution $x_w(t, t_0)$ that starts from the lower threshold at $t = t_0$ with an initial value $x_w(t_0) = x_0$. Since the solution starts at the lower threshold we also have $H^-(t_0) = x_0$. The solution will evolve according to equation (7.1) until it hits the upper threshold at $t = T_1$ with a state value $x_w(T_1) = x_1$. We denote the duration of the wake episode by $\Delta_1 = T_1 - t_0$. At the upper threshold $H^+(T_1) = x_1$ holds and the sleep state starts. Then the solution $x_s(t, T_1)$ will evolve according to equation (7.2) until it hits the lower threshold at $t = 1 + t_0$ with a state value $x_w(\Delta_2) = x_2$ where $\Delta_2 = 1 - \Delta_1$ denotes the duration of the sleep episode. At the lower threshold $H^-(t) = x_2$ holds and a switch from sleep to awake occurs. Due to periodicity we also have that $x_2 = x_0$. To complete the procedure we need to determine the unknowns $(t_0, x_0, \Delta_1, x_1, x_2)$ by simultaneously solving a system of five equations:

$$\begin{aligned} x_0 &= H_0^- + a \sin(2\pi t_0); & x_1 &= 1 - (1 - x_0)e^{-\Delta_1/\tau_w} \\ x_1 &= H_0^+ + a \sin(2\pi T_1); & x_2 &= x_1 e^{-\Delta_2/\tau_s}; & x_2 &= x_0. \end{aligned} \tag{7.10}$$

In general, to build any (p, q) periodic orbit one needs to solve system of equations with more unknown parameters, for example to construct a $(2, 3)$ periodic orbit nine equations are required to determine nine unknowns. We illustrate the shape of $(1, 1)$ and $(2, 3)$ periodic orbits in Fig 7.3 where we

denote the duration of wake and sleep episodes by Δ_{2i+1} and Δ_{2i} , respectively, $i \in \mathbb{Z}$.

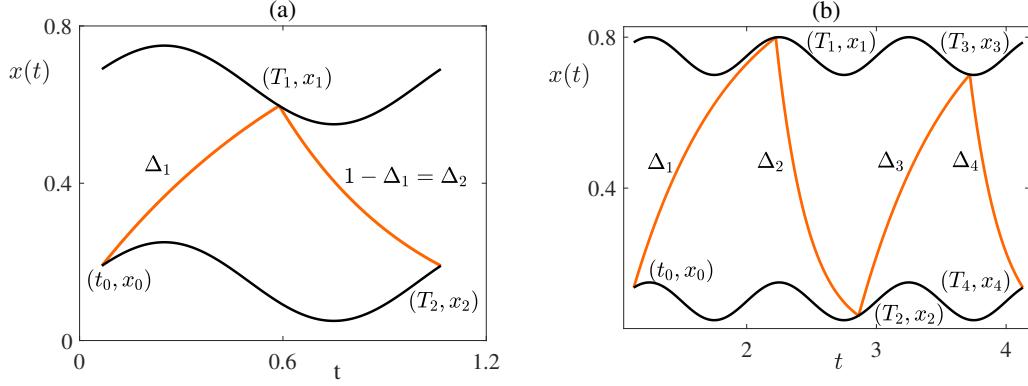


Figure 7.3: *Left panel: A $(1,1)$ -periodic orbit. In order to construct this orbit explicitly, we need to determine $(t_0, x_0, \Delta_1, x_1, x_2)$. Here t_0 is the waking up time with initial homeostatic sleep pressure x_0 , Δ_1 is the total awake time, x_1 is the homeostatic sleep pressure for which switching from wake to sleep occurs, and x_2 is the homeostatic sleep pressure for which switching from sleep to wake occurs. We can find five equations using the explicit solution and threshold matching conditions to solve these five unknowns uniquely. Parameters: $\tau_w = 0.75$, $\tau_s = 0.417$, $H_0^+ = 0.65$, $H_0^- = 0.15$, and $a = 0.1$. Right panel: A $(2,3)$ -periodic orbit, and to construct this we need to determine nine unknowns $(t_0, x_0, \Delta_1, x_1, \Delta_2, x_2, \Delta_3, x_3, x_4)$. Here we denote $T_1 = t_0 + \Delta_1$, $T_2 = T_1 + \Delta_2$, $T_3 = T_2 + \Delta_3$, $T_4 = t_0 + 3$, and $\Delta_4 = T_4 - T_3$. At the lower threshold, switching from sleep to wake occurs at (t_0, x_0) , (T_2, x_2) , and (T_4, x_4) . At the upper threshold, switching from wake to sleep occurs at (T_1, x_1) and (T_3, x_3) . Parameters: $\tau_w = 0.75$, $\tau_s = 0.25$, $H_0^+ = 0.75$, $H_0^- = 0.1$, and $a = 0.05$.*

7.3.1 Stability I: Saltation approach

To determine the stability of periodic solutions we implement a similar method to that presented in Section 4.2. However, we note that in this case switching thresholds are not constant, and indicator functions are explicitly state and time dependent [211]. Therefore we need to adapt Floquet theory and obtain saltation matrices accordingly.

Let us consider a (p, q) periodic orbit $\bar{x}(t)$ of the system (7.1)-(7.2) and a perturbed solution by $\tilde{x}(t) = \bar{x}(t) + \delta x(t)$, for some small perturbation $\delta x(t)$. Then during a wake state when $T_0 < t < T_1$ (or in general between $T_{2i} < t < T_{2i+1}$), $\delta x(t)$ evolves depend upon to

$$\frac{d}{dt}\delta x(t) = -\frac{1}{\tau_w}\delta x(t). \quad (7.11)$$

During a sleep state when $T_1 < t < T_2$ (or in general between $T_{2i+1} < t < T_{2i+2}$), $\delta x(t)$ evolves according to

$$\frac{d}{dt}\delta x(t) = -\frac{1}{\tau_s}\delta x(t). \quad (7.12)$$

Here we derive the saltation rule at event time $t = T_1$ on the upper threshold. A similar calculation can be done at any event time $t = T_{2i+1}$ ($t = T_{2i}$), $i \in \mathbb{Z}$, on the upper (lower) threshold. We introduce indicator functions $h_1(x(t), t) = x(t) - H_0^+ - a \sin(2\pi t)$ and $h_2(x(t), t) = x(t) - H_0^- - a \sin(2\pi t)$ such that switching events occur when $h_1(x(t), t) = 0$ and $h_2(x(t), t) = 0$ on the upper and lower threshold, respectively. Hence the unperturbed (perturbed) trajectory intersects with upper threshold at $t = T_1$ ($\tilde{T}_1 = T_1 + \delta T_1$) that is prescribed by $h_1(x(T_1), T_1) = 0$ ($h_1(x(\tilde{T}_1), \tilde{T}_1) = 0$). Here we assume $\delta T_1 > 0$, however for the case $\delta T_1 < 0$ a similar argument holds. A Taylor expansion up to the first order terms yields

$$\begin{aligned} h_1(\tilde{x}(\tilde{T}_1), \tilde{T}_1) &= h_1(\tilde{x}(T_1 + \delta T_1), T_1 + \delta T_1) \simeq h_1(\tilde{x}(T_1) + \tilde{x}'(T_1)\delta T_1, T_1 + \delta T_1) \\ &\simeq h_1(\bar{x}(T_1) + \delta x(T_1) + \bar{x}'(T_1^-)\delta T_1, T_1 + \delta T_1) \\ &\simeq h_1(\bar{x}(T_1), T_1) + \nabla_x h_1(\bar{x}(T_1), T_1) [\delta x(T_1) + \bar{x}'(T_1^-)\delta T_1] \\ &\quad + \nabla_t h_1(\bar{x}(T_1), T_1)\delta T_1. \end{aligned} \quad (7.13)$$

Using this along with the property $h_1(\tilde{x}(\tilde{T}_1), \tilde{T}_1) = 0 = h_1(\bar{x}(T_1), T_1)$, we obtain

$$\nabla_x h_1(\bar{x}(T_1), T_1) [\delta x(T_1) + \bar{x}'(T_1^-)\delta T_1] + \nabla_t h_1(\bar{x}(T_1), T_1)\delta T_1 = 0. \quad (7.14)$$

Moreover we have

$$\nabla_x h_1(x, t) = 1 \quad \text{and} \quad \nabla_t h_1(x, t) = -2a\pi \cos(2\pi t). \quad (7.15)$$

Then by combining equation (7.14) and (7.15) we obtain

$$\delta x(T_1) + \bar{x}'(T_1^-)\delta T_1 - 2a\pi \cos(2\pi t)\delta T_1 = 0. \quad (7.16)$$

Hence by solving equation (7.16) for δT_1 we find

$$\delta T_1 = -\frac{\delta x(t)}{\bar{x}'(t) - 2a\pi \cos(2\pi t)}\Big|_{t=T_1^-} = -\frac{\delta x(T_1^-)}{(1 - x(T_1^-))/\tau_w - 2a\pi \cos(2\pi T_1^-)}. \quad (7.17)$$

We can approximate $\tilde{x}(T_1^+)$ by pulling back the perturbed solution an amount of time δt starting from $\tilde{x}(\tilde{T}_1^+)$ and therefore we have that

$$\begin{aligned} \delta x(T_1^+) &\simeq \tilde{x}(T_1^+ + \delta T_1) - \tilde{x}'(T_1^+ + \delta T_1)\delta T_1 - \bar{x}(T_1^+) \\ &\simeq \bar{x}(T_1^+) + \delta x(T_1^-) + \bar{x}'(T_1^-)\delta T_1 - \bar{x}'(T_1^+)\delta T_1 - \bar{x}(T_1^+) \\ &= \delta x(T_1^-) + [\bar{x}'(T_1^-) - \bar{x}'(T_1^+)]\delta T_1 \\ &= \delta x(T_1^-) + \left[\frac{1 - x(T_1^-)}{\tau_w} + \frac{x(T_1^+)}{\tau_s} \right] \delta T_1. \end{aligned} \quad (7.18)$$

As a result, using equation (7.17) and (7.18) we obtain

$$\begin{aligned} \delta x(T_1^+) &= \left[1 - \frac{\left(\frac{1 - \bar{x}(T_1^-)}{\tau_w} \right) - \left(-\frac{\bar{x}(T_1^+)}{\tau_s} \right)}{\frac{1 - \bar{x}(T_1^-)}{\tau_w} - 2a\pi \cos(2\pi T_1^-)} \right] \delta x(T_1^-) \\ &\equiv K_1(T_1)\delta x(T_1^-), \end{aligned} \quad (7.19)$$

where $K_1(T_1)$ denotes the saltation rule and is given by

$$K_1(T_1) = \frac{\tau_w}{\tau_s} \left[\frac{2a\pi\tau_s \cos(2\pi T_1) + a \sin(2\pi T_1) + H_0^+}{2a\pi\tau_w \cos(2\pi T_1) + a \sin(2\pi T_1) + H_0^+ - 1} \right]. \quad (7.20)$$

By following a similar method, the saltation rule $K_2(T_2)$ at $t = T_2$ on the lower threshold can be computed as

$$K_2(T_2) = \frac{\tau_s}{\tau_w} \left[\frac{2a\pi\tau_w \cos(2\pi T_2) + a \sin(2\pi T_2) + H_0^- - 1}{2a\pi\tau_s \cos(2\pi T_2) + a \sin(2\pi T_2) + H_0^-} \right]. \quad (7.21)$$

We note that the saltation rule at any $t = T_{2i+1}$ on the upper threshold is equal to $K_1(T_{2i+1})$ and that of at any $t = T_{2i}$ on the lower threshold is equal to $K_2(T_{2i})$.

Therefore for any (p, q) -periodic solution (p sleep and p wake in q days, $\Delta = q$), after one period of oscillation, a perturbed trajectory evolves according to $\delta x(q) = M\delta x(t_0)$ where

$$M = K_2(T_{2p})e^{-\frac{\Delta_{2p}}{\tau_s}} K_1(T_{2p-1})e^{-\frac{\Delta_{2p-1}}{\tau_w}} \dots K_2(T_2)e^{-\frac{\Delta_2}{\tau_s}} K_1(T_1)e^{-\frac{\Delta_1}{\tau_w}}. \quad (7.22)$$

Hence, the Floquet exponent is

$$\begin{aligned} \kappa = \frac{1}{q} \left[- \left(\frac{1}{\tau_w}(\Delta_1 + \Delta_3 + \dots + \Delta_{2p-1}) + \frac{1}{\tau_s}(\Delta_2 + \Delta_4 + \dots + \Delta_{2p}) \right) \right. \\ \left. + \sum_{j=1}^p \ln |K_1(T_{2j-1})| + \ln |K_2(T_{2j})| \right]. \end{aligned} \quad (7.23)$$

The periodic orbit will be stable if the Floquet exponent κ has negative real part. For example, in Figure 7.3, the $(1, 1)$ and $(2, 3)$ periodic solutions have $\kappa = -2.73$ and $\kappa = -1.253$, respectively, thus both solutions are stable.

7.3.2 Implicit relation of the event times

Explicit solutions of the two process model during wake and sleep episodes are given by equation (7.5) and (7.6), using these solutions we can obtain an implicit relation between consecutive event times. Thus for a wake episode when $T_{2i} \leq t \leq T_{2i+1}$ we have,

$$T_{2i+1} + \tau_w \ln |x(T_{2i+1}) - 1| = T_{2i} + \tau_w \ln |x(T_{2i}) - 1|. \quad (7.24)$$

Using the state values on the upper and lower thresholds, we can rewrite this as

$$T_{2i+1} + \tau_w \ln |H_0^+ + a \sin(2\pi T_{2i+1}) - 1| = T_{2i} + \tau_w \ln |H_0^- + a \sin(2\pi T_{2i}) - 1|. \quad (7.25)$$

It is clear from equation (7.25) that T_{2i+1} can not be explicitly solved in terms of T_{2i} , but we can define an implicit function $G_1(T_{2i}, T_{2i+1}) = 0$ where

$$G_1(T_{2i}, T_{2i+1}) = T_{2i+1} - T_{2i} - \tau_w \ln \left| \frac{H_0^- + a \sin(2\pi T_{2i}) - 1}{H_0^+ + a \sin(2\pi T_{2i+1}) - 1} \right|. \quad (7.26)$$

Moreover, for a sleep episode when $T_{2i+1} \leq t \leq T_{2i+2}$ we have,

$$T_{2i+2} + \tau_s \ln |x(T_{2i+2})| = T_{2i+1} + \tau_s \ln |x(T_{2i+1})|. \quad (7.27)$$

Using the state values on the upper and lower thresholds, we obtain

$$T_{2i+2} + \tau_s \ln |H_0^- + a \sin(2\pi T_{2i+2})| = T_{2i+1} + \tau_s \ln |H_0^+ + a \sin(2\pi T_{2i+1})|. \quad (7.28)$$

We observe that T_{2i+2} also can not be explicitly solved in terms of T_{2i+1} , however we can define an implicit function $G_2(T_{2i+1}, T_{2i+2}) = 0$ where

$$G_2(T_{2i+1}, T_{2i+2}) = T_{2i+2} - T_{2i+1} - \tau_s \ln \left| \frac{H_0^+ + a \sin(2\pi T_{2i+1})}{H_0^- + a \sin(2\pi T_{2i+2})} \right|. \quad (7.29)$$

In the next section we will use these implicit relations to assess the stability of periodic orbits.

7.3.3 Stability II: Using the implicit relation of the event times

A one dimensional map $t_{n+1} = g(t_n)$, where we assume g is differentiable, has a fixed point if $t_n = t_{n+1}$. Thus to find fixed points t^* of the map we need to solve $t^* = g(t^*)$ for t^* . To investigate the stability of these fixed points we consider a nearby orbit $t_n = t^* + \delta_n$ and determine whether this orbit is attracted or repelled from t^* . Then using a first order approximation we obtain

$$t^* + \delta_{n+1} = g(t^* + \delta_n) \simeq g(t^*) + g'(t^*)\delta_n, \quad (7.30)$$

since $t^* = g(t^*)$, this yields the linearised map

$$\delta_{n+1} = g'(t^*)\delta_n. \quad (7.31)$$

The derivative of map at t^* is called multiplier of the fixed point. Then the fixed point t^* is

- i. Unstable (local repeller) if $|g'(t^*)| > 1$,
- ii. Marginal if $|g'(t^*)| = 1$,
- iii. Stable (local attractor) if $|g'(t^*)| < 1$,
- iv. Superstable if $|g'(t^*)| = 0$.

We can use this to determine stability of any (p, q) periodic solution of the two process model. To see this, let us take a (p, q) periodic orbit and assume it start from lower threshold at $t = T_{2i}$ and consider a perturbed trajectory that starts at a perturbed time $t = T_{2i} + \delta T_{2i}$. Periodic and perturbed solutions reach to the upper threshold at $t = T_{2i+1}$ and $t = T_{2i+1} + \delta T_{2i+1}$, respectively. A first order Taylor expansion of equation (7.26) gives

$$G_1(T_{2i} + \delta T_{2i}, T_{2i+1} + \delta T_{2i+1}) = G_1(T_{2i}, T_{2i+1}) + \frac{\partial G_1}{\partial T_{2i}} \delta T_{2i} + \frac{\partial G_1}{\partial T_{2i+1}} \delta T_{2i+1}. \quad (7.32)$$

Then using $G_1(T_{2i} + \delta T_{2i}, T_{2i+1} + \delta T_{2i+1}) = G_1(T_{2i}, T_{2i+1}) = 0$, we obtain

$$\delta T_{2i+1} = -\frac{\frac{\partial G_1}{\partial T_{2i}}}{\frac{\partial G_1}{\partial T_{2i+1}}} \delta T_{2i} \equiv S_1(T_{2i}, T_{2i+1}) \delta T_{2i}, \quad (7.33)$$

where

$$S_1(T_{2i}, T_{2i+1}) = -\frac{\left(-1 - \tau_w \left(\frac{2\pi a \cos(2\pi T_{2i})}{H_0^- + a \sin(2\pi T_{2i}) - 1}\right)\right)}{\left(1 + \tau_w \left(\frac{2\pi a \cos(2\pi T_{2i+1})}{H_0^+ + a \sin(2\pi T_{2i+1}) - 1}\right)\right)}, \quad (7.34)$$

Similarly a first order expansion of equation (7.29) yields

$$\begin{aligned} G_2(T_{2i+1} + \delta T_{2i+1}, T_{2i+2} + \delta T_{2i+2}) &= G_2(T_{2i+1}, T_{2i+2}) + \frac{\partial G_2}{\partial T_{2i+1}} \delta T_{2i+1} \\ &+ \frac{\partial G_2}{\partial T_{2i+2}} \delta T_{2i+2}. \end{aligned} \quad (7.35)$$

We know $G_2(T_{2i+1} + \delta T_{2i+1}, T_{2i+2} + \delta T_{2i+2}) = G_2(T_{2i+1}, T_{2i+2}) = 0$, therefore

$$\delta T_{2i+2} = -\frac{\frac{\partial G_2}{\partial T_{2i+1}}}{\frac{\partial G_2}{\partial T_{2i+2}}} \delta T_{2i+1} \equiv S_2(T_{2i+1}, T_{2i+2}) \delta T_{2i+1}, \quad (7.36)$$

where

$$S_2(T_{2i+1}, T_{2i+2}) = -\frac{\left(-1 - \tau_s \left(\frac{2\pi a \cos(2\pi T_{2i+1})}{H_0^+ + a \sin(2\pi T_{2i+1})}\right)\right)}{\left(1 + \tau_s \left(\frac{2\pi a \cos(2\pi T_{2i+2})}{H_0^- + a \sin(2\pi T_{2i+2})}\right)\right)}. \quad (7.37)$$

Hence for a (p, q) periodic orbit we have $\delta T_{2p} = \mu \delta T_0$ where

$$\mu = S_2(T_{2p-1}, T_{2p}) S_1(T_{2p-2}, T_{2p-1}) \dots S_2(T_1, T_2) S_1(T_0, T_1). \quad (7.38)$$

Thus the periodic orbit is stable when $|\mu| < 1$. We note that the first method (given in Section 7.3.1) and the second method (presented here) yield the same stability result for a periodic orbit. In following subsections we will use the first method to compute Lyapunov exponents and the second method to determine parameter sets that give rise to superstable periodic orbits. A bifurcation diagram, showing the Floquet exponents of periodic orbits under variation of H_0^- is presented in Fig. 7.4. At $H_0^- = 0.2102$ and $H_0^- = 0.381$ saddle-node bifurcation of $(1, 1)$ periodic orbits is observed. Examples of stable and unstable periodic orbits are also shown. In Fig. 7.5 we plot the map $T_s(t_0)$ for various H_0^- values to show the creation/annihilation of $(1, 1)$ periodic solutions via saddle-node bifurcation. Both methods agree, i.e. bifurcations occur for the same values of H_0^- .

7.3.4 Lyapunov exponents

Lyapunov exponents quantify the exponential rates of convergence or divergence of initially close orbits of an attractor in state space and are useful to determine regions of parameter space with different emergent behaviour. Periodic attractors have non-positive exponents whereas chaotic attractors have at least one positive Lyapunov exponent.

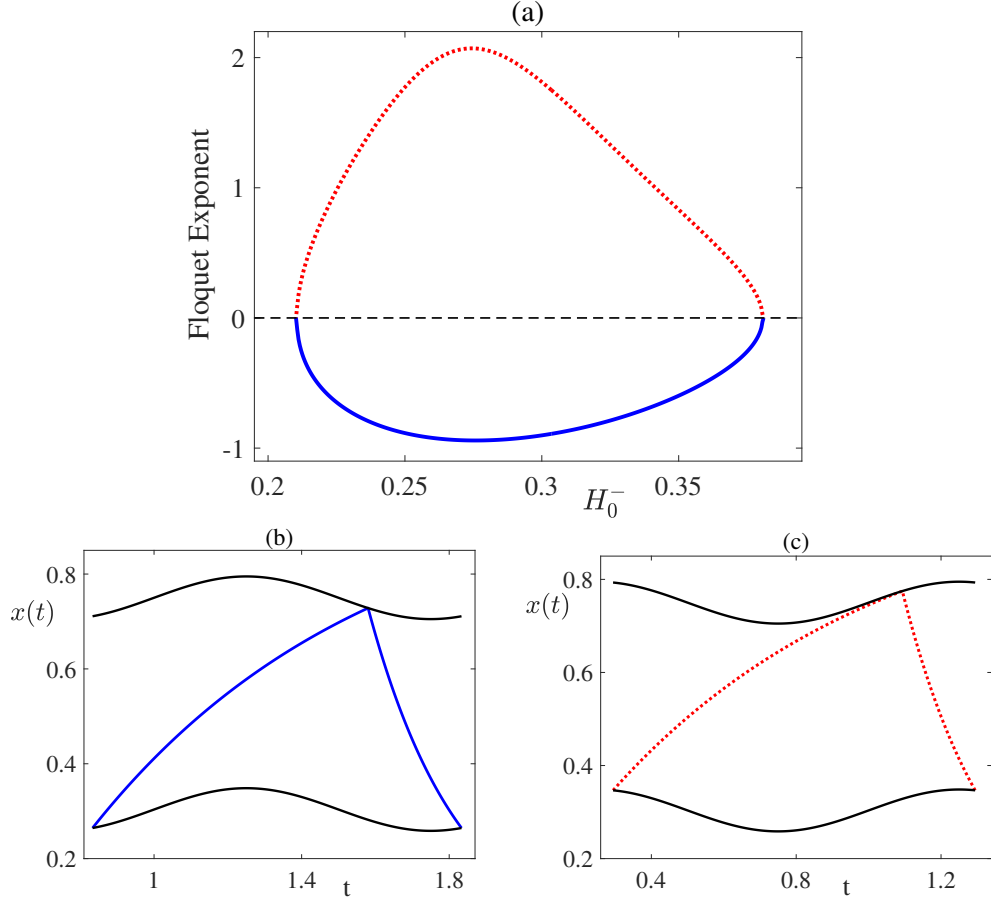


Figure 7.4: (a) A bifurcation diagram for (1,1) periodic orbits. When $H_0^- \in (0.2102, 0.381)$ stable and unstable periodic solutions coexist. At $H_0^- = 0.2102$ and $H_0^- = 0.381$ these solutions coincide and annihilate each other via saddle-node bifurcation of periodic orbits. (b) An example of a stable periodic orbit with Floquet exponent $= -0.8905$, and $H_0^- = 0.3035$. (c) An example of an unstable periodic orbit with Floquet exponent $= 1.7508$, and $H_0^- = 0.3035$. Parameters: $\tau_w = 0.75$, $\tau_s = 0.25$, $H_0^+ = 0.75$, and $a = 0.04498$.

For a general dynamical system $\dot{x} = f(x)$, $x \in \mathbb{R}^n$, the spectrum of the LEs, λ_i , is given for some different initial conditions $\delta x_i(t_0)$ as:

$$\lambda_i = \lim_{t \rightarrow \infty} \frac{1}{t - t_0} \ln \left| \frac{\delta x(t)}{\delta x_i(t_0)} \right|, \quad (7.39)$$

where $\delta x(t)$ indicates evolution of the distance $\bar{x}(t) - \tilde{x}(t)$ between $\bar{x}(t)$ and the perturbed trajectory $\tilde{x}(t)$ with an initial condition $\bar{x}(t_0) + \delta x(t_0)$. For smooth continuous dynamical systems, LEs are generally computed by solving a variational equation where the Jacobian of the system is evaluated along an orbit. Indeed, algorithms for computing the LEs of smooth continuous systems

are well developed [22, 83, 258]. However, these classical algorithms cannot be directly applied to compute LEs of nonsmooth dynamical systems. As we have shown in Section 4.2, evaluation of the variational equation of a nonsmooth system requires careful consideration. Here we develop the notion of Lyapunov exponent for the two process model, by re-visiting techniques originally applied in the analysis of impacting systems [68, 211].

Similar to the derivation of equation (7.22), for any arbitrary time t , the overall deviation between two trajectories $\bar{x}(t)$ and $\tilde{x}(t)$ of the two process model can be written as

$$\delta x(t) = e^{-\frac{(t-\Delta_k)}{\tau_w}} K_2(T_k) e^{-\frac{\Delta_k}{\tau_s}} K_1(T_{k-1}) e^{-\frac{\Delta_{k-1}}{\tau_w}} \dots K_1(T_1) e^{-\frac{\Delta_1}{\tau_w}} \delta x(t_0), \quad (7.40)$$

where $K_1(t)$ and $K_2(t)$ are saltation rules given by equations (7.20) and (7.21), respectively. Thus using formula (7.39) along with equation (7.40), we can

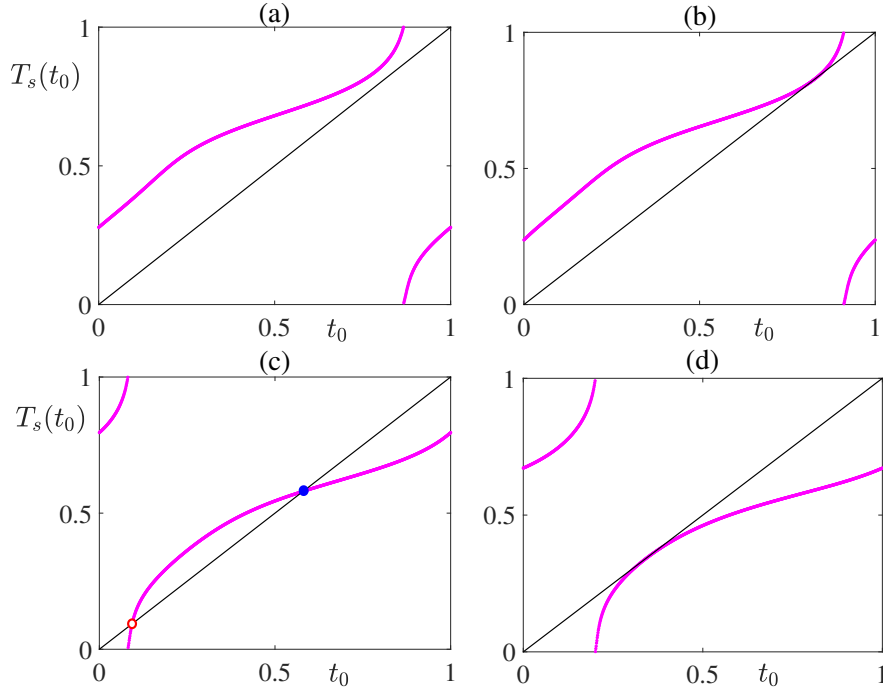


Figure 7.5: The creation/annihilation of a pair of $(1,1)$ periodic orbits via a saddle-node bifurcation as H_0^- varying. (a) When $H_0^- = 0.19$ no fixed point observed. (b) At $H_0^- = 0.2102$ the saddle-node bifurcation is occurred. (c) The map has two fixed points, $H_0^- = 0.3035$. (d) At $H_0^- = 0.381$ the saddle-node bifurcation reappeared. Parameters: $\tau_w = 0.75$, $\tau_s = 0.25$, $H_0^+ = 0.75$, and $a = 0.04498$.

formulate the Lyapunov exponent of the two process model as

$$\begin{aligned}\lambda &= \lim_{k \rightarrow \infty} \frac{1}{T^k - T^0} \ln \left| \prod_{j=1}^k K_\mu(T_j) e^{-\frac{1}{\tau_w}(\Delta_1 + \Delta_3 + \dots + \Delta_{k-1})} e^{-\frac{1}{\tau_s}(\Delta_2 + \Delta_4 + \dots + \Delta_k)} \right| \\ &= \lim_{k \rightarrow \infty} \frac{1}{T^k - T^0} \left[-\frac{1}{\tau_w}(\Delta_1 + \Delta_3 + \dots + \Delta_{k-1}) - \frac{1}{\tau_s}(\Delta_2 + \Delta_4 + \dots + \Delta_k) \right. \\ &\quad \left. + \sum_{j=1}^k \ln |K_\mu(T_j)| \right],\end{aligned}$$

where $\mu = 1$ if j is odd and $\mu = 2$ if j is even. Here we consider the trajectory $\bar{x}(t)$ to start from the lower threshold but a similar formula can easily be obtained when it starts from the upper threshold. We note that there are two contributions to λ , one from the smooth flow during sleep and awake episodes and the other from the discontinuous nature of the switching mechanism at threshold crossings. We depict a LE diagram for the two process model in Fig. 7.6. We observe that the diagram shades parameter regions in which different periodic solutions are occur.

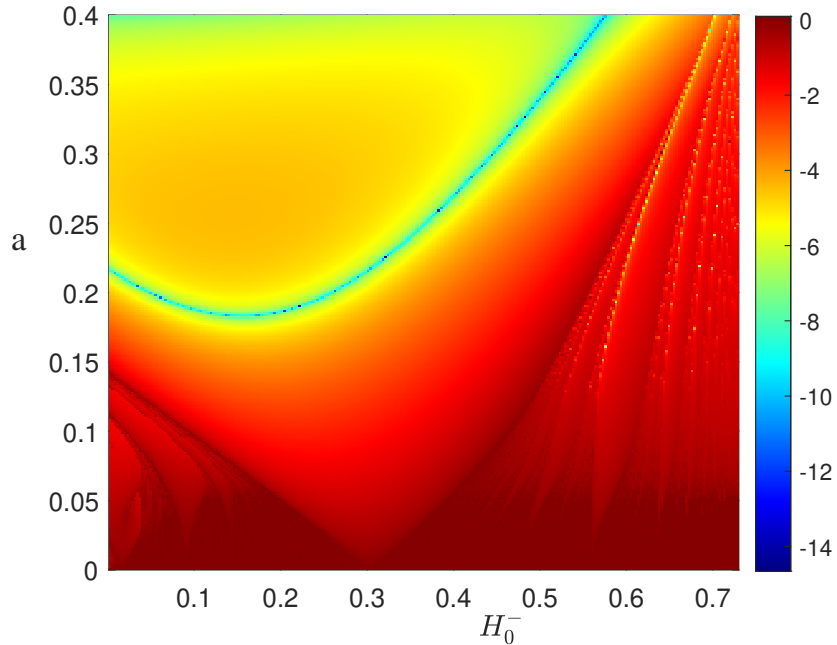


Figure 7.6: The Lyapunov exponents plot of the two process model in the (H_0^-, a) . The diagram shades parameter regions in which different periodic solutions are observed. Parameters: $\tau_w = 0.75$, $\tau_s = 0.25$, and $H_0^+ = 0.75$.

7.3.5 Superstable solutions

Inside the region where $(1, 1)$ periodic orbits exist in Fig. 7.6, we observe a turquoise curve on which the LE is minimised. This indicates that the model may support some superstable periodic solutions. Then using this observation, over that region we computed $g'(t^*) = (T_d(T_u(t^*)))'$ as follows

$$\mu = S_2(T_1, T_2)S_1(T_0, T_1), \quad (7.41)$$

and obtained that $|g'(t^*)| = |\mu| = 0$ holds along this curve, hence, the two process model exhibits $(1, 1)$ superstable periodic orbits. The parameters in the (a, H_0^-) plane that yield such orbits are illustrated in Fig. 7.7. The superposition of the turquoise curve in Fig. 7.6 and the blue curve in Fig. 7.7 are shown in Fig. 7.14.

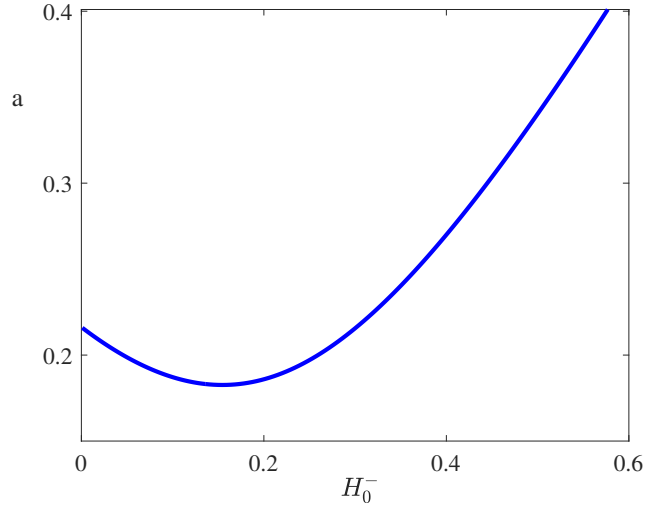


Figure 7.7: Blue curve shows the parameters in the (a, H_0^-) plane that yield $(1, 1)$ superstable periodic solutions of the two process model. Other parameters: $\tau_w = 0.75$, $\tau_s = 0.25$, and $H_0^+ = 0.75$.

7.4 Bifurcation of periodic solutions

In modern society, the most common sleep-wake pattern for adults is monophasic (one wake and one sleep episodes per day). However, Daan *et. al* [62] have shown that the two process model can describe a wide range of sleep-wake pat-

terns including both fewer or more sleep-wake cycles per day. The sleep-wake patterns with more than one sleep-wake cycle per day are called polyphasic. Understanding the polyphasic patterns that the model displays is also biologically significant. For instance babies have polyphasic patterns that gradually change into monophasic over the first few years of development [18, 204]. In this section we aim to understand how transitions between different sleep-wake patterns occur in the model by investigating the regions of existence of periodic solutions.

7.4.1 Arnol'd tongues

Regions in the parameter space of the two process model where the rotation number ρ is a fixed rational number shape tongue structures and these regions are known as Arnol'd tongues. If the one dimensional map of the circle is continuous saddle-node bifurcations are the only mechanism by which fixed points are created and destroyed. Namely, at the tongue boundary a fixed point for the map is generated via a saddle-node bifurcation. Then inside the tongue, this fixed point breaks up into two fixed points, each of them goes around the unit circle until intersecting at another saddle-node bifurcation on the other tongue boundary, and then fixed points disappear. However, if the map is discontinuous fixed points can be created/annihilated via both saddle-node bifurcations and border collisions [74]. In the following subsections, we will construct Arnol'd tongue borders in the (H_0^-, a) plane of the two process model by investigating both saddle-node bifurcations and grazing bifurcations where the one dimensional map of events is discontinuous.

7.4.2 Borders created by saddle-node bifurcations

Bailey *et. al* [18] have shown that for small circadian amplitude, a , the one dimensional map of the circle is continuous and the creation/destruction of periodic orbits are only related to saddle-node bifurcations. Here we will use

results from Section 7.3 to determine Arnol'd tongue structures for the regions in parameter space where stable and unstable (p, q) periodic orbits co-exist. At the tongue borders the following two conditions must hold: (i) a (p, q) periodic solution must exist, and (ii) the Floquet exponent of the orbit must be zero (since stable and unstable periodic solutions intersect). To clarify this method we will construct saddle-node bifurcation boundaries of $(2, 3)$ periodic orbits. In order to construct a $(2, 3)$ periodic solution that starts from the lower threshold we need to determine nine unknowns $(t_0, x_0, \Delta_1, x_1, \Delta_2, x_2, \Delta_3, x_3, x_4)$ where (t_0, x_0) is the initial condition, Δ_1, Δ_3 (Δ_2, Δ_4) are duration of awake (sleep) episodes, x_1, x_3 (x_2, x_4) are state values at the upper (lower) threshold crossing, and at the saddle-node bifurcation points the orbit must have $\kappa = 0$ (a zero Floquet exponent). Using formula (7.23), the Floquet exponent of a $(2, 3)$ periodic orbit is

$$\kappa = \frac{1}{3} \left[- \left(\frac{1}{\tau_w} (\Delta_1 + \Delta_3) + \frac{1}{\tau_s} (\Delta_2 + \Delta_4) \right) + \ln |K_1(T_1) K_1(T_3) K_2(T_2) K_2(T_4)| \right]. \quad (7.42)$$

We will determine the saddle-node bifurcations of the $(2, 3)$ periodic orbit on the (H_0^-, a) plane, treating H_0^- as a bifurcation parameter and computing a using the final condition $\kappa = 0$. Hence at each saddle-node bifurcation point we need to determine ten unknown $(t_0, x_0, \Delta_1, x_1, \Delta_2, x_2, \Delta_3, x_3, x_4, a)$ by solving the following ten equation simultaneously

$$\begin{aligned} x_0 &= H_0^- + a \sin(2\pi t_0); & x_1 &= 1 - (1 - x_0)e^{-\Delta_1/\tau_w}, \\ x_1 &= H_0^+ + a \sin(2\pi T_1); & x_2 &= x_1 e^{-\Delta_2/\tau_s}, \\ x_2 &= H_0^- + a \sin(2\pi T_2); & x_3 &= 1 - (1 - x_2)e^{-\Delta_3/\tau_w}, \\ x_3 &= H_0^+ + a \sin(2\pi T_3); & x_4 &= x_3 e^{-\Delta_4/\tau_s}, \\ x_4 &= x_0; & \kappa &= 0. \end{aligned} \quad (7.43)$$

We can solve this by using a nonlinear system solver in Matlab, such as `fsolve`. We illustrate an example of the $(2, 3)$ periodic orbit obtained by solving equa-

tion (7.43) in Fig. 7.8. Then in the (H_0^-, a) plane, to build tongue borders of

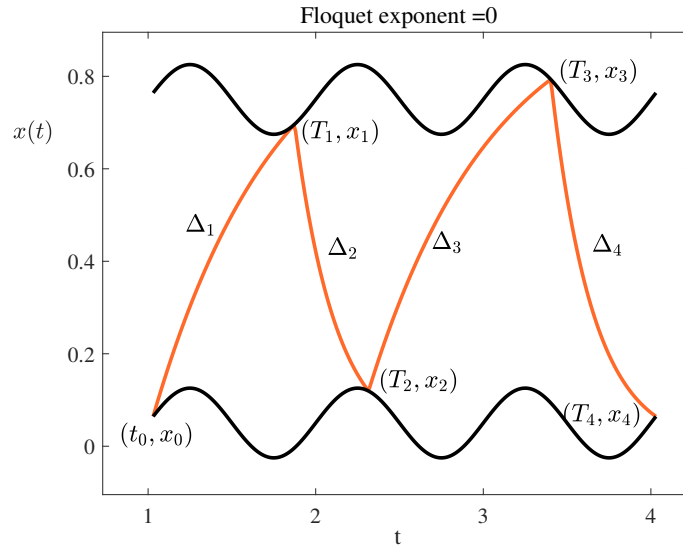


Figure 7.8: A $(2,3)$ periodic orbit that obtained at a saddle-node bifurcation point with zero Floquet exponent. To construct this we find the ten unknowns $(t_0, x_0, \Delta_1, x_1, \Delta_2, x_2, \Delta_3, x_3, \Delta_4, a)$ by solving ten simultaneous equation given in (7.43). Here (t_0, x_0) denotes the initial condition, Δ_1, Δ_3 (Δ_2, Δ_4) are duration of awake (sleep) episodes, x_1, x_3 (x_2, x_4) state values at the upper (lower) threshold crossing. We obtained $a = 0.0754$ by solving this system for $H_0^- = 0.0499$. Other parameters: $\tau_w = 0.75$, $\tau_s = 0.25$, $H_0^+ = 0.75$

the $(2,3)$ periodic orbit, we follow the solution path of a values by adjusting H_0^- with small step sizes, where at each step we use the previous values of $(t_0, x_0, \Delta_1, x_1, \Delta_2, x_2, \Delta_3, x_3, \Delta_4, a)$ as an initial guess. Utilising similar methods, tongue borders related to a saddle-node bifurcations of any (p, q) periodic solution can be constructed. In Fig 7.9 we illustrated a few example of the largest tongue boundaries. We note that the right-hand boundary of each tongue terminates at a point where the saddle-node bifurcations cease to exist. In the following subsections, we will investigate this and determine the full bifurcation sets including for large circadian amplitude, a .

7.4.3 Borders created by grazing bifurcations

We observed that the one dimensional map of the two process model has discontinuities for some parameters, see for example Figs. 7.1 and 7.16. In such maps border collision bifurcations occur when a fixed point of the map coincides with

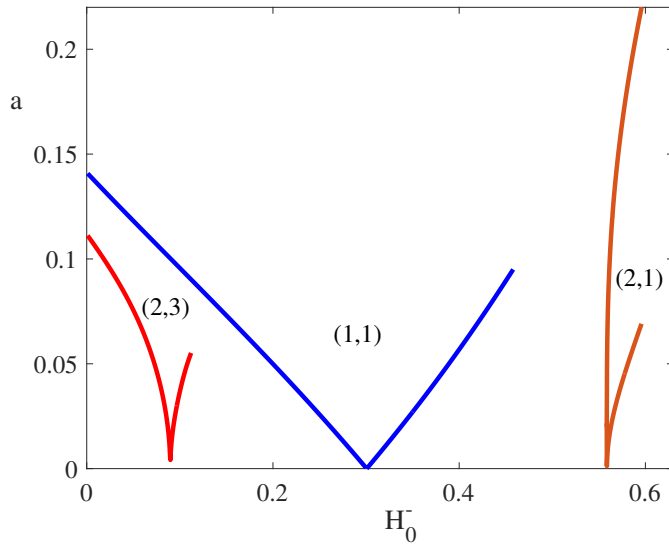


Figure 7.9: The saddle-node bifurcation curves in the (a, H_0^-) plane. We observed that for small circadian amplitude, a the boundaries of Arnol'd tongues related to the saddle-node bifurcations, and as a is increasing the right branches of each tongue comes to an end. Here we show the largest few tongues, $(1, 1)$ is in blue, $(2, 1)$ is in brown, and $(2, 3)$ is in red, though tongue boundaries of any (p, q) periodic solution have a similar behaviour. Parameters: $\tau_w = 0.75$, $\tau_s = 0.25$, and $H_0^+ = 0.75$.

the endpoint of a gap. As parameters are varied, this yields a new mechanism for the creation/destruction of periodic solutions of the model. Border collision bifurcations have been studied for many nonsmooth systems including piecewise smooth systems [120], piecewise smooth system with sliding orbit [298], impact oscillator [38], switching systems [85], and also a classification of such bifurcations for one dimensional maps is given in [147].

Skeldon *et. al* [286] have shown that gaps in the map of the two process model can emerge when either the homeostatic sleep pressure during awake $w_w(t, t_0^w)$, becomes tangential to the upper threshold, $H^+(t)$, or the homeostatic sleep pressure on sleep, $w_s(t, t_0^s)$, becomes tangential to the lower threshold, $H^-(t)$, many examples of such scenarios can be found in [18]. Near the bifurcation points, a small difference in the initial conditions of two sleep/wake trajectories may lead to a large change in the duration of a sleep/wake episodes. The relation between solutions of the the two process model with tangencies and sleep deprivation experiments is discussed in [286].

Bailey *et. al* [18] have shown that the two process model can lead two

types of border collision, namely Type I and Type II border collisions. Type I border collisions yield the creation/destruction of an unstable fixed point and occur when a fixed point of the map coincides with the side of the gap where the derivative of the map is infinite. This corresponds to periodic orbits of the model such that the homeostatic sleep pressure switches at a tangency point. Type II border collisions result in creation/annihilation of either an unstable or a stable fixed point and occur when a fixed point of the map coincides with the side of the gap where the derivative is finite. This corresponds to periodic orbits in the two process model such that the homeostatic sleep pressure *bypass* the tangency point and switches at a later time. For a detailed discussion on analytical computation of map derivatives we refer the reader to [17]. We depict examples of such periodic orbits and discontinuous maps in Fig. 7.16. Gaps in the maps may occur due to tangencies at either the upper threshold or lower threshold, therefore we need to examine Type I and II border collisions for both the upper and lower thresholds. These border collisions are also called grazing bifurcations or tangent bifurcations [147, 286].

7.4.4 Type I grazing bifurcation

The necessary conditions for a Type I grazing bifurcation at the upper (lower) threshold of a (p, q) periodic orbit are: (i) a (p, q) periodic solution must exist, and (ii) the homeostatic sleep pressure on wake (sleep) state must switch to sleep (wake) state at the tangency point. To determine Type I grazing bifurcations of a (p, q) periodic solution we simultaneously solve the equations that are needed to build the orbit and the equation that holds at the tangency point by utilising `fsolve` in Matlab.

To clarify this method we show how to determine Type I grazing bifurcations of $(1, 1)$ periodic orbits. For an orbit starting from lower threshold, to achieve this we need to determine $(t_0, x_0, \Delta_1, x_1, x_2, a)$, where these parameters

are same as in equation (7.10), by simultaneously solving

$$\begin{aligned} x_0 &= H_0^- + a \sin(2\pi t_0); & x_1 &= 1 - (1 - x_0)e^{-\Delta_1/\tau_w}, \\ x_1 &= H_0^+ + a \sin(2\pi T_1); & x_2 &= x_1 e^{-\Delta_2/\tau_s}, \\ x_2 &= x_0; & (1 - x_1)/\tau_w &= 2a\pi \cos(2\pi(t_0 + \Delta_1)). \end{aligned} \quad (7.44)$$

The final equation is derived from the tangency condition at the upper threshold. In the left panel of Fig. 7.10 we illustrate a Type I grazing (1, 1) periodic orbit obtained by solving (7.44). In the right panel of Fig. 7.10, we build the corresponding one dimensional map with a gap where an unstable fixed point of the map coincides with the side of the gap where the derivative of map is infinite. Utilising similar methods, we can determine Type I grazing solutions of any (p, q) periodic orbit.

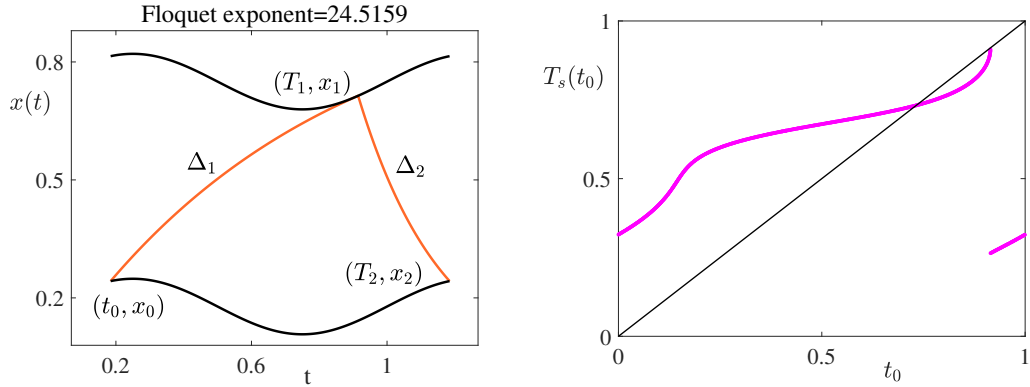


Figure 7.10: *Left panel: An example of Type I grazing (1,1) periodic solution where (t_0, x_0) is initial value, $\Delta_1(\Delta_2)$ duration of awake (sleep) episodes, (T_1, x_1) ((T_2, x_2)) are switching time and state on the upper (lower) threshold. The orbit tangentially intersect with the upper threshold and at the tangency point transition from wake state to sleep state occur. For $H_0^- = 0.178$ we find $a = 0.0706$, and calculated Floquet exponent = 24.5159 hence periodic orbit is unstable. Right panel: For the same parameter values we build the one dimensional map with gap. Unstable fixed point of the map coincides with the side of the gap where the derivative of map is infinite. Other parameters: $\tau_w = 0.75$, $\tau_s = 0.25$, $H_0^+ = 0.75$.*

7.4.5 Type II grazing bifurcation

The necessary conditions for a Type II grazing bifurcation at the upper (lower) threshold of a (p, q) periodic solution are: (i) a (p, q) periodic solution must

exist, and (ii) the homeostatic sleep pressure on wake (sleep) state must continuously passes through the tangency point without switching. Similar to the description in subsection 7.4.4, in order to determine Type II grazing bifurcations of a (p, q) periodic solution we simultaneously solve the equations needed to build the orbit and the equation that holds at tangency point.

To shed light on this method we show how to determine Type II grazing bifurcations of $(1, 1)$ periodic orbits. For an orbit starting from lower threshold, to achieve this we need to determine $(t_0, x_0, \Delta_1^t, x_1^t, \bar{\Delta}_1, x_1, x_2, a)$, by simultaneously solving

$$\begin{aligned}
x_0 &= H_0^- + a \sin(2\pi t_0); & x_1^t &= 1 - (1 - x_0)e^{-\Delta_1^t/\tau_w}, \\
x_1^t &= H_0^+ + a \sin(2\pi T_1^t); & (1 - x_1^t)/\tau_w &= 2a\pi \cos(2\pi T_1^t) \\
x_1 &= 1 - (1 - x_1^t)e^{-\bar{\Delta}_1/\tau_w}; & x_1 &= H_0^+ + a \sin(2\pi T_1) \\
x_2 &= x_1 e^{-\Delta_2/\tau_s}; & x_2 &= x_0,
\end{aligned} \tag{7.45}$$

where two additional equations to that of equation (7.10) are obtained from the tangency condition at (Δ_1^t, x_1^t) . In the left panel of Fig. 7.11 we depict a Type II grazing $(1, 1)$ periodic solution obtained by solving (7.45). In the right panel of Fig. 7.11, we illustrate the corresponding one dimensional map with gap where a stable fixed point of the map coincides with the side of the gap where the derivative of map is finite. Similarly, we can determine Type II grazing solutions of any (p, q) periodic orbit.

In the following subsection we extend the bifurcation set depicted in Fig. 7.9 by including tongue boundaries related to grazing bifurcations.

7.4.6 Extended bifurcation set

We have shown that for the two process model both saddle-node bifurcations and grazing bifurcations are related to creation and annihilation of periodic solutions. Now we will explain how the presence of gaps in the map (when a fixed point of the map coincides with one the side of the gap) augment the

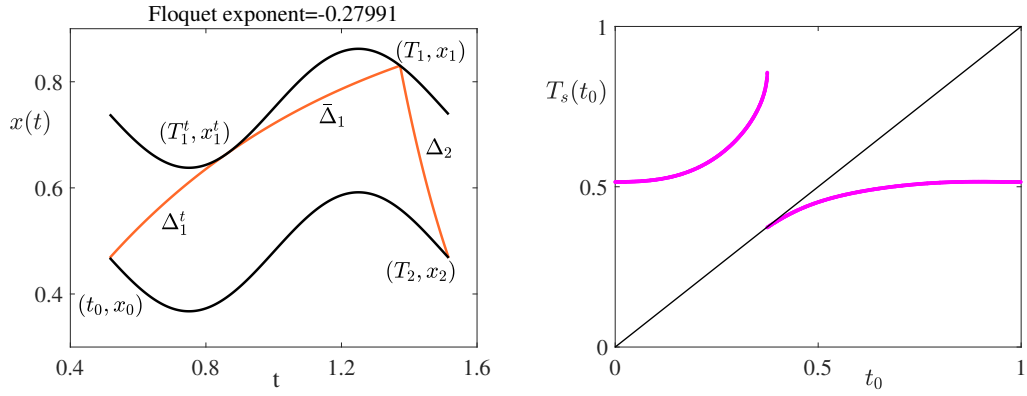


Figure 7.11: Left panel: An example of Type II grazing (1,1) periodic solution where (t_0, x_0) is the initial value, $\Delta_1^t, \bar{\Delta}_1(\Delta_2)$ duration of awake (sleep) episodes, (T_1, x_1) $((T_2, x_2))$ are switching time and state on the upper (lower) threshold. (T_1^t, x_1^t) is the tangency point on the upper threshold where the orbit passes through this point continuously without switching. For $H_0^- = 0.4809$ we find $a = 0.1121$, and calculated Floquet exponent = -0.27991 hence periodic orbit is stable. Right panel: For the same parameter values we build the one dimensional map with gap. Stable fixed point of the map coincides with the side of the gap where the derivative of map is finite. Other parameters: $\tau_w = 0.75$, $\tau_s = 0.25$, $H_0^+ = 0.75$.

saddle-node bifurcation diagram shown in Fig 7.9 and examine the effect that has on creation/annihilation of periodic solutions in each region.

In the (H_0^-, a) parameter space, we depict the curves associated with the saddle-node bifurcations and the two types of grazing bifurcations in Fig. 7.12. For small circadian amplitude, a , the one dimensional map is continuous (no grazing bifurcation is observed) and Arnol'd tongue borders of (p, q) periodic orbits are created by saddle-node bifurcations, where inside each tongue a stable and an unstable periodic solutions coexist. However, as the magnitude of a increases, gaps that lead to border collision in the map cease to exist and form a approximately *U-shaped* regions inside each tongue. The left-hand boundaries of these U-shaped regions are related to Type I grazing bifurcations and cannot intersect with saddle-node bifurcation curve (gradient of the maps cannot be equal). The right-hand sides of these U-shaped regions are associated with Type II grazing bifurcations. When the gradient of the map at the border collision point is one, Type II grazing bifurcations and saddle-node bifurcations coincide. At the intersection point, the right branch of a saddle-node bifurcation curve terminates and the rest of tongue border is built

by only Type II grazing bifurcations.

We observe that for the (1,1) and (2,1) tongues, Type I and Type II grazing bifurcations occur due to a tangency at the upper threshold only. However, for the (2,3) tongue Type I (Type II) grazing bifurcations occur due to a tangency at the lower (upper) threshold. To illustrate this we show an example of a (2,3) Type I (Type II) grazing periodic solution with a tangency at the lower (upper) threshold in left (right) panel Fig. 7.13. Note that LEs depicted in Fig. 7.6 shed light on the tongue borders. In Fig. 7.14, we plot extended bifurcation curves on the LEs diagram and, as expected, bifurcation curves sit in correspondence with the structure seen in LE diagrams.

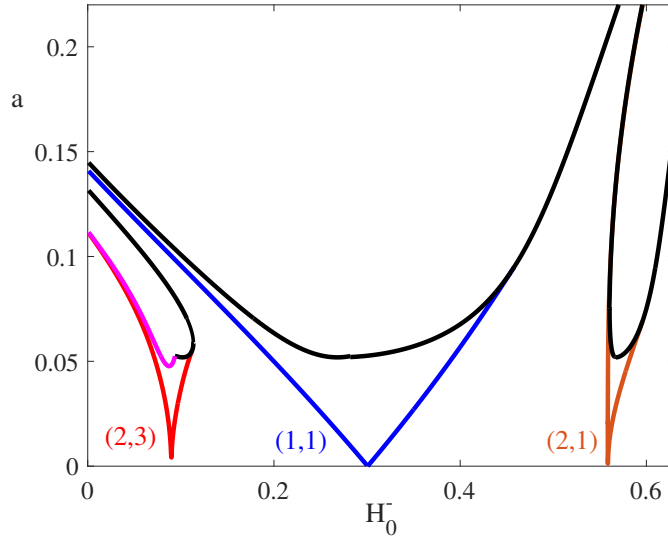


Figure 7.12: Shapes of the extended bifurcation curves in the (a, H_0^-) plane. Here we show the largest few tongues, namely (1,1), (2,1), and (2,3). Saddle-node bifurcation curves are same that of Fig. 7.9. Inside each tongue regime, Type I and Type II grazing bifurcations form a U-shaped region. Type I grazing bifurcations occur at the left boundary of U-shaped regime and Type II grazing bifurcations occur at the right boundary. Grazing bifurcations that occur due to a tangency on the upper threshold depicted in black and those emerged due to a tangency on the lower threshold shown in magenta. Parameters: $\tau_w = 0.75$, $\tau_s = 0.25$, and $H_0^+ = 0.75$.

To better explain the creation/annihilation of periodic solutions in each regime, in Fig. 7.15 we depict the (1,1) tongue by labelling regions inside and outside of the tongue boundaries. Inside the region (c) a stable and unstable periodic orbit coexist. While moving from region (c) to (b) and (c) to (e) along the solid blue curve, periodic orbits annihilated via a saddle-node bifurcation.

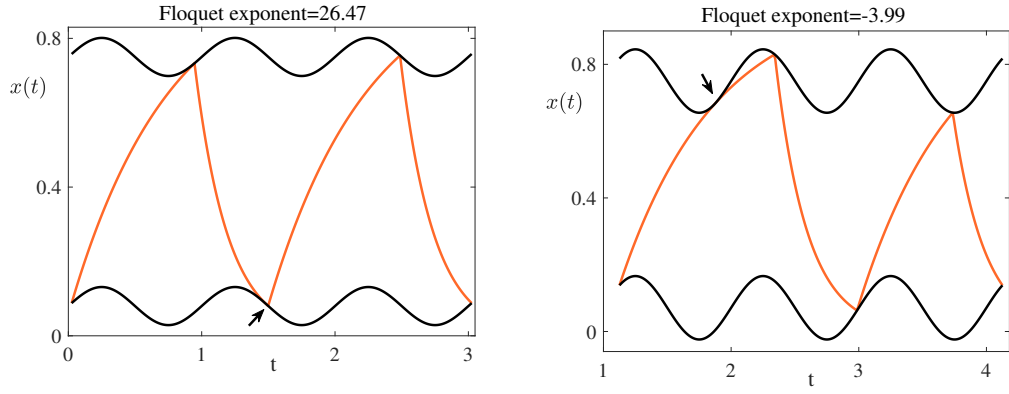


Figure 7.13: *Left panel: An example of Type I grazing (2,3) periodic solution. The orbit has a tangency point on the lower threshold indicated by the black arrow. As expected orbit is unstable with Floquet exponent= 26.471. For $H_0^- = 0.08$ we find $a = 0.0512$. Right panel: An example of Type II grazing (2,3) periodic solution. The orbit has a tangency point on the upper threshold indicated by the black arrow. For $H_0^- = 0.0703$ we find $a = 0.095$, and calculated Floquet exponent= -3.99 hence periodic orbit is stable. Other parameters: $\tau_w = 0.75$, $\tau_s = 0.25$, $H_0^+ = 0.75$.*

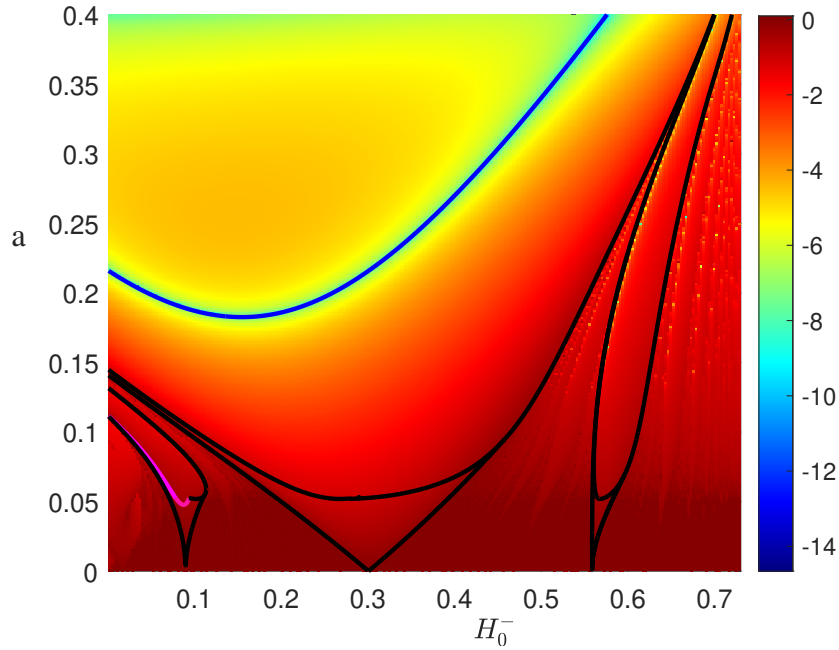


Figure 7.14: *We depict bifurcation curves that shown in Fig. 7.12 on the top of LEs diagram 7.6. Actual bifurcation curves and indication of LEs are well agreed. Here we exhibit only a few large tongues borders but the other small tongues also agree with what LEs diagram 7.6 indicates, to check this see Figure 8 in [18].*

An example of this case is shown in Fig. 7.4. While going from region (c) to (d) along the red dashed curve, Type II grazing bifurcations occur due to tangency with the upper threshold and unstable periodic solutions are lost. In the middle panel of Fig 7.16 we illustrate an unstable Type II grazing

periodic orbit, and the corresponding one dimensional map with gap. While entering from region (c) to (d) along the green dashed curve, Type I grazing bifurcations occur due to a tangency with the upper threshold and unstable periodic solutions are lost. In the lower panel of Fig 7.16 we show an unstable Type I grazing periodic orbit, and the corresponding one dimensional map with a gap. While moving from region (d) to (e) along the solid red curve, Type II grazing bifurcations occur as a result of a tangency with the upper threshold and stable periodic solutions are lost. In the top panel of Fig 7.16 we demonstrate a stable Type II grazing periodic orbit, and the corresponding one dimensional map with a gap. Hence, inside the region (d) only stable periodic orbits exist, and in regions (b) and (e) there is no $(1, 1)$ periodic solution. For a more detailed bifurcation analysis of the two process model using a map-based approach we refer the reader to [17, 18].

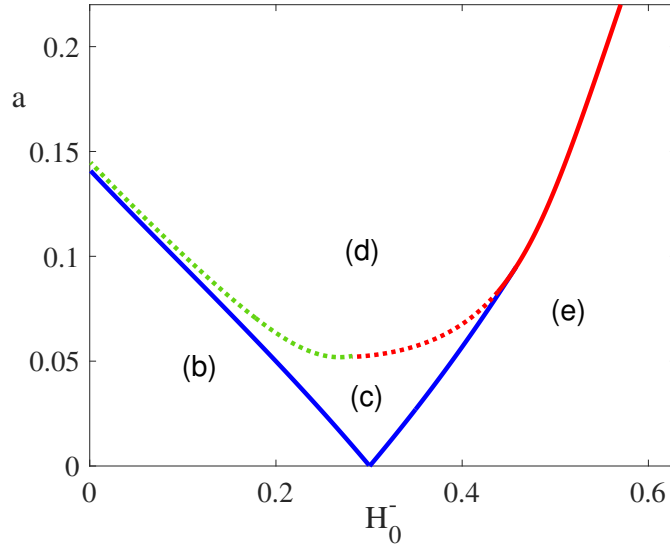


Figure 7.15: *Enlarged shape of the $(1, 1)$ tongue in the (a, H_0^-) plane where separate regions are labelled. Solid blue curve shows the saddle-node bifurcations. Dashed red (green) curve demonstrates Type II (Type I) grazing bifurcations due to tangency with the upper threshold where unstable periodic solutions are lost. Solid red curve depict Type II grazing bifurcations due to tangency with the upper threshold where stable periodic solutions are lost. Inside the region (c) the model support both stable and unstable periodic orbits however in (d) only stable solutions stand. The model does not have any $(1, 1)$ periodic solution in region (b) and (e). Other parameters: $\tau_w = 0.75$, $\tau_s = 0.25$, and $H_0^+ = 0.75$.*

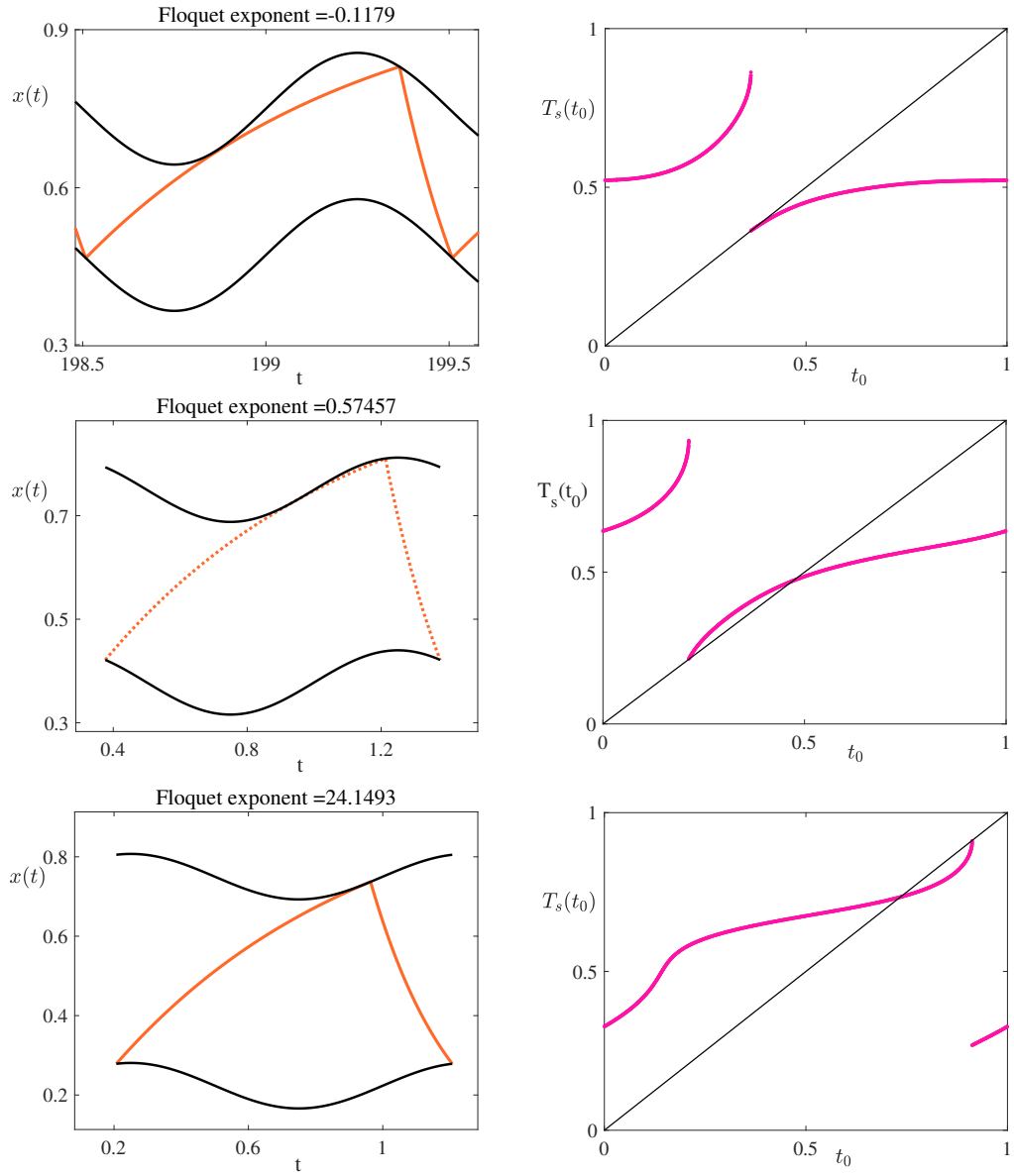


Figure 7.16: Examples of Type I and Type II grazing (1,1) periodic solutions and the corresponding one dimensional maps with gap. Top left: A Type II grazing stable periodic orbit that occurs on the solid red curve in Fig. 7.15. Top right: Corresponding map with gap where fixed point of the map coincides with the side of the gap where the derivative of the map is less than 1. Parameters: $a = 0.106$ and $H_0^- = 0.4724$. Middle left: A Type II grazing unstable periodic orbit that occurs on the dashed red curve in Fig. 7.15. Middle right: Corresponding map with gap where fixed point of the map coincides with the side of the gap where the derivative of the map is greater than 1 but finite. Parameters: $a = 0.06205$ and $H_0^- = 0.3779$. Bottom left: A Type I grazing unstable periodic orbit that occurs on the dashed green curve in Fig. 7.15. Bottom right: Corresponding map with gap where fixed point of the map coincides with the side of the gap where the derivative of the map is infinite. Parameters: $a = 0.05729$ and $H_0^- = 0.2235$. Other parameters: $\tau_w = 0.75$, $\tau_s = 0.25$, $H_0^+ = 0.75$

7.5 The two process model and co-sleeping

Sleep studies have a strong history but the vast majority of clinical articles and research reports have focused on sleep dynamics at the level of the individual [24, 190, 248, 294, 301]. Troxel [307] has stated that sleep is influenced by both complex biological mechanisms and social factors. Arber *et. al* [9] have reviewed links between individual's sleep and society by focusing on the concept from both macro and micro aspects. At the macro scale they have addressed how cultural norms and rules effect sleep timing and patterns. At the micro scale they reviewed impacts of social inequalities, gender relations, power dynamics, and life course positions on sleep quality and duration. Undoubtedly sleep is embedded in a family context and in the literature there are a number of studies that explore interrelations between parents' and children's sleep with a particular focus on gender role and chronotype, see for example [165, 314] and references therein.

In medieval times, people rarely slept alone. Bedrooms and beds were shared by married couples and their children even sometimes including servants and relatives [9]. In modern society, although bedrooms have become a more private space, still most adults share their bed with a partner [87, 250, 256]. There is some evidence that the individual sleeping behaviour of one partner influences the other's sleep [29, 293, 307, 338]. Therefore, exploring human sleep in the context of a dyad is an important topic. Drews *et. al* [87] have shown that the synchronisation of sleep stages is more effective when couples sleep together than when they sleep in separate rooms. Troxel [307] has investigated the effects of co-sleeping on the health of partners by introducing a conceptual model. Strawbridge *et. al* [293] have analysed relationships between partners' sleep problems and spouses' marital quality, social involvement, well-being, mental health, and physical health in a sample of 405 couples aged 51 to 94 years, and found association between these issues. Pankhurst *et. al* [223] have investigated how one bed partner's movements during sleep influence the other. Yoon *et. al* [338] have studied the synchronisation of heart rhythms

of bed partners during co-sleeping, by considering the mechanical interaction between individuals via vibration through the bed. Moreover, Rosenblatt [256] discussed this topic from various perspectives in his book “*Two in a bed: the social system of couple bed sharing*”.

Although several studies have been undertaken to investigate co-sleeping patterns [133, 203, 250], these are commonly based on observations and statistical analysis, and to the best of our knowledge there is no study to explore this via a network science approach. Here we aim to build a network of the two process model composed of heterogeneous male ($x_M(t)$) and female ($x_F(t)$) sleep dynamics each of which evolve according to equations (7.1) and (7.2) and with a suitable interaction. With in this mind we first compute LEs of the two process model in the (τ_w, τ_s) plane, see Fig. 7.17, planning to introduce heterogeneity by picking up different time scales for males and females. Since most

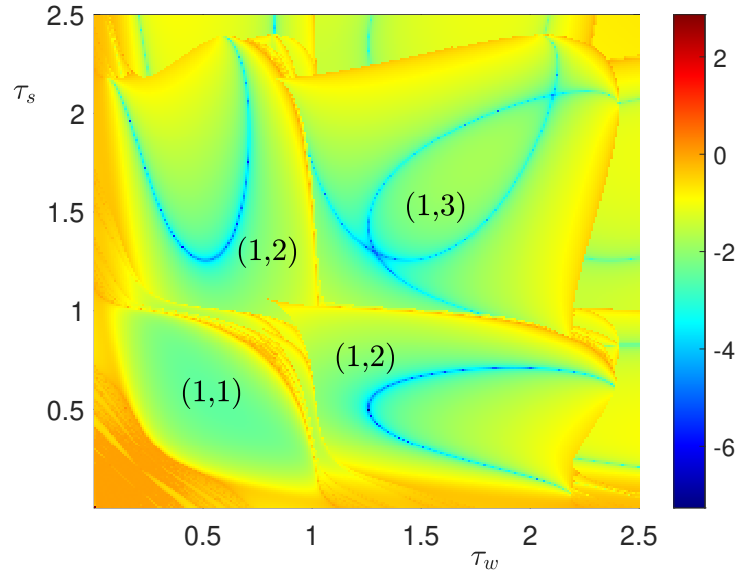


Figure 7.17: Lyapunov exponent diagram in the (τ_s, τ_w) plane. LEs shaded different tongue borders where (1,1), (1,2) and (1,3) tongues constitute the biggest regions. Parameters: $H_0^- = 0.2469$, $H_0^+ = 0.75$, $a = 0.09478$. Note that these are chosen from the (1,1) tongue of Fig. 7.14.

adults have a (1,1) sleep-wake cycle, we pick up male (τ_s^M, τ_w^M) and female (τ_s^F, τ_w^F) sleep-wake time scale parameters from inside the (1,1) tongue given in Fig. 7.17. We couple them through thresholds by introducing shifts [140] to the circadian processes timing mediated by a linear/PWL interaction function

of sleep homeostasis $x_M(t)$ and $x_F(t)$. We define the circadian processes of each individual as

$$H_M^\alpha(t) = H_{M_0}^\alpha + a \sin(2\pi\phi_M(t)), \quad (7.46)$$

$$H_F^\alpha(t) = H_{F_0}^\alpha + a \sin(2\pi\phi_F(t)), \quad (7.47)$$

where $\alpha \in \{+, -\}$ and

$$\dot{\phi}_M(t) = 1 + \sigma R_M(x_M(t), x_F(t)), \quad (7.48)$$

$$\dot{\phi}_F(t) = 1 + \sigma R_F(x_F(t), x_M(t)). \quad (7.49)$$

Here H_M^α and H_F^α denote the circadian thresholds of male and female, respectively, and, $H_{M_0}^\alpha$ and $H_{F_0}^\alpha$ are their mean values. Coupling functions are denoted by R_β , $\beta \in \{M, F\}$, and the parameter σ represents the coupling strength. Circadian shifts are governed by the evolution of ϕ_β . For concreteness, we choose $R_\beta(x, y) = y - x$ and $R_\beta(x, y) = \Theta(y - x)$ (Θ is the Heaviside step function), and observe $(1, 1)$ locked or synchronised patterns where initially each individual has their own $(1, 1)$ sleep-wake cycles. An example of this is illustrated in Fig. 7.18. In that case, as time evolves, the circadian processes approach each other, and the couple starts to sleep almost at the same time though the male wakes up slightly later. We also coupled them through a diffusive linear/PWL interaction of $x_M(t)$ and $x_F(t)$ as follows:

$$\dot{x}_M(t) = f_M(x_M(t)) + \sigma R_M(x_M(t), x_F(t)), \quad (7.50)$$

$$\dot{x}_F(t) = f_F(x_F(t)) + \sigma R_F(x_F(t), x_M(t)), \quad (7.51)$$

whilst keeping the circadian process evolution (given by equation (7.3) and (7.4)) identical for each individual. Here the intrinsic sleep dynamics (given by equation (7.1) and (7.2)) of the male and female are governed by $f_M(x_M(t))$ and $f_F(x_F(t))$, respectively. Again depending on the coupling strength we

detect (numerically) $(1, 1)$ locked or synchronised patterns. We plan to extend this initial pilot study in future work.

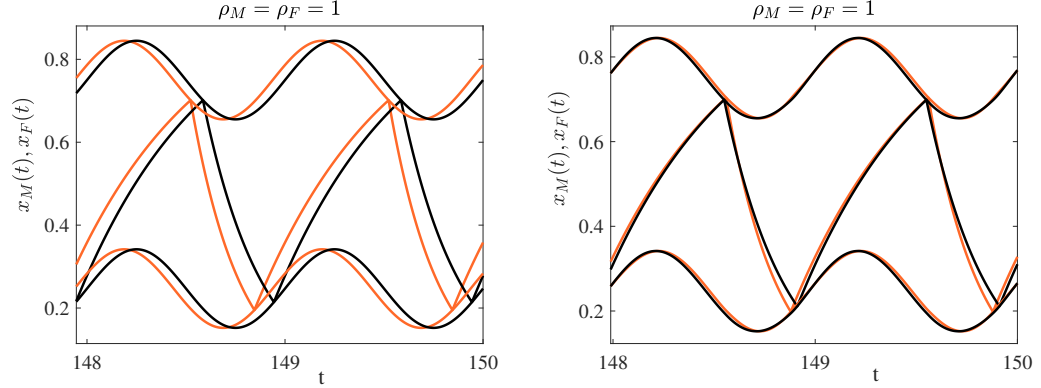


Figure 7.18: A network simulation of the two process model. We coupled them through thresholds by introducing shifts to the circadian processes timing mediated by a linear interaction function of $x_\beta(t)$, $\beta \in \{M, F\}$. Left panel: Coupling strength is $\sigma = 0$. Male and female have their own sleep-wake cycle with rotation number $\rho_\beta = 1$. Right panel: As we increased coupling strength to $\sigma = 2.32$, after sharing the same bed for an amount of time, circadian processes approach to each other. We also observe that couple almost sleep together but male waking up slightly later. Again both have same rotation number $\rho_\beta = 1$. Male (female) thresholds and solution are given in black (light brown). Parameters: $\tau_s^M = 0.3021, \tau_w^M = 0.6634, \tau_s^F = 0.2519, \tau_w^F = 0.6835, \phi_M(0) = 0.06255, \phi_F(0) = 0, a = 0.09478, H_{\beta_0}^- = 0.2469$ and $H_{\beta_0}^+ = 0.75$.

7.6 Discussion

Sleep is fundamental for the maintenance of mental health, body functioning and cognitive performance, but many aspects of the sleep-wake mechanism still need further investigation and mathematical modelling has a significant role to play [250, 286]. The utilisation of mathematical models in sleep studies has a strong history and early models of sleep-wake regulation have been reviewed by Moore-Ede *et. al* [208]. Almost four decades ago, Borbely [32], and Daan *et. al* [62] proposed the two process model which was then extended in [31] by exploiting experimental data. This seminal work had a big impact on sleep studies and is still a popular model in the field of sleep research. Particularly, the model has been used to analyse and conceptualise the major two processes (circadian and homeostatic) underlying sleep-wake regulation, and their nonlinear interactions. Moreover, in a wide range of experimental

protocols the model replicates the intensity and timing of sleep [33]. The physiological basis/relevance of the model and comparison with other models have been discussed in [30, 237] and reference therein.

Recently, Bailey *et. al* [18] readdressed the two process model by formally defining associated one dimensional maps. They explored the shape of Arnol'd tongues by utilising properties of one dimensional maps of the circle and maps with gaps. Here we reviewed and extended their result by using an analytical modelling approach in the context of PWL systems. We constructed periodic orbits semi analytically as in Section 3.3, and assessed the stability of such solutions with a modification of Floquet theory to treat systems with time-dependent switches. Around the periodic solutions, we also performed a linear stability analysis of the maps of switching event times to compare both approaches. We formulated computation of Lyapunov exponents for the model by implementing techniques built for nonsmooth dynamical systems. The LE diagrams gave an indication about Arnol'd tongue structure and parameter regions where the model supports superstable periodic solutions. Utilising these observations we performed a detailed bifurcation analysis where both saddle-node bifurcation of periodic orbits and grazing bifurcations arose.

In most societies, the majority of adults share their bed with a partner. Although there is a lot of medical and psychological studies on sleep and sleep related problems, in most cases sleep is considered at the level of the individual [250], hence the topic of co-sleeping still needs investigation. With this motivation we discussed a conceptual network of the two process model at an simple phenomenological level. We numerically observed that when the coupling strength between partners (with heterogeneous sleep dynamics) increased, their sleep patterns approached each other. In a sociological context, Meadows *et. al* [202] propose that at the start of relationship couples have their personal *sleep habitus* (sleep latency, timing of going to bed, dark/light ratio etc.) and clashes emerge when these do not match over time. Thus understanding networks of the two process model may help to predict/solve such conflicts.

Chapter 8

Summary and future perspectives

In this thesis, I explored the dynamics of nonsmooth oscillatory systems at both nodal and network levels. The intrinsic dynamics of nonsmooth models can be complex and this complexity scales up when we couple them to build networks. Emergent network patterns depend both on nodal dynamics and the form of coupling mediating interactions. Thus having a good understanding of nodal unit dynamics is necessary to uncover dynamics at the network level. As an emergent network behaviour, we focused on synchronisation and investigated the utilisation of various mathematical frameworks including weak coupling theory, a recent phase-amplitude network formalism, and the MSF methodology for networks of piecewise linear models. Depending upon the (dis)continuous changes in vector fields or trajectories of nodal components and their (dis)continuous interactions at *switches* we confronted different scenarios to determine the stability of periodic orbits and bifurcations of the synchronous network state.

In Chapter 1, I presented the main motivation and a brief overview of the thesis. In Chapter 2, I provided some background information by introducing relevant terminology and reviewing the existing literature for smooth dynamical systems that was adapted and applied to nonsmooth ones in later

chapters. In the final part of that chapter, I studied the MSF methodology for nonlinear smooth systems and illustrated the concept by exploring bifurcations of a (linearly coupled) network of Stuart-Landau oscillators. In Chapter 3, I briefly introduced nonsmooth dynamical systems and presented a natural classification of them according to their degree of nonsmoothness. I then showed how to build periodic solutions of planar PWL systems semi-analytically by using matrix exponentials. I revisited the McKean model (a well known PWL approximation to the FHN model) and showed that the model supports a fold limit cycle bifurcation where a stable periodic orbit coincides with an unstable sliding orbit. I also studied the absolute model that exhibits a nonsmooth Andronov-Hopf bifurcation, as well as a homoclinic loop model. Afterwards I reviewed the PML model that display periodic orbits with four distinct pieces lying over three linear regimes. I concluded that chapter by discussing the practicalities and wide use of PWL modelling in various branches of the applied sciences.

I began Chapter 4 by modifying standard Floquet theory to study the linear stability of periodic solutions for PWL systems by making use of a saltation operator. I then considered nonsmooth terms for the second-order accurate phase-amplitude reduction of limit cycle oscillators solving the relevant PWL adjoint equations. I showed that this method may become discontinuous during a boundary crossing, and explained how to derive relevant jump conditions. Additionally, I reviewed the MSF methodology for PWL systems and explored the inclusion of saltation operators into the master variational equation. Next I addressed diffusively coupled networks of McKean, absolute, homoclinic loop, and PML nodes. I compared the accuracy of the above mentioned methods by measuring the effect of variation in coupling strength to detect network bifurcations. I determined that the popular weak coupling theory does not give accurate result about the stability of network states. Although the phase-amplitude network formalism gives improved results in some cases it detected bifurcation points inaccurately. However, the MSF approach gives exact bifur-

cation points in excellent agreement with direct numerical simulations. Thus, the MSF approach was adopted in the next two chapters for studying other PWL network models.

The shuttling mechanism of a conductive particle between two metal charged plates has been studied at both microscopic and macroscopic scales [13, 84, 145, 162], as exemplified by Franklin’s bell. This was the topic of Chapter 5. The original Franklin bell is an electro-mechanical oscillator that can generate a repeating chime in the presence of an electric field, and Benjamin Franklin famously used it as a lightning detector. I first investigated a single Franklin bell, showing how to construct periodic orbits and how to determine their linear stability and bifurcation. To cope with the nonsmooth nature of the impacts I used saltation operators to develop the correct Floquet theory. We further introduced a new smoothing technique that circumvents the need for saltation and that recovers the saltation operators in some appropriate limit. The proposed smoothing technique originated from the question that, instead of imposing direct instantaneous impact conditions at the discontinuity surfaces, for any given arbitrary time-of-flight, is it possible to imitate (in a smooth fashion) this sudden change with an impact-like motion by introducing some new supplementary (virtual) PWL dynamics outside of the rigid constraints. This idea is quite consistent with the soft impact modelling approach where an impacting base is cushioned with a spring-damper [27, 142, 143, 274]. Next, I considered the dynamics of a network of Franklin bells, using the augmented MSF approach. I also used this to determine conditions for network induced instabilities. In this case, I found working with the MSF approach particularly useful as compared with time-dependent Lyapunov functions, inequality techniques, and comparison principles, which were studied in [189, 318, 343]. This is because impacting moments of the model are prescribed by the state of the system and this prevents direct utilisation of standard time-dependent Lyapunov function approach. Baumann *et. al* [21] modified this method to treat state-dependent impact oscillators and constructed a state-dependent

Lyapunov function to explore synchronisation properties of networks of only two oscillators.

In Chapter 6, I considered the famous Wilson-Cowan neural mass model that describes large scale brain dynamics by replacing the classic sigmoidal nonlinearity with a continuous piecewise linear firing rate function. Using techniques from previous chapters, I used the network eigenvectors to predict the onset of spatio-temporal network patterns arising from a synchronous instability. I further considered the case of a discontinuous choice for the node nonlinearity, namely the replacement of the sigmoid by a Heaviside nonlinearity. At the node level this allows for the existence of an unstable sliding periodic orbit, which I explicitly constructed. At the network level the stability analysis of the synchronous state was considerably more challenging than for the continuous PWL case. Here I reported on the use of ideas originally developed for the study of Glass networks to treat the stability of periodic network states in neural mass models with discontinuous interactions.

A possible extension of the work presented in Chapter 6 can be done by adding state and time dependent delays to the model to investigate large-scale spatio-temporal patterns of brain activity. Also constant external inputs in the model can be replaced by time dependent functions. From the biological point of view the presence of delay terms is necessary for various reasons including the finite propagation speed of action potentials along axons, and the transduction between electrical and biochemical signals at synapses [20, 70]. The MSF methodology has been applied to networks of smooth systems with homogeneous delay [48], distributed time delays [172], heterogeneous delay [222], and these can be extended to PWL models. Moreover, the recent MSF formalism for the multilayer networks with smooth nodal elements [71] can be generalised to nonsmooth ones.

Finally, in Chapter 7, I considered the two process sleep model in the context of nonsmooth dynamical system, and studied the construction and stability of periodic solution. I then derived a formula for Lyapunov expo-

nents and built Arnol'd tongue boundaries. I performed a bifurcation analysis based on the nonsmooth Floquet theory, and compared results with that of a map-based approach [18]. Afterwards, I addressed the influences of social interactions on human sleep dynamics with a particular focus on partners sharing the same bed. I also numerically studied dynamics of a simple phenomenological network model. Individuals can be categorised as short/long sleepers and early/late risers [126], and social factors have effects on individual's sleep [9] and one partner could be dominant. For future work, I will continue to explore sleep in a dyad framework by picking two co-habiting people (A,B). I will model their interaction by considering that if A goes to bed early s/he puts pressure on B to join her/him immediately. On weekday mornings they might both awake at the same time (alarm clock driven), whilst at weekends they have no constraints. Moreover, investigating sleep synchronisation of N coupled individuals where coupling is described by physical or virtual interactions including sharing same environment, mobile connection, social media communication or TV broadcast, is another topic of interest.

Bibliography

- [1] L. F. Abbott and T. B. Kepler. Model neurons: from Hodgkin-Huxley to hopfield. In *Statistical mechanics of neural networks*, pages 5–18. Springer, 1990.
- [2] J. A. Acebrón, L. L. Bonilla, C. J. P. Vicente, F. Ritort, and R. Spigler. The kuramoto model: A simple paradigm for synchronization phenomena. *Reviews of modern physics*, 77(1):137, 2005.
- [3] A. Afsharfard. Application of nonlinear magnetic vibro-impact vibration suppressor and energy harvester. *Mechanical Systems and Signal Processing*, 98:371–381, 2018.
- [4] S. Ahmadizadeh, D. Nesic, D. B. Grayden, and D. R. Freestone. Analytic synchronization conditions for a network of Wilson and Cowan oscillators. *IEEE 54th Annual Conference on Decision and Control*, 2015.
- [5] K. Aihara and H. Suzuki. Theory of hybrid dynamical systems and its applications to biological and medical systems. *Philosophical Transactions of the Royal Society A*, 368:4893–4914, 2010.
- [6] S.-i. Amari. Heaviside world: excitation and self-organization of neural fields. In *Neural fields*, pages 97–118. Springer, 2014.
- [7] A. A. Andronov, A. A. Vitt, and S. E. Khaikin. *Theory of Oscillators: Adiwes International Series in Physics*, volume 4. Elsevier, 2013.
- [8] T. Aoyagi. Network of neural oscillators for retrieving phase information. *Physical review letters*, 74(20):4075, 1995.
- [9] S. Arber, R. Meadows, and S. Venn. Sleep and society. In *The Oxford handbook of sleep and sleep disorders*, pages 223–247. Oxford University Press Oxford, 2012.
- [10] A. Arenas, A. Díaz-Guilera, J. Kurths, Y. Moreno, and C. Zhou. Synchronization in complex networks. *Physics Reports*, 469:93–153, 2008.
- [11] J. T. Ariaratnam and S. H. Strogatz. Phase diagram for the winfree model of coupled nonlinear oscillators. *Physical Review Letters*, 86:4278–4281, 2001.
- [12] V. I. Arnold. Cardiac arrhythmias and circle mappings. *Chaos: An Interdisciplinary Journal of Nonlinear Science*, 1(1):20–24, 1991.

- [13] K. Asano. On the theory of an electrostatic pendulum oscillator. *American Journal of Physics*, 43:423–427, 1975.
- [14] P. Ashwin and J. W. Swift. The dynamics of n weakly coupled identical oscillators. *Journal of Nonlinear Science*, 2(1):69–108, 1992.
- [15] P. Ashwin, S. Coombes, and R. Nicks. Mathematical frameworks for oscillatory network dynamics in neuroscience. *The Journal of Mathematical Neuroscience*, 6(1):2, 2016.
- [16] V. Avrutin and M. R. Jeffrey. Remarks on bifurcations of hidden orbits in discontinuous maps. 2020.
- [17] M. P. Bailey. *Modelling sleep-wake regulation: the dynamics, bifurcations and applications of the two process model*. PhD thesis, University of Surrey, 2020.
- [18] M. P. Bailey, G. Derks, and A. C. Skeldon. Circle maps with gaps: Understanding the dynamics of the two-process model for sleep–wake regulation. *European Journal of Applied Mathematics*, 29(5):845–868, 2018.
- [19] A. Balanov, N. Janson, D. Postnov, and O. Sosnovtseva. *Synchronization: from simple to complex*. Springer Science & Business Media, 2008.
- [20] P. Baldi and A. F. Atiya. How delays affect neural dynamics and learning. *IEEE Transactions on Neural Networks*, 5(4):612–621, 1994.
- [21] M. Baumann, J. J. B. Biemond, R. I. Leine, and L. N. Wouw. Synchronization of impacting mechanical systems with a single constraint. *Physica D: Nonlinear Phenomena*, 362:9–23, 2018.
- [22] G. Benettin, L. Galgani, A. Giorgilli, and J.-M. Strelcyn. Lyapunov characteristic exponents for smooth dynamical systems and for hamiltonian systems; a method for computing all of them. part 1: Theory. *Meccanica*, 15(1):9–20, 1980.
- [23] A. Bergner, M. Frasca, G. Sciuto, A. Buscarino, E. J. Ngamga, L. Fortuna, and J. Kurths. Remote synchronization in star networks. *Physical Review E*, 85(2):026208, 2012.
- [24] L. Besedovsky, T. Lange, and J. Born. Sleep and immune function. *Pflügers Archiv-European Journal of Physiology*, 463(1):121–137, 2012.
- [25] S. R. Bishop. Impact oscillators. *Philosophical Transactions: Physical Sciences and Engineering*, 347:341–351, 1994.
- [26] F. Bizzarri, D. Linaro, and M. Storace. Pwl approximation of the Hindmarsh-Rose neuron model in view of its circuit implementation. In *2007 18th European Conference on Circuit Theory and Design*, pages 878–881. IEEE, 2007.

- [27] B. Blazejczyk-Okolewska, K. Czołczynski, and K. Kapitaniak. Hard versus soft impacts in oscillatory systems modeling. *Communications in Nonlinear Science and Numerical Simulation*, 15:1358–1367, 2010.
- [28] I. I. Blekhman. *Synchronization in science and technology*. ASME press, 1988.
- [29] M. B. Blumen, M. A. Q. Salva, I. Vaugier, K. Leroux, M.-P. d’Ortho, F. Barbot, F. Chabolle, and F. Lofaso. Is snoring intensity responsible for the sleep partner’s poor quality of sleep? *Sleep and Breathing*, 16(3):903–907, 2012.
- [30] V. Booth and C. G. D. Behn. Physiologically-based modeling of sleep–wake regulatory networks. *Mathematical biosciences*, 250:54–68, 2014.
- [31] A. A. Borb and P. Achermann. Sleep homeostasis and models of sleep regulation. *Journal of biological rhythms*, 14(6):559–570, 1999.
- [32] A. A. Borbély. A two process model of sleep regulation. *Hum neurobiol*, 1(3):195–204, 1982.
- [33] A. A. Borbély, S. Daan, A. Wirz-Justice, and T. Deboer. The two-process model of sleep regulation: a reappraisal. *Journal of sleep research*, 25(2):131–143, 2016.
- [34] M. Breakspear. Dynamic models of large-scale brain activity. *Nature Neuroscience*, 20:340–352, 2017.
- [35] B. Brogliato. *Nonsmooth mechanics*. Springer, 1999.
- [36] B. Brogliato. *Impacts in mechanical systems: analysis and modelling*, volume 551. Springer Science & Business Media, 2000.
- [37] E. Brown, P. Holmes, and J. Moehlis. Globally coupled oscillator networks. In *Perspectives and Problems in Nonlinear Science*, pages 183–215. Springer, 2003.
- [38] C. Budd. Grazing in impact oscillators. In *Real and complex dynamical systems*, pages 47–63. Springer, 1995.
- [39] S. Campbell and D. Wang. Synchronization and desynchronization in a network of locally coupled Wilson-Cowan oscillators. *IEEE Transactions on Neural Networks*, 7:541–554, 1996.
- [40] V. Carmona, S. Fernández-García, E. Freire, and F. Torres. Melnikov theory for a class of planar hybrid systems. *Physica D: Nonlinear Phenomena*, 248:44–54, 2013.
- [41] T. W. Carr, M. L. Taylor, and I. B. Schwartz. Negative-coupling resonances in pump-coupled lasers. *Physica D: Nonlinear Phenomena*, 213(2):152–163, 2006.

- [42] R. Casey, H. De Jong, and J.-L. Gouzé. Piecewise-linear models of genetic regulatory networks: equilibria and their stability. *Journal of mathematical biology*, 52(1):27–56, 2006.
- [43] O. Castejón, A. Guillamon, and G. Huguet. Phase-amplitude response functions for transient-state stimuli. *The Journal of Mathematical Neuroscience*, 3(1):13, 2013.
- [44] A. J. Catllá, D. G. Schaeffer, T. P. Witelski, E. E. Monson, and A. L. Lin. On spiking models for synaptic activity and impulsive differential equations. *SIAM Review*, 50:553–569, 2008.
- [45] J.-P. Chaput and C. Dutil. Lack of sleep as a contributor to obesity in adolescents: impacts on eating and activity behaviors. *International Journal of Behavioral Nutrition and Physical Activity*, 13(1):1–9, 2016.
- [46] T. Chartrand, M. S. Goldman, and T. J. Lewis. Synchronization of electrically coupled resonate-and-fire neurons. *SIAM Journal on Applied Dynamical Systems*, 18(3):1643–1693, 2019.
- [47] H. Chen, D. Li, J. Xie, and Y. Yue. Limit cycles in planar continuous piecewise linear systems. *Communications in Nonlinear Science and Numerical Simulation*, 47:438–454, 2017.
- [48] C.-U. Choe, T. Dahms, P. Hövel, and E. Schöll. Controlling synchrony by delay coupling in networks: from in-phase to splay and cluster states. *Physical Review E*, 81(2):025205, 2010.
- [49] L. O. Chua and S. M. Kang. Section-wise piecewise-linear functions: Canonical representation, properties, and applications. *Proceedings of the IEEE*, 65(6):915–929, 1977.
- [50] J. R. Clay and A. Shrier. On the role of subthreshold dynamics in neuronal signaling. *Journal of theoretical biology*, 197(2):207–216, 1999.
- [51] A. Colombo, M. di Bernardo, S. J. Hogan, and M. R. Jeffrey. Bifurcations of piecewise smooth flows: Perspectives, methodologies and open problems. *Physica D: Nonlinear Phenomena*, 241(22):1845–1860, 2012.
- [52] S. Coombes. Neuronal networks with gap junctions: A study of piecewise linear planar neuron models. *SIAM Journal on Applied Dynamical Systems*, 7(3):1101–1129, 2008.
- [53] S. Coombes and A. H. Osbaldestin. Period-adding bifurcations and chaos in a periodically stimulated excitable neural relaxation oscillator. *Physical Review E*, 62(3):4057, 2000.
- [54] S. Coombes and R. Thul. Synchrony in networks of coupled non-smooth dynamical systems: Extending the master stability function. *European Journal of Applied Mathematics*, 27:904–922, 2016.
- [55] S. Coombes, R. Thul, and K. C. A. Wedgwood. Nonsmooth dynamics in spiking neuron models. *Physica D: Nonlinear Phenomena*, 241(22):2042–2057, 2012.

- [56] S. Coombes, P. beim Graben, R. Potthast, and J. Wright, editors. *Neural Fields: Theory and Applications*. Springer, 2014.
- [57] S. Coombes, Y. M. Lai, M. Şayli, and R. Thul. Networks of piecewise linear neural mass models. *European Journal of Applied Mathematics*, 29(5):869–890, 2018.
- [58] M. Coraggio, P. De Lellis, and M. di Bernardo. Convergence and synchronization in networks of piecewise-smooth systems via distributed discontinuous coupling. *Automatica*, 129:109596, 2021.
- [59] J. D. Cowan. History of concepts and techniques. *Intelligent Systems*, 3:375–400, 2004.
- [60] J. D. Cowan, J. Neuman, and W. van Drongelen. Wilson-Cowan equations for neocortical dynamics. *The Journal of Mathematical Neuroscience*, 6(1), 2016.
- [61] R. Cross. The bounce of a ball. *American Journal of Physics*, 67:222–227, 1999.
- [62] S. Daan, D. G. Beersma, and A. A. Borbély. Timing of human sleep: recovery process gated by a circadian pacemaker. *American Journal of Physiology-Regulatory, Integrative and Comparative Physiology*, 246(2):R161–R183, 1984.
- [63] A. Dabrowski. The largest transversal Lyapunov exponent and master stability function from the perturbation vector and its derivative dot product (TLEVDP). *Nonlinear Dynamics*, 69(3):1225–1235, 2012.
- [64] T. Dahms, J. Lehnert, and E. Schöll. Cluster and group synchronization in delay-coupled networks. *Physical Review E*, 86(1):016202, 2012.
- [65] O. David and K. J. Friston. A neural mass model for MEG/EEG:: coupling and neuronal dynamics. *NeuroImage*, 20(3):1743–1755, 2003.
- [66] H. De Jong, J.-L. Gouzé, C. Hernandez, M. Page, T. Sari, and J. Geiselman. Qualitative simulation of genetic regulatory networks using piecewise-linear models. *Bulletin of mathematical biology*, 66(2):301–340, 2004.
- [67] G. F. de S. Reboucas, I. Santos, and J. J. Thomsen. Unilateral vibro-impact systems-experimental observations against theoretical predictions based on the coefficient of restitution. *Journal of Sound and Vibration*, 440:346–371, 2019.
- [68] S. L. T. De Souza and I. L. Caldas. Calculation of Lyapunov exponents in systems with impacts. *Chaos, Solitons & Fractals*, 19(3):569–579, 2004.
- [69] G. Deco, V. K. Jirsa, P. A. Robinson, M. Breakspear, and K. Friston. The dynamic brain: from spiking neurons to neural masses and cortical fields. *PLoS Comput Biol*, 4(8):e1000092, 2008.

- [70] G. Deco, V. Jirsa, A. R. McIntosh, O. Sporns, and R. Kötter. Key role of coupling, delay, and noise in resting brain fluctuations. *Proceedings of the National Academy of Sciences*, 106(25):10302–10307, 2009.
- [71] F. Della Rossa, L. Pecora, K. Blaha, A. Shirin, I. Klickstein, and F. Sorrentino. Symmetries and cluster synchronization in multilayer networks. *Nature communications*, 11(1):1–17, 2020.
- [72] S. Denève and C. K. Machens. Efficient codes and balanced networks. *Nature neuroscience*, 19(3):375–382, 2016.
- [73] F. Dercole, A. Gragnani, and S. Rinaldi. Bifurcation analysis of piecewise smooth ecological models. *Theoretical Population Biology*, 72(2):197–213, 2007.
- [74] G. Derks, P. A. Glendinning, and A. C. Skeldon. Creation of discontinuities in circle maps. *Proceedings of the Royal Society A*, 477(2251):20200872, 2021.
- [75] M. Desroches and M. R. Jeffrey. Canards and curvature: nonsmooth approximation by pinching. *Nonlinearity*, 24(5):1655, 2011.
- [76] M. Desroches and M. R. Jeffrey. Canards and curvature: the ‘smallness of ϵ ’ in slow-fast dynamics. *Proceedings of the Royal Society A: Mathematical, Physical and Engineering Sciences*, 467(2132):2404–2421, 2011.
- [77] A. Destexhe and T. J. Sejnowski. The Wilson–Cowan model, 36 years later. *Biological Cybernetics*, 101:1–2, 2009.
- [78] M. di Bernardo and S. J. Hogan. Discontinuity-induced bifurcations of piecewise smooth dynamical systems. *Philosophical Transactions of the Royal Society A: Mathematical, Physical and Engineering Sciences*, 368(1930):4915–4935, 2010.
- [79] M. di Bernardo, M. I. Feigin, S. J. Hogan, and M. E. Homer. Local analysis of C-bifurcations in n-dimensional piecewise-smooth dynamical systems. *Chaos, Solitons and Fractals: the interdisciplinary journal of Nonlinear Science, and Nonequilibrium and Complex Phenomena*, 11(10):1881–1908, 1999.
- [80] M. di Bernardo, C. J. Budd, and A. R. Champneys. Grazing and border-collision in piecewise-smooth systems: A unified analytical framework. *Physical Review Letters*, 86:2553–2556, 2001.
- [81] M. di Bernardo, C. Budd, A. R. Champneys, and P. Kowalczyk. *Piecewise-smooth dynamical systems: theory and applications*, volume 163. Springer Science & Business Media, 2008.
- [82] M. di Bernardo, C. J. Budd, A. R. Champneys, P. Kowalczyk, A. B. Nordmark, G. O. Tost, and P. T. Piiroinen. Bifurcations in nonsmooth dynamical systems. *SIAM review*, 50(4):629–701, 2008.

- [83] L. Dieci, R. D. Russell, and E. S. Van Vleck. On the computation of Lyapunov exponents for continuous dynamical systems. *SIAM journal on numerical analysis*, 34(1):402–423, 1997.
- [84] K. P. Disna Jayampathi Karunanayake and Y. Hoshino. Electrostatic force acting on conductive ball between electrodes. *Journal of Electrostatics*, 685:91–95, 2010.
- [85] I. Dobson. Stability of ideal thyristor and diode switching circuits. *IEEE Transactions on Circuits and Systems I: Fundamental Theory and Applications*, 42(9):517–529, 1995.
- [86] F. Dörfler and F. Bullo. Synchronization in complex networks of phase oscillators: A survey. *Automatica*, 50(6):1539–1564, 2014.
- [87] H. J. Drews, S. Wallot, S. L. Weinhold, P. Mitkidis, P. C. Baier, A. Roepstorff, and R. Göder. “Are we in sync with each other?” Exploring the effects of cosleeping on heterosexual couples’ sleep using simultaneous polysomnography: A pilot study. *Sleep disorders*, 2017.
- [88] F. Dumortier, J. Llibre, and J. C. Artés. *Qualitative theory of planar differential systems*. Springer, 2006.
- [89] R. Edwards. Analysis of continuous-time switching networks. *Physica D*, 146:165–199, 2000.
- [90] R. Edwards and L. Glass. Combinatorial explosion in model gene networks. *Chaos*, 10:691–704, 2000.
- [91] B. Ermentrout. *Simulating, analyzing, and animating dynamical systems: A guide to XPPAUT for researchers and students*. SIAM, 2002.
- [92] B. Ermentrout, Y. Park, and D. Wilson. Recent advances in coupled oscillator theory. *Philosophical Transactions of the Royal Society A*, 377 (2160):20190092, 2019.
- [93] G. B. Ermentrout. The behavior of rings of coupled oscillators. *Journal of mathematical biology*, 23(1):55–74, 1985.
- [94] G. B. Ermentrout and N. Kopell. Frequency plateaus in a chain of weakly coupled oscillators, I. *SIAM journal on Mathematical Analysis*, 15(2): 215–237, 1984.
- [95] G. B. Ermentrout and N. Kopell. Multiple pulse interactions and averaging in systems of coupled neural oscillators. *Journal of Mathematical Biology*, 29(3):195–217, 1991.
- [96] G. B. Ermentrout and D. H. Terman. *Mathematical foundations of neuroscience*, volume 35. Springer Science & Business Media, 2010.
- [97] R. Euzébio, R. Pazim, and E. Ponce. Jump bifurcations in some degenerate planar piecewise linear differential systems with three zones. *Physica D: Nonlinear Phenomena*, 325:74–85, 2016.

- [98] E. D. Fagerholm, R. J. Moran, I. R. Violante, R. Leech, and K. J. Friston. Dynamic causal modelling of phase-amplitude interactions. *Neuroimage*, 208:116452, 2020.
- [99] M. I. Feigin. Forced oscillations in systems with discontinuous nonlinearities. *Science*, page 285, 1994.
- [100] A. F. Filippov. *Differential equations with discontinuous righthand sides*, volume 18. Springer Netherlands, 1988.
- [101] R. FitzHugh. Impulses and physiological states in theoretical models of nerve membrane. *Biophysical journal*, 1(6):445, 1961.
- [102] S. Folkard and T. Åkerstedt. A three-process model of the regulation of alertness-sleepiness. *Sleep, arousal and performance*, pages 11–26, 1992.
- [103] B. Franklin. *The Collected Papers of Benjamin Franklin*. New Haven: Yale University Press, 1962.
- [104] M. Frasca, A. Bergner, J. Kurths, and L. Fortuna. Bifurcations in a star-like network of Stuart–Landau oscillators. *International Journal of Bifurcation and Chaos*, 22(07):1250173, 2012.
- [105] M. H. Fredriksson and A. B. Nordmark. On normal form calculations in impact oscillators. *Proceedings of the Royal Society of London. Series A: Mathematical, Physical and Engineering Sciences*, 456(1994):315–329, 2000.
- [106] W. J. Freeman. Models of the dynamics of neural populations. *Electroencephalography and clinical neurophysiology. Supplement*, (34):9–18, 1978.
- [107] E. Freire, E. Ponce, F. Rodrigo, and F. Torres. Bifurcation sets of continuous piecewise linear systems with two zones. *International Journal of Bifurcation and Chaos*, 8(11):2073–2097, 1998.
- [108] E. Freire, E. Ponce, and F. Torres. Canonical discontinuous planar piecewise linear systems. *SIAM Journal on Applied Dynamical Systems*, 11(1):181–211, 2012.
- [109] E. Freire, E. Ponce, and F. Torres. A general mechanism to generate three limit cycles in planar Filippov systems with two zones. *Nonlinear Dynamics*, 78(1):251–263, 2014.
- [110] V. A. Gaiko and W. T. Van Horssen. Global analysis of a piecewise linear Liénard-type dynamical system. *International Journal of Dynamical Systems and Differential Equations*, 2(1-2):115–128, 2009.
- [111] L. Gardini, T. Puu, and I. Sushko. A goodwin-type model with a piecewise linear investment function. In *Business Cycle Dynamics*, pages 317–333. Springer, 2006.

- [112] J. Gebert, N. Radde, and G.-W. Weber. Modeling gene regulatory networks with piecewise linear differential equations. *European Journal of Operational Research*, 181(3):1148–1165, 2007.
- [113] O. V. Gendelman. Modeling of inelastic impacts with the help of smooth-functions. *Chaos, Solitons and Fractals*, 28:522–526, 2006.
- [114] O. V. Gendelman. Exact solutions for discrete breathers in a forced-damped chain. *Physical Review E*, 87:062911, 2013.
- [115] O. V. Gendelman and L. I. Manevitch. Discrete breathers in vibroimpact chains: Analytic solutions. *Physical Review E*, 78:026609, 2008.
- [116] W. Gerstner. Spiking neurons. In *Pulsed neural networks*, pages 3–53. MIT Press, Cambridge, Massachusetts, 1999.
- [117] L. Glass. Classification of biological networks by their qualitative dynamics. *Journal of Theoretical Biology*, 54:85–107, 1975.
- [118] L. Glass and S. A. Kauffman. The logical analysis of continuous, non-linear biochemical control networks. *Journal of theoretical Biology*, 39(1):103–129, 1973.
- [119] L. Glass and J. S. Pasternack. Stable oscillations in mathematical models of biological control systems. *Journal of Mathematical Biology*, 6(3):207–223, 1978.
- [120] P. Glendinning and M. R. Jeffrey. Grazing-sliding bifurcations, border collision maps and the curse of dimensionality for piecewise smooth bifurcation theory. *Nonlinearity*, 28(1):263, 2014.
- [121] P. Glendinning and M. R. Jeffrey. *An introduction to piecewise smooth dynamics (Advanced Courses in Mathematics-CRM Barcelona)*. Berlin: Springer, 2019.
- [122] P. Goel and B. Ermentrout. Synchrony, stability, and firing patterns in pulse-coupled oscillators. *Physica D*, 163:191 – 216, 2002.
- [123] D. Gonze, S. Bernard, C. Waltermann, A. Kramer, and H. Herzel. Spontaneous synchronization of coupled circadian oscillators. *Biophysical journal*, 89(1):120–129, 2005.
- [124] J.-L. Gouzé and T. Sari. A class of piecewise linear differential equations arising in biological models. *Dynamical systems*, 17(4):299–316, 2002.
- [125] W. Govaerts and B. Sautois. Computation of the phase response curve: a direct numerical approach. *Neural Computation*, 18(4):817–847, 2006.
- [126] D. A. Grant and H. P. Van Dongen. Individual differences in sleep duration and responses to sleep loss. *The genetic basis of sleep and sleep disorders*, pages 189–196, 2013.
- [127] R. Grimshaw. *Nonlinear ordinary differential equations*, volume 2. CRC Press, 1991.

- [128] I. Grinberg and O. V. Gendelman. Localization in finite vibroimpact chains: Discrete breathers and multibreathers. *Physical Review E*, 94: 032204, 2016.
- [129] J. Guckenheimer. Isochrons and phaseless sets. *Journal of Mathematical Biology*, 1(3):259–273, 1975.
- [130] J. Guckenheimer and P. Holmes. *Nonlinear oscillations, dynamical systems, and bifurcations of vector fields*, volume 42. Springer Science & Business Media, 2013.
- [131] A. Guillemon and G. Huguet. A computational and geometric approach to phase resetting curves and surfaces. *SIAM Journal on Applied Dynamical Systems*, 8(3):1005–1042, 2009.
- [132] K. Gümüstekin, B. Seven, N. Karabulut, Ö. Aktas, N. Gürsan, S. Aslan, M. Keles, E. Varoglu, and S. Dane. Effects of sleep deprivation, nicotine, and selenium on wound healing in rats. *International journal of neuroscience*, 114(11):1433–1442, 2004.
- [133] H. E. Gunn, D. J. Buysse, B. P. Hasler, A. Begley, and W. M. Troxel. Sleep concordance in couples is associated with relationship characteristics. *Sleep*, 38(6):933–939, 2015.
- [134] J. Harris and B. Ermentrout. Bifurcations in the Wilson–Cowan Equations with Nonsmooth Firing Rate. *SIAM Journal on Applied Dynamical Systems*, 14:43–72, 2015.
- [135] A. L. Hodgkin and A. F. Huxley. A quantitative description of membrane current and its application to conduction and excitation in nerve. *The Journal of physiology*, 117(4):500, 1952.
- [136] A. L. Hodgkin and A. F. Huxley. Propagation of electrical signals along giant nerve fibres. *Proceedings of the Royal Society of London. Series B-Biological Sciences*, 140(899):177–183, 1952.
- [137] F. C. Hoppensteadt and E. M. Izhikevich. *Weakly connected neural networks*, volume 126. Springer Science & Business Media, 2012.
- [138] S.-M. Huan and X.-S. Yang. On the number of limit cycles in general planar piecewise linear systems of node–node types. *Journal of Mathematical Analysis and Applications*, 411(1):340–353, 2014.
- [139] M. J. Hülsemann, E. Naumann, and B. Rasch. Quantification of phase-amplitude coupling in neuronal oscillations: comparison of phase-locking value, mean vector length, modulation index, and generalized-linear-modeling-cross-frequency-coupling. *Frontiers in neuroscience*, 13:573, 2019.
- [140] J. Husse, G. Eichele, and H. Oster. Synchronization of the mammalian circadian timing system: light can control peripheral clocks independently of the SCN clock: alternate routes of entrainment optimize the alignment of the body’s circadian clock network with external time. *BioEssays*, 37(10):1119–1128, 2015.

- [141] C. Huygens. *Oeuvres Complètes De Christiaan Huygens*. La HayeM. Nijhoff, 1893.
- [142] J. Ing, E. Pavlovskaja, and M. Wiercigroch. Dynamics of a nearly symmetrical piecewise linear oscillator close to grazing incidence: Modeling and experimental verification. *Nonlinear Dynamics*, 46:225–238, 2006.
- [143] J. Ing, E. Pavlovskaja, M. Wiercigroch, and S. Banerjee. Experimental study of impact oscillator with one side elastic constraint. *Philosophical Transactions of The Royal Society A Mathematical Physical and Engineering Sciences*, 366:679–704, 2008.
- [144] M. Ipsen, F. Hynne, and P. G. Sørensen. Amplitude equations and chemical reaction–diffusion systems. *International Journal of Bifurcation and Chaos*, 7(07):1539–1554, 1997.
- [145] A. Isacson, L. Y. Gorelik, M. V. Voinova, B. Kasemo, R. I. Shekhter, and M. Jonson. Shuttle instability in self-assembled Coulomb blockade nanostructures. *Physica B*, 255:150–163, 1998.
- [146] E. M. Izhikevich. *Dynamical systems in neuroscience*. MIT press, 2007.
- [147] P. Jain and S. Banerjee. Border-collision bifurcations in one-dimensional discontinuous maps. *International Journal of Bifurcation and Chaos*, 13(11):3341–3351, 2003.
- [148] G. James, V. Acary, and F. Pèrignon. Periodic motions of coupled impact oscillators. In R. Leine, V. Acary, and O. Brùls, editors, *Advanced Topics in Nonsmooth Dynamics*, pages 93–134. Springer, Cham, Switzerland, 2018.
- [149] M. R. Jeffrey. Sliding bifurcations and non-determinism in systems with switching. *IFAC Proceedings Volumes*, 44(1):13275–13280, 2011.
- [150] M. R. Jeffrey. Smoothing tautologies, hidden dynamics, and sigmoid asymptotics for piecewise smooth systems. *Chaos: An Interdisciplinary Journal of Nonlinear Science*, 25(10):103125, 2015.
- [151] M. R. Jeffrey. The ghosts of departed quantities in switches and transitions. *SIAM Review*, 60(1):116–136, 2018.
- [152] M. R. Jeffrey. *Hidden Dynamics*. Springer, 2018.
- [153] M. R. Jeffrey and S. J. Hogan. The geometry of generic sliding bifurcations. *SIAM review*, 53(3):505–525, 2011.
- [154] M. R. Jeffrey and S. Webber. The hidden unstable orbits of maps with gaps. *Proceedings of the Royal Society A*, 476(2234):20190473, 2020.
- [155] H. Jiang and M. Wiercigroch. Geometrical insight into non-smooth bifurcations of a soft impact oscillator. *IMA Journal of Applied Mathematics*, 81:662–678, 2016.

- [156] H. Jiang, A. S. E. Chong, Y. Ueda, and M. Wiercigroch. Grazing-induced bifurcations in impact oscillators with elastic and rigid constraints. *International Journal of Mechanical Sciences*, 127:204–214, 2017.
- [157] D. Jordan and P. Smith. *Nonlinear ordinary differential equations: an introduction for scientists and engineers*, volume 10. Oxford University Press on Demand, 2007.
- [158] J. P. Junior and W. De Melo. *Geometric theory of dynamical systems: an introduction*. Springer-Verlag, 1982.
- [159] Y. Kawamura and H. Nakao. Phase description of oscillatory convection with a spatially translational mode. *Physica D: Nonlinear Phenomena*, 295:11–29, 2015.
- [160] H. Kielblock, C. Kirst, and M. Timme. Breakdown of order preservation in symmetric oscillator networks with pulse-coupling. *Chaos: An Interdisciplinary Journal of Nonlinear Science*, 21:025113, 2011.
- [161] C. A. Klausmeier. Floquet theory: a useful tool for understanding nonequilibrium dynamics. *Theoretical Ecology*, 1(3):153–161, 2008.
- [162] C. R. Knutson, K. V. Edmond, M. T. Tuominen, and A. Dinsmore. Shuttling of charge by a metallic sphere in viscous oil. *Journal of Applied Physics*, 101:013706, 2007.
- [163] C. Koch and I. Segev. *Methods in neuronal modeling: from ions to networks*. MIT press, 1998.
- [164] K. Kotani, Y. Ogawa, S. Shirasaka, A. Akao, Y. Jimbo, and H. Nakao. Nonlinear phase-amplitude reduction of delay-induced oscillations. *Physical Review Research*, 2(3):033106, 2020.
- [165] C. D. Kouros and M. El-Sheikh. Within-family relations in objective sleep duration, quality, and schedule. *Child development*, 88(6):1983–2000, 2017.
- [166] R. E. Kronauer, C. A. Czeisler, S. F. Pilato, M. C. Moore-Ede, and E. D. Weitzman. Mathematical model of the human circadian system with two interacting oscillators. *American Journal of Physiology-Regulatory, Integrative and Comparative Physiology*, 242(1):R3–R17, 1982.
- [167] R. Kumar, A. Bose, and B. N. Mallick. A mathematical model towards understanding the mechanism of neuronal regulation of wake-NREMS-REMS states. *PLoS One*, 7(8):e42059, 2012.
- [168] M. Kunze. *Non-smooth dynamical systems*, volume 1744. Springer Science & Business Media, 2000.
- [169] Y. Kuramoto. *Chemical oscillations, waves, and turbulence*. Courier Corporation, 2003.
- [170] Y. A. Kuznetsov. *Elements of applied bifurcation theory*, volume 112. Springer Science & Business Media, 2013.

- [171] M. D. Kvalheim and S. Revzen. Existence and uniqueness of global Koopman eigenfunctions for stable fixed points and periodic orbits. *Physica D: Nonlinear Phenomena*, page 132959, 2021.
- [172] Y. N. Kyrychko, K. B. Blyuss, and E. Schöll. Synchronization of networks of oscillators with distributed delay coupling. *Chaos: An Interdisciplinary Journal of Nonlinear Science*, 24(4):043117, 2014.
- [173] J. Ladenbauer, M. Augustin, L. Shiau, and K. Obermayer. Impact of adaptation currents on synchronization of coupled exponential integrate-and-fire neurons. *PLoS Comput Biol*, 8(4):e1002478, 2012.
- [174] Y. M. Lai, R. Thul, and S. Coombes. Analysis of networks where discontinuities and nonsmooth dynamics collide: understanding synchrony. *The European Physical Journal Special Topics*, 227(10):1251–1265, 2018.
- [175] Y. M. Lai, J. Veasy, S. Coombes, and R. Thul. A master stability function approach to cardiac alternans. *Applied Network Science*, 4(1):1–16, 2019.
- [176] C. R. Laing and C. C. Chow. A spiking neuron model for binocular rivalry. *Journal of Computational Neuroscience*, 12:39–53, 2002.
- [177] A. C. Lazer and P. J. McKenna. Large-amplitude periodic oscillations in suspension bridges: some new connections with nonlinear analysis. *Siam Review*, 32(4):537–578, 1990.
- [178] C. A. Lea-Carnall, M. A. Montemurro, N. J. Trujillo-Barreto, L. M. Parkes, and W. El-Deredy. Cortical resonance frequencies emerge from network size and connectivity. *PLoS computational biology*, 12(2):e1004740, 2016.
- [179] D. Leenaerts and W. M. G. Van Bokhoven. *Piecewise linear modeling and analysis*. Springer Science & Business Media, 2013.
- [180] R. I. Leine and H. Nijmeijer. *Dynamics and bifurcations of non-smooth mechanical systems*, volume 18. Springer Science & Business Media, 2013.
- [181] B. Letson and J. E. Rubin. A new frame for an old (phase) portrait: Finding rivers and other flow features in the plane. *SIAM Journal on Applied Dynamical Systems*, 17(4):2414–2445, 2018.
- [182] H. Lin and P. J. Antsaklis. Stability and stabilizability of switched linear systems: a survey of recent results. *IEEE Transactions on Automatic control*, 54(2):308–322, 2009.
- [183] J. M. Lipton and K. P. Dabke. Softening the nonlinearity in Chua’s circuit. *International Journal of Bifurcation and Chaos*, 6(01):179–183, 1996.
- [184] X. Liu and Q. Wang. Stability of nontrivial solution of delay differential equations with state-dependent impulses. *Applied Mathematics and Computation*, 174:271–288, 2006.

- [185] J. Llibre and Y. Tang. Limit cycles of discontinuous piecewise quadratic and cubic polynomial perturbations of a linear center. *arXiv preprint arXiv:1708.03282*, 2017.
- [186] J. Llibre and X. Zhang. Limit cycles created by piecewise linear centers. *Chaos: An Interdisciplinary Journal of Nonlinear Science*, 29(5):053116, 2019.
- [187] J. Llibre, E. Ponce, and F. Torres. On the existence and uniqueness of limit cycles in Liénard differential equations allowing discontinuities. *Nonlinearity*, 21(9):2121, 2008.
- [188] I. Lodato, S. Boccaletti, and V. Latora. Synchronization properties of network motifs. *Europhysics Letters*, 78(2):28001, 2007.
- [189] J. Lu, D. W. C. Ho, and J. Cao. A unified synchronization criterion for impulsive dynamical networks. *Automatica*, 46:1215–1221, 2010.
- [190] F. S. Luyster, P. J. Strollo, P. C. Zee, and J. K. Walsh. Sleep: a health imperative. *Sleep*, 35(6):727–734, 2012.
- [191] Y. Ma, M. Agarwal, and S. Benerjee. Border collision bifurcations in a soft impact system. *Physics Letters A*, 354:281–287, 2006.
- [192] Y. Ma, J. Ing, S. Banerjee, M. Wiercigroch, and E. Pavlovskia. The nature of the normal form map for soft impacting systems. *International Journal of Non-Linear Mechanics*, 43:504–513, 2008.
- [193] Y. Ma, R. Yuan, Y. Li, P. Ao, and B. Yuan. Lyapunov functions in piecewise linear systems: From fixed point to limit cycle. *arXiv preprint arXiv:1306.6880*, 2013.
- [194] O. Makarenkov and J. S. W. Lamb. Dynamics and bifurcations of non-smooth systems: A survey. *Physica D: Nonlinear Phenomena*, 241(22):1826–1844, 2012.
- [195] I. G. Malkin. Methods of Poincare and Liapunov in theory of non-linear oscillations. *Gostexizdat, Moscow*, 1949.
- [196] A. Mauroy and I. Mezić. On the use of Fourier averages to compute the global isochrons of (quasi) periodic dynamics. *Chaos: An Interdisciplinary Journal of Nonlinear Science*, 22(3):033112, 2012.
- [197] R. W. McCarley and J. A. Hobson. Neuronal excitability modulation over the sleep cycle: a structural and mathematical model. *Science*, 189(4196):58–60, 1975.
- [198] R. W. McCarley and S. G. Massaquoi. A limit cycle mathematical model of the REM sleep oscillator system. *American Journal of Physiology-Regulatory, Integrative and Comparative Physiology*, 251(6):R1011–R1029, 1986.

- [199] Z. T. McCleney and Z. P. Kilpatrick. Entrainment in up and down states of neural populations: non-smooth and stochastic models. *Journal of Mathematical Biology*, 73:1131–1160, 2016.
- [200] A. R. McIntosh. Towards a network theory of cognition. *Neural Networks*, 13(8-9):861–870, 2000.
- [201] H. P. McKean Jr. Nagumo’s equation. *Advances in mathematics*, 4(3): 209–223, 1970.
- [202] R. Meadows, S. Arber, S. Venn, and J. Hislop. Engaging with sleep: male definitions, understandings and attitudes. *Sociology of health & illness*, 30(5):696–710, 2008.
- [203] R. Meadows, S. Arber, S. Venn, J. Hislop, and N. Stanley. Exploring the interdependence of couples’ rest-wake cycles: An actigraphic study. *Chronobiology international*, 26(1):80–92, 2009.
- [204] L. Menna-Barreto, A. A. Benedito-Silva, N. Marques, M. M. M. de Andrade, and F. Louzada. Ultradian components of the sleep-wake cycle in babies. *Chronobiology international*, 10(2):103–108, 1993.
- [205] R. E. Mirollo and S. H. Strogatz. Amplitude death in an array of limit-cycle oscillators. *Journal of Statistical Physics*, 60(1-2):245–262, 1990.
- [206] B. Monga and J. Moehlis. Augmented phase reduction for periodic orbits near a homoclinic bifurcation and for relaxation oscillators. *Nonlinear Theory and Its Applications, IEICE*, 12(1):103–116, 2021.
- [207] B. Monga, D. Wilson, T. Matchen, and J. Moehlis. Phase reduction and phase-based optimal control for biological systems: a tutorial. *Biological cybernetics*, 113(1-2):11–46, 2019.
- [208] M. C. Moore-Ede. Mathematical models of the circadian sleep-wake cycle. Technical report, Harvard Medical School Boston Ma Dept of Physiology and Biophysics, 1984.
- [209] C. Morris and H. Lecar. Voltage oscillations in the barnacle giant muscle fiber. *Biophysical journal*, 35(1):193–213, 1981.
- [210] A. S. Morse. Control using logic-based switching. *Trends in control*, pages 69–113, 1995.
- [211] P. C. Müller. Calculation of Lyapunov exponents for dynamical systems with discontinuities. *Chaos, Solitons and Fractals*, 5:1671–1681, 1995.
- [212] J. Nagumo, S. Arimoto, and S. Yoshizawa. An active pulse transmission line simulating nerve axon. *Proceedings of the IRE*, 50(10):2061–2070, 1962.
- [213] H. Nakao. Phase reduction approach to synchronisation of nonlinear oscillators. *Contemporary Physics*, 57(2):188–214, 2016.

- [214] M. Nakao and M. Yamamoto. Bifurcation properties of the two process model. *Psychiatry and clinical neurosciences*, 52(2):131–133, 1998.
- [215] M. Nakao, H. Sakai, and M. Yamamoto. An interpretation of the internal desynchronizations based on dynamics of the two-process model. *Methods of information in medicine*, 36(04/05):282–285, 1997.
- [216] J. C. Neu. Large populations of coupled chemical oscillators. *SIAM Journal on Applied Mathematics*, 38(2):305–316, 1980.
- [217] R. Nicks, L. Chambon, and S. Coombes. Clusters in nonsmooth oscillator networks. *Physical Review E*, 97:032213, 2018.
- [218] H. Nijmeijer and A. Rodriguez-Angeles. *Synchronization of Mechanical Systems*. Singapore: World Scientific, 2003.
- [219] V. Novičenko and K. Pyragas. Phase reduction of weakly perturbed limit cycle oscillations in time-delay systems. *Physica D: Nonlinear Phenomena*, 241(12):1090–1098, 2012.
- [220] A. C. E. Onslow, M. W. Jones, and R. Bogacz. A canonical circuit for generating phase-amplitude coupling. *PloS one*, 9(8):e102591, 2014.
- [221] H. M. Osinga and J. Moehlis. Continuation-based computation of global isochrons. *SIAM Journal on Applied Dynamical Systems*, 9(4):1201–1228, 2010.
- [222] A. Otto, G. Radons, D. Bachrathy, and G. Orosz. Synchronization in networks with heterogeneous coupling delays. *Physical Review E*, 97(1):012311, 2018.
- [223] F. P. Pankhurst and J. A. Home. The influence of bed partners on movement during sleep. *Sleep*, 17(4):308–315, 1994.
- [224] E. Panteley, A. Loria, and A. El Ati. On the stability and robustness of Stuart-Landau oscillators. *IFAC-PapersOnLine*, 48(11):645–650, 2015.
- [225] E. Panteley, A. Loria, and A. El-Ati. Practical dynamic consensus of Stuart–Landau oscillators over heterogeneous networks. *International Journal of Control*, 93(2):261–273, 2020.
- [226] Y. Park and D. Wilson. High-order accuracy computation of coupling functions for strongly coupled oscillators. *arXiv preprint arXiv:2010.01194*, 2020.
- [227] Y. Park, K. M. Shaw, H. J. Chiel, and P. J. Thomas. The infinitesimal phase response curves of oscillators in piecewise smooth dynamical systems. *European Journal of Applied Mathematics*, 29(5):905–940, 2018.
- [228] R. Pavani. The numerical approximation of the rotation number of planar maps. *Computers & Mathematics with Applications*, 33(5):103–110, 1997.

- [229] L. M. Pecora and T. L. Carroll. Master stability functions for synchronized coupled systems. *Physical Review Letters*, 80:2109–2112, 1998.
- [230] L. M. Pecora and T. L. Carroll. *Master Stability Function for Globally Synchronized Systems*, pages 1–13. Springer New York, New York, NY, 2013.
- [231] L. M. Pecora, T. L. Carroll, G. A. Johnson, D. J. Mar, and J. F. Heagy. Fundamentals of synchronization in chaotic systems, concepts, and applications. *Chaos*, 7:520–543, 1997.
- [232] L. M. Pecora, F. Sorrentino, A. M. Hagerstrom, T. E. Murphy, and R. Roy. Cluster synchronization and isolated desynchronization in complex networks with symmetries. *Nature Communications*, 5, 2014.
- [233] N. Perchikov and O. V. Gendelman. Dynamics and stability of a discrete breather in a harmonically excited chain with vibro-impact on-site potential. *Physica D*, 292-293:8–28, 2015.
- [234] C. Pereti and D. Fanelli. Stabilizing Stuart-Landau oscillators via time-varying networks. *Chaos, Solitons & Fractals*, 133:109587, 2020.
- [235] L. Perko. *Differential equations and dynamical systems*, volume 7. Springer Science & Business Media, 2013.
- [236] A. J. K. Phillips and P. A. Robinson. A quantitative model of sleep-wake dynamics based on the physiology of the brainstem ascending arousal system. *Journal of Biological Rhythms*, 22(2):167–179, 2007.
- [237] A. J. K. Phillips and P. A. Robinson. Sleep deprivation in a quantitative physiologically based model of the ascending arousal system. *Journal of theoretical biology*, 255(4):413–423, 2008.
- [238] A. J. K. Phillips, P. A. Robinson, D. J. Kedziora, and R. G. Abeyesuriya. Mammalian sleep dynamics: how diverse features arise from a common physiological framework. *PLoS Comput Biol*, 6(6):e1000826, 2010.
- [239] B. Pietras and A. Daffertshofer. Network dynamics of coupled oscillators and phase reduction techniques. *Physics Reports*, 2019.
- [240] A. Pikovsky, M. Rosenblum, and J. Kurths. *Synchronization: a universal concept in nonlinear sciences*, volume 12. Cambridge university press, 2003.
- [241] A. Pogromsky, G. Santoboni, and H. Nijmeijer. Partial synchronization: from symmetry towards stability. *Physica D: Nonlinear Phenomena*, 172: 65–87, 2002.
- [242] E. Ponce. Bifurcations in piecewise linear systems: Case studies. In *VI Workshop on Dynamical Systems-MAT 70 An International Conference on Dynamical Systems celebrating the 70th birthday of Marco Antonio Teixeira*. Electronically available at http://www.ime.unicamp.br/rmiranda/mat70/MAT70/Welcome_files/NotesMAT70EPN.pdf, (viewed on 05/03/2021), 2014.

- [243] M. A. Porter and J. P. Gleeson. Dynamical systems on networks. *Frontiers in Applied Dynamical Systems: Reviews and Tutorials*, 4, 2016.
- [244] K. Premalatha, V. K. Chandrasekar, M. Senthilvelan, and M. Lakshmanan. Stable amplitude chimera states in a network of locally coupled Stuart-Landau oscillators. *Chaos: An Interdisciplinary Journal of Nonlinear Science*, 28(3):033110, 2018.
- [245] S. R. Pring and C. J. Budd. The dynamics of a simplified pinball machine. *IMA Journal of Applied Mathematics*, 76:67–84, 2011.
- [246] M. Puckeridge, B. D. Fulcher, A. J. K. Phillips, and P. A. Robinson. Incorporation of caffeine into a quantitative model of fatigue and sleep. *Journal of theoretical biology*, 273(1):44–54, 2011.
- [247] K. Pyragas and V. Novičenko. Phase reduction of a limit cycle oscillator perturbed by a strong amplitude-modulated high-frequency force. *Physical Review E*, 92(1):012910, 2015.
- [248] B. Rasch and J. Born. About sleep’s role in memory. *Physiological reviews*, 2013.
- [249] F. Rhodes and C. L. Thompson. Rotation numbers for monotone functions on the circle. *Journal of the London Mathematical Society*, 2(2):360–368, 1986.
- [250] K. Richter, S. Adam, L. Geiss, L. Peter, and G. Niklewski. Two in a bed: The influence of couple sleeping and chronotypes on relationship and sleep. An overview. *Chronobiology international*, 33(10):1464–1472, 2016.
- [251] RimstarOrg. Franklin’s Bell - How it Works. *YouTube*, 2012, (viewed on 06/05/2018). URL <https://www.youtube.com/watch?v=ffEqudsyIWzk>.
- [252] J. Rinzel. Spatial stability of traveling wave solutions of a nerve conduction equation. *Biophysical journal*, 15(10):975–988, 1975.
- [253] J. Rinzel. Excitation dynamics: insights from simplified membrane models. In *Fed. Proc*, volume 44 (15), pages 2944–2946, 1985.
- [254] J. Rinzel and J. B. Keller. Traveling wave solutions of a nerve conduction equation. *Biophysical journal*, 13(12):1313–1337, 1973.
- [255] F. A. Rodrigues, T. K. D. Peron, P. Ji, and J. Kurths. The Kuramoto model in complex networks. *Physics Reports*, 610:1–98, 2016.
- [256] P. C. Rosenblatt. *Two in a bed: The social system of couple bed sharing*. SUNY Press, 2012.
- [257] M. Rosenblum and A. Pikovsky. Numerical phase reduction beyond the first order approximation. *Chaos: An Interdisciplinary Journal of Nonlinear Science*, 29(1):011105, 2019.

- [258] M. T. Rosenstein, J. J. Collins, and C. J. De Luca. A practical method for calculating largest Lyapunov exponents from small data sets. *Physica D: Nonlinear Phenomena*, 65(1-2):117–134, 1993.
- [259] H. G. Rotstein, S. Coombes, and A. M. Gheorghe. Canard-like explosion of limit cycles in two-dimensional piecewise-linear models of FitzHugh–Nagumo type. *SIAM Journal on Applied Dynamical Systems*, 11(1):135–180, 2012.
- [260] Y. Roudi and P. E. Latham. A balanced memory network. *PLoS Comput Biol*, 3(9):e141, 2007.
- [261] J. E. Rubin and D. Terman. High frequency stimulation of the subthalamic nucleus eliminates pathological thalamic rhythmicity in a computational model. *Journal of computational neuroscience*, 16(3):211–235, 2004.
- [262] R. Rubin, L. F. Abbott, and H. Sompolinsky. Balanced excitation and inhibition are required for high-capacity, noise-robust neuronal selectivity. *Proceedings of the National Academy of Sciences*, 114(44):E9366–E9375, 2017.
- [263] A. Salova and R. M. D’Souza. Decoupled synchronized states in networks of linearly coupled limit cycle oscillators. *Physical Review Research*, 2(4):043261, 2020.
- [264] A. M. Samoilenko and N. A. Perestyuk. *Impulsive Differential Equations*. Singapore: World Scientific, 1995.
- [265] J. A. Sanders, F. Verhulst, and J. Murdock. *Averaging methods in non-linear dynamical systems*, volume 59. Springer, 2007.
- [266] P. Sanz-Leon, S. A. Knock, A. Spiegler, and V. K. Jirsa. Mathematical framework for large-scale brain network modeling in The Virtual Brain. *NeuroImage*, 111:385–430, 2015.
- [267] C. B. Saper, T. E. Scammell, and J. Lu. Hypothalamic regulation of sleep and circadian rhythms. *Nature*, 437(7063):1257–1263, 2005.
- [268] M. Şayli and S. Coombes. Networks of Franklin bells - an experiment, 2019, viewed on 20/02/2021. URL <https://www.maths.nottingham.ac.uk/plp/pmzsc/movies/FranklinBell.mp4>.
- [269] M. Şayli, Y. M. Lai, R. Thul, and S. Coombes. Synchrony in networks of franklin bells. *IMA Journal of Applied Mathematics*, 84(5):1001–1021, 2019.
- [270] M. A. Schwemmer and T. J. Lewis. The theory of weakly coupled oscillators. In *Phase response curves in neuroscience*, pages 3–31. Springer, 2012.
- [271] D. V. Senthilkumar and M. Lakshmanan. Bifurcations and chaos in time delayed piecewise linear dynamical systems. *International Journal of Bifurcation and Chaos*, 15(09):2895–2912, 2005.

- [272] W. Serweta, A. Okolewski, B. Blazejczyk-Okolewska, K. Czołczynski, and T. Kapitaniak. Lyapunov exponents of impact oscillators with Hertz's and Newton's contact models. *International Journal of Mechanical Sciences*, 89:194–206, 2014.
- [273] Z. Shan, H. Ma, M. Xie, P. Yan, Y. Guo, W. Bao, Y. Rong, C. L. Jackson, F. B. Hu, and L. Liu. Sleep duration and risk of Type 2 diabetes: A meta-analysis of prospective studies. *Diabetes care*, 38(3):529–537, 2015.
- [274] S. W. Shaw and P. J. Holmes. A periodically forced piecewise linear oscillator. *Journal of sound and vibration*, 90(1):129–155, 1983.
- [275] S. Shirasaka, W. Kurebayashi, and H. Nakao. Phase-amplitude reduction of transient dynamics far from attractors for limit-cycling systems. *Chaos: An Interdisciplinary Journal of Nonlinear Science*, 27(2):023119, 2017.
- [276] S. Shirasaka, W. Kurebayashi, and H. Nakao. Phase reduction theory for hybrid nonlinear oscillators. *Physical Review E*, 95(1):012212, 2017.
- [277] S. Shirasaka, W. Kurebayashi, and H. Nakao. Phase-amplitude reduction of limit cycling systems. In *The Koopman Operator in Systems and Control*, pages 383–417. Springer, 2020.
- [278] I. B. Shiroky and O. V. Gendelman. Dcreate breathers in an array of self-excited oscillator: Exact solutions and stability. *Chaos*, 26:103112, 2016.
- [279] D. J. W. Simpson. Twenty Hopf-like bifurcations in piecewise-smooth dynamical systems. *arXiv preprint arXiv:1905.01329*, 2019.
- [280] D. J. W. Simpson and R. Kuske. The influence of localized randomness on regular grazing bifurcations with applications to impacting dynamics. *Journal of Vibration and Control*, 24(2):407–426, 2018.
- [281] D. J. W. Simpson and J. D. Meiss. Andronov–Hopf bifurcations in planar, piecewise-smooth, continuous flows. *Physics Letters A*, 371(3):213–220, 2007.
- [282] D. J. W. Simpson and J. D. Meiss. Unfolding a codimension-two, discontinuous, Andronov–Hopf bifurcation. *Chaos: An Interdisciplinary Journal of Nonlinear Science*, 18(3):033125, 2008.
- [283] E. Sitnikova, E. Pavlovskaja, and M. Wiercigroch. Dynamics of an impact oscillator with SMA constraint. *The European Physical Journal Special Topics*, 165:229–238, 2008.
- [284] E. Sitnikova, E. Pavlovskaja, M. Wiercigroch, and M. A. Savi. Vibration reduction of the impact system by an SMA restraint: numerical studies. *International Journal of Non-Linear Mechanics*, 45:837–849, 2010.
- [285] P. S. Skardal and J. G. Restrepo. Hierarchical synchrony of phase oscillators in modular networks. *Physical Review E*, 85(1):016208, 2012.

- [286] A. C. Skeldon, D.-J. Dijk, and G. Derks. Mathematical models for sleep-wake dynamics: comparison of the two-process model and a mutual inhibition neuronal model. *PloS one*, 9(8):e103877, 2014.
- [287] A. C. Skeldon, G. Derks, and V. Booth. Nonsmooth maps and the fast-slow dynamics of sleep-wake regulation: Part II. In *Extended Abstracts Spring 2016*, pages 171–175. Springer, 2017.
- [288] R. M. Smeal, G. B. Ermentrout, and J. A. White. Phase-response curves and synchronized neural networks. *Philosophical Transactions of the Royal Society B: Biological Sciences*, 365(1551):2407–2422, 2010.
- [289] R. Snari, M. R. Tinsley, D. Wilson, S. Faramarzi, T. I. Netoff, J. Moehlis, and K. Showalter. Desynchronization of stochastically synchronized chemical oscillators. *Chaos: An Interdisciplinary Journal of Nonlinear Science*, 25(12):123116, 2015.
- [290] F. Sofi, F. Cesari, A. Casini, C. Macchi, R. Abbate, and G. F. Gensini. Insomnia and risk of cardiovascular disease: a meta-analysis. *European journal of preventive cardiology*, 21(1):57–64, 2014.
- [291] F. Sorrentino, L. M. Pecora, A. M. Hagerstrom, T. E. Murphy, and R. Roy. Complete characterization of the stability of cluster synchronization in complex dynamical networks. *Science Advances*, 2:e1501737–e1501737, 2016.
- [292] E. Steur, W. Michiels, H. Huijberts, and H. Nijmeijer. Networks of diffusively time-delay coupled systems: Conditions for synchronization and its relation to the network topology. *Physica D*, 277:22–39, 2014.
- [293] W. J. Strawbridge, S. J. Shema, and R. E. Roberts. Impact of spouses’ sleep problems on partners. *Sleep*, 27(3):527–531, 2004.
- [294] C. Stroemel-Scheder, B. Kundermann, and S. Lautenbacher. The effects of recovery sleep on pain perception: A systematic review. *Neuroscience & Biobehavioral Reviews*, 2020.
- [295] S. H. Strogatz. Human sleep and circadian rhythms: a simple model based on two coupled oscillators. *Journal of mathematical biology*, 25(3):327–347, 1987.
- [296] J. Sun, E. M. Bollt, and T. Nishikawa. Master stability functions for coupled nearly identical dynamical systems. *Europhysics Letters*, 85(6):60011, 2009.
- [297] Ö. Suvak and A. Demir. Quadratic approximations for the isochrons of oscillators: a general theory, advanced numerical methods, and accurate phase computations. *IEEE Transactions on Computer-Aided Design of Integrated Circuits and Systems*, 29(8):1215–1228, 2010.
- [298] R. Szalai and H. M. Osinga. Arnol’d tongues arising from a grazing-sliding bifurcation. *SIAM Journal on Applied Dynamical Systems*, 8(4):1434–1461, 2009.

- [299] D. Takeshita and R. Feres. Higher order approximation of isochrons. *Nonlinearity*, 23(6):1303, 2010.
- [300] Y. Tamakawa, A. Karashima, Y. Koyama, N. Katayama, and M. Nakao. A quartet neural system model orchestrating sleep and wakefulness mechanisms. *Journal of neurophysiology*, 95(4):2055–2069, 2006.
- [301] M. E. Thase. Depression and sleep: pathophysiology and treatment. *Dialogues in clinical neuroscience*, 8(2):217, 2006.
- [302] A. Thorin, P. Delezoide, and M. Legrand. Nonsmooth modal analysis of piecewise-linear impact oscillators. *SIAM Journal on Applied Dynamical Systems*, 16:1710–1747, 2017.
- [303] R. Thul and S. Coombes. Understanding cardiac alternans: a piecewise linear modeling framework. *Chaos: An Interdisciplinary Journal of Nonlinear Science*, 20(4):045102, 2010.
- [304] M. Timme, F. Wolf, and T. Geisel. Coexistence of regular and irregular dynamics in complex networks of pulse-coupled oscillators. *Physical Review Letters*, 89:258701, 2002.
- [305] A. Tonnelier. The McKean’s caricature of the Fitzhugh–Nagumo model I. The space-clamped system. *SIAM Journal on Applied Mathematics*, 63(2):459–484, 2003.
- [306] A. Tonnelier and W. Gerstner. Piecewise linear differential equations and integrate-and-fire neurons: insights from two-dimensional membrane models. *Physical Review E*, 67(2):021908, 2003.
- [307] W. M. Troxel. It’s more than sex: Exploring the dyadic nature of sleep and implications for health. *Psychosomatic medicine*, 72(6):578, 2010.
- [308] K. Tsumoto, H. Kitajima, T. Yoshinaga, K. Aihara, and H. Kawakami. Bifurcations in Morris-Lecar neuron model. *Neurocomputing*, 69(4-6): 293–316, 2006.
- [309] L. Tumash, A. Zakharova, J. Lehnert, W. Just, and E. Schöll. Stability of amplitude chimeras in oscillator networks. *Europhysics Letters*, 117(2):20001, 2017.
- [310] L. Tumash, E. Panteley, A. Zakharova, and E. Schöll. Synchronization patterns in Stuart–Landau networks: a reduced system approach. *The European Physical Journal B*, 92(5):100, 2019.
- [311] T. Ueta and G. Chen. On synchronization and control of coupled Wilson-Cowan neural oscillators. *International Journal of Bifurcation and Chaos*, 13:163–175, 2003.
- [312] A. F. Vakakis. Inducing passive nonlinear energy sinks in linear vibrating systems. *Journal of Vibration and Acoustics*, 123:324–332, 2001.

- [313] C. Van Vreeswijk and H. Sompolinsky. Chaos in neuronal networks with balanced excitatory and inhibitory activity. *Science*, 274(5293):1724–1726, 1996.
- [314] S. Venn, S. Arber, R. Meadows, and J. Hislop. The fourth shift: exploring the gendered nature of sleep disruption among couples with children. *The British Journal of Sociology*, 59(1):79–97, 2008.
- [315] W.-P. Wang. Multiple impulse solutions to McKean’s caricature of the nerve equation. I—existence. *Communications on pure and applied mathematics*, 41(1):71–103, 1988.
- [316] X. Wang and G. Chen. Synchronization in scale-free dynamical networks: robustness and fragility. *IEEE Transactions on circuits and systems*, 49: 54–62, 2002.
- [317] Y. Wang, J. P. Gill, H. J. Chiel, and P. J. Thomas. Shape versus timing: linear responses of a limit cycle with hard boundaries under instantaneous and static perturbation. *SIAM Journal on Applied Dynamical Systems*, 20(2):701–744, 2021.
- [318] Z. Wang, Z. Duan, and J. Cao. Impulsive synchronization of coupled dynamical networks with nonidentical Duffing oscillators and coupling delays. *Chaos*, 22:013140, 2012.
- [319] K. C. A. Wedgwood, K. K. Lin, R. Thul, and S. Coombes. Phase-amplitude descriptions of neural oscillator models. *The Journal of Mathematical Neuroscience*, 3(1):2, 2013.
- [320] D. Wilson. Isostable reduction of oscillators with piecewise smooth dynamics and complex Floquet multipliers. *Physical Review E*, 99(2): 022210, 2019.
- [321] D. Wilson. An optimal framework for nonfeedback stability control of chaos. *SIAM Journal on Applied Dynamical Systems*, 18(4):1982–1999, 2019.
- [322] D. Wilson. An adaptive phase-amplitude reduction framework without $\mathcal{O}(\epsilon)$ constraints on inputs. *arXiv preprint arXiv:2011.10410*, 2020.
- [323] D. Wilson. Phase-amplitude reduction far beyond the weakly perturbed paradigm. *Physical Review E*, 101(2):022220, 2020.
- [324] D. Wilson. Analysis of input-induced oscillations using the isostable coordinate framework. *Chaos: An Interdisciplinary Journal of Nonlinear Science*, 31(2):023131, 2021.
- [325] D. Wilson and B. Ermentrout. Greater accuracy and broadened applicability of phase reduction using isostable coordinates. *Journal of mathematical biology*, 76(1-2):37–66, 2018.
- [326] D. Wilson and B. Ermentrout. Phase models beyond weak coupling. *Physical review letters*, 123(16):164101, 2019.

- [327] D. Wilson and J. Moehlis. Optimal chaotic desynchronization for neural populations. *SIAM Journal on Applied Dynamical Systems*, 13(1):276, 2014.
- [328] D. Wilson and J. Moehlis. Isostable reduction of periodic orbits. *Physical Review E*, 94(5):052213, 2016.
- [329] H. R. Wilson and J. D. Cowan. Excitatory and inhibitory interactions in localized populations of model neurons. *Biophysical Journal*, 12:1–24, 1972.
- [330] H. R. Wilson and J. D. Cowan. A mathematical theory of the functional dynamics of cortical and thalamic nervous tissue. *Kybernetik*, 13:55–80, 1973.
- [331] A. T. Winfree. Biological rhythms and the behavior of populations of coupled oscillators. *Journal of theoretical biology*, 16(1):15–42, 1967.
- [332] A. T. Winfree. *The geometry of biological time*, volume 12. Springer Science & Business Media, 2001.
- [333] H. Wolf, J. Kodvanj, and S. Bjelovučić-Kopilović. Effect of smoothing piecewise-linear oscillators on their stability predictions. *Journal of sound and vibration*, 270(4-5):917–932, 2004.
- [334] M. W. Woolrich and K. E. Stephan. Biophysical network models and the human connectome. *NeuroImage*, 80:330–338, 2013.
- [335] B. Xu, F. Yang, Y. Tang, and M. Lin. Homoclinic bifurcations in planar piecewise-linear systems. *Discrete Dynamics in Nature and Society*, 2013, 2013.
- [336] T. Yang. *Impulsive Control Theory*. Verlag Berlin Heidelberg: Springer, 2001.
- [337] M. Yi, C. Wang, and K. Yang. Discontinuity-induced intermittent synchronization transitions in coupled non-smooth systems. *Chaos: An Interdisciplinary Journal of Nonlinear Science*, 30(3):033113, 2020.
- [338] H. Yoon, S. H. Choi, S. K. Kim, H. B. Kwon, S. M. Oh, J.-W. Choi, Y. J. Lee, D.-U. Jeong, and K. S. Park. Human heart rhythms synchronize while co-sleeping. *Frontiers in physiology*, 10:190, 2019.
- [339] K. Yoshimura and K. Arai. Phase reduction of stochastic limit cycle oscillators. *Physical review letters*, 101(15):154101, 2008.
- [340] J. Yu, C. Hu, H. Jiang, and X. Fan. Projective synchronization for fractional neural networks. *Neural Networks*, 49:87–95, 2014.
- [341] D. Yurchenko, Z. H. Lai, G. Thomson, D. V. Val, and R. V. Bobryk. Parametric study of a novel vibro-impact energy harvesting system with dielectric elastomer. *Applied Energy*, 208:456–470, 2017.

- [342] G. Zhang, Z. Liu, and Z. Ma. Generalized synchronization of different dimensional chaotic dynamical systems. *Chaos, Solitons and Fractals*, 32:773–779, 2007.
- [343] W. Zhang, Y. Tang, X. Wu, and J. A. Fang. Synchronization of nonlinear dynamical networks with heterogeneous impulses. *IEEE Transactions on Circuits and Systems-I*, 61:1220–1228, 2014.
- [344] Z. Zhao and H. Gu. Transitions between classes of neuronal excitability and bifurcations induced by autapse. *Scientific Reports*, 7(1):1–15, 2017.
- [345] C. Zou and J. Yang. Piecewise linear differential system with a center-saddle type singularity. *Journal of Mathematical Analysis and Applications*, 459(1):453–463, 2018.

Appendix A

Saltation matrix and the Floquet exponent formula

Let us consider a periodic orbit $x^\gamma(t)$ of the system (4.4) and a perturbed trajectory $\tilde{x}(t) = x^\gamma(t) + \delta x(t)$, for some small perturbations $\delta x(t) \in \mathbb{R}^n$, and then linearise the equation of motion around the periodic trajectory. Between switching events, perturbations are governed by

$$\frac{d\delta x(t)}{dt} = Df_\mu \delta x(t), \quad \delta x(0) = \delta x_0, \quad (\text{A.1})$$

where the Jacobian Df_μ is a piecewise constant matrix (independent from the periodic solution),

$$Df_\mu = A_\mu, \quad \mu = 1, \dots, N, \quad (\text{A.2})$$

inside the regions R_μ , so that $\delta x(t) \equiv G(A_\mu; t)\delta x_0 = \exp(A_\mu t)\delta x_0$ where δx_0 is the initial perturbation at each region. We denote unperturbed event times by t_μ and that of perturbed events by $\tilde{t}_\mu = t_\mu + \delta t_\mu$, which are prescribed by $h_\mu(x^\gamma(t_\mu)) = 0$ and $h_\mu(\tilde{x}(\tilde{t}_\mu)) = 0$, respectively. The periodic and perturbed states after the switching event are given by $x^\gamma(t_\mu^+) = \mathcal{J}_\mu(x^\gamma(t_\mu^-))$ and $\tilde{x}(\tilde{t}_\mu^+) = \mathcal{J}_\mu(\tilde{x}(\tilde{t}_\mu^-))$, where \mathcal{J}_μ is the switch rule. Here we introduce $x(t_\mu^-) = \lim_{\Delta \rightarrow 0^+} x(t_\mu - \Delta)$ so that the superscript shows that we evaluate $x(t)$ (or its derivative) immediately before the switching event, and similarly $x(t_\mu^+) = \lim_{\Delta \rightarrow 0^+} x(t_\mu + \Delta)$ that immediately after. Now we consider the case $\delta t_\mu > 0$, in which $x^\gamma(t)$ and $\tilde{x}(t)$ are on opposite sides of the switching man-

ifold ($x^\gamma(t)$ have already crossed the switching boundary). One can easily obtain a similar derivation for $\delta t_\mu < 0$, see for example [217]. Then we have $\tilde{x}(\tilde{t}_\mu^-) = \tilde{x}(t_\mu^- + \delta t_\mu) \simeq x^\gamma(t_\mu^-) + \delta x(t_\mu^-) + \dot{x}^\gamma(t_\mu^-)\delta t_\mu$, and using a first order Taylor expansion of \mathcal{J}_μ we obtain

$$\begin{aligned}\tilde{x}(\tilde{t}_\mu^+) &= \mathcal{J}_\mu(\tilde{x}(\tilde{t}_\mu^-)) \simeq \mathcal{J}_\mu(x^\gamma(t_\mu^-) + \delta x(t_\mu^-) + \dot{x}^\gamma(t_\mu^-)\delta t_\mu) \\ &\simeq \mathcal{J}_\mu(x^\gamma(t_\mu^-)) + D\mathcal{J}_\mu(x^\gamma(t_\mu^-))[\delta x(t_\mu^-) + \dot{x}^\gamma(t_\mu^-)\delta t_\mu] \\ &\simeq x^\gamma(t_\mu^+) + D\mathcal{J}_\mu(x^\gamma(t_\mu^-))[\delta x(t_\mu^-) + \dot{x}^\gamma(t_\mu^-)\delta t_\mu],\end{aligned}\tag{A.3}$$

where $D\mathcal{J}_\mu$ is the Jacobian of \mathcal{J}_μ . In addition to this, a Taylor expansion of $h_\mu(\tilde{x}(\tilde{t}_\mu^-))$ (up to the first order) can be calculated as

$$\begin{aligned}h_\mu(\tilde{x}(\tilde{t}_\mu^-)) &= h_\mu(\tilde{x}(t_\mu^- + \delta t_\mu)) = h_\mu(x^\gamma(t_\mu^- + \delta t_\mu) + \delta x(t_\mu^- + \delta t_\mu)) \\ &\simeq h_\mu(x^\gamma(t_\mu^-) + \dot{x}^\gamma(t_\mu^-)\delta t_\mu) + \nabla_x h_\mu(x^\gamma(t_\mu^- + \delta t_\mu)) \cdot \delta x(t_\mu^- + \delta t_\mu) \\ &\simeq h_\mu(x^\gamma(t_\mu^-)) + \nabla_x h_\mu(x^\gamma(t_\mu^-)) \cdot \dot{x}^\gamma(t_\mu^-)\delta t_\mu \\ &+ \nabla_x h_\mu(x^\gamma(t_\mu^-)) \cdot \delta x(t_\mu^-).\end{aligned}\tag{A.4}$$

Using this along with the definition of the continuous indicator functions $h_\mu(x^\gamma(t_\mu)) = 0 = h_\mu(\tilde{x}(\tilde{t}_\mu))$, we obtain

$$\delta t_\mu = -\frac{\nabla_x h_\mu(x^\gamma(t_\mu^-)) \cdot \delta x(t_\mu^-)}{\nabla_x h_\mu(x^\gamma(t_\mu^-)) \cdot \dot{x}^\gamma(t_\mu^-)}.\tag{A.5}$$

Furthermore, we can approximate $\tilde{x}(t_\mu^+)$ by pulling back the perturbed solution δt_μ time unit starting from $\tilde{x}(\tilde{t}_\mu^+)$ as

$$\begin{aligned}\tilde{x}(t_\mu^+) &\simeq \tilde{x}(\tilde{t}_\mu^+) - \dot{\tilde{x}}(\tilde{t}_\mu^+)\delta t_\mu \simeq \tilde{x}(\tilde{t}_\mu^+) - \dot{x}^\gamma(t_\mu^+ + \delta t_\mu)\delta t_\mu \\ &\simeq \tilde{x}(\tilde{t}_\mu^+) - \dot{x}^\gamma(t_\mu^+)\delta t_\mu.\end{aligned}\tag{A.6}$$

Then, using (A.3) and (A.6) we find

$$\begin{aligned}
\delta x(t_\mu^+) &= \tilde{x}(t_\mu^+) - x^\gamma(t_\mu^+) \simeq \tilde{x}(t_\mu^+) - \dot{x}^\gamma(t_\mu^+) \delta t_\mu - x^\gamma(t_\mu^+) \\
&\simeq x^\gamma(t_\mu^+) + D\mathcal{J}_\mu(x^\gamma(t_\mu^-))[\delta x(t_\mu^-) + \dot{x}^\gamma(t_\mu^-) \delta t_\mu] \\
&- [x^\gamma(t_\mu^+) + \dot{x}^\gamma(t_\mu^+) \delta t_\mu] \\
&= D\mathcal{J}_\mu(x^\gamma(t_\mu^-))\delta x(t_\mu^-) + [D\mathcal{J}_\mu(x^\gamma(t_\mu^-))\dot{x}^\gamma(t_\mu^-) - \dot{x}^\gamma(t_\mu^+)]\delta t_\mu. \quad (\text{A.7})
\end{aligned}$$

Hence, using (A.5) and (A.7) we may write δx^+ in the form

$$\delta x^+ = S(t_\mu)\delta x^-,$$

where $S(t)$ is the saltation matrix:

$$\begin{aligned}
S(t_\mu) &= D\mathcal{J}_\mu(x^\gamma(t_\mu^-)) \\
&+ \frac{[\dot{x}^\gamma(t_\mu^+) - D\mathcal{J}_\mu(x^\gamma(t_\mu^-))\dot{x}^\gamma(t_\mu^-)][\nabla_x h_\mu(x^\gamma(t_\mu^-))]^\top}{\nabla_x h_\mu(x^\gamma(t_\mu^-)) \cdot \dot{x}^\gamma(t_\mu^-)}. \quad (\text{A.8})
\end{aligned}$$

Therefore, the overall evaluation of $\delta x(t)$ after one period of motion is

$$\delta x(T) = \mathcal{M}\delta x(0), \quad (\text{A.9})$$

with the (generalised) monodromy matrix

$$\mathcal{M} = S(t_N) G(A_N; T_N) \dots S(t_2) G(A_2; T_2) S(t_1) G(A_1; T_1), \quad (\text{A.10})$$

where T_1, \dots, T_N are the times of flight in each region. Hence, the periodic solution $x^\gamma(t)$ will be stable if the nontrivial eigenvalues, which are also called Floquet multiplier, of the matrix \mathcal{M} reside within the unit disc.

Particularly, for the planar PWL models considered in the Chapter 3, the switching rule is $\mathcal{J}(x) = x$, so that $D\mathcal{J} = I_2$, where I_2 is 2×2 identity matrix, and $\nabla_x h_\mu(x) = (\partial_v, \partial_w)(v - a_\mu) = (1, 0)^\top$, therefore using the formula (A.8) along with the system equations, we can explicitly calculate the saltation matrix as

$$S(t_\mu) = \begin{bmatrix} \frac{\dot{v}^\gamma(t_\mu^+)}{\dot{v}^\gamma(t_\mu^-)} & 0 \\ \frac{(\dot{w}^\gamma(t_\mu^+) - \dot{w}^\gamma(t_\mu^-))}{\dot{v}^\gamma(t_\mu^-)} & 1 \end{bmatrix}. \quad (\text{A.11})$$

In the following Fig. A.1, we illustrate a schematic representation of this switching process. Remembering that one eigenvalues of the matrix \mathcal{M} is equal to 1,

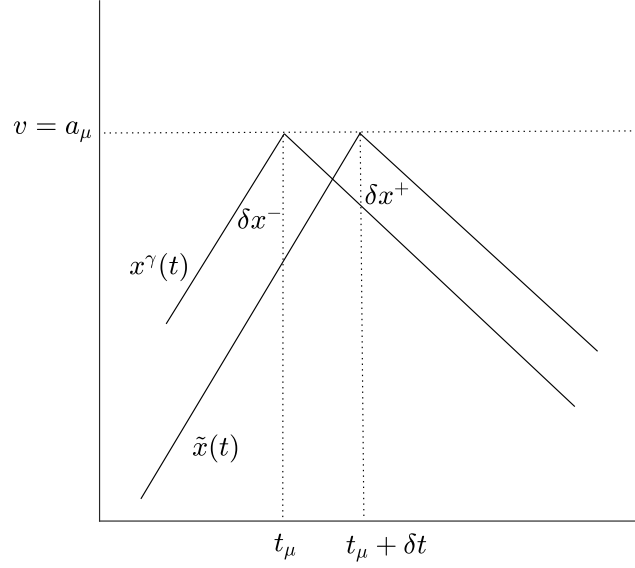


Figure A.1: Schematic representation of a switching event for the models considered in the Chapter 3. A periodic orbit $x^\gamma(t)$ crosses switching manifold $v = a_\mu$ at $t = t_\mu$ and a perturbed orbit $\tilde{x}(t)$ crosses at $t = t_\mu + \delta t$. A saltation matrix $S(t_\mu)$ maps δx^- to δx^+ at $t = t_\mu$.

that corresponds to perturbations along the periodic orbit, and denoting the nontrivial multiplier by $e^{\kappa T}$, we find $\det \mathcal{M} = e^{\kappa T} \times 1$. Thus,

$$\begin{aligned}
 e^{\kappa T} &= \det [S(t_N) G(A_N; T_N) \dots S(t_2) G(A_2; T_2) S(t_1) G(A_1; T_1)] \\
 &= \det S(t_N) \dots \det S(t_1) \det G(A_N; T_N) \dots \det G(A_1; T_1) \\
 &= \frac{\dot{v}^\gamma(t_N^+)}{\dot{v}^\gamma(t_N^-)} \dots \frac{\dot{v}^\gamma(t_1^+)}{\dot{v}^\gamma(t_1^-)} \det e^{A_N T_N} \dots \det e^{A_1 T_1}
 \end{aligned} \tag{A.12}$$

Finally, using the well known fact $\det e^{At} = e^{\text{Tr} At}$, we derive the useful formula

$$\kappa = \frac{1}{T} \sum_{\mu=1}^N \left[T_\mu \text{Tr } A_\mu + \log \frac{\dot{v}^\gamma(t_\mu^+)}{\dot{v}^\gamma(t_\mu^-)} \right]. \tag{A.13}$$

Appendix B

The absolute model: Period is independent of \bar{w}

The absolute model (3.30)-(3.31) by choosing parameter $a = 0$ has the switching manifold $h(x) = v$. Therefore it can be written in the form (3.7) with

$$b_1 = b_2 = \begin{bmatrix} 0 \\ \bar{w}/2 - \bar{v} \end{bmatrix} \equiv \begin{bmatrix} 0 \\ \xi \end{bmatrix}. \quad (\text{B.1})$$

Using (3.11), we can write the solution in the form

$$x(t) = \begin{cases} G^1(t)x^1(0) + K^1(t)b_1 & \text{if } v \geq 0, \\ G^2(t)x^2(0) + K^2(t)b_2 & \text{if } v < 0, \end{cases} \quad (\text{B.2})$$

where G^μ and K^μ , $\mu = 1, 2$, are given in (3.12). Then we can construct a periodic orbit that satisfies

$$\begin{aligned} x^1(T_1) &= G^1(T_1)x^1(0) + K^1(T_1)b_1, \\ x^2(T_2) &= G^2(T_2)x^2(0) + K^2(T_2)b_2, \end{aligned} \quad (\text{B.3})$$

at T_1 and T_2 . Denoting $x = (v, w)^\top$ and setting the conditions (3.15) such that $x^1(T_1) = (0, w^1)^\top = x^2(0)$ and $x^2(T_2) = (0, w^0)^\top = x^1(0)$ we may write the component of (B.3) as

$$\begin{aligned} 0 &= G_{12}^1(T_1)w^0 + K_{12}^1(T_1)\xi, & w^1 &= G_{22}^1(T_1)w^0 + K_{22}^1(T_1)\xi, \\ 0 &= G_{12}^2(T_2)w^1 + K_{12}^2(T_2)\xi, & w^0 &= G_{22}^2(T_2)w^1 + K_{22}^2(T_2)\xi, \end{aligned}$$

by rearranging this, we find

$$\begin{aligned} w^0 &= -K_{12}^1(T_1)\xi/G_{12}^1(T_1), & w^0 &= (w^1 - K_{22}^1(T_1)\xi)/G_{22}^1(T_1), \\ w^1 &= -K_{12}^2(T_2)\xi/G_{12}^2(T_2), & w^1 &= (w^0 - K_{22}^2(T_2)\xi)/G_{22}^2(T_2). \end{aligned}$$

By combining these equations we obtain,

$$\begin{aligned} -K_{12}^1(T_1)\xi/G_{12}^1(T_1) &= [-K_{12}^2(T_2)\xi/G_{12}^2(T_2) - K_{22}^1(T_1)\xi]/G_{22}^1(T_1), \\ -K_{12}^2(T_2)\xi/G_{12}^2(T_2) &= [-K_{12}^1(T_1)\xi/G_{12}^1(T_1) - K_{22}^2(T_2)\xi]/G_{22}^2(T_2). \end{aligned}$$

We observe that ξ cancels in both equations on both sides. Also using the explicit formulations (3.18)-(3.19), we see that entries of G^μ and K^μ are independent from ξ . Thus the remaining equations for solving T_1 and T_2 are not depend on ξ and hence the period is independent from the choice of \bar{w} and \bar{v} . Numerically, this is shown in Fig. 3.6 while \bar{w} is varying.

Appendix C

Coupling functions

Here we illustrate shape of the necessary 2π –periodic coupling functions $H_1(\chi)$, $H_3(\chi)$, $H_4(\chi)$ and $H_6(\chi)$ to determine the stability of the synchronous state by implementing phase-amplitude network formalism in following Fig. C.1, Fig. C.2, Fig. C.3, and Fig. C.4, respectively.

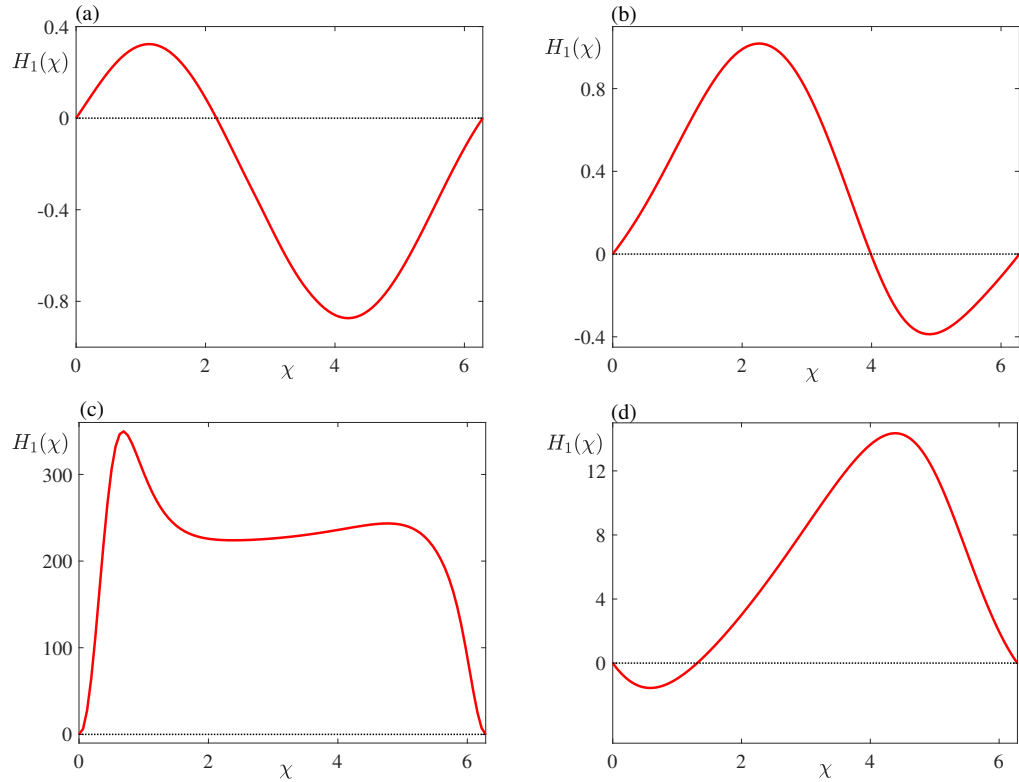


Figure C.1: Illustration of $H_1(\chi)$. (a)-The McKean model with parameters as in Fig. 3.3. (b)-The absolute model with parameters as in Fig. 3.5. (c) Homoclinic loop model with parameters as in Fig. 3.7. (d)-PML model with parameters as in Fig. 3.10.

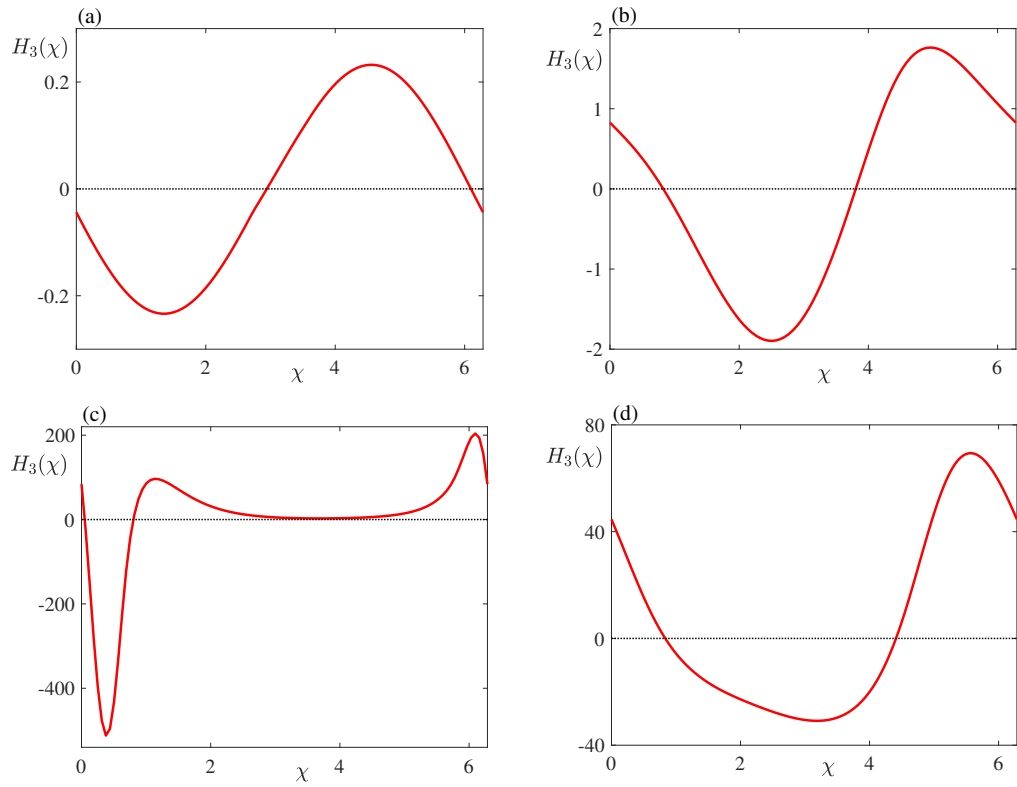


Figure C.2: Illustration of $H_3(\chi)$. (a)-The McKean model with parameters as in Fig. 3.3. (b)-The absolute model with parameters as in Fig. 3.5. (c) Homoclinic loop model with parameters as in Fig. 3.7. (d)-PML model with parameters as in Fig. 3.10.

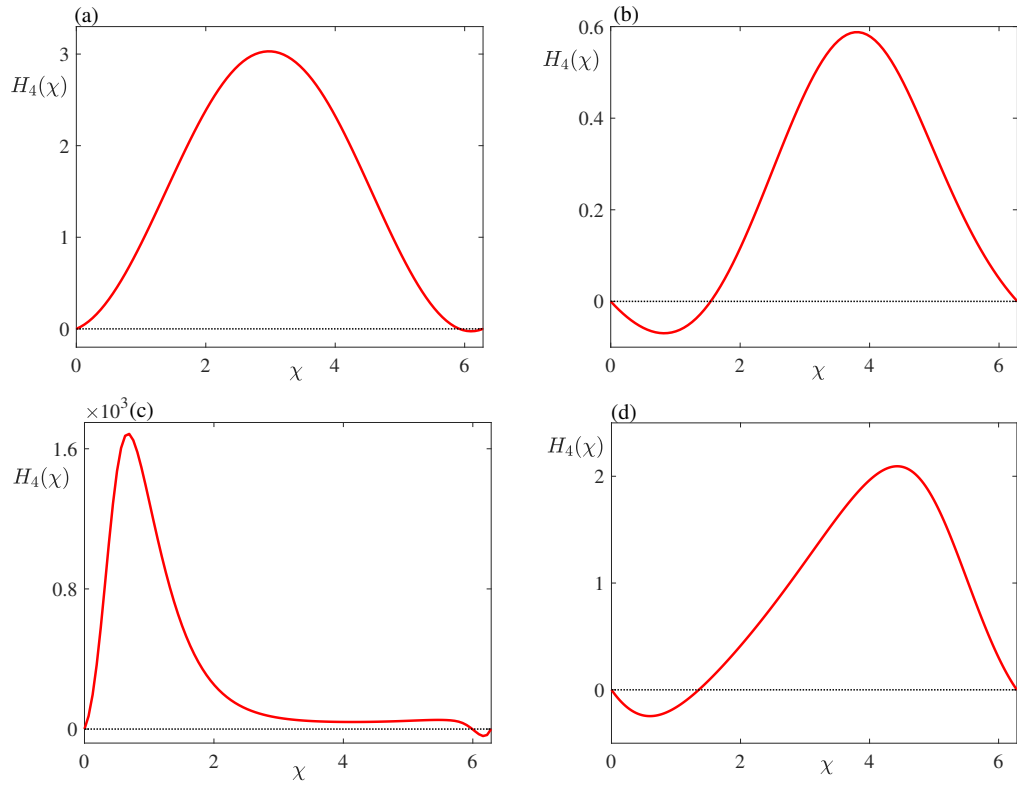


Figure C.3: Illustration of $H_4(\chi)$. (a)-The McKean model with parameters as in Fig. 3.3. (b)-The absolute model with parameters as in Fig. 3.5. (c) Homoclinic loop model with parameters as in Fig. 3.7. (d)-PML model with parameters as in Fig. 3.10.

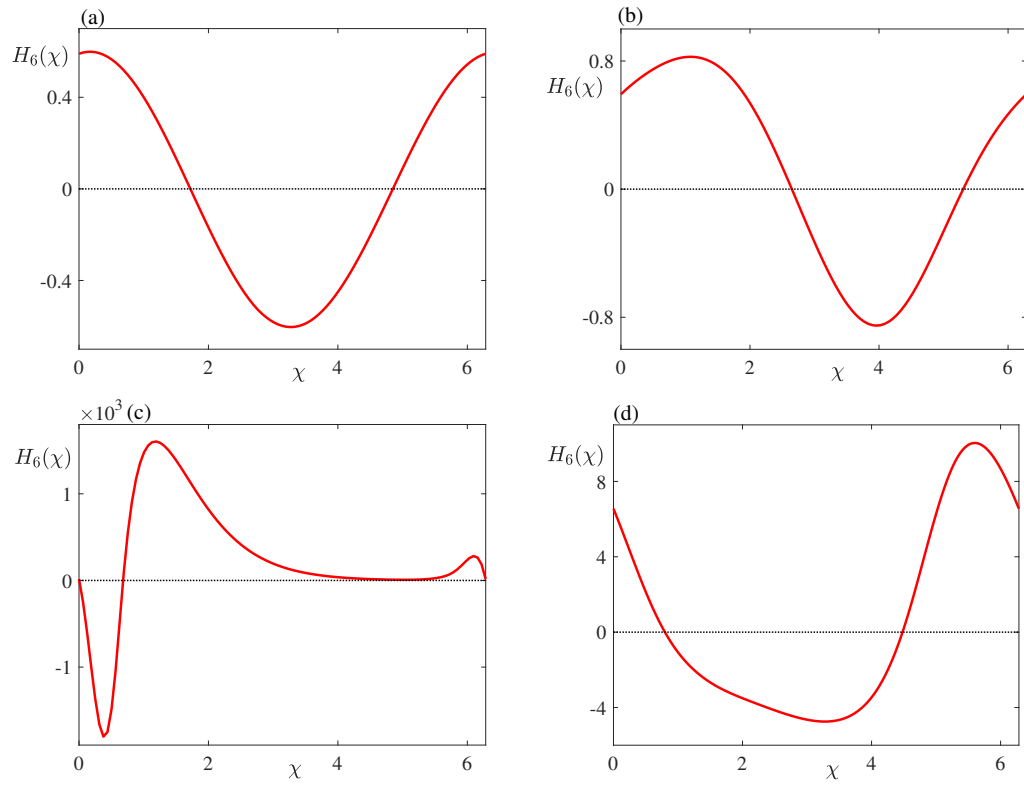


Figure C.4: Illustration of $H_6(\chi)$. (a)-The McKean model with parameters as in Fig. 3.3. (b)-The absolute model with parameters as in Fig. 3.5. (c) Homoclinic loop model with parameters as in Fig. 3.7. (d)-PML model with parameters as in Fig. 3.10.